Multiphysics Computational Modelling of High-Speed Partially-Rarefied Flows

by
Simone Colonia

Supervisors:
Rene Steijl
Geroge Barakos

School of Engineering - University of Liverpool

September 2015

Abstract

Hypersonic flows of practical importance often involve flow fields having continuum and rarefied regions. It is well known that Boltzmann equation based methods can provide more physically accurate results in flows having rarefied and non-equilibrium regions than continuum flow models. However, these methods are extremely computational expensive in near-equilibrium regions, which prohibits their application to practical problems with complex geometries and large domains where continuum and rarefied regions coexist. On the other hand, Navier-Stokes (or Euler) based methods are computationally efficient in simulating a wide variety of flow problems, but the use of continuum theories for the flow problems involving rarefied gas or very small length scales produces inaccurate results due to the breakdown of the continuum assumption and occurrence of strong thermal non-equilibrium. A practical approach for solving flow fields having continuum to rarefied regions is to develop numerical methods combining approaches able to compute the continuum regime and/or the rarefied (or thermal non-equilibrium) regime. The aim of this thesis is to investigate and develop new methods for the calculation of hypersonic flow fields that contain both continuum and rarefied flow regions.

The first part of the work is dedicated to the continuum regime. Among the different numerical inviscid flux functions available in the literature, the AUSM-family has been shown to be capable of solving to a good accuracy flow fields at a wide range of Mach regime including high-speed flows. For this reason an implicit formulation of the AUSM$^+$ and AUSM$^+$*up* schemes, with a Jacobian defined fully analytically, has been implemented in the Helicopter Multi-Block CFD code (HMB2), developed at the University of Liverpool, to predict continuum high-speed flow. The original form of the schemes lead to the presence of different branches in the computational algorithm for the Jacobian since do not guarantee the fluxes to be continuously differenciable functions of the primitive variables. Thus, a novel formulation of the

AUSM$^+$ and AUSM$^+$*up* schemes is proposed in chapter 2. Here, a blending is introduced by means of parametric sigmoidal functions at the points of discontinuity in the schemes formulations. Predictions for wide range of test cases obtained employing the proposed formulation are compared with results available in the literature in chapter 3 to show that the reliability of the schemes has been preserved in the proposed formulation.

Later on, the work focuses on partially-rarefied high-speed flows. At the University of Liverpool, this kind of flows are simulated using the hybrid approach available in the Multi-Physics Code (MΦC) where a discrete velocity method for kinetic Boltzmann equations is coupled with a traditional Navier-Stokes solver. Firstly, the discrete velocity method has been improved with the implementation of kinetic models for diatomic gases in the framework. A validation of the correctness of the implemented models is discussed in chapter 6. However, employing a discrete velocity method in hybrid simulation leads to high computational and memory cost. In this context, gas-kinetic schemes have been identified by the author, in the related literature, as efficient approaches, relative to discrete velocity methods, capable of modelling complex gas flows with moderate rarefaction effects but with significant thermal non-equilibrium. Thus, two gas-kinetic schemes, analytically defined on the basis of the Chapman-Enskog expansion of non-dimensional Shakhov and Rykov models, have been proposed in chapter 5. Compared with similar gas-kinetic schemes available in the literature, the presented schemes differ in the approach employed to evaluate the terms of Chapman-Enskog solutions and in the kinetic models used as mathematical foundations of the schemes. In chapters 6 and 7 the scheme is tested for various cases and Mach numbers, including complex 3D flows, proving to be a viable way to improve the performance of hybrid simulations, maintaining an acceptable level of reliability, if used in place of more complex methods for weakly rarefied flows. Finally, chapter 8 includes a summary of the findings as well as suggestions for future works.

Contents

List of Figures

Acknowledgement

The financial support by the University of Liverpool is gratefully acknowledged. Furthermore, this work has made use of the University of Liverpool cluster Chadwick [8], the SuperMUC supercomputer at Leibniz-Rechenzentrum [9] through a PRACE project and the facilities of N8 HPC [10] provided and funded by the EPSRC and N8 consortium coordinated by the Universities of Leeds and Manchester. A special thank goes to both my supervisors for their guidance and support over these years.

Publications

Journals:

- Implicit implementation of the AUSM$^+$ and AUSM$^+$up schemes. Colonia S., Steijl R. and Barakos G.N., International Journal for Numerical Methods in Fluids, Volume 75, Issue 10, pages 687-712, DOI: 10.1002/fld.3891.

- Kinetic Models and Gas Kinetic Schemes for Hybrid Simulation of Partially Rarefied Flows. Colonia S., Steijl R. and Barakos G.N., AIAA Journal (Articles in Advance), DOI: 10.2514/1.J054137.

- A Gas Kinetic Scheme for Hybrid Simulation of Partially Rarefied Flows. Colonia S., Steijl R. and Barakos G.N., Progress in Flight Physics Volume 8 - EUCASS book series, accepted.

Conferences:

- Assessment of Implicit Implementation of the AUSM$^+$ Method and the SST Model for Viscous High Speed Flow. Colonia S., Steijl R. and Barakos G.N., 5^{th} European Conference for Aeronautics and Space Sciences, 1-5 July 2013, Munich (Germany).

- Kinetic Models with Rotational Degrees of Freedom for Hybrid Methods. Colonia S., Steijl R. and Barakos G.N., 6th European Conference on Computational Fluid Dynamics (ECFD VI), ECCOMAS 2014, 20-25 July 2014, Barcelona (Spain).

- Kinetic Models and Gas Kinetic Schemes for Hybrid Simulation of Partially Rarefied Flows. Colonia S., Steijl R. and Barakos G.N., AIAA Atmospheric Flight Mechanics Conference 2015, 5-9 January 2015, Kissimmee (Florida), DOI: 10.2514/6.2015-0521.

- Gas Kinetic Schemes for Hybrid Simulation of Partially Rarefied Flows. Colonia S., Steijl R. and Barakos G.N., 6^{th} European Conference for Aeronautics and Space Sciences, 29 June to 3 July 2015, Krakow (Poland).

- Coupling of Particle-Based and Grid-Based Methods within Object-Oriented Multi-Physics CFD Framework. Steijl R., Colonia S. and Barakos G.N., 4^{th} International Conference on Particle-Based Methods, PARTICLES 2015, 28-30 September 2015, Barcelona (Spain).

Technical notes:

- Shakhov Model and GKS for Monoatomic Gases in MΦC. Colonia S., MΦC-TN15-001, University of Liverpool.

- Rykov Model and GKS with Rotational Degrees of Freedom in MΦC. Colonia S., MΦC-TN15-002, University of Liverpool.

Nomenclature

a	Speed of sound
$a_{n=1,2,3...}$	Taylor expansion coefficient
$\mathbf{c}$	Particle velocity vector
c_p	Pressure coefficient
c_x	Particle velocity in x-direction
c'_x	$c_x - u_x$, particle velocity fluctuation
e	Specific energy
E	Energy/Error
f	Particle/velocity distribution function
F	mf
f_{vol}	Mass forces
$\mathbf{F}$	Flux vector
h	Specific enthalpy
H	Enthalpy
J	Jacobian matrix
Kn	Knudsen Number
m	Molecular mass
M	Mach number
$\mathbf{n}$	Cell face normal vector
n_x	Unit vector in x-direction
p	ρT (non-dimensional equilibrium pressure)
$\mathbf{P}$	Primitive variables vector
p_r	ρT_r (non-dimensional rotational pressure)
p_t	ρT_t (non-dimensional translational pressure)
q_x	Total heat flux in x-direction
q_x^r	Rotational heat flux in x-direction
q_x^t	Translational heat flux in x-direction
R	Gas constant
Re	Reynolds number
sig	Sigmoidal function
t	Time variable
T	Total temperature
T_r	Rotational temperature
T_t	Translational temperature
u_x	Velocity in x-direction

$\mathbf{V}$	Velocity Vector
$\mathbf{W}$	Conservative variables vector
$\mathbf{W}_{S/R}$	Conservative variables, Shakhov/Rykov model
$\mathbf{x}$	Spatial coordinates vector
Z_r	Collision number
γ	Specific heat ratio
δ	Boundary layer thickness / Standoff distance / Kronecker Delta
Δ	Increment / Step
ζ	Rotational degrees of freedom
λ	Particle mean free path
μ	Viscosity
ξ	Degree of departure from the local thermodynamic equilibrium
ρ	Density
τ	Viscous stress, particle collision time
Φ	Generic macroscopic variable
$\mathbf{\Phi}$	Vector of macroscopic variables
$\mathbf{\Psi}$	Vector of the velocity distribution function moments

Subscripts and Superscripts

$\overline{\Phi}$	Average value of Φ
$\hat{\Phi}$	Non-dimensional value of Φ
Φ_{ref}	Reference value of Φ
Φ_{∞}	Free stream value of Φ
$\Phi_{-\infty}$	Free stream value of Φ upstream of the normal shock
$\Phi_{+\infty}$	Free stream value of Φ downstream of the normal shock
Φ_i, Φ_L	Value of Φ at the left state
Φ_{i+1}, Φ_R	Value of Φ at right state
$\Phi_{j+1/2}$	Value of Φ at interface
Φ_n	Value of Φ normal to the cell face

Acronyms

ADI	Alternating Direction Implicit
AUSM	Advection Upstream Splitting Method
BGK	Bhatnagar-Gross-Krook model
BGK-NS	Gas-Kinetic BGK scheme for the NS equations
BSL	Baseline
BTE	Boltzmann Transport Equation
CE	Chapman-Enskog
CEV	Crew Exploration Vehicle
CFD	Computational Fluid Dynamics
CFL	Courant Friedrichs Lewy
DSMC	Direct Simulation Monte Carlo
DVM	Discrete Velocity Method
EFM	Equilibrium Flux Method
ES	Ellipsoidal-Statistical
ESA	European Space Agency
FEM	Finite Element Method
GCG	Generalised Conjugate Gradient
GMRES	Generalised Minimal Residual
GKS	Gas Kinetic Scheme
GKS τ^*	GKS with modified τ
HEXAFLY	High-Speed Experimental Fly Vehicles
HLLE	Harten, Lax, van Leer and Einfeldt
HMB	Helicopter Multi-Block Code
ILU	Incomplete Lower Upper
ISS	International Space Stations
IXV	Intermediate eXperimental Vehicle
LAPCAT	Long-Term Advanced Propulsion Concepts and Technologies
LAURA	Langley Aerothermodynamic Upwind Relaxation Algorithm
LE	Leading Edge
LM-Roe	Low-Mach Roe
LU-SGS	Lower-Upper Symmetric Gauss-Seidel
MD	Molecular Dynamics
MΦC	Multi-Physics Code
MPC	Modular Particle-Continuum method
MPCV	Multi-Purpose Crew Vehicle
MUSCL	Monotone Upstream-Centred Scheme for Conservation Laws

NS	Navier-Stokes equations
ONERA	Office National d'Etudes et de Recherches Aérospatiales
OTV	Orbital Test Vehicle
RANS	Reynolds-Averaged Navier-Stokes
SABRE	Synergetic Air-Breathing Rocket Engine
R-GKS	GKS based on the Rykov model
R-Model	Rykov Model
S-GKS	GKS based on the Shakhov model
S-Model	Shakhov Model
SST	Shear-Stress Transport
S-UGKS	UGKS based on the Shakhov model
TE	Trailing Edge
TVD	Total Variation Diminishing
UGKS	Unified Gas Kinetic Scheme
VDF	Velocity Distribution Function

Chapter 1

Introduction

1.1 Motivation

Until its last flight in 2011, the Space Shuttle has been the only manned lifting body re-entry vehicle, while among ballistic re-entry capsules the Russian Soyuz, whose program started in the late 1960's, and the Chinese Shenzhou, from early 2000's, are still operational. However, in the United States, works on unmanned hypersonic and re-entry vehicles has continued since the early 2000's with recent examples being the Boeing X-37 Orbital Test Vehicle (OTV) and X-51 Waverider still under development. Moreover, in these years, the NASA Orion Multi-Purpose Crew Vehicle (MPCV) and the SpaceX Dragon V2 spacecraft are being developed with the intend to facilitate space human exploration as well as to provide means to deliver or retrieve crews to or from the International Space Station (ISS), mission at the moment accomplished by the Soyuz. On the European front, at the beginning of 2015, the European Space Agency (ESA) has successfully launched the Intermediate eXperimental re-entry Vehicle (IXV) to validate European reusable lifting body technologies.

Regarding the United Kingdom, nowadays an important ongoing project sees the country as primary investor. The program is led by Reaction Engines Limited and it aims to develop a single-stage-to-orbit space-plane named Skylon and its engine SABRE, a combined air-breathing rocket propulsion system. In July 2013 the British government pledged 60m to support the production of a full-scale prototype of the SABRE engine.

Development of new hypersonic and re-entry vehicles demands accurate predictions of pressure, heat flux and shear stress distributions along the entire vehicle and across all possible flight environments.

Indeed, these quantities define the aerothermodynamic performance of the vehicle necessary to design the structure as well as the navigation, control and thermal protection systems.

A gas is composed of atoms and molecules in continuous motion colliding with each other. Molecules in a gas contain translational, rotational and vibrtional energy (as well as chemical and electrical energy) and an important aspect in modelling hypersonic flows involves predicting the energy transfer between these different modes. When perturbed, the molecular collisions in the gas change the macroscopic quantities and push the flow towards local thermodynamic equilibrium [1]. However, a redistribution of energy among the internal degrees of freedom requires a certain number of molecular collisions and thus a characteristic time depending on temperature and density of the gas. If a very large amount of collisions take place over a change in the state of the gas, the flow energy is instantaneously distributed equally among all modes and the fluid can be considered continuum. On the other hand, if very few collisions occur, significant non-equilibrium can take place such that the flow must be considered rarefied.

The Navier-Stokes equations (NS) provide the conventional mathematical model to represent at macroscopic level a continuum fluid. However, the conservation equations do not form a determinate set unless it is possible to define a constitutive equation for the fluid which links the shear stress tensor and the deformation of the fluid. When the gradients of the macroscopic variables become so steep that their length scale is of the same order as the average distance travelled by molecules between collisions, the number of impacts is not enough to drive the fluid towards a local thermodynamic equilibrium. At these conditions the flow can no longer be considered a continuum and the transport terms in the Navier-Stokes equations fail since the constitutive relation is not valid. The mathematical model at molecular level is the Boltzmann equation (BTE) [11] which recognizes the particle structure of the gas as a system of n discrete molecules and is valid in the whole range of Knudsen numbers [12]. The Boltzmann equation describes the behaviour of a gas by a distribution function representing the probability of particles with certain position and particle-velocity at time t. The macroscopic quantities at each position at time t are given by the moments of the distribution function in the velocity, or phase, space, a Cartesian space having the particle-velocity components as coordinates.

[1] over the time scale of interest all particle degrees of freedom are in equilibrium with each other and can be described by a single temperature.

The parameter that is generally employed to describe the degree of rarefaction in a flow is the Knudsen number, Kn.

$$Kn = \frac{\lambda_\infty}{L_{ref}}. \tag{1.1}$$

Indeed, the latter represents the ratio between the mean-free-path [2] (λ_∞) and a reference length (L_{ref}) of the problem. Locally it can be expressed by means of local mean-free-path and gradients' scale as

$$Kn_Q = \frac{\lambda}{Q}\left|\frac{dQ}{dl}\right| \tag{1.2}$$

where Q represents a generic flow quantity. As $Kn \to 0$ a sufficiently large amount of collisions take

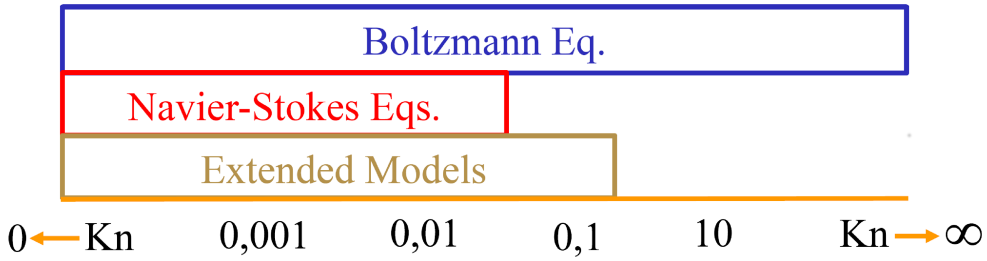

Figure 1.1: The Knudsen number limits on the mathematical models.

place so that even in presence of a perturbation the particles distribution function presents only a small departure from the equilibrium Maxwellian distribution. At this condition, the Navier-Stokes equations can be obtained as hydrodynamic limit of the Boltzmann equation [13]. In contrast, when $Kn \to \infty$, the gas particles experience very few collisions when perturbed and the velocity distribution function is far from the equilibrium Maxwellian. The traditional requirement for the Navier-Stokes equations to be valid is that the Knudsen number should be less than 0.05.

As can be seen from the example in figure 1.2 for the Orion and Apollo re-entry capsules, hypersonic vehicles experience flow fields that can range from being completely free molecular to continuum. At very high altitudes (90Km and up) the flow around these vehicles can be considered entirely rarefied whereas at low altitudes (70Km or below) the flow field could be considered predominantly continuum. At intermediate altitudes, the flow around hypersonic aircraft can be characterised as mainly continuum with localised areas, generated by the rapid expansion in the wake of the vehicle as well as by strong

[2] The distance travelled by a particle between successive collisions.

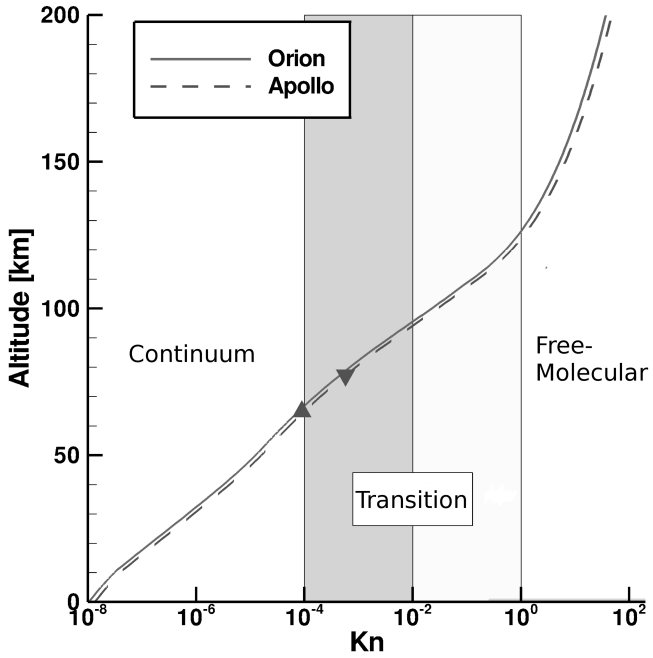

Figure 1.2: Knudsen number as a function of the altitude for the Orion and Apollo re-entry vehicles, from [1].

gradients in shock waves and boundary layers, that display rarefaction effects.

Moreover, it is well known that, due to the high free stream enthalpies and steep flow field gradients, hypersonic flows may display different forms of non-equilibrium processes. At low temperatures (< 800K) air can be modelled as a mixture of calorically perfect gases having constant specific heats since only translational and rotational modes are fully excited; above 800K the specific heats become functions of the temperature due to the gradual excitation of the vibrational degrees of freedom. As the air temperature increases to 2500K also chemical reactions occur. The classical continuum approach to model flows in chemical non-equilibrium employs N species continuity equations (where N is the number of species considered), 3 momentum equations, and 3 energy equations describing the conservation of vibrational, electronic, and total energies [14, 15]. Alternatively, a reduced two-temperature model can be obtained by combining the equations for vibrational energy conservation and electronic energy conservation into a single relation for vibrational-electronic energy conservation. The latter approximation may be invalid in the viscous boundary layer adjacent to the wall (where the physically correct boundary conditions on the vibrational and electronic energies are inconsistent with a single temperature) but it allows for a

computationally more appealing formulation [14]. Regarding the reaction rates required by the source terms of the continuity equations, several chemical kinetic models, based on Arrhenius formulations of the reaction rates, for air are available in the literature [16]. In contrast, rarefied simulations of flows using the BTE can intrinsically account for the effects of both chemical and thermal non-equilibrium, provided the gas components are modeled with the appropriate degrees of freedom [17].

Thus, the development of present and future hypersonic and re-entry vehicles requires predictions for a wide range of conditions and flow regimes. Wind tunnel facilities can not reproduce realistic simulations of many of these flow conditions and regimes, and for this reason numerical approaches are becoming more and more relevant in the design of high-speed vehicles. As an example, the aerodynamic design of the Space Shuttle was based on experimental data from cold hypersonic wind tunnels and, since high temperature effects could not be modelled properly, they were extrapolated to flight condition using simplified models. This led in the first flight of the STS-1 to an unpredicted increase in the nose-up pitching moment that almost caused the loss of the aircraft.

In this context, the purpose of the current dissertation is to deliver an improvement among the current available numerical approaches for partially-rarefied, high-speed, flows involving temperatures at which translational and rotational modes can be considered fully excited and vibrational-chemical non-equilibrium does not occur. This kind of flows are often encountered by hypersonic vehicles, for commercial and defense applications, in their flight path.

1.2 Literature Survey About Methods for Partially-Rarefied Flow

Because the Navier-Stokes equations are an accurate model of the flow for $Kn < 0.05$ [12] traditional continuum computational fluid dynamics models can simulate gas flows only if their Knudsen number is below this limit. On the other hand the mathematical model at molecular level is the Boltzmann equation and for flow fields where strong rarefaction effects occur the Direct Simulation Monte Carlo method (DSMC) [17, 18, 19] is typically employed to statistically estimate the solution of the BTE. Alternatively a discrete velocity method (DVM) [20, 21, 22, 23, 24] can be used to solve a kinetic model approximation of the BTE such as the Bhatnagar-Gross-Krook (BGK) model [25], the Shakhov model [26] and Ellipsoidal-Statistical (ES) model [27] for monoatomic gases or the Rykov model [28] and ES model [29] for diatomic gases with rotational non-equilibrium. Recently an alternative method has been presented in [30] where inelastic collisions are the same as in the Rykov model, but elastic collisions are modelled by the Boltzmann collision operator for monoatomic gases.

Numerical approaches based on the BTE can represent well any regime, but incur a cost in computational time and memory that is considerably higher than continuum flows methods by several orders of magnitude, due to the larger number of degrees of freedom that the BTE involves, and become rapidly too expensive, often impossible, as the Knudsen number becomes smaller. For this reason, various numerical methods for partially-rarefied flows have been proposed in the literature.

For almost continuum flows, to overcome the limitation of the NS equations the standard procedure is to use slip velocity and temperature jump boundary conditions [31, 32, 33], but the constants which are involved are hard to identify and their validity is still questionable.

It is well known that in the limit of a continuum flow the BTE leads to the Euler or the NS equations when a zeroth or first order Chapman-Enskog (CE) expansion [34] is employed to represent the distribution function, respectively [13]. Different sets of equations, called Burnett and Super-Burnett equations are obtained when higher order CE expansions are used [35]. The Burnett equations provide greater accuracy than the NS equations for shock structures [36]. However, this improvement is achieved only for cases in which the NS equations still represent an adequate model and the Burnett and super-Burnett

equations exhibit also instabilities in transient processes so that small wavelength fluctuations could blow up in time [37].

Another particular class of solutions of the BTE is the one obtained employing a moment method. As example the Grad's 13-moment equations is a set of moments of the BTE in which closure is achieved assuming a Grad-type polynomial series expansions form for the distribution function [38]. In [39] the so-called regularized Grads 13-moment equations are proposed employing a different closure method to add some terms of Super-Burnett order to the usual 13 equations. The latter has been extensively employed in [40] to successfully predict shock wave structures in a monoatomic gas for a wide range of Mach numbers. Alternatively, moment equations can be generated employing the maximum-entropy moment closures as addressed in [41] for one-dimensional normal shock structures in monoatomic gases.

However, the most commonly used approach to simulate partially-rarefied flows is probably represented by hybrid techniques. Firstly introduced in [42, 43, 44, 45], these methods propose to employ the expensive approach only where strictly required, leaving the rest of the domain to a traditional continuum approach. An extensive discussion about this kind of methods is presented in section 1.2.1.

A different but similarly successful approach is the Unified Gas-Kinetic Scheme (UGKS) presented in [46, 47]. The UGKS uses a finite-volume method where the numerical fluxes are based on the solution of the Shakhov model for a monoatomic gas, or the Rykov model for a diatomic gas with rotational non-equilibrium. Its particular formulation allows the scheme to simulate flows in both rarefied and continuum regimes. The latter will be discussed in more detail in section 1.2.2.

1.2.1 Hybrid Methods

To simulate flow fields where continuum and rarefied regimes coexist, hybrid techniques have been introduced in [42, 43, 44, 45]. In these methods, the expensive approach is employed only in regions of the domain where rarefaction effects become predominant and it is coupled with a finite-volume scheme for the NS equations used where the flow can be considered continuum.

A first main challenge of these approaches is how to accurately identify the different regions. The

following continuum breakdown parameter for expanding flows has been proposed firstly in [48]

$$P = M\sqrt{\frac{\pi\gamma}{8}}\left|\frac{dp}{ds}\right| \tag{1.3}$$

where s is the curvilinear coordinate along the streamline and a value P of about 0.05 has been indicated for the limit of the continuum approach. Subsequently, in [49] an expensive numerical investigation of one-dimensional normal shock waves and two-dimensional bow shocks comparing DSMC and NS results has been carried out with the purpose of determining an appropriate and more general breakdown parameter represented by the local Knudsen number (1.2). This led in [50] to state the following breakdown criteria

$$Kn_{max} = max(Kn_\rho, Kn_V, Kn_T) > 0.05 \tag{1.4}$$

where the gradients of all the macroscopic variables are considered. In [51] it has been noticed that, when rotational non-equilibrium is considered, equation (1.4) fails to predict the position of the interfaces between continuum and rarefied domains in the post-shock region where the fluid is still in thermal non-equilibrium. Thus, in [52] a new criterion has been suggested to also consider the latter effect

$$Kn_{max} = max(Kn_\rho, Kn_V, Kn_T, 5 \times \frac{T_t - T_r}{T_r}) > 0.05; \tag{1.5}$$

the new parameter switches on in a compression region where $T_{TRA} > T_{ROT}$ more than 1%. Finally in [53] an improvement on the results has been noticed when also the magnitude of the energy transferred by the rotation-translation relaxation processes compared with the total amount of energy stored in rotational energy was taken into account. This, led to the following revised version of the breakdown criteria

$$Kn_{max} = max(Kn_\rho, Kn_V, Kn_T, \frac{|T_t - T_r|}{2T_r}) > 0.05. \tag{1.6}$$

Since vibrational-translational relaxation is much slower than rotational-translational relaxation, no additional breakdown parameter is needed when also vibrational excitation models are considered [54]. While the most widely used breakdown criteria remains to evaluate the set of local Knudsen numbers based on the characteristic length scales for the local macroscopic quantities shown in equations (1.5) and (1.6) [2, 55, 56, 54, 57]; other more elaborated criteria such as the ratio between the heat flux and

the equilibrium energy flux [58], the residual of the Grad13 moments equations [3] [43] and an indicator function only of density, temperature, heat flux and stress tensor [59] have been proposed.

In hybrid techniques the coupling between the two different simulation methods is achieved by means of an exchange of information among the parts of the domain where they are employed. In recent works, this has been achieved exchanging, between the two solvers, numerical fluxes at the interface, figure 1.3a, or flow state variables throughout an overlap region, figure 1.3b,[2, 55, 56, 54]. Alternatively, a buffer re-

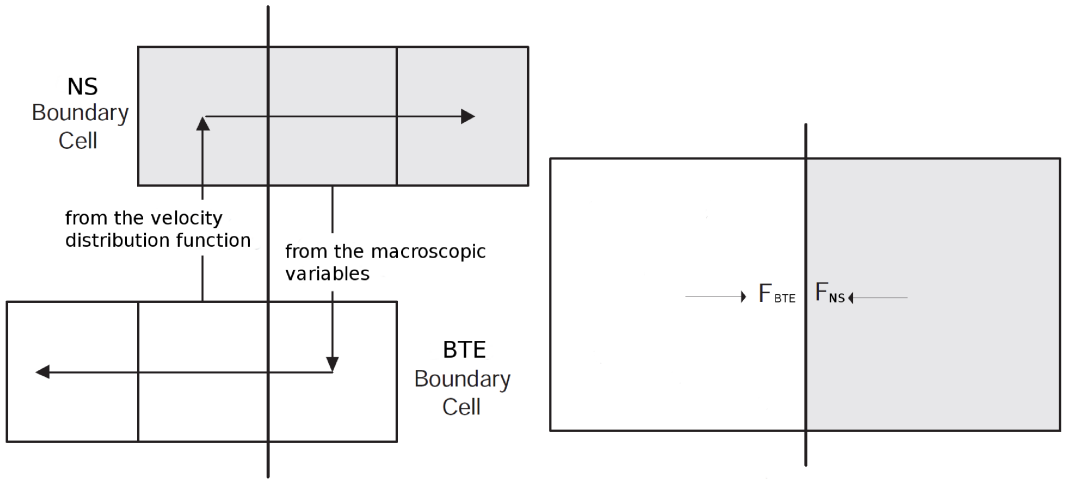

(a) State-based coupling (b) Flux-based coupling

Figure 1.3: Coupling techniques, adapted from [2].

gion where the two models are blended at equation level has been employed [58, 57, 59]. The flux-coupling approach when used to couple a continuum solver and the DSMC suffers from a main disadvantage that reduce its efficiency as reported in [56] and [2]. This is due to the statistical scatter, that affect DSMC results. Indeed, in [60] the statistical error, E, in the flux quantities has been shown to scale as

$$E_{flux} \sim \frac{E_{state}}{Kn} \tag{1.7}$$

meaning that the state-coupling is a preferable choice when the DSMC method is employed in the hybrid approach. However, the scattering error also affects this approach and a sampling procedure is needed. Different efforts have been done to reduce the statistical errors that affect the DSMC. Among them the ones proposed in [61] and [62] have been used in the context of hybrid simulations.

[3] Moments of the BTE that correspond to mass, momentum, and energy conservation laws and moment equations for heat flux and viscous stress tensor

Regarding the macroscopic and microscopic numerical methods employed in a hybrid approach, different choices have been made. The most common and mature approach is to couple a DSMC and a standard continuum solver [2, 56, 54, 57, 59] for which also vibrational non-equilibrium has been considered [1]. Nonetheless, alternative options have been explored such as in [58], in which a DVM for the BGK model has been used instead of the DSMC, and [59], where a DVM for the ES model is employed as mid-stage between DSMC and continuum solver. Furthermore, in [55] a direct numerical simulation of the full collision term of the BTE has been coupled with the BGK-NS gas-kinetic scheme [63] (for further information see section 1.2.2). A common aspect in all these works, except [1], is that, due to the choice of the continuum approach, the interfaces between the two domain have to be placed where the flow is close to thermal-equilibrium. In [1] a multitemperature continuum approach is employed to overcome this limitation. Another hybrid method is the 'all particle' hybrid scheme presented in [64, 65, 66], where particles type methods are employed throughout the whole domain. This method can handle very strong coupling between the two flow regimes and allows a simpler code development due the similarity between continuum and rarefied simulation schemes. However, the latter has been considered not relevant for the present work being more suitable for cases in which a mainly rarefied flow shows small continuum regions due to the higher computational cost of the particle approach to the NS equations. Finally, the majority of the works cited are focused on steady state simulations and only few works have successfully simulated unsteady flows [67, 56, 68].

1.2.2 Gas-Kinetic Schemes, the BGK-NS Method and the Unified Gas-Kinetic Scheme

Upwind shock-capturing schemes for the numerical solution of the Euler equations can use two different methods to evaluate the numerical fluxes at the interface [69]. One is based on the method of characteristics and solves a local Riemann problem, the other locally reconstructs a kinetic problem and integrates the gas distribution function over the phase space. Indeed, the latter uses a conventional discontinuous reconstruction and a Chapman-Enskog expansions truncated at Euler of Navier-Stokes level to model the two gas states on either side of an interface. For the NS equations the classical approach estimates the inviscid fluxes employing a Riemann solver and the viscous fluxes with a central discreti-

sation scheme while gas-kinetic schemes can evaluate both contributions as a single entity.

First examples of gas-kinetic schemes are the Equilibrium Flux Method (EFM) [70] and the Kinetic Flux Vector Splitting (KFVS) [71] based on the collisionless BTE. Due to this, the EFM and the KFVS suffer a high dissipative behaviour as well as a high computational cost, relative to traditional upwind-based schemes, since error and exponential functions arise from the half integrals of the interface distribution function. This is due to the fact that both schemes split the flux vector according to the sign of the particle velocity and thus taking moments of the distribution function in the velocity space require the evaluation of left and right half integrals. To improve the efficiency, by avoiding error and exponential functions, the Kinetic Wave/Particle Splitting method (KWPS) has been developed in [72, 73] combining both the particle and the wave propagation models [4] of fluid flows. However, the KWPS is even more dissipative than the EFM and KFVS schemes. For this reason in an effort to reduce the numerical dissipation, the modified EFM has been proposed [74].

During the same period, the BGK-NS method has been presented by Xu in [63, 75] where the update of the conservative variables is obtained integrating the BGK equation to model the gas evolution process more accurately. Since the BGK-NS method takes into account the particle collisions in the gas evolution process, no modification to reduce the numerical dissipation are required in contrast to the EFM and no shock instabilities are observed [76]. A general solution of the kinetic model equation, with an equilibrium initial state, is employed to represent the velocity distribution function. It is known that the BGK model recovers the incorrect Prandtl number in the continuum limit and for this reason a simple correction, that consists in scaling the energy numerical flux, has been proposed by Xu [63]. The approach has been often applied by Xu and co-workers [77, 7] also in the limiting case of a well-resolved flow when the solution assumes a simplified form based on the CE expansion. In this case a multi-temperature BGK model without [77] and with [7] excited rotational degrees of freedom, and more recently including also vibrational degrees of freedom [78], has been used. The assumption of a well-resolved flow leads to a simpler scheme but rules out discontinuities in the reconstructed distribution function and therefore it is

[4] In the particle propagation model the flux vector is splitted according to the sign of the particle velocity, while in the wave propagation model the jump at the interface results into waves accordingly to the Riemann approach and the flux vector is split into the respective contributions from each wave speed.

valid only for relatively small perturbances from equilibrium. However, as suggested in [79] it is possible to regularise the CE expansion in order to extend the validity of the approach. Recently a GKS has been proposed in [80] where an analytical solutions of the BGK equation up to third order CE expansion, which gives the Burnett equations, is used. Furthermore, based on previous theoretical works [81], recent studies in [82, 83] employing the BGK-NS scheme showed how GKS methods can also improve simulations of turbulent flows thanks to their multiscalar approach. In these works, a turbulent gas-kinetic scheme is obtained by establishing a relation between the relaxation time of the employed kinetic model and the turbulent quantities evaluated by means of a turbulence model. Similar improvements have been observed also when a DVM is employed to study turbulent flows [84], however the latter results much more expensive.

In [85] the BGK-NS method has been improved, resulting in the Unified Gas Kinetic Scheme (UGKS), and then successfully employed with the Shakhov (S-UGKS) [46] and Rykov model (R-UGKS) [47]. The UGKS also involves the update of the non-equilibrium distribution function and employs a discrete integration method in the phase space as well as a non-equilibrium initial distribution function, based on the CE expansion of the kinetic model. This allows to extend the validity of the scheme towards rarefied flow conditions.

Finally, it is important to notice that the required moments in velocity space and the complex formulation make the BGK-NS and UGKS significantly more expensive than classical continuum flow methods [86].

1.3 Aim of the Thesis

The current project aim is to develop the numerical tools available at the CFD Laboratory of the University of Liverpool towards the simulation of high-speed flow and, in doing so, to deliver an improvement among the current available numerical approaches to simulate flow fields encountered by hypersonic vehicles in their flight path. Among them, the work focuses in particular on partially-rarefied, high-speed, flows involving temperatures at which translational and rotational modes can be considered fully excited and vibrational-chemical non-equilibrium does not occur. To achieve the stated aim the following objectives have been identified:

- improvement of the continuum methods employed at the CFD Laboratory with the implementation of a numerical flux function reliable for high-speed flows;
- implementation and assessment of kinetic models for diatomic gases with translational and rotational non-equilibrium to improve the discrete velocity method solver employed at the CFD Laboratory to simulate rarefied flows;
- development and assessment of an alternative method, less expensive compared to the discrete velocity method, to simulate partially-rarefied flows with significant translational and rotational non-equilibrium;
- integration of the latter method in the hybrid solver, available at the CFD Laboratory, to be coupled with the previously improved discrete velocity method to simulate partially-rarefied flows with high translational and rotational non-equilibrium.

A further discussion of the stated aim and objectives can be found in the next section 1.4.

1.4 Thesis Overview

At the CFD Laboratory of the University of Liverpool two Computational Fluid Dynamics codes are available. The Helicopter Multi-Block (HMB2) CFD code is a continuum solver based on a finite volume spatial discretisation and a fully un-factored time discretisation. The solver has been revised and updated over many years and successfully employed in a wide range of fluid dynamics applications including subsonic and transonic flows [87, 88, 89]. The code uses Roe's or Osher's schemes for the evaluation of the inviscid fluxes. The Multi-Physics Code (MΦC) presented in [90, 91, 92], instead, is a computational framework designed for simulations of complex flows, where different mathematical models can be employed in different regions of the flow domain depending on the flow physics. The continuum flow solver is based on the compressible NS equations, and a cell-centred block-structured finite-volume method is employed using the AUSM$^+$ and AUSM$^+$*up* formulations proposed in chapter 2 for the inviscid fluxes. For flows with strong rarefied effects, the framework includes Molecular Dynamics (MD) methods as well as deterministic DVM for a range of kinetic Boltzmann equations. To couple continuum and rarefied flow solvers both state and flux based approaches, see section 4.5 for further information, are available in MΦC.

To develop a numerical method for high-speed partially-rarefied flows a reliable continuum solver is an essential requirement. Thus, to improve the capability of the codes available at the CFD Laboratory to predict high-speed flow, the first part of the project has been dedicated to the implicit implementation of the AUSM$^+$ and AUSM$^+$*up* schemes [93, 94] with an analytically defined Jacobian. The latter, when possible, is favoured over the numerical evaluation because more efficient. The AUSM-family has been shown to be capable of solving to a good accuracy flow fields at a wide range of Mach regime including high-speed flows [95, 96], but, in their original formulations, they do not guarantee the fluxes to be continuously differentiable functions of the primitive variables. This would imply the presence of different branches in the computational algorithm, increasing the computational cost, and reduced stability for cases with complex flow transient or grid geometry. Thus, a novel formulation of the AUSM$^+$ and AUSM$^+$*up* schemes is proposed in chapter 2, and published in the literature [97, 98], where a blending

is introduced by means of parametric sigmoidal functions at the points of discontinuity. Considering an implicit implementation is important for the further development of the solver in the context of high-Mach flows; implicit time marching approaches can relieve the restriction in time step due to the presence of stiff source terms when chemically reacting flow are considered. For this work HMB2 has been employed and an assessment of the proposed AUSM$^+$ and AUSM$^+$*up* schemes is presented in chapter 3. Afterwards, the proposed schemes have been implemented also in MΦC.

Later on, the focus has been shifted entirely on MΦC in order to improve the capability of the framework to simulate high-speed partially-rarefied flows in the context of hybrid approaches.

In MΦC a DVM solver is available to predict flows in rarefied conditions. At the beginning of the project for non-continuum flow modelling, the Shakhov and ES models were included for monoatomic gas flows. However, in rarefied gas flows at high velocities it is necessary to take into account the excitation of the internal degrees of freedom. Thus, as a step towards realistic simulations, the framework has been firstly improved with the addition of the Rykov model and an Ellipsoidal-Statistical (ES) model [29] for diatomic gases with rotational non-equilibrium. Results employing these models can be found in chapter 6 and are part of two publications [99, 100].

A major drawback using a DVM in hybrid simulations is the computational and memory cost. Based on the literature survey of related works, the author believes that a GKS can represent an efficient methods, relative to DVM, capable of modelling complex diatomic gas flows with moderate rarefaction effects but with significant rotational non-equilibrium and thus, when employed in the context of hybrid simulation, it can extend the validity of the continuum formulation. For this reason, two GKS methods, analytically-defined on the basis of the Chapman-Enskog (CE) expansion of non-dimensional Shakhov and Rykov models, are proposed in chapter 5 to simulate weakly rarefied flows. The derivatives of the equilibrium function and the time derivatives of the primitive variables are defined analytically employing the compatibility condition of the kinetic model for the latter. In previous works from Xu and co-workers [77, 7] similar gas-kinetic schemes are defined using the CE solution of the BGK model with rotational non-equilibrium and the required derivatives are expressed in terms of Taylor series where the coefficient are calculated by means of properties of the employed BGK model. Moreover, in the work of Xu et al. a

correct constant Prandtl number in the continuum limit is obtained by rescaling the energy flux [63], while in the present work a kinetic model involving a Prandtl number correction is directly employed to define the GKS. As demonstrated in appendix H the Rykov model leads in the continuum limit to a variable Prandtl number, depending on the collision number Z_r and this should lead to more accurate results for diatomic gases where thermal non-equilibrium effects are important. As shown in chapter 6 the proposed GKS approaches are able to resolve shock structures with and without rotational non-equilibrium, in contrast to traditional single-/multi-temperature NS approaches [15, 14], and are cheaper alternatives to the DVM for a range of relevant flows. Thus, they can be a viable way to improve the performance of hybrid simulations reducing the domain where more complex methods are required, maintaining an acceptable level of reliability. The formulation as well as an assessment of the two schemes have been published in the literature [100, 101, 102].

Finally, since for the development of a CFD solver it is important to guarantee the capability to cope with practical and realistic applications; the proposed methods have been tested to predict flow fields around waverider shapes in chapter 7. These geometries have been chosen due to their easy access, methods to build own waverider shapes are available in the literature, and the renewed interest in these shapes for high-velocity commercial and defense applications, as discussed in section 7.1.

Chapter 2

Continuum Flows Solver - HMB2

In the context of the present project a fully analytical Jacobian of the AUSM$^+$ and AUSM$^+$up schemes have been implemented in HMB2 in order to improve the capability of the solver to predict flow fields over a large interval of Mach numbers including high-speed flows. The schemes are presented in the current chapter and available in the following publications:

- Assessment of Implicit Implementation of the AUSM$^+$ Method and the SST Model for Viscous High-Speed Flow. Colonia S., Steijl R. and Barakos G.N., 5^th European Conference for Aeronautics and Space Sciences, 1-5 July 2013, Munich (Germany).

- Implicit implementation of the AUSM$^+$ and AUSM$^+$up schemes. Colonia S., Steijl R. and Barakos G.N., International Journal for Numerical Methods in Fluids, Volume 75, Issue 10, pages 687-712, DOI: 10.1002/fld.3891.

2.1 Introduction

Computational fluid dynamics methods based on the Navier-Stokes equations have gained significant prominence in recent years and have been used for a wide range of Mach numbers; however, a number of challenges remain, including the derivation of accurate and robust numerical schemes for the convective flux computation that are able to cope with a wide range of Mach numbers as well as turbulent flows.

In the context of this work, the CFD code developed at the University of Liverpool, HMB2, has been employed and extended. This solver uses a finite-volume spatial discretisation [103] and a fully un-factored implicit time discretisation with a GCG/ILU(0) linear solver. It has been used successfully

for a wide range of aerospace applications including subsonic and transonic flows ([87] and [88]). The code generally employs Roe's or Osher's schemes for the evaluation of the inviscid fluxes. In the context of the present work, the AUSM$^+$ and AUSM^+up schemes have been implemented.

Nowadays, upwind flux functions have overcome the challenge to compute compressible flow phenomena reliably and with reasonable accuracy, and several approximation procedures for solving the Riemann problem have been proposed including the methods of Roe [104], Van Leer [105], HLLE [106], and AUSM [93] amongst others. In order to solve the interface Riemann problem, the left and the right states at the surfaces of each finite volume need to be extrapolated from the centroid. The most common choice is the Monotone Upstream-Centred Scheme for Conservation Laws, MUSCL, introduced by Van Leer in [107]. Another interpolation technique that has been successfully used in the literature for high-speed flows ([108], [109]) is the Spekreijse's interpolation introduced in [110]. As a limiter for both schemes the Van Albada limiter [111] seems to be the most popular.

Among the different Riemann solvers the AUSM-family has been shown to be capable of solving to a good accuracy flow fields at a wide range of Mach regime. The original AUSM scheme was introduced by M.-S. Liou in [93] and then improved in [112] obtaining the AUSM$^+$. The aim of the AUSM-family was to combine the desirable attributes of the flux difference (Roe) and flux vector splitting (Van Leer) methods. The basic idea is the recognition of the convection and acoustic waves as two physically distinct processes. Recently, Liou [94] extended the AUSM$^+$-family to solve flows at all speed regimes with the AUSM^+up scheme. In the low Mach number regime the speed of sound and the convective speed are quite different. This results in an large amount of numerical dissipation which affects the solution along with possible slowing or stalling of the convergence. To avoid both problems, Liou introduced a rescaling factor [94], so that the resulting sound and convective speeds become of equal order.

Various explicit and implicit schemes have been proposed to advance in time the system of ordinary differential equations, obtained by the spatial discretisation. In an explicit method, the solution at the time step $n+1$ depends only on the known solution at the previous time step. In the implicit schemes, the new solution does not only depend on the known solution at the previous time step, but also on a coupling between the cell variables at the new time step. Thus, an implicit approach, after the linearisation of the

residual at the new time step, results in a large system of linear equations which as the time step tends to infinity results in the standard Newton's method. A system of linear equations needs to be solved, and this task can be accomplished using direct or iterative methods. The former are based on the exact inversion of the system sparse matrix by means of the Gaussian elimination, as can be found in [113], or a direct sparse matrix method, like the Boeing Real Sparse Library [114]. Although the recovery of the standard Newton's method, and of the quadratic convergence when the Jacobian is well defined, was demonstrated on both structured and unstructured grids [113], [115], their application in complex three dimensional problems requires an excessively high computational effort. Thus, in these cases the linear system has to be solved using an iterative matrix inversion methodology. Different iterative methods have been proposed in the literature. Among them there are the Alternating Direction Implicit (ADI) scheme [116], the line Jacobi scheme [117], the Lower-Upper Symmetric Gauss-Seidel (LU-SGS) scheme [118], and Newton-Krylov methods. The first four methods are based on splitting the implicit operator into a sum or products of decoupled parts, that are easily inverted. For this reason they introduce a factorisation error and are less implicit (the coupling between the grid point variables at the new time step is not considered overall but only along particular directions). The Newton-Krylov methods, instead, treat the system of linear equation in a more global way, allowing a fully un-factored approach in which the new time level is introduced simultaneously for all the cells. Obviously, this leads to increased computational effort. Among the Krylov methods two examples are the Generalised Conjugate Gradient (GCG) methods introduced in [119] and [120, 121] and the Generalised Minimal Residual (GMRES) method introduced in [122]. It has to be noted that the efficiency of Krylov-subspace methods depends strongly on the pre-conditioning operation. The purpose of the pre-conditioning is to cluster the eigenvalues of the system matrix around unity. One of the most successful pre-conditioners is the Incomplete Lower Upper factorisation method, [123], with different levels of fill-in (commonly zero, ILU(0)). Until the early nineties memory intensive methods like the Newton's method were severely restricted by computer technology. One of the first attempts to employ a Newton method solver to high-speed flows is reported in [108] and [109]. The work follows some of the ideas developed in [113] for subsonic and transonic flows, one in particular was to add a damping term to the Jacobian matrix diagonal to alleviate the start-up

problems of the Newton's method. In both these line of works [108, 109] and [113] a direct method has been used, but in following works, [124] and [125] respectively, iterative methods have been taken into account with an ILU(0) factorisation.

For the implicit formulation, the derivatives of the interface fluxes are needed. In [126], [127] and [128] numerical Jacobians for the AUSM$^+$, AUSM$^+$up and AUSMPW$^+$ schemes, respectively, have been chosen and successfully employed for low Mach, subsonic, transonic and hypersonic flows. However, when possible, an analytical Jacobian is preferred because it is more efficient. Analytical Jacobians for the AUSM and AUSM$^+$ schemes were studied in [129] and [130] respectively. In [129] a comparative study of analytical Jacobians for different schemes is shown, and the AUSM Jacobian failed to converge, though no information was given about its derivation. In [130], instead, a complete study of the derivation of a simplified analytical Jacobian for the AUSM$^+$ was presented. Moreover, the latter has been successfully applied in a point implicit Runge-Kutta scheme to solve subsonic and transonic flows. Since this work was not focused on high-speed cases no discussion about the impact of the simplifications on the solution of these flow fields was reported.

2.2 Conservation Laws

Fluid mechanics is based on the conservation laws for mass, momentum, and energy. These laws can be stated in the integral form, applicable to an extended region, or in the differential form, applicable at a point. In the integral form, the expressions of the laws depend on whether they relate to a material volume, which consists of the same fluid particles and whose bounding surface moves with the fluid, or to a fixed volume field in space. The system of the aforementioned laws, stated in the integral form and related to a material volume, can be written as follow

$$\frac{d}{dt}\iiint_V \mathbf{U}\ dV + \iint_S \mathbf{P}_j\ n_j\ dS = \iint_S \mathbf{G}_j\ dS + \iiint_V \mathbf{Q}\ dV \tag{2.1}$$

where

$$\mathbf{U} = \begin{bmatrix} \rho \\ \rho u_i \\ E \end{bmatrix} \quad \mathbf{P}_j = \begin{bmatrix} 0 \\ p\delta_{ij} \\ \rho u_j \end{bmatrix} \quad \mathbf{G}_j = \begin{bmatrix} 0 \\ \sigma_{ij} \\ \sigma_{ij}u_i + k\frac{dT}{dx_j} \end{bmatrix} \quad \mathbf{Q} = \begin{bmatrix} 0 \\ \rho f_{vol,\ i} \\ \rho f_{vol,\ j}\ u_j \end{bmatrix}. \tag{2.2}$$

It is often useful to relate the integral form to a fixed volume field in space. This can be done by applying the Reynolds transport theorem to the system (2.1)

$$\frac{d}{dt}\iiint_{\overline{V}} \mathbf{U}\ d\overline{V} + \iint_{\overline{S}} \mathbf{F}_j n_j\ d\overline{S} = \iint_{\overline{S}} \mathbf{G}_j\ d\overline{S} + \iiint_{\overline{V}} \mathbf{Q}\ d\overline{V} \tag{2.3}$$

with

$$\mathbf{F}_j = \mathbf{U}u_j + \mathbf{P}_j. \tag{2.4}$$

Since the volume that appears in equations (2.3) does not depend on time, it is possible to reverse the operations of derivation and integration. Then the surface integrals appearing in these equations can be transformed in volume integrals using the Gauss divergence theorem. Thus, equations (2.3) can be reduced to another form which does relate flow properties at a given point, the differential form

$$\frac{\partial}{\partial t}\mathbf{U} + \frac{\partial}{\partial x_j}F_j = \frac{\partial}{\partial x_j}\mathbf{G}_j + \mathbf{Q}. \tag{2.5}$$

System (2.5) is called conservation form of the fundamental equations. A non-conservation form, i.e. in terms of the substantial derivative, can be also given as follows

$$\begin{cases} \dfrac{D\rho}{Dt} + \rho\vec{\bigtriangledown}\cdot\mathbf{V} = 0 \\ \rho\dfrac{D\mathbf{V}}{Dt} = \rho\mathbf{F}_{vol} + \vec{\bigtriangledown}\cdot\bar{\bar{\sigma}} - \bigtriangledown p \\ \rho\dfrac{De}{Dt} = \rho\mathbf{F}_{vol}\cdot\mathbf{V} + \vec{\bigtriangledown}\cdot(\bar{\bar{\sigma}}\cdot\mathbf{V}) - \bigtriangledown\cdot(p\mathbf{V}) + k\bigtriangledown^2 T \end{cases}. \tag{2.6}$$

Both forms are equally valid statements of the fundamental principles. In order to be properly formulated the problem is subject to initial and boundary conditions.

The relation between the stress and the velocity of deformation in a continuum is called a constitutive equation and it depends on the nature of the fluid. The velocity gradient tensor can be decomposed into symmetric and antisymmetric parts. The antisymmetric part represents fluid rotation without deformation, and can not by itself generate stress. Thus, stresses are generated by the strain rate tensor (the symmetric part of the velocity gradient tensor). Assuming a linear relation, that the medium is isotropic and that the stress tensor is symmetric the following relation can be derived

$$\sigma_{ij} = \lambda'(\bigtriangledown \cdot \mathbf{V})\delta_{ij} + 2\mu(symm \bigtriangledown V_{ij}) \tag{2.7}$$

where $(symm \bigtriangledown V_{ij})$ is the symmetric part of the velocity gradient tensor and μ and λ' are the first and second viscosity coefficients. A fluid obeying equation (2.7) is called a Newtonian fluid. The momentum equations written for a Newtonian fluid are the so-called Navier -Stokes equations

$$\left[\frac{\partial(\rho u_i)}{\partial t} + \frac{\partial(\rho u_i u_j)}{\partial x_j}\right] = \rho f_{vol,\ i} - \frac{\partial p}{\partial x_i} + \mu\frac{\partial^2 u_i}{\partial x_j \partial x_j} + (\lambda' + \mu)\frac{\partial}{\partial x_i}\left[\frac{\partial u_j}{\partial x_j}\right] \tag{2.8}$$

if we consider an inviscid fluid, we obtain the Euler equations

$$\left[\frac{\partial(\rho u_i)}{\partial t} + \frac{\partial(\rho u_i u_j)}{\partial x_j}\right] = \rho f_{vol,\ i} - \frac{\partial p}{\partial x_i}. \tag{2.9}$$

In HMB2, the Sutherland's law [131] is employed for the viscosity

$$\mu = \mu_{ref}\left(\frac{T}{T_{ref}}\right)^{3/2}\frac{T_{ref} + T_S}{T + T_S} \tag{2.10}$$

where, T is the temperature of the fluid, T_{ref} is a reference temperature ($T_{ref} = 273.15K$), μ_{ref} is the viscosity at that reference temperature ($\mu_{ref} = 1.716 \cdot 10^{-5} kg/ms$) and T_S is the Sutherland temperature ($T_S = 110.4K$). The heat flux vector, q_i, is calculated using Fourier's Law

$$q_i = -k\frac{\partial T}{\partial x_i} \tag{2.11}$$

where k is the heat transfer coefficient. Finally, an ideal gas approximation is used, with the adiabatic index set to $\gamma = 1.4$ and R the specific gas constant as $R = c_p - c_v = 287.058 Jkg^{-1}K^{-1}$.

2.3 Turbulence modelling

By time-averaging the mass, momentum and energy equations, the Reynolds-Averaged Navier-Stokes (RANS) equations can be obtained. While the continuity equation remains the same since it is linear with respect to velocity, extra terms appear in the momentum and energy equations due to the non-linearity of the convection term. The time-averaged momentum equation then takes the form

$$\frac{\partial\left(\rho u_i\right)}{\partial t}+\frac{\partial\left(\rho u_i u_j\right)}{\partial x_j}=\rho f_{vol,i}-\frac{\partial p}{\partial x_i}+\frac{\partial}{\partial x_j}\left(\tau_{ij}+\tau_{ij}^R\right) \tag{2.12}$$

while for the energy equation (Equation 2.13)

$$\frac{\partial \rho E}{\partial t}+\frac{\partial}{\partial x_j}\left[u_j\left(\rho E+p\right)\right]-\frac{\partial}{\partial x_j}\left(u_i\left(\tau_{ij}+\tau_{ij}^R\right)-q_j\right)=0 \tag{2.13}$$

where the average symbol has been dropped for simplicity. The extra terms, τ_{ij}^R, are called the Reynolds Stresses and are defined in tensor notation as being equivalent to $-\rho\overline{u_i' u_j'}$. At this point, the main problem in turbulence modelling involves calculating the Reynolds stresses, from the known mean quantities. One common approach is the approximation first introduced by Boussinesq. The latter is based on an analogy between viscous and Reynolds stresses and expresses the Reynolds stresses as a product of the eddy viscosity (μ_t) and the velocity gradient. Thus, the Boussinesq's eddy viscosity hypothesis states that

$$-\rho\overline{u_i' u_j'}=\mu_t\left[\left(\frac{\partial u_i}{\partial x_j}+\frac{\partial u_j}{\partial x_i}\right)-\frac{2}{3}\delta_{ij}\frac{\partial u_k}{\partial x_k}\right]-\frac{2}{3}\rho\delta_{ij}k \tag{2.14}$$

with k representing the specific kinetic energy of the fluctuations and given by

$$k\equiv\frac{u_i' u_i'}{2}. \tag{2.15}$$

The eddy viscosity, μ_t, is a scalar and consequently the Reynolds stress components are linearly proportional to the mean strain-rate tensor. To compute μ_t, further modelling is required and it is at this point that turbulence models come into play. Turbulence models are classified into categories based on the number of transport equations required to calculate the eddy viscosity. Among the various turbulence models available in the literature, HMB2 employs one-equation models, such as the Spalart-Allmaras (SA)[132] model, and two-equation models, such as the $k-\omega$[133], $k-\omega$ baseline (BSL) and shear-stress transport (SST)[134] models.

2.4 Fully Implicit Formulation for a Steady Case

In the Helicopter Multi-Block (HMB2) code, the Navier-Stokes (NS) equations are discretised using a cell-centred finite-volume approach. The computational domain is divided into a finite number of non-overlapping control-volumes, and the governing equations are applied in integral-conservation form at each cell. The equations are written in a curvilinear co-ordinate system. The spatial discretisation of the NS equations leads to a set of ordinary differential equations in time. Following the pseudo-time approach, after the linearisation of the residual at the new pseudo time step the latter results in a large system of linear equations which, rewritten in terms of the primitive variables $\mathbf{P}$, for a steady case is given by

$$\left[\frac{V_{i,j,k}}{\Delta t^*}\frac{\partial \mathbf{W}_{i,j,k}}{\partial \mathbf{P}_{i,j,k}} + \frac{\partial \mathbf{R}_{i,j,k}}{\partial \mathbf{P}_{i,j,k}}\right]\Delta \mathbf{P}_{i,j,k} = -\mathbf{R}_{i,j,k}(\mathbf{W}^m) \tag{2.16}$$

where $\mathbf{R}$ represents the residual vector. The Jacobian matrix is calculated analytically by repeated application of the chain rule and the residual for one cell is built up as a summation of the fluxes through the cell faces. Considering the convective part of the flux at the interface, denoted by $f_{i+\frac{1}{2}}$, to avoid ill-conditioning a first order Jacobian is employed (regardless of its numerical or analytical evaluation). Thus, the exact Jacobian matrix is approximated by removing the dependence of the MUSCL interpolation;

$$\frac{\partial \mathbf{f}_{i-\frac{1}{2}}}{\partial \mathbf{P}_{i-2}} \approx 0; \quad \frac{\partial \mathbf{f}_{i+\frac{1}{2}}}{\partial \mathbf{P}_{i-1}} \approx \frac{\partial \mathbf{f}_{i+\frac{1}{2}}}{\partial \mathbf{P}_{L}}; \quad \frac{\partial \mathbf{f}_{i+\frac{1}{2}}}{\partial \mathbf{P}_{i}} \approx \frac{\partial \mathbf{f}_{i+\frac{1}{2}}}{\partial \mathbf{P}_{R}}; \quad \frac{\partial \mathbf{f}_{i+\frac{1}{2}}}{\partial \mathbf{P}_{i+1}} \approx 0. \tag{2.17}$$

This leads to a lower quality Jacobian which, however, is much more computationally efficient. Indeed, it has been experienced that the conditioning of the system gets worse when additional off-diagonal terms are included.

In the present work the first order Jacobian has been employed with first order reconstruction in the high-speed regime. In the transonic and low Mach regimes, instead, it has been used together with a, formally, third order MUSCL scheme and the Van Albada limiter. The reason for this choice is due to the fact that the current implementation of the MUSCL reconstruction approach and the Van Albada limiter in HMB2 is not optimised for high-Mach flows.

2.5 Variable extrapolation - MUSCL

The Monotone Upstream-Centred Scheme for Conservation Laws (MUSCL) was introduced by Van Leer [107]. It is a compact scheme which is used to discretise the convective part of the Navier-Stokes equations. In one dimension and considering uniform spacing, the extrapolation to both sides of the interface at $i + 1/2$ is

$$\begin{aligned} \mathbf{f}^L_{i+1/2} &= \mathbf{f}_i + \tfrac{\phi(r_i)}{4}\left[(1-\chi)\Delta_-\mathbf{f}_i + (1+\chi)\Delta_+\mathbf{f}_i\right] \\ \mathbf{f}^R_{i+1/2} &= \mathbf{f}_{i+1} - \tfrac{\phi(r_{i+1})}{4}\left[(1-\chi)\Delta_+\mathbf{f}_{i+1} + (1+\chi)\Delta_-\mathbf{f}_{i+1}\right] \end{aligned} \tag{2.18}$$

where $\Delta_+\mathbf{f}_i = \mathbf{f}_{i+1} - \mathbf{f}_i$, $\Delta_-\mathbf{f}_i = \mathbf{f}_i - \mathbf{f}_{i-1}$, $\phi(r_i)$ is the limiter and $r_i = \Delta_-\mathbf{F}_i/\Delta_+\mathbf{F}_i$. If $\phi(r_i) = 0$ then this is only a first order scheme but if $\phi(r_i) = 1$ then higher order schemes are activated which are at least second order for all values of χ. The current scheme in HMB2 uses the van Albada limiter [111]

$$\phi(r) = \frac{2r}{r^2 + 1}. \tag{2.19}$$

It should be noted that this limiter is not second order TVD since for any $r \in (1, 2)$, $\phi(r) < 1$. Then value of χ is set to zero giving the final formulation

$$\mathbf{f}^L_{i+1/2} = \mathbf{f}_i + \frac{\Delta_-\mathbf{f}_i\Delta_+\mathbf{f}_i}{2(\Delta_+\mathbf{f}_i^2 + \Delta_-\mathbf{f}_i^2)}\left[\Delta_-\mathbf{f}_i + \Delta_+\mathbf{f}_i\right]. \tag{2.20}$$

2.6 A Jacobian Matrix for the AUSM$^+$ Scheme

For the definition of the AUSM$^+$ and AUSM$^+$up schemes the works of Liou [112, 94] are used, and their notation is preserved in the present work. The Jacobian matrix is calculated analytically by repeated application of the chain rule. The residual for one cell is built up as a summation of the fluxes through the cell faces. Then, the inviscid numerical flux is expressed as

$$\frac{\partial \mathbf{f}_{i-\frac{1}{2}}}{\partial \mathbf{P}_{L/R}} = \frac{\partial \dot{m}_{1/2}}{\partial \mathbf{P}_{L/R}} \mathbf{\Psi} + \dot{m}_{1/2} \frac{\partial \mathbf{\Psi}}{\partial \mathbf{P}_{L/R}} + \frac{\partial \mathbf{p}_{1/2}}{\partial \mathbf{P}_{L/R}} \tag{2.21}$$

where as defined in [112, 94]

$$\dot{m}_{1/2} = a_{1/2} M_{1/2} \rho \tag{2.22}$$

$$a_{1/2} = min(\ \widehat{a}_L, \widehat{a}_R\ ); \quad \widehat{a}_L = a_L^{*2}/max(\ a_L^*, u_{n,L}\ ); \quad \widehat{a}_R = a_R^{*2}/max(\ a_R^*, -u_{n,R}\ ) \tag{2.23}$$

$$M_{1/2} = M^+_{(4)}(M_L) + M^-_{(4)}(M_R) \tag{2.24}$$

$$\mathbf{p}_{1/2} = \left\{0,\ p_{1/2} n_x,\ p_{1/2} n_y,\ p_{1/2} n_z,\ 0\right\}^T; \quad p_{1/2} = P^+_{(5)}(M_L) p_L + P^-_{(5)}(M_R) p_R. \tag{2.25}$$

In order to have a continuously differentiable function, the original definition of the primitive variables vector, $\mathbf{\Psi}$, is replaced by

$$\mathbf{\Psi} = sig(\dot{m}_{1/2},) \mathbf{\Psi}_L + [1 - sig(\dot{m}_{1/2}, 0)] \mathbf{\Psi}_R \tag{2.26}$$

$$\mathbf{\Psi_{L/R}} = \left\{1,\ u_{L/R},\ v_{L/R},\ w_{L/R},\ H_{L/R}\right\}^T = \frac{\mathbf{W_{L/R}}}{\rho_{L/R}}. \tag{2.27}$$

The density, ρ, in the mass flux is defined, from the left and right state densities, employing the same approach used for $\mathbf{\Psi}$ instead of the original definition given in [112, 94]

$$\rho = sig(M_{1/2}, 0) \rho_L + [1 - sig(M_{1/2}, 0)] \rho_R. \tag{2.28}$$

The original AUSM$^+$ scheme [112], did not provide a fully differentiable flux function. Indeed, although the fourth and fifth order polynomials, of equations (C.5) and (C.6), are C^1, the interface speed of

sound definition and the upwind approach do not guarantee the resulting fluxes to be continuously differentiable functions of the primitive variables. This would imply the presence of different branches in the computational algorithm, which increase the computational cost, and reduced stability for cases with complex flow transient or grid geometry. To avoid this, a blending is introduced in the present work, by means of parametric sigmoidal functions applied at the points of discontinuity in the Jacobian and, for consistency, in the formulation of the scheme. The parametric sigmoidal function, employed to blend the left and right limits at the points of discontinuity, is defined as

$$sig(x,y) = \frac{1}{2}\left(-(1+K)\frac{x-y}{-|x-y|-K}+1\right) \tag{2.29}$$

with K chosen to have the desired level of blending. The choice of this sigmoidal in equation (2.29) lies in the fact that it does not involve complex trigonometric or exponential functions that require a higher computational cost to be evaluated. Examples of parametric sigmoidal functions for different values of

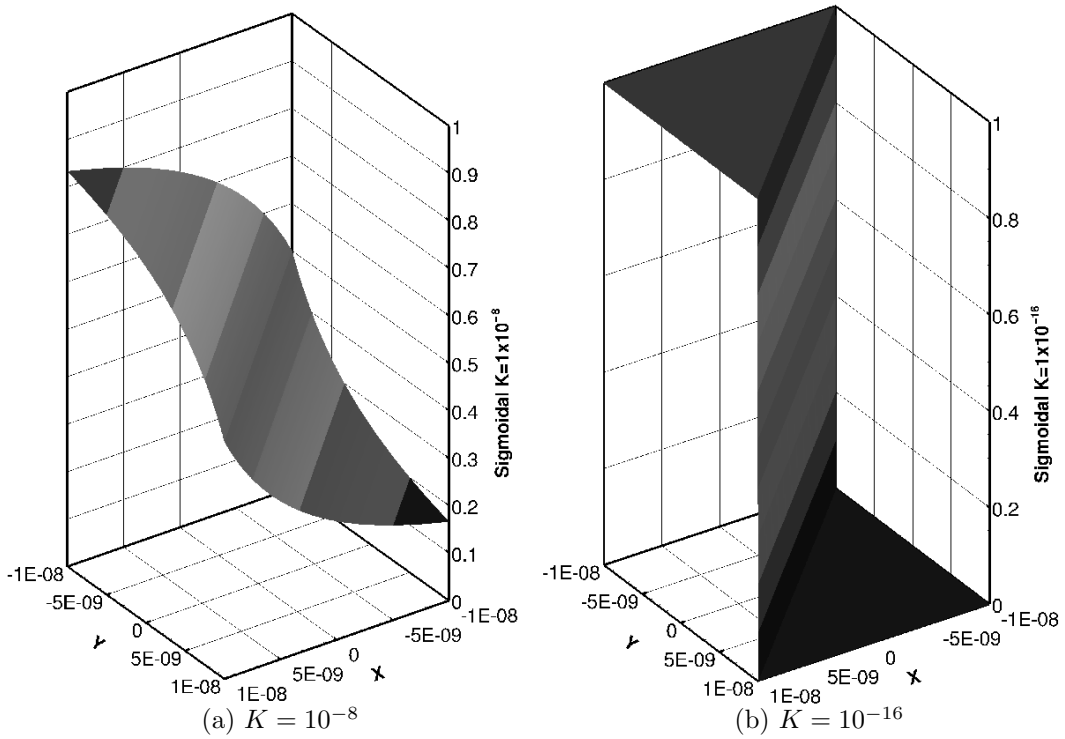

(a) $K = 10^{-8}$ (b) $K = 10^{-16}$

Figure 2.1: Sigmoidal function examples for different values of K.

K are shown in figures 2.1a and 2.1b. Note that a value of $K = 10^{-16}$ has been used in the present work. In order to avoid introducing singularities, the derivatives of the sigmoidal functions are not taken

into account in the formulation of the analytical Jacobian. Thus, the resulting Jacobian is not the exact analytical derivation of the sigmoidal blended AUSM$^+$ scheme but rather a C^0 approximation of it.

To complete the definition of the interface flux derivatives, the derivative of the mass and pressure fluxes, equation (2.22) and (2.25) respectively, have to be computed

$$\frac{\partial \dot{m}_{_{1/2}}}{\partial \mathbf{P}_{_{L/R}}} = \frac{\partial a_{_{1/2}}}{\partial \mathbf{P}_{_{L/R}}} M_{_{1/2}} \rho + a_{_{1/2}} \frac{\partial M_{_{1/2}}}{\partial \mathbf{P}_{_{L/R}}} \rho + a_{_{1/2}} M_{_{1/2}} \frac{\partial \rho}{\partial \mathbf{P}_{_{L/R}}} \tag{2.30}$$

$$\frac{\partial \mathbf{p}_{_{1/2}}}{\partial \mathbf{P}_{_{L/R}}} = \left\{ 0,\ \frac{\partial p_{_{1/2}}}{\partial \mathbf{P}_{_{L/R}}} n_x,\ \frac{\partial p_{_{1/2}}}{\partial \mathbf{P}_{_{L/R}}} n_y,\ \frac{\partial p_{_{1/2}}}{\partial \mathbf{P}_{_{L/R}}} n_z,\ 0 \right\}^T . \tag{2.31}$$

2.6.1 Derivatives of the Interface Speed of Sound

The definition of the interface speed of sound is central in AUSM$^+$ solvers. In the present work the entropy-satisfying interface speed of sound, introduced in [94], has been employed

$$a_{_{1/2}} = min(\ \widehat{a}_{_L}, \widehat{a}_{_R}\ ); \quad \widehat{a}_{_L} = a_{_L}^{*2} / max(\ a_{_L}^*, u_{_{n,L}}\ ), \quad \widehat{a}_{_R} = a_{_R}^{*2} / max(\ a_{_R}^*, -u_{_{n,R}}\ ) \tag{2.32}$$

where $u_{_{n,L/R}}$ and $a^*_{_{L/R}}$ are the left and right normal velocities and critical speed of sounds at the cell face.

A good Jacobian definition for this scheme has to represent $a_{_{1/2}}$ dependencies as best as possible. The presence of the min/max operators in the original formulation leads to discontinuous derivatives at the border-lines $\widehat{a}_{_L} = \widehat{a}_{_R}$ and $a^*_{_{L/R}} = u_{_{n,L/R}}$. Indeed, the interface speed of sound is not a continuously differentiable function of $a^*_{_{L/R}}$ and $u_{_{n,L/R}}$. Moreover, the min/max formulation leads to the following dualities

- when $\widehat{a}_{_L} = \widehat{a}_{_R}$ both the left and right state could be chosen by the min/max operators to evaluate $a_{_{1/2}}$
- when $a^*_{_{L/R}} = \pm u_{_{n,L/R}}$ the interface speed of sound could be either a function only of the critical speeds of sound or a function of $a^*_{_{L/R}}$ and the normal velocities $u_{_{n,L/R}}$.

in which the definition of the Jacobian is not unique. To deal with these situations, we consider the interface speed of sound as in equation (2.33) where the min/max operators have been replaced by

parametric sigmoidal functions.

$$a_{_{1/2}} = (1 - sig(\widehat{a}_{_L}, \widehat{a}_{_R}))\frac{a^{*2}_{_L}}{\widehat{a}(a^*_{_L}, u_{_{n,L}})} + sig(\widehat{a}_{_L}, \widehat{a}_{_R})\frac{a^{*2}_{_R}}{\widehat{a}(a^*_{_R}, -u_{_{n,R}})} \tag{2.33}$$

where

$$\widehat{a}(x, y) = sig(x, y)x + (1 - sig(x, y))y. \tag{2.34}$$

Then, the respective derivatives are given by

$$\begin{aligned}\frac{\partial a_{_{1/2}}}{\partial \mathbf{P}_{_{L/R}}} = \quad & (1 - sig(\widehat{a}_{_L}, \widehat{a}_{_R}))\left(\frac{2a^*_{_L}}{\widehat{a}(a^*_{_L}, u_{_{n,L}})}\frac{\partial a^*_{_L}}{\partial \mathbf{P}_{_{L/R}}} - \frac{a^{*2}_{_L}}{\widehat{a}^2(a^*_{_L}, u_{_{n,L}})}\frac{\partial \widehat{a}(a^*_{_L}, u_{_{n,L}})}{\partial \mathbf{P}_{_{L/R}}}\right) \\ & + sig(\widehat{a}_{_L}, \widehat{a}_{_R})\left(\frac{2a^*_{_R}}{\widehat{a}(a^*_{_R}, -u_{_{n,R}})}\frac{\partial a^*_{_R}}{\partial \mathbf{P}_{_{L/R}}} - \frac{a^{*2}_{_R}}{\widehat{a}^2(a^*_{_R}, -u_{_{n,R}})}\frac{\partial \widehat{a}(a^*_{_R}, -u_{_{n,R}})}{\partial \mathbf{P}_{_{L/R}}}\right)\end{aligned} \tag{2.35}$$

with

$$\frac{\partial \widehat{a}(x, y)}{\partial \mathbf{P}_{_{L/R}}} = sig(x, y)\frac{\partial x}{\partial \mathbf{P}_{_{L/R}}} + (1 - sig(x, y))\frac{\partial y}{\partial \mathbf{P}_{_{L/R}}}. \tag{2.36}$$

This approach leads to an approximated, but continuous, derivative of the interface speed of sound where towards the points of discontinuity the right and left limit are blended to their average. The derivative of the critical speeds of sound and cell face normal velocities can be obtained directly from their definitions

$$\begin{aligned}\frac{\partial a^*_{_{L/R}}}{\partial \mathbf{P}_{_{L/R}}} &= \frac{\gamma - 1}{a^*_{_{L/R}}(\gamma + 1)}\left\{-\frac{\gamma}{\gamma - 1}\frac{p_{_{L/R}}}{\rho^2_{_{L/R}}},\ u_{_{L/R}},\ v_{_{L/R}},\ w_{_{L/R}},\ \frac{\gamma}{\gamma - 1}\frac{1}{\rho_{_{L/R}}}\right\} \\ \frac{\partial a^*_{_L}}{\partial \mathbf{P}_{_R}} &= \frac{\partial a^*_{_R}}{\partial \mathbf{P}_{_L}} = 0\end{aligned} \tag{2.37}$$

$$\begin{aligned}\frac{\partial u_{_{n,L}}}{\partial \mathbf{P}_{_L}} &= \frac{\partial u_{_{n,R}}}{\partial \mathbf{P}_{_R}} = \{0,\ n_x,\ n_y,\ n_z,\ 0\} \\ \frac{\partial u_{_{n,L}}}{\partial \mathbf{P}_{_R}} &= \frac{\partial u_{_{n,R}}}{\partial \mathbf{P}_{_L}} = 0\end{aligned} \tag{2.38}$$

where $n = \{n_x,\ n_y,\ n_z\}^T$ is the cell face normal. It has to be noticed that for subsonic flows the sigmoidal blending in equations (2.34) and (2.36) drop since the left and right cell face normal velocities, $u_{_{n,L/R}}$, are always smaller than the relative critical speed of sounds, $a^*_{_{L/R}}$.

2.6.2 Derivatives of the Interface Mach Number

The derivative of the interface Mach number is given by

$$\frac{\partial M_{1/2}}{\partial \mathbf{P}_{L/R}} = \frac{\partial M^{+}_{(4)}(M_L)}{\partial \mathbf{P}_{L/R}} + \frac{\partial M^{-}_{(4)}(M_R)}{\partial \mathbf{P}_{L/R}}. \tag{2.39}$$

Deriving the definition of the mass flow polynomials $M^{+}_{(4)}(M_L)$ and $M^{-}_{(4)}(M_R)$ one obtains

$$\frac{\partial M^{+}_{(4)}(M_L)}{\partial \mathbf{P}_{L/R}} = \begin{cases} \frac{\partial M^{+}_{(1)}(M_L)}{\partial \mathbf{P}_{L/R}} & \text{if } |M_L| \geq 1 \\ \frac{\partial M^{+}_{(2)}(M_L)}{\partial \mathbf{P}_{L/R}}(1+\beta' M^{-}_{(2)}(M_L)) - \beta' M^{+}_{(2)}(M_L)\frac{\partial M^{-}_{(2)}(M_L)}{\partial \mathbf{P}_{L/R}} & \text{otherwise} \end{cases} \tag{2.40}$$

$$\frac{\partial M^{-}_{(4)}(M_R)}{\partial \mathbf{P}_{L/R}} = \begin{cases} \frac{\partial M^{-}_{(1)}(M_R)}{\partial \mathbf{P}_{L/R}} & \text{if } |M_R| \geq 1 \\ \frac{\partial M^{-}_{(2)}(M_R)}{\partial \mathbf{P}_{L/R}}(1+\beta' M^{+}_{(2)}(M_R)) + \beta' M^{-}_{(2)}(M_R)\frac{\partial M^{+}_{(2)}(M_R)}{\partial \mathbf{P}_{L/R}} & \text{otherwise} \end{cases} \tag{2.41}$$

where β'$= 16\beta$ and

$$\frac{\partial M^{\pm}_{(1)}(M_{L/R})}{\partial \mathbf{P}_{L/R}} = \pm\frac{1}{2}\left(\frac{\partial M_{L/R}}{\partial \mathbf{P}_{L/R}} \pm \frac{\partial |M_{L/R}|}{\partial \mathbf{P}_{L/R}}\right) \tag{2.42}$$

$$\frac{\partial M^{\pm}_{(2)}(M_{L/R})}{\partial \mathbf{P}_{L/R}} = \pm\frac{1}{2}(M_{L/R} \pm 1)\frac{\partial M_{L/R}}{\partial \mathbf{P}_{L/R}}. \tag{2.43}$$

Substituting equations (2.42), (2.43) and the definition of $M^{\pm}_{(2)}$ in equation (2.40), $\frac{\partial M^{+}_{(4)}(M_L)}{\partial \mathbf{P}_{L/R}}$ and $\frac{\partial M^{-}_{(4)}(M_R)}{\partial \mathbf{P}_{L/R}}$ can be expressed in terms of the left and right Mach numbers and the relative derivatives

$$\frac{\partial M^{+}_{(4)}(M_L)}{\partial \mathbf{P}_{L/R}} = \begin{cases} \frac{\partial M_L}{\partial \mathbf{P}_{L/R}} & \text{if } M_L \geq 1 \\ \frac{1}{2}(8\beta M_L^3 - (8\beta - 1)M_L + 1)\frac{\partial M_L}{\partial \mathbf{P}_{L/R}} & \text{if } -1 \geq M_L \leq 1 \\ 0 & \text{if } M_L \leq -1 \end{cases} \tag{2.44}$$

$$\frac{\partial M^{-}_{(4)}(M_R)}{\partial \mathbf{P}_{L/R}} = \begin{cases} 0 & \text{if } M_R \geq 1 \\ \frac{1}{2}(-8\beta M_R^3 + (8\beta - 1)M_R + 1)\frac{\partial M_R}{\partial \mathbf{P}_{L/R}} & \text{if } -1 \geq M_R \leq 1 \\ \frac{\partial M_R}{\partial \mathbf{P}_{L/R}} & \text{if } M_R \leq -1 \end{cases}. \tag{2.45}$$

As shown in figures 2.2a and 2.2b, both the fourth-order polynomials and their derivatives are continuous functions.

2.6.3 Derivatives of the Interface Pressure Formula

Finally, the interface pressure derivative, after using the same approach applied to the interface Mach number, is given by

$$\frac{\partial p_{1/2}}{\partial \mathbf{P}_{L/R}} = \frac{\partial P^{+}_{(5)}(M_L)}{\partial \mathbf{P}_{L/R}} p_L + \frac{\partial P^{-}_{(5)}(M_R)}{\partial \mathbf{P}_{L/R}} p_R + P^{+}_{(5)}(M_L)\frac{\partial p_L}{\partial \mathbf{P}_{L/R}} + P^{-}_{(5)}(M_R)\frac{\partial p_R}{\partial \mathbf{P}_{L/R}} \tag{2.46}$$

with

$$\frac{\partial P^{+}_{(5)}(M_L)}{\partial \mathbf{P}_{L/R}} = \begin{cases} 0 & \text{if } |M_L| \geq 1 \\ \frac{1}{2}(10\alpha M_L^4 - (\frac{3}{2} + 12\alpha)M_L^2 + \frac{3}{2} + 2\alpha)\frac{\partial M_L}{\partial \mathbf{P}_{L/R}} & \text{otherwise} \end{cases} \tag{2.47}$$

and

$$\frac{\partial P^{-}_{(5)}(M_R)}{\partial \mathbf{P}_{L/R}} = \begin{cases} 0 & \text{if } |M_R| \geq 1 \\ \frac{1}{2}(-10\alpha M_R^4 + (\frac{3}{2} + 12\alpha)M_R^2 - \frac{3}{2} - 2\alpha)\frac{\partial M_R}{\partial \mathbf{P}_{L/R}} & \text{otherwise} \end{cases}. \tag{2.48}$$

Also, the derivatives of the pressure flux are continuous as the polynomials themselves, see figures 2.3a and 2.3b.

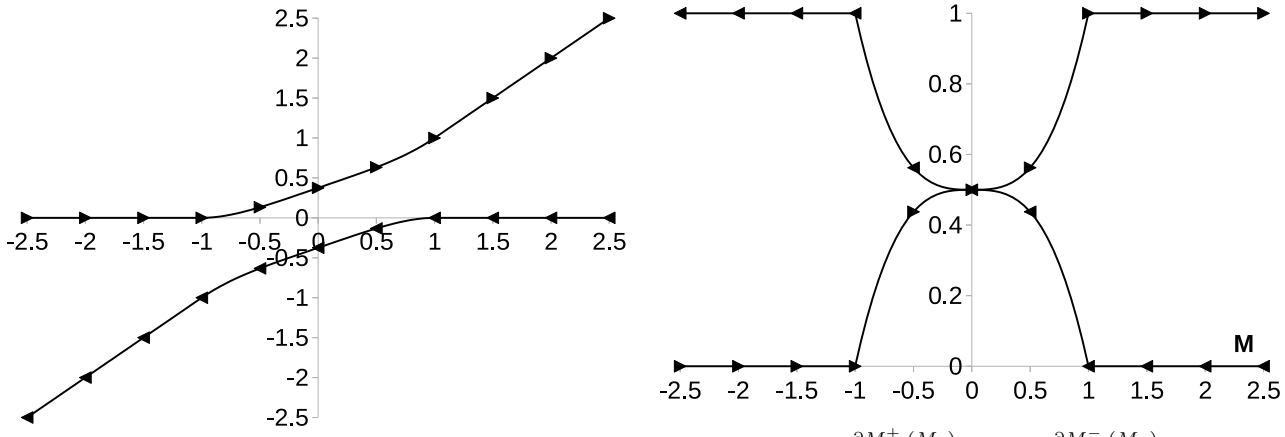

(a) $\triangleright$ $M^{+}_{(4)}(M_L)$ and $\triangleleft$ $M^{-}_{(4)}(M_R)$

(b) $\triangleright$ $\frac{\partial M^{+}_{(4)}(M_L)}{\partial M_L}$ and $\triangleleft$ $\frac{\partial M^{-}_{(4)}(M_R)}{\partial M_R}$

Figure 2.2: Split Mach number functions and derivatives.

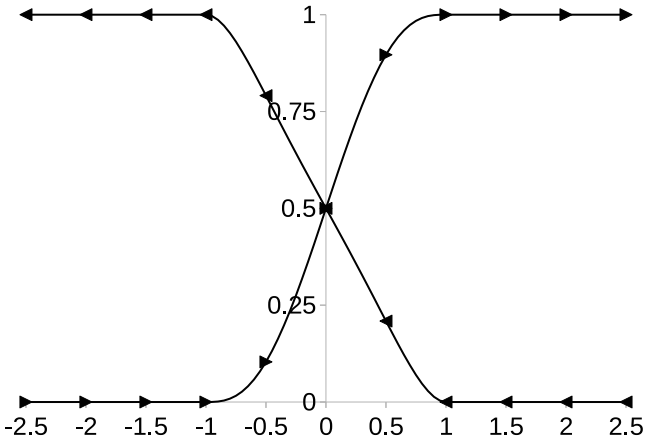

(a) $\triangleright\ P^{+}_{(5)}(M_L)$ and $\triangleleft\ P^{-}_{(5)}(M_R)$

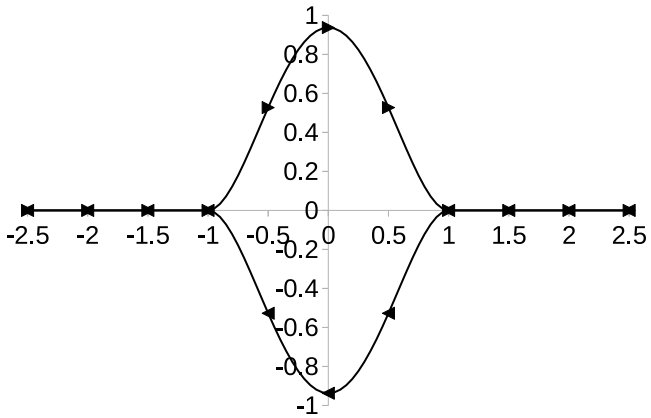

(b) $\triangleright \frac{\partial P^{+}_{(5)}(M_L)}{\partial M_L}$ and $\triangleleft \frac{\partial P^{-}_{(5)}(M_R)}{\partial M_R}$

Figure 2.3: Split pressure functions and derivatives.

2.7 Extension to the AUSM$^+$up Scheme

For subsonic cases, the solver automatically extends the AUSM$^+$ scheme to the AUSM$^+$up. The major difference between these schemes lies in the additional couplings between velocity and pressure fields that are considered in the AUSM$^+$up. These couplings are introduced in the convective and pressure fluxes by means of a pressure and a velocity diffusion term. In these terms a factor, f_a, is considered to scale the two additional terms with the flow speed. Moreover the latter is used to evaluate a more suitable value of the parameter α, in the fifth order polynomials definition, for low speed regime.

2.7.1 Derivatives of the interface Mach number with the pressure diffusion term

Considering the pressure diffusion term, the derivative of the interface Mach number becomes

$$\frac{\partial M_{1/2}}{\partial \mathbf{P}_{L/R}} = \frac{\partial M^+_{(4)}(M_L)}{\partial \mathbf{P}_{L/R}} + \frac{\partial M^-_{(4)}(M_R)}{\partial \mathbf{P}_{L/R}} + \frac{\partial M_p}{\partial \mathbf{P}_{L/R}}. \tag{2.49}$$

Again, in order to have a continuous derivative of the pressure diffusion term its original formulation is replaced by the following

$$M_p = -2\frac{K_p}{f_a} sig(1-\sigma\bar{M}^2, 0)(1-\sigma\bar{M}^2)\frac{p_R - p_L}{a^2_{1/2}(\rho_L + \rho_R)} \tag{2.50}$$

where the max operator has been replaced with the sigmoidal function. At this point the respective derivative can be evaluated using the chain rule on equation (2.50) and considering the sigmoidal function as a constant weight. Note that for subsonic flow the $(1-\sigma\bar{M}^2)$ is always positive,thus the sigmoidal blending drops.

2.7.2 Derivatives of the Scaling Factor f_a

As for the interface speed of sound, the definition of f_a includes min/max operators

$$f_a = M_0(2 - M_0) \tag{2.51}$$

$$M_0^2 = min(1, max(\bar{M}^2, M_\infty^2)); \quad \bar{M}^2 = \tfrac{1}{2}(M_L^2 + M_R^2). \tag{2.52}$$

This formulation would lead to the following derivative for $M_\infty^2 < 1$

$$\frac{\partial f_a}{\partial \mathbf{P}_{L/R}} = f(\bar{M}, M_\infty)\left(M_L \frac{\partial M_L}{\partial \mathbf{P}_{L/R}} + M_R \frac{\partial M_R}{\partial \mathbf{P}_{L/R}}\right) \tag{2.53}$$

where

$$f(\bar{M}, M_\infty) \begin{cases} 0 & \text{if } \bar{M}^2 > 1 \\ 0 & \text{if } \bar{M}^2 < M_\infty^2 \\ \frac{1-\bar{M}}{\bar{M}} & \text{otherwise} \end{cases} . \tag{2.54}$$

The latter function has a point of discontinuity at $\bar{M}^2 = M_\infty^2$. To avoid this, the sigmoidal (2.29) has been employed again to blend the left and the right limits for $\bar{M}^2 \to M_\infty^2$. Then, the resulting new formulation of function (2.54) is

$$f(\bar{M}, M_\infty) \begin{cases} 0 & \text{if } \bar{M}^2 > 1 \\ sig(\bar{M}^2, M_\infty^2)\frac{1-\bar{M}}{\bar{M}} & \text{otherwise} \end{cases} . \tag{2.55}$$

Thus, introducing equation (2.55) in equation (2.53) a continuous formulation of the derivative of the scaling factor f_a is given.

2.7.3 Derivatives of the Interface Pressure Formula with the Velocity Diffusion Term

In the AUSM$^+$up scheme the derivative of the interface pressure formula can be given as

$$\frac{\partial p_{1/2}}{\partial \mathbf{P}_{L/R}} = \frac{\partial P^+_{(5)}(M_L)}{\partial \mathbf{P}_{L/R}} p_L + \frac{\partial P^-_{(5)}(M_R)}{\partial \mathbf{P}_{L/R}} p_R + P^+_{(5)}(M_L)\frac{\partial p_L}{\partial \mathbf{P}_{L/R}} + P^-_{(5)}(M_R)\frac{\partial p_R}{\partial \mathbf{P}_{L/R}} + \frac{\partial p_u}{\partial \mathbf{P}_{L/R}} \tag{2.56}$$

where the derivative of the velocity diffusion term can be obtained employing directly the chain rule on its original definition, equation (2.57).

$$p_u = -K_u f_a P^+_{(5)}(M_L) P^-_{(5)}(M_R)(\rho_L + \rho_R) a_{1/2}(u_{n,R} - u_{n,L}). \tag{2.57}$$

Due to the fact that α is not a constant anymore, additional terms need to be considered in the derivatives of the fifth order polynomials of the pressure fluxes as follow

$$\frac{\partial P^{\pm}_{(5)}(M_{L/R})}{\partial \mathbf{P}_{L/R}} = \left(\frac{\partial P^{\pm}_{(5)}}{\partial \mathbf{P}_{L/R}}\right)_{\text{AUSM}^+} + \begin{cases} 0 & \text{if } |M_{L/R}| \geq 1 \\ \pm M_{L/R}(M_{L/R}^2 - 1)^2 \frac{\partial \alpha}{\partial \mathbf{P}_{L/R}} & \text{otherwise} \end{cases} \tag{2.58}$$

where the derivative of α can be obtained straight from equations (2.53) and (2.55), considering

$$\frac{\partial \alpha}{\partial \mathbf{P}_{L/R}} = \frac{15}{8} f_a \frac{\partial f_a}{\partial \mathbf{P}_{L/R}}. \tag{2.59}$$

Chapter 3

Continuum Flows Results and Discussion - HMB2

To evaluate the performance of the implicit implementation of the AUSM$^+$ and AUSM$^+$up schemes proposed in chapter 2, and to verify that the changes made to the schemes, to make them more suitable to differentiate, did not affect their reliability, different practical applications for a wide range of Mach numbers have been considered. As high-speed flows, five test cases which represent typical flow fields of aerospace interest have been considered: an infinite cylinder, the Orion spacecraft, a single cone with a blunt nose and two compression ramps. For the transonic regime, two external flows, an aerofoil and a wing, have been selected from the experimental databases reported in the AGARD AR 138, [135] and [136], for CFD validation. Finally, a wind turbine section as well as a wind turbine blade have been employed as test cases for low-speeds flows. The results presented in the current chapter are part of the following publications:

- Assessment of Implicit Implementation of the AUSM$^+$ Method and the SST Model for Viscous High-Speed Flow. Colonia S., Steijl R. and Barakos G.N., 5^th European Conference for Aeronautics and Space Sciences, 1-5 July 2013, Munich (Germany).

- Implicit implementation of the AUSM$^+$ and AUSM$^+$up schemes. Colonia S., Steijl R. and Barakos G.N., International Journal for Numerical Methods in Fluids, Volume 75, Issue 10, pages 687712, DOI: 10.1002/fld.3891.

3.1 High-Mach Regime: AUSM$^+$ Scheme

3.1.1 Performance and accuracy of the implicit implementation

Firstly, the inviscid flow field around an infinite cylinder has been considered. In order to evaluate the maximum CFL numbers that can be run at different residual L2-norms (as defined in equation (B.1) of appendix B) with the implicit scheme, two different Mach numbers have been considered. The Euler grid, figure 3.1a, was of the multi-block structured type with 90000 cells divided in 24 blocks. Looking at figure 3.1b it can be seen that the analytical Jacobian is well defined. For both Mach 3 and 5 the proposed implicit implementation allowed the solver to run at a CFL numbers equal and often even higher than the numerical Jacobian of the original scheme. The numerical Jacobian is evaluated by second order central finite differences. The steps were equal to 10^{-5} times the left or right value, for the left or right derivatives, of the variable relative to the flux which is being derived. The minimum step allowed was 10^{-8}. The fact that the interface speed of sound definition does not result in a continuously differentiable function could poorly affect the numerical approximations of its derivative. This justifies the lower performance, in terms of CFL, of the numerically Jacobian.

To evaluate the scheme coping with a more complex case, a laminar flow field around the Orion CEV has been considered. The employed grid is shown in figure 3.2a, and had a spatial resolution normal to the shock similar to the infinite cylinder Euler grid. The grid was made out of 3.2 million nodes divided in 294 blocks. As can be seen from figure 3.2b the implicit scheme allows to run at least CFL numbers around 2.5 also in presence of the strong shocks, expansions and interactions characterising the flow field around the Orion.

Regarding the computational time various tests have been conducted on a quad-core Xeon® CPU machine. Figure 3.3a shows some results for the infinite cylinder Mach 3. It can be noticed that the analytical Jacobian leads to a solver that is two times faster than the respective numerical one. This is due mainly to the higher computational efficiency of evaluating an analytical Jacobian compared to the numerical approach. Indeed, an investigation on the computational time required to evaluate analytically or numerically the Jacobian has shown that the former approach is three times faster than the latter. In

comparison to the explicit, 4-stage Runge Kutta, time marching the implicit approach becomes 30% and 40% faster after the logarithm of the normalised residual has dropped to -1 and -2, respectively, due to the increased CFL numbers.

Finally, in order to confirm the reliability of the predictions given by the implicit implementation of the AUSM$^+$ scheme, a comparison with the standard Roe scheme has been conducted. The geometry considered for the comparison is a 15° cone with a blunt nose of radius $R = 0.01L$, where L is the length of the cone. Some results are also compared with theory and the correlation of [137]. The comparisons are listed in table 3.1. The AUSM$^+$ predictions showed the best agreement with the theory and the correlation results. The agreement for the stagnation quantities is quite remarkable, the differences are less than 0.2%. The standoff distance is slightly under-predicted, about 7%. The Roe scheme, instead, gives over-predicted stagnation point quantities, 5% and 18%, and an underestimated, about 15%, standoff distance. Looking at figures 3.4a and 3.4b is possible to notice that, as shown before in [138] and [139], the shock predicted by the AUSM$^+$, unlike the Roe scheme, is less affected by the carbuncle problem. This is a well known local oscillatory displacement of the bow shock wave shape, mainly within the blunt nose region of a vehicle, which affect many numerical schemes and compromises the accuracy of numerical predictions of hypersonic flows. Various efforts have succeeded in reducing this oscillatory behaviour but none have yet removed completely the problem [140]. For this test case, the 4-stage Runge Kutta time marching, with a CFL number of 0.9, has been employed till a logarithm of the residual of -1 and then the implicit scheme has been used till -8 with a CFL number of 3. The computational domain consisted of 15 blocks with 0.5 million point overall; a detail is shown in figure 3.5a. The time needed to obtain the solution was 13 minutes on quad-core Xeon® CPU machine; again 30% faster than using the 4-stage Runge Kutta, which needed 19 minutes, thanks to the higher CFL number allowed, see figure 3.5b.

	AUSM$^+$	Roe	THEORY, [137]
7 Stagnation point ρ/ρ_∞	5.439	5.716	5.442
Stagnation point p/p_∞	32.593	38.5	32.653
Standoff distance δ/R_n	0.152	0.128	0.163

Table 3.1: AUSM$^+$ and Roe results compared to theory and correlation [137]. R_n is the nose radius.

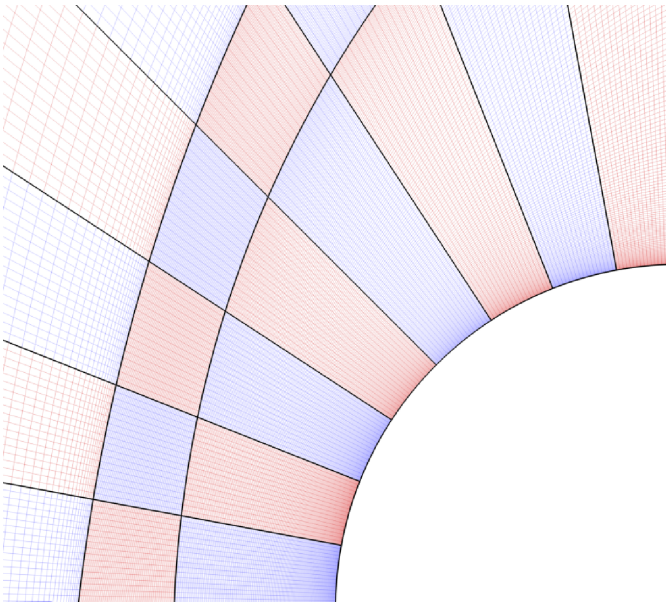

(a) Euler grid, 24 blocks and 90000 cells.

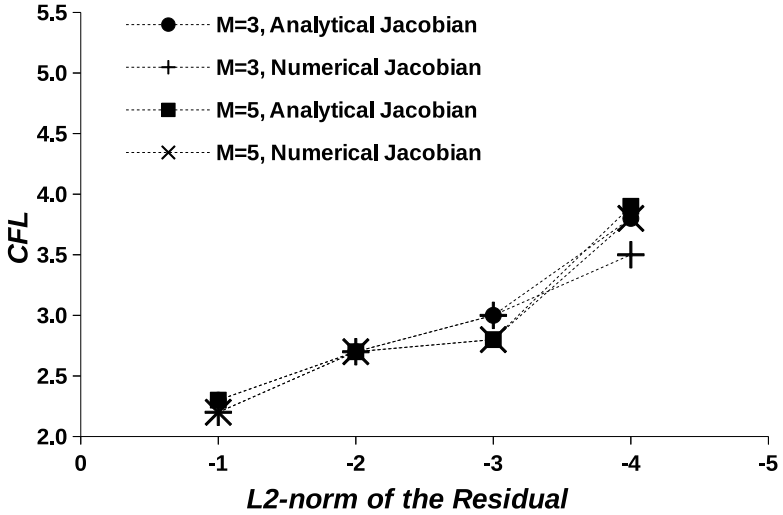

(b) CFL comparison: numerical and analytical Jacobian, AUSM$^+$.

Figure 3.1: Infinite cylinder ($R = 1$)

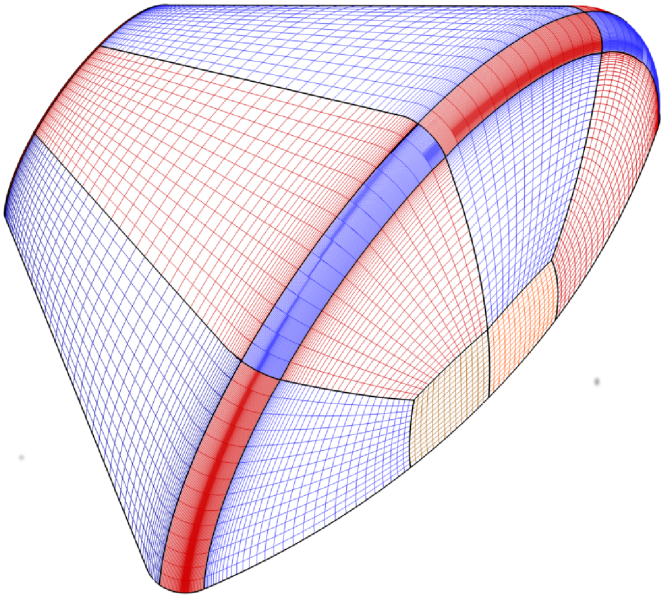

(a) Navier-Stokes grid, 294 blocks and 3.2 million cells.

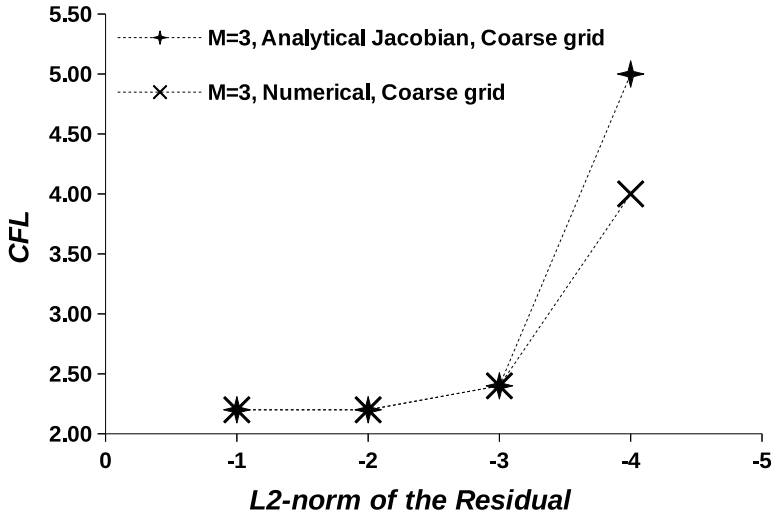

(b) CFL comparison: numerical and analytical Jacobian, AUSM$^+$, $M = 3$ laminar flow ($Re = \times 10^5$).

Figure 3.2: Orion CEV

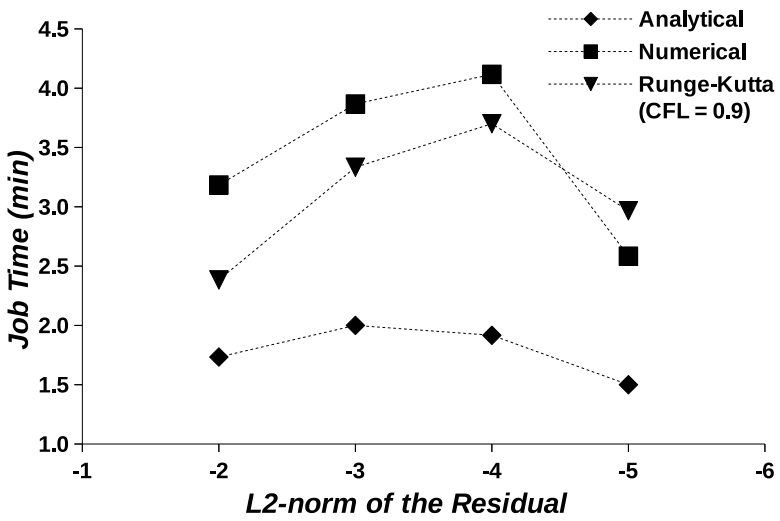

(a)

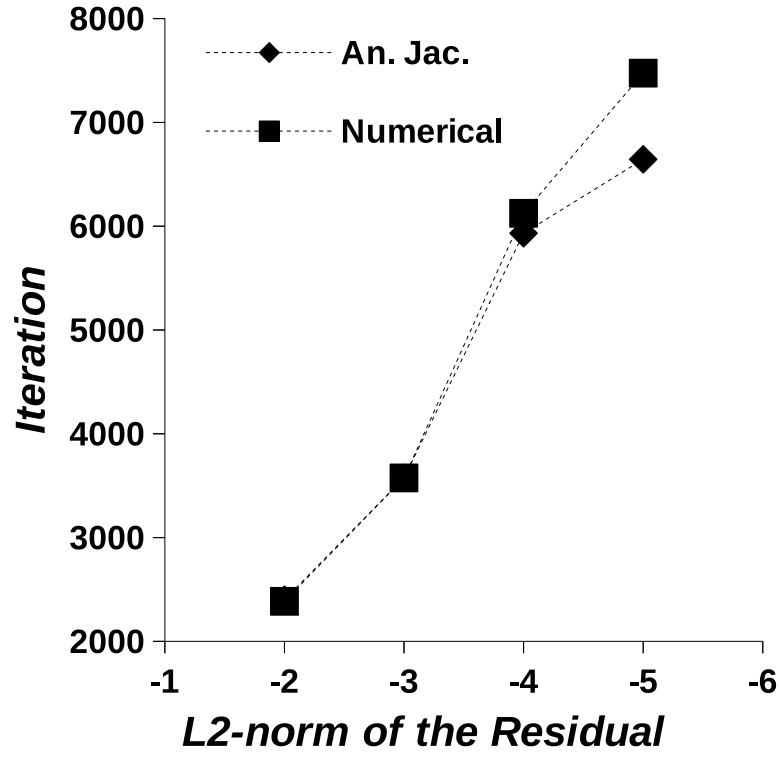

(b)

Figure 3.3: Infinite cylinder, Euler grid, AUSM$^+$, $M = 3$.

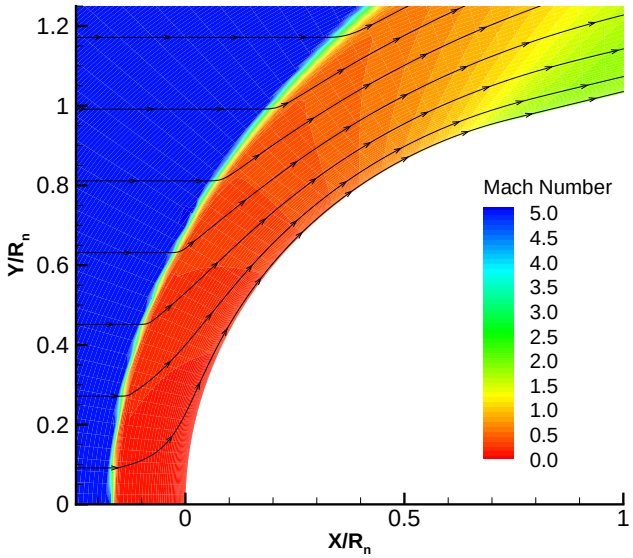

(a) AUSM$^+$

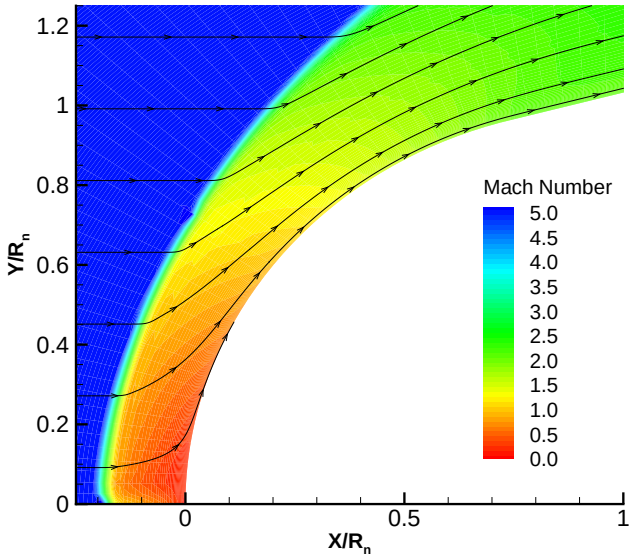

(b) Roe

Figure 3.4: Inviscid flow around a 15° cone with blunt nose ($R = 0.01L$) at $M = 5$.

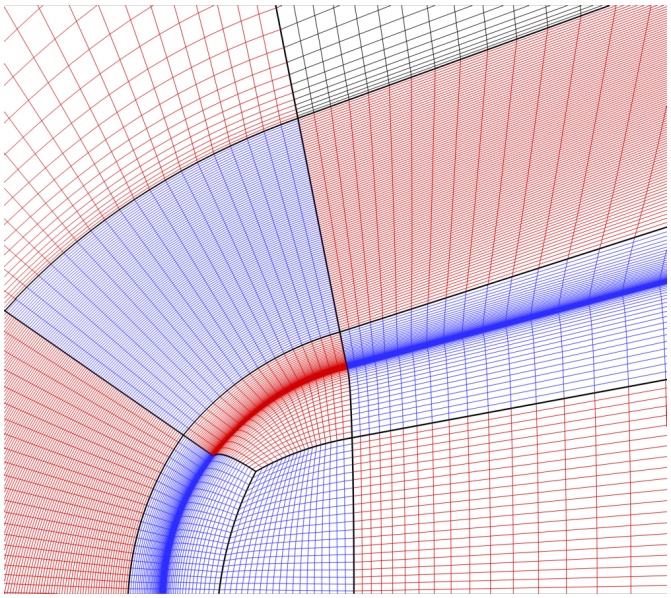

(a) Euler grid, 15 blocks and 0.5 million cells.

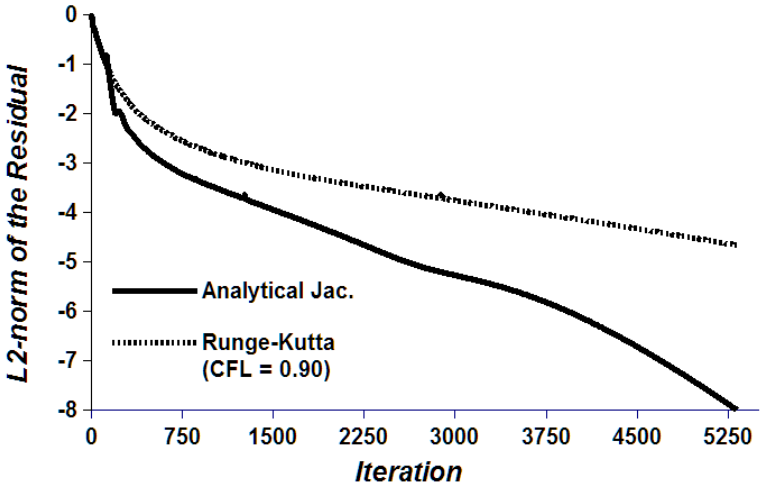

(b) Computational cost comparison: explicit and implicit schemes, AUSM$^+$, $M = 5$ inviscid flow.

Figure 3.5: 15° cone with blunt nose ($R = 0.01L$)

3.1.2 Shock-wave / turbulent boundary-layer interactions

In [141] shock-wave/boundary-layer interactions, generated using two-dimensional compression ramps, were studied experimentally. The characteristics of the incoming boundary layer were: $\delta = 24mm$, $M_\infty = 2.84$, $Re = 6.5 \times 10^7 m^{-1}$ and different ramp angle have been considered. In this work, we solved numerically the same flow fields using the SST turbulence model of Menter and the AUSM$^+$ scheme. The computational domains were both divided in 21 blocks with an overall number of cells equal to 24000 and 27000 for the $\theta = 16°$ and $\theta = 20°$ ramps, respectively.

Figure 3.6a shows the comparison of the pressure curve obtained with the CFD code and the one reported in [141], while in figures 3.6b, 3.7a and 3.7b the Mach contours are presented for the two ramp angles. The numerical solutions fit reasonably the experimental data. Indeed, the positions of the recirculation zones predicted by the CFD code are comparable to the ones given by the experiment. Figures 3.7a and 3.7b confirm that the SST model and the AUSM$^+$ scheme are able to capture the recirculation zones with a reasonable level of accuracy.

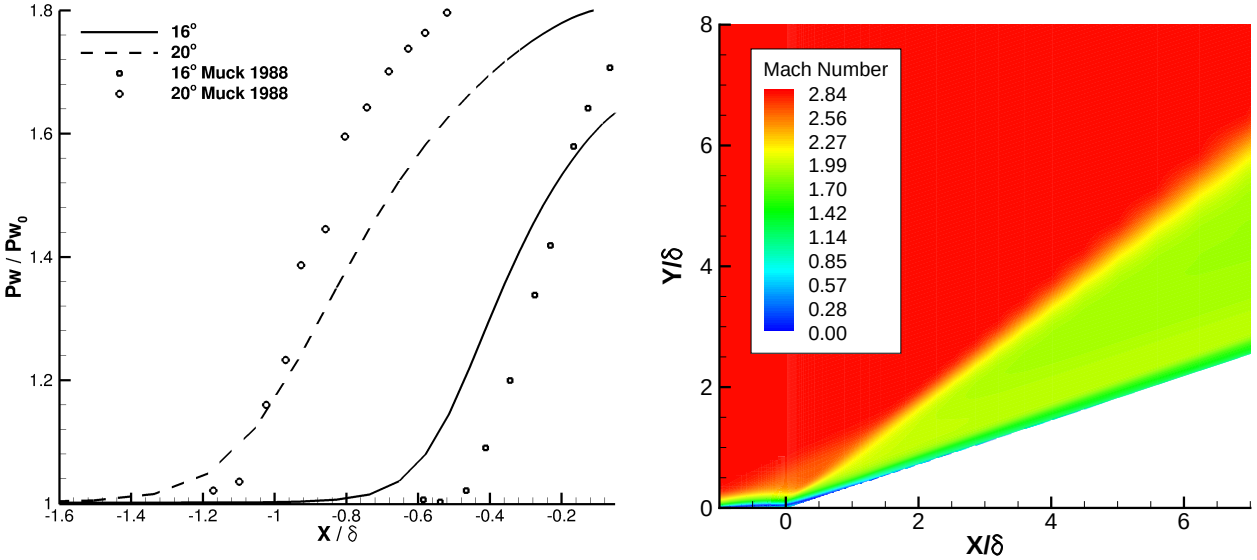

(a) Pressure curves for $\theta = 16°$ and $\theta = 20°$.

(b) Mach contours for $\theta = 20°$.

Figure 3.6: SST, AUSM$^+$ with entropy satisfying $a_{1/2}$, $M = 2.84$, $Re = 6.5 \times 10^7 m^{-1}$.

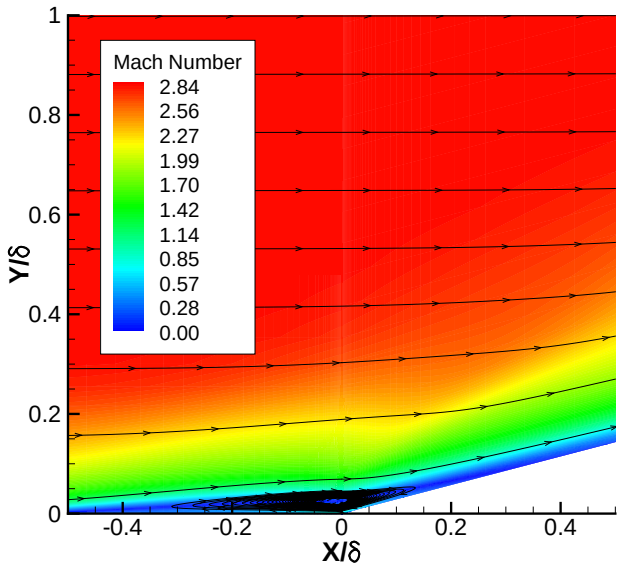

(a) Mach contours for $\theta = 16^o$.

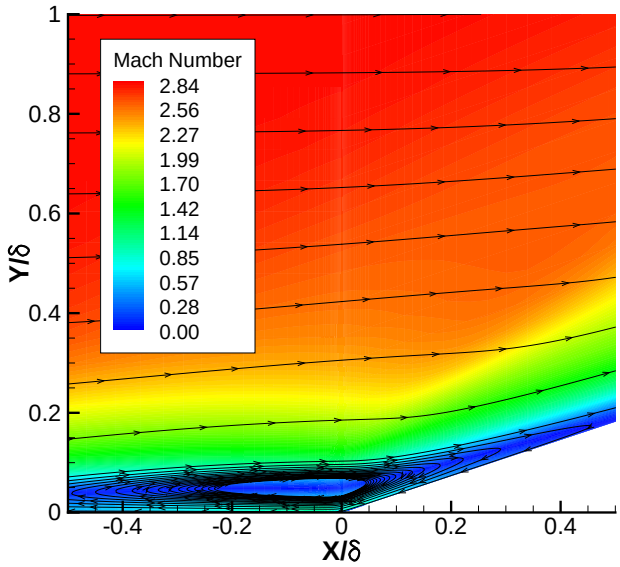

(b) Mach contours for $\theta = 20^o$.

Figure 3.7: SST, AUSM$^+$ with entropy satisfying $a_{1/2}$, $M = 2.84$, $Re = 6.5 \times 10^7 m^{-1}$.

3.1.3 Orion CEV aerodynamic testing

In this section, firstly predictions of the aerodynamic coefficients of the Orion CEV (figures 3.2a and 3.8) are compared with data from reference [3] that is a summary of the experimental static aerodynamic data of the Orion CEV. These data were collected during wind-tunnel tests at different facilities to support the development of the spacecraft. The results for the test cases at Mach 3 with Reynolds 1.5×10^6 and

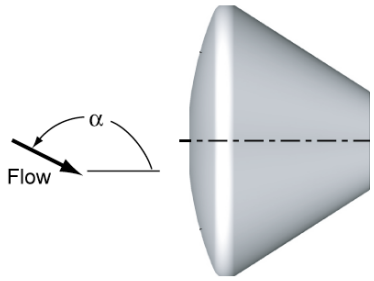

Figure 3.8: Orion CEV sketch with angle of attack definition, from [3].

Mach 6 with Reynolds 1×10^6 have been used. As can be seen from figure 3.9, the predictions given by the CFD code are in good agreement with the experimental data. Indeed, the relative differences between the numerical and the experimental results are not more than 4% and both follow the same trends.

In [142], experimental and numerical investigations of the aero-heating environment of the Orion CEV were reported with the primary goal to provide convective heating data for use in assessing the accuracy of computational techniques. In figures 3.10a and 3.10b two comparisons between the experimental results obtained at the Langley Research Center 20-Inch Mach 6 Air Tunnel, the numerical results obtained by the NASA code LAURA, [143], and the CFD predictions given by HMB2 are presented. The agreement between the experimental results and the numerical predictions given by HMB2 with the proposed implementation of the AUSM$^+$ scheme, as for the LAURA solver, is good. Indeed, the discrepancies are lower than the uncertainty of the data reported in [143]. This shows that the AUSM$^+$ scheme is a reliable tool also for heating predictions for the this test case.

Finally, the Mach contours for two test cases are presented in figures 3.11a and 3.11b. It has to be noted that no shock instabilities were observed during these simulations.

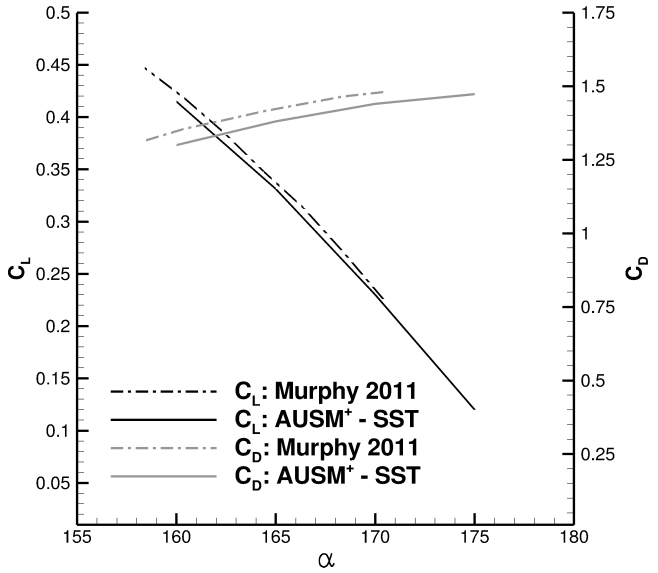

Figure 3.9: Orion CEV C_L and C_D: SST, AUSM$^+$, $M = 3$, $Re_D = 1.5 \times 10^6$.

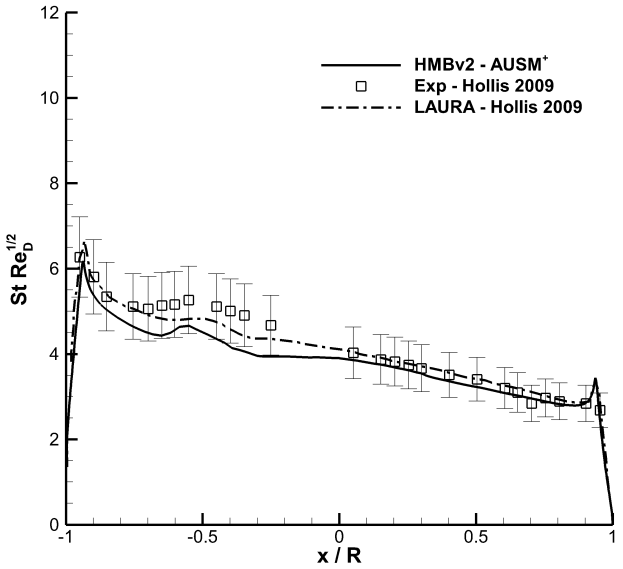

(a) $M = 6$, $Re_D = 1.76 \times 10^6$, $\alpha = 16°$.

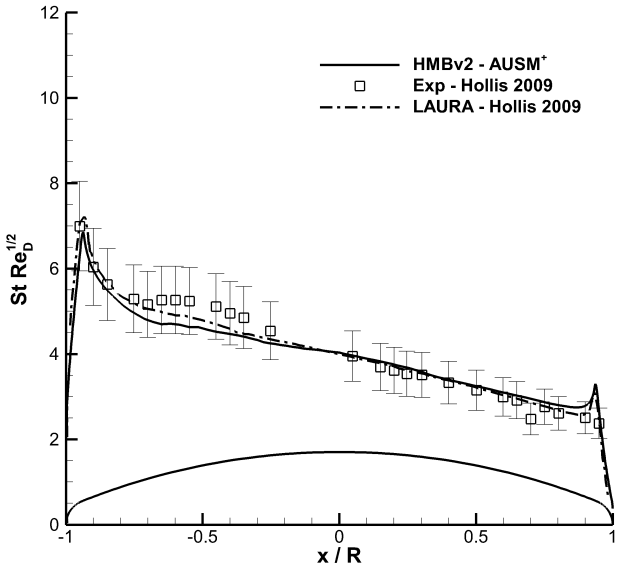

(b) $M = 6$, $Re_D = 1.17 \times 10^6$, $\alpha = 20°$.

Figure 3.10: Orion CEV $StRe_D^{1/2}$: laminar flow, AUSM$^+$ with entropy satisfying $a_{1/2}$.

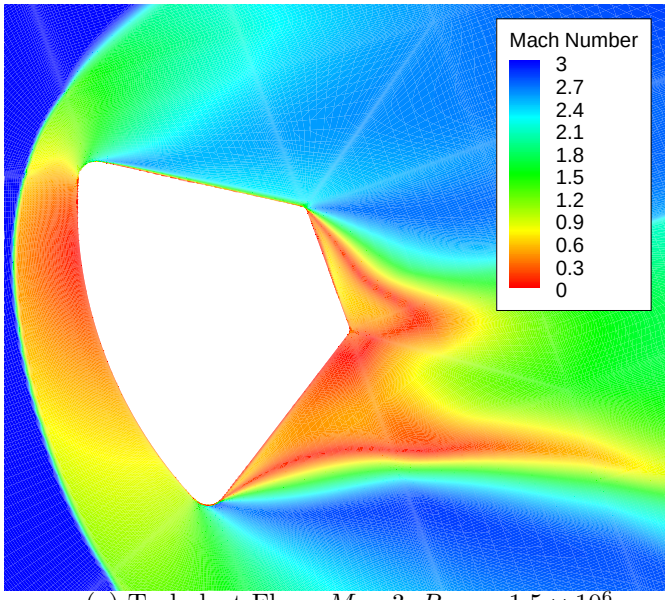

(a) Turbulent Flow: $M = 3$, $Re_D = 1.5 \times 10^6$, $\alpha = 20°$.

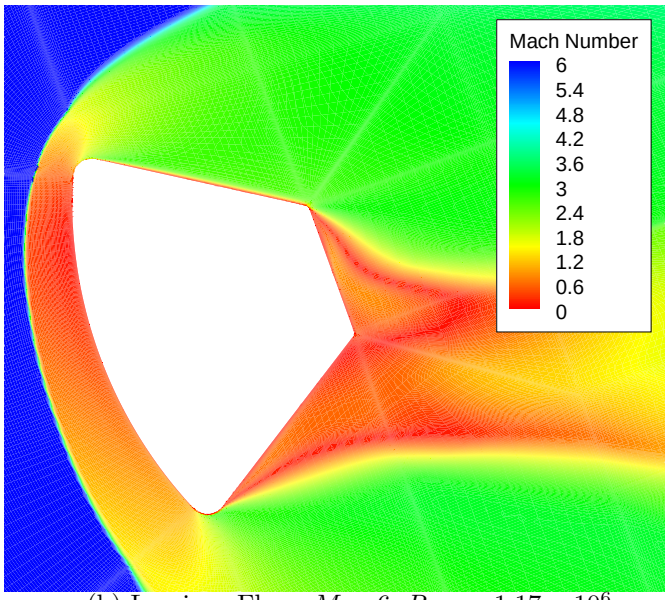

(b) Laminar Flow: $M = 6$, $Re_D = 1.17 \times 10^6$, $\alpha = 20°$.

Figure 3.11: Orion CEV Mach Contours.

3.2 Transonic Regime: AUSM$^+$up Scheme

To evaluate the approximated analytical Jacobian proposed for the AUSM$^+$up scheme in the transonic regime, the viscous flow over the RAE2822 aerofoil [135] and the ONERA M6 wing [136] have been considered as test cases.

The RAE2822 airfoil grid consisted of 3 blocks and 34000 cells while the test condition were $M = 0.73$ and Reynolds number 6.5×10^6 with an angle of attack of 2.31 degrees. The turbulence model employed was the $k-\omega$. The maximum CFL number obtained with the AUSM$^+$up scheme for the present test case was equal to 25, A prediction with 7 orders of reduction of the $L2$ norm of the residuals, was obtained in 5 minutes on one processor of a quad-core Xeon ® CPU machine. This was 40% less than the time needed with the numerical approximation of the Jacobian, and was achieved after about 1500 iterations as shown in figure 3.12. As for the AUSM$^+$ in section 3.1, the computational time required to compute analytically the Jacobian of the AUSM$^+$up was found to be three times less than for the numerical evaluation. The Osher scheme, employed in previous works [144], for the same test case allowed a CFL number of 90 reducing the computational time by 35%. An explanation of the higher performance of the Osher implicit implementation can be found in the fact that for this scheme an exact Jacobian can be defined. The pressure coefficient profiles obtained by the CFD method based on the AUSM$^+$up scheme agree with the experimental results of [135], confirming the reliability of the numerical scheme, as shown in figure 3.13.

The ONERA M6 wing computational domain was composed by 94 blocks with 2.15 million cells overall. The chosen test conditions were: $M = 0.84$, angle of attack equal to 3.06^o. For the Euler 3D test case the solution has been obtained employing the 4-stage Runge-Kutta method, CFL equal to 0.5, till 1 order of reduction and then the proposed implicit implementation, which achieved a CFL equal to 10. This allowed the solver to give a prediction, with 6 orders of reduction, in 120 minutes, 3407 iterations, on 2 quad-core Xeon® CPU machines in parallel. On the same test case the implicit implementation of the Osher scheme with the same time marching approach allowed the same CFL number. Also in this case the reliability of the AUSM$^+$up scheme prediction was confirmed. As seen from figures 3.14a and

3.14b, the agreement in the trends of the pressure coefficient profiles predicted by the AUSM$^+$up scheme with the experimental data from [136] and the inviscid numerical results provided in [145] confirmed the reliability of the solution also for a transonic 3D test case. Looking at figure 3.15a is possible to notice the typical flow field on the upper surface of the ONERA M6 wing, in which the two shocks present at the front and rear part of the root region coalesce in a single shock at the triple point towards the tip. Moreover, the flow fields predicted by the AUSM$^+$up and Osher schemes are in good agreement (figure 3.15b).

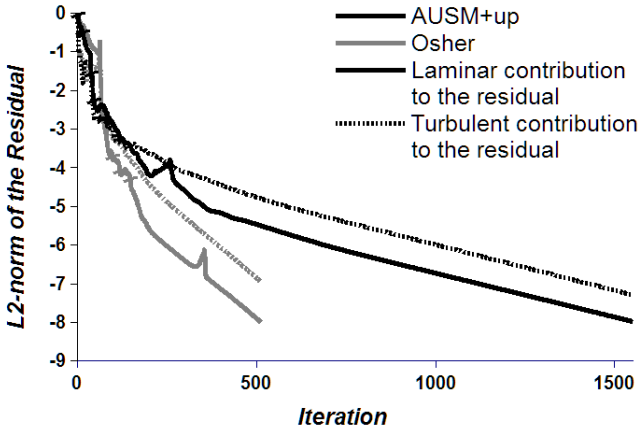

Figure 3.12: Convergence history: RAE2822 aerofoil , $M = 0.73$, $\alpha = -2.31°$ and $Re = 6.5 \times 10^6$.

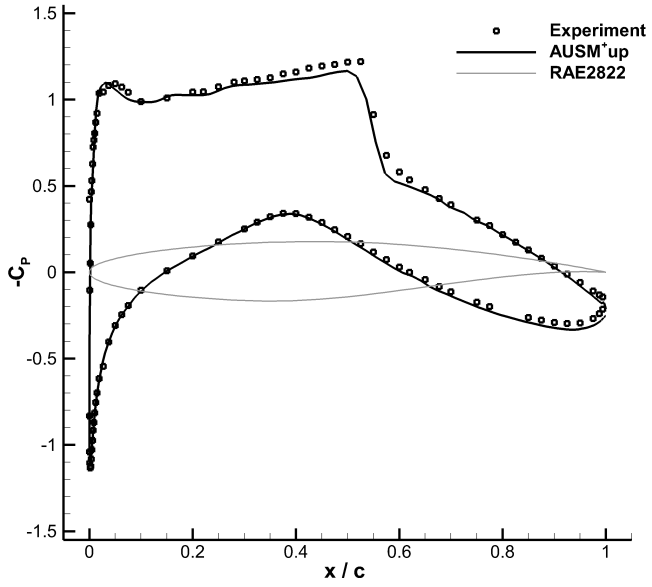

Figure 3.13: Surface C_P: RAE2822 aerofoil , $M = 0.73$, $\alpha = -2.31°$ and $Re = 6.5 \times 10^6$.

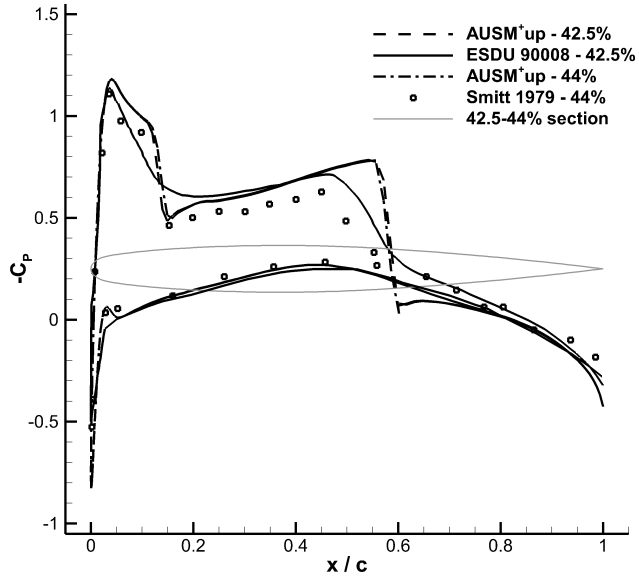

(a) Mid-span region

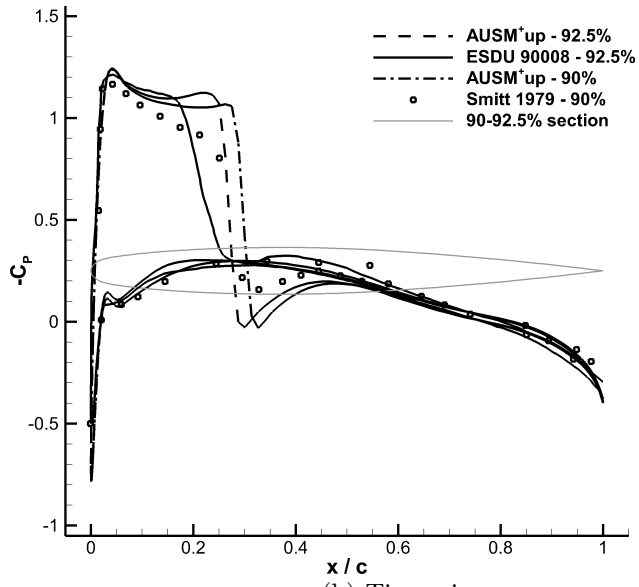

(b) Tip region

Figure 3.14: ONERA M6 wing $-C_p$ profiles at two different sections along the span, $M = 0.84$, angle of attack 3.06°.

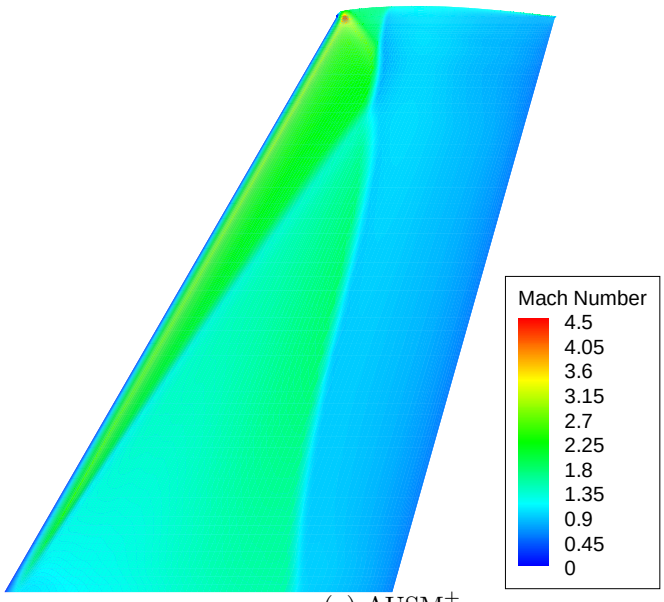

(a) AUSM$^+$up

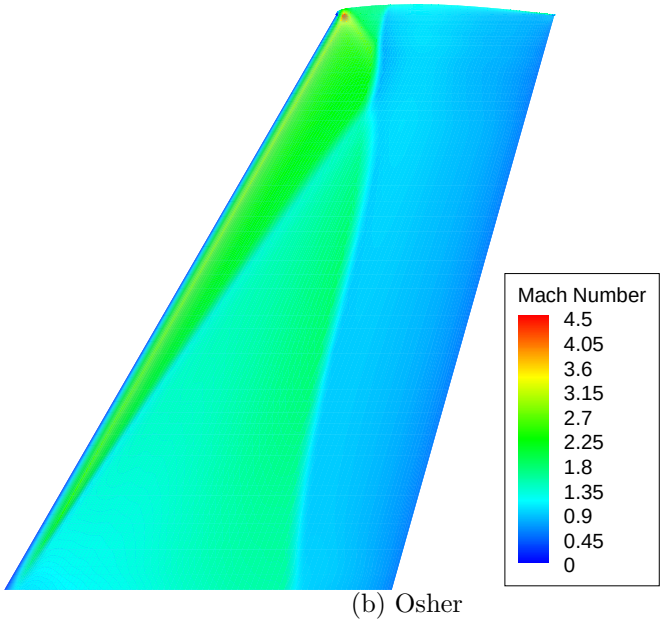

(b) Osher

Figure 3.15: ONERA M6 wing upper surface Mach lines and contours, $M = 0.84$, angle of attack 3.06°.

3.3 Low-Mach Regime: AUSM$^+$up Scheme

For the low-speed regime, the viscous flow over the S809 aerofoil [146] at 2.1 degrees of incidence and the MEXICO blade [147] have been chosen as test cases. Both cases are comprehensively discussed in [144] and used here to validate and evaluate the performance of the fully analytical Jacobian proposed for the AUSM$^+$up scheme in low-Mach regime.

For the S809 airfoil the grid consisted of 12 blocks and 60000 cells and two low Mach numbers have been considered, $M = 0.1$ and $M = 0.01$, both with a Reynolds number of 1×10^6. The adopted turbulence model was the $k - \omega$. At $M = 0.1$ the AUSM$^+$up allowed the solver to run at a maximum CFL number of 50. A prediction, with 8 orders of reduction for the laminar and turbulent residuals, needed 3100 iteration, see figure 3.18a. The computational time on a quad-core Xeon® CPU machine was 6 minutes, 40% faster than the approach with the numerical Jacobian. For $M = 0.01$ the maximum allowed CFL number was higher, reaching 500. For this reason a prediction, with 8 and 9 orders of reduction for the laminar and turbulent residuals respectively, was obtained in only 5 minutes, 2531 iteration, on the same machine, see figure 3.18b, which is 45% less than the time needed employing the numerical Jacobian. The LM-ROE scheme implicit implementation documented in [144] achieved CFL numbers of 50 and 200 on the same test cases. The LM-ROE resulted in a 30% slower simulation than with the AUSM$^+$up scheme for the $M = 0.01$ case due the lower CFL while 40% faster for the $M = 0.1$ case since the CFL numbers are comparable and the evaluation of the original ROE Jacobian used in [144] for the LM-ROE scheme is more efficient. The reliability of the solution was, once again, confirmed as it is possible to see from figure 3.17. Indeed, the pressure coefficient profiles obtained by the CFD method fit quite well the experimental results of Ramsay [148].

For the 3D parked MEXICO blade the computational domain was composed by 94 blocks with 2.15 million cells overall and the high performance of the proposed implicit implementation of the AUSM$^+$up scheme was confirmed. The chosen test condition was a parked position with $M = 0.029$ wind and pitch angle equal to 81^o, see figure 3.16; the Reynolds number was 4.93×10^5. The parked position means a non-rotating blade positioned to have the wind direction transversal to the chord in order to not generate

torque. The $k-\omega$ turbulence model of Menter was employed also in this case. The maximum CFL

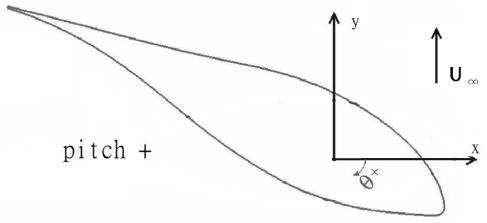

Figure 3.16: Parked position and pitch angle definition

obtained was equal to 20, which allowed the solver to compute a prediction, with 6 and 7 orders of reduction for the laminar and turbulent residuals respectively, in 193 minutes, 3624 iteration, on 3 quad-core Xeon® CPU machines in parallel. Looking at figures 3.19a and 3.19b no particular differences, except small discrepancies due to the different numerical dissipations of the schemes, can be spotted between the AUSM$^+$up prediction and the one obtained with the LM-ROE in [144].

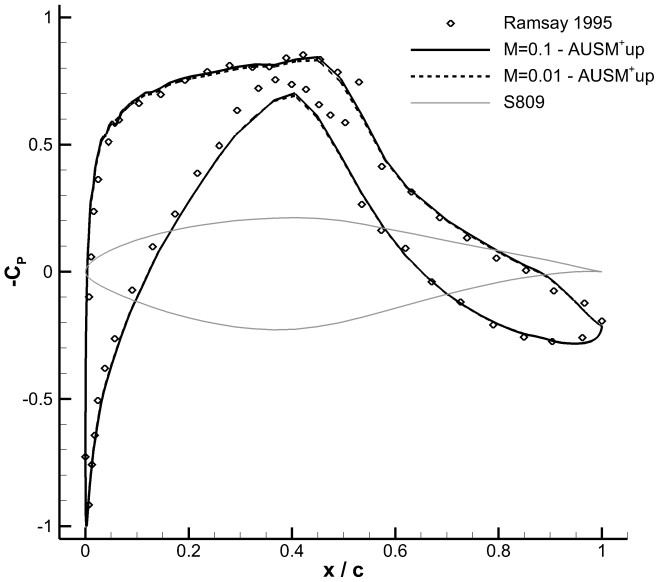

Figure 3.17: S809 aerofoil $-C_p$ profiles, $\alpha = -2.1°$ and $Re = 1 \times 10^6$.

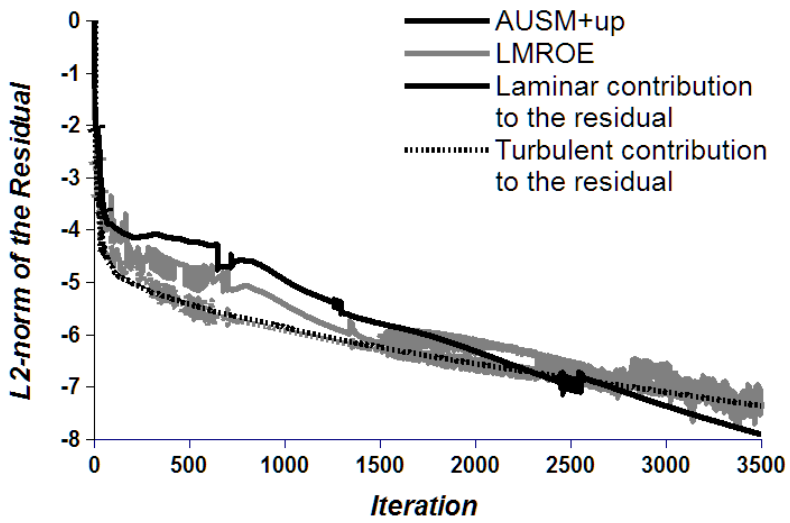

(a) $M = 0.1$, CFL=50.

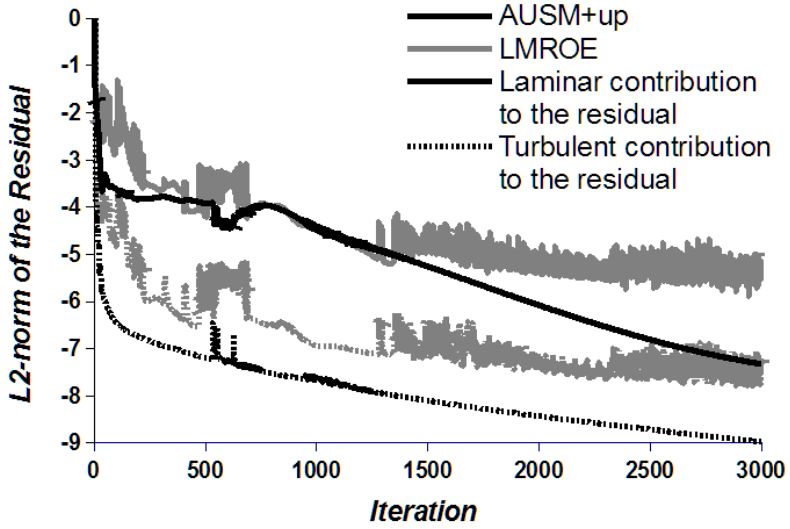

(b) $M = 0.01$, CFL=500

Figure 3.18: S809 aerofoil Residual vs Iteration, $\alpha = -2.1°$ and $Re = 1 \times 10^6$.

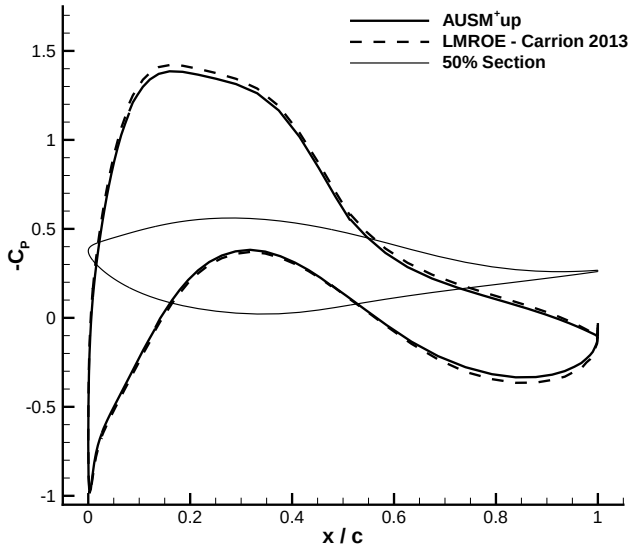

(a) 50%

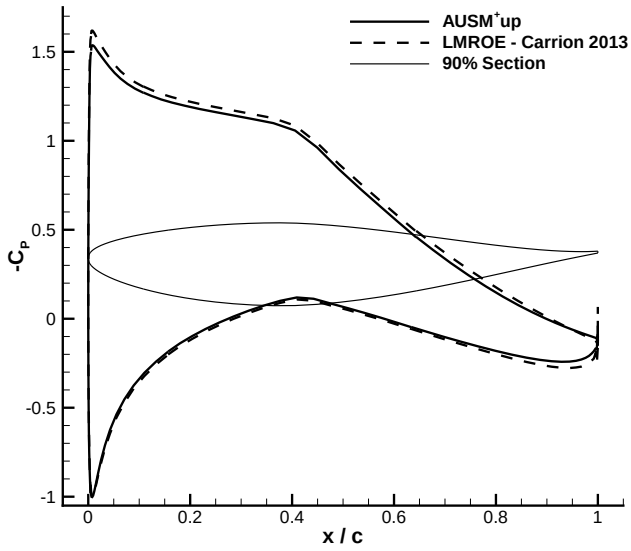

(b) 90%

Figure 3.19: Parked MEXICO blade $-C_p$ profiles at two different sections along the blade, $M = 0.029$, pitch angle 81° and $Re = 4.93 \times 10^5$.

3.4 Conclusions

In chapter 2 the derivation of a novel formulation of the AUSM$^+$ scheme and its extension to the AUSM$^+$up scheme and a continuous approximation of its analytical Jacobian have been presented. In this chapter, the implicit schemes with the proposed analytical Jacobian have been tested in a wide range of Mach numbers covering high-speed, transonic and low-Mach regimes.

In section 3.1 it has been shown that the analytical Jacobian for AUSM$^+$ led to a solver $30-40\%$ faster than a 4-stage Runge-Kutta method, thanks to the higher CFL numbers allowed by the implicit time discretisation, and 50% faster than an implicit approach with a numerical approximation of the Jacobian matrix by finite differences. This is due mainly to the lower computational efficiency of evaluating numerically the Jacobian and partially to the higher CFL number allowed by the analytical Jacobian approach.

Regarding the Osher scheme that is routinely employed in HMB2, the proposed implementation of the AUSM$^+$up is about 35% slower as shown in section 3.2. The reason for the lower performance is that the Osher scheme involves only continuously differentiable functions that make the implicit implementation of the scheme more efficient.

In the low-Mach regime, section 3.3, the performance of the proposed implementation has been compared to the LM-ROE scheme discussed in [144]. The results suggest that the proposed AUSM$^+$up formulation led to a faster solver for very low Mach numbers, see figure 3.18b, due the higher CFL number allowed; while at relatively higher Mach numbers, see figure 3.18a, the allowed CFL numbers for the implicit LM-ROE and AUSM$^+$up schemes are comparable and the LM-ROE becomes faster. This is probably due to the fact that the implicit implementation of the LM-ROE proposed in [144] employs the Jacobian matrix of the original Roe scheme, which is more efficient, involving just C^1 functions, but limits the maximum allowed CFL number at very low Mach.

Finally, comparing the prediction obtained employing the proposed AUSM$^+$ and AUSM$^+$up formulation with results available in the literature, it has been shown that the reliability of the AUSM$^+$ and AUSM$^+$up schemes for the convective fluxes is preserved after introducing the sigmoidal function.

Chapter 4

Rarefied and Hybrid Flow Solvers - MΦC

4.1 Introduction

The methods described in the present chapter are built in the Multi-Physics Code (MΦC) developed at the University of Liverpool [90, 91, 92]. MΦC is a computational framework designed for simulations of complex flows and it is able to employ different mathematical models in different regions of the flow domain depending on the flow physics. The aim of the hybrid approach is to use more computationally expensive approaches only where strictly needed and use the continuum-level modelling elsewhere.

For the continuum flow solver, as in HMB2, a cell-centred block-structured finite-volume method is employed to discretise the compressible NS equations and the AUSM$^+$/up method can be used for the convective fluxes, see chapter 2. Alternatively, the GKS methods presented in chapter 5 can be employed in the continuum solver to extend the capability of the latter to simulate flows in slightly rarefied conditions as shown in chapter 6. For the analysis of low-speed flows with rarefaction effects, a Lattice Boltzmann method as well as a Vortex-In-Cell method for vortex-dominated incompressible flows are also available in the framework. To predict rarefied flow fields with strong non-equilibrium the framework includes Molecular Dynamics methods as well as the deterministic Discrete Velocity Method described in section 4.6 for the Shakhov, Rykov and ES kinetic Boltzmann equations.

Previous works on coupled NS/MD simulations using the Multi-Physics Code are mainly focused on developing coupling techniques and applications to micro-fluidics [90, 91]. The developed coupling techniques involved continuum state reconstruction for the coupling from MD to NS and particle-forcing

techniques for imposing continuum flow derived interface conditions on the MD simulation.

In the present work, the emphasis is on the simulation of hypersonic, partially-rarefied flows. For this purpose the hybrid approach and the DVM included in the framework have been employed and thus are described in this chapter. The work made use mainly of the Shakhov and Rykov models, then the relative non-dimensional forms implemented in MΦC are presented in sections 4.3 and 4.4, respectively. For the assessment of the Rykov model implementation presented in chapter 6, the ES model for diatomic gases proposed in [29], and previously implemented in the framework, has been employed as comparison. Detail of the latter model can be found in appendix D,

4.2 Boltzmann Equation

The fundamental equation employed to model the behaviour of gases at molecular level is the Boltzmann transport equation, presented in [12] in the following form

$$\frac{\partial[nf(\mathbf{x},\mathbf{c},t)]}{\partial t} + \mathbf{V}\cdot\bigtriangledown[nf(\mathbf{x},t,\mathbf{c})] = \triangle\left[Q(f)\right]. \tag{4.1}$$

The BTE describes the evolution of the velocity distribution function (VDF), $f(\mathbf{x},t,\mathbf{c})$, which represents the molecular density of particles with position $\mathbf{x}$ and particle-velocity $\mathbf{c}$ at time t. The operator, $\triangle\left[Q(f)\right]$, describes the rate of change of f due to binary collisions among particles. Unlike calculation of the other terms in equation (4.1), $\triangle\left[Q(f)\right]$ involves integrating over all velocity space in order to account for collisions between particles of all velocities. In contrast with the NS equations, since no assumption about the form of f is made, the BTE is physically accurate for dilute gases under all conditions ranging from continuum to free-molecular flow. If m denotes the molecular mass, the continuum-level state can be obtained by the following moments $\mathbf{\Psi} = (m,\ m\mathbf{c},\ \frac{1}{2}m\mathbf{c}^2,\ \frac{1}{2}m\mathbf{c}'c'^2)^T$ of the VDF

$$(\rho,\ \rho\mathbf{u},\ \rho e_{tot},\ \mathbf{q})^T = \iiint_{-\infty}^{+\infty} \mathbf{\Psi} f d\mathbf{c}. \tag{4.2}$$

4.3 Non-dimensional Shakhov Model

The complex collision term in the right-hand side of the BTE, poses a major challenge in modelling flows using this equation [149]. For this reason kinetic model equations have been developed which approximate the BTE such that the exact moment equations up to a desired order are respected. The first kinetic model equation to be proposed has been the Bhatnagar-Gross-Krook model [25] where the complex collision term has been replaced with a relaxation term towards the equilibrium Maxwellian (4.6). However, it is well known [11] that the BGK model recovers a unit Prandtl number in the continuum limit and for this reason various corrected models have been presented in the literature. Several attempts have been made to improve the BGK model to recover the correct Prandtl number in the continuum limit, while keeping the same simplicity of the approach. Among them, two very well established kinetic models, for flows where only translational non-equilibrium is considered, are the Ellipsoidal Statistical model [27] and the Shakhov model [26]. Both maintain the overall structure of the BGK model where the Maxwellian is replaced with a velocity distribution function such that the resulting moments recover the correct Prandtl number in the hydrodynamic limit. The two models differ in the way the latter function is defined. The ES model introduces a modified collision operator replacing the Maxwellian equilibrium function by a generalised Gaussian function defined to obtain the continuum expressions for the stress tensor and the thermal flux vector with the proper viscosity and thermal conductivity. In the Shakhov model the correct continuum Prandtl number is achieved by scaling the heat fluxes and the equilibrium distribution function consists in the Maxwellian multiplied by a correction term determined by imposing the agreement of the moments up the third order between the BGK type approximation and the full BTE equation. Although these models provide the correct limit, it is not guaranteed that they yield accurate results in the transition regime. The present work made use of the Shakhov model, which has been proved to be a reliable kinetic approximation where only translational non-equilibrium is considered [150].

Defining the following non-dimensional variables

$$\begin{aligned} &\rho = \hat{\rho}/\rho_\infty \quad ; \quad T = \hat{T}/T_\infty \quad ; \quad u = \hat{c}/\sqrt{2RT_\infty} \\ &t = \hat{t}/(\mu_\infty p_\infty^{-1}) \quad ; \quad \mathbf{x} = \hat{\mathbf{x}}/\left(\sqrt{2RT_\infty}\mu_\infty p_\infty^{-1}\right) \quad ; \quad q = \hat{q}/\left(\rho_\infty (2RT_\infty)^{3/2}\right) \\ &\mu = \hat{\mu}/\mu_\infty \quad ; \quad \tau = \hat{\tau}/(\mu_\infty p_\infty^{-1}) \end{aligned} \tag{4.3}$$

where the dimensional variables are denoted with a hat and $c_\infty = \sqrt{2RT_\infty}$ represents the most probable molecular velocity magnitude at equilibrium at the reference temperature T_∞, the non-dimensional distribution function for the Shakhov model results

$$F_S = \hat{F_S}/\left(\rho_\infty (2RT_\infty)^{-3/2}\right). \tag{4.4}$$

Then, substituting the latter variables in the Shakhov model written in terms of $F = mf$ we obtain

$$\begin{aligned} &\frac{\partial F}{\partial t} + \mathbf{c}\frac{\partial F}{\partial \mathbf{x}} = \frac{F_S - F}{\tau} \\ &F_S = F_M\left[1 + \frac{8}{15}\frac{q_x}{\rho T}\frac{c'_x}{T}\left(\frac{\mathbf{c}'^2}{T} - \frac{5}{2}\right)\right] \end{aligned} \tag{4.5}$$

where

$$F_M = \frac{\rho}{(\pi T)^{3/2}}\exp\left(-\frac{\mathbf{c}'^2}{T}\right) \tag{4.6}$$

is the non-dimensional Maxwellian and the total collision time τ is expressed as μ/p. For the viscosity temperature dependency, the following power law

$$\mu(T) = \mu(T_\infty)\left(\frac{T}{T_\infty}\right)^\omega \tag{4.7}$$

is employed in MΦC, generally with an exponential factor of 0.72 [151]. The dimensionless macroscopic quantities can be obtained from F by means of the following moments $\mathbf{\Psi} = (1,\ c_x,\ \mathbf{c}^2,\ \frac{1}{2}c'_x c'^2)^T$

$$\left(\rho.\ \rho u_x,\ \frac{3}{2}\rho T + \rho u_x^2,\ q_x\right)^T = \int_{-\infty}^{+\infty} \mathbf{\Psi} F d\mathbf{c}. \tag{4.8}$$

4.4 Non-dimensional Rykov Model

The Shakhov and the ES models present a single relaxation term. This means that these models are able to represent only problems where a single relaxation process takes place, narrowing their applicability only to monoatomic gases or flow fields without rotational non-equilibrium. However, hypersonic and re-entry vehicles encounter temperatures associated with translational, rotational and, often, vibrational non-equilibrium [152]. For this reason, various works have been made in order to extend the the Shakhov model and the ES model to include multiple relaxation processes for polyatomic gases. Among them, the Rykov model [28] and the ES polyatomic model [29] are the most commonly employed when rotational non-equilibrium is considered. In the present work the Rykov model has been extensively used and for this reason is described in this section. The ES polyatomic model of Andries and co-workers [29], described in appendix D, is also available in MΦC.

Considering the flow of a diatomic gas, we will assume that the gas temperature is not too high, so that the vibrational degrees of freedom are not excited, and not too low, so that the rotational degrees of freedom can be considered fully excited. In this case, the particle distribution function $f(\mathbf{x}, \mathbf{c}, t, \zeta)$, which describes the state of the gas, will be a function not only of the spatial coordinate $\mathbf{x}$, the particle velocity $\mathbf{c}$ and the time t, but also of the rotational degrees of freedom ζ. The Rykov model represents an extension of the Shakhov model where also rotational non-equilibrium is considered and has been proved to be a reliable kinetic approximation, up to the heat fluxes moments of the BTE, for this kind of flows [28, 153, 4, 47] . Since the rotational degrees of freedom are considered fully excited, ζ is reduced by the model and a second distribution function is obtained.

Employing the non-dimensional variables defined in equations (4.3), the non-dimensional distribution functions of the model result

$$F_0 = \hat{F}_0 / \left(\rho_\infty (2RT_\infty)^{-3/2}\right) \quad ; \quad F_1 = \hat{F}_1 / \left(mRT_\infty \rho_\infty (2RT_\infty)^{-3/2}\right) \tag{4.9}$$

thus, for the Rykov model written in terms of $F = mf$ we obtain

$$
\begin{aligned}
&\frac{\partial F_0}{\partial t} + \mathbf{c}\frac{\partial F_0}{\partial \mathbf{x}} = \frac{F_0^{eq} - F_0}{\tau} \qquad ; \quad \frac{\partial F_1}{\partial t} + \mathbf{c}\frac{\partial F_1}{\partial \mathbf{x}} = \frac{F_1^{eq} - F_1}{\tau} \\
&F_0^{eq} = \frac{1}{Z_r}F_0^r + \left(1 - \frac{1}{Z_r}\right)F_0^t \quad ; \quad F_1^{eq} = \frac{1}{Z_r}F_1^r + \left(1 - \frac{1}{Z_r}\right)F_1^t \\
&F_0^r = F_M(T)\left[1 + \frac{8}{15}\omega_0 \frac{q_x^t}{\rho T}\frac{c'_x}{T}\left(\frac{\mathbf{c}'^2}{T} - \frac{5}{2}\right)\right] \\
&F_0^t = F_M(T_t)\left[1 + \frac{8}{15}\frac{q_x^t}{\rho T_t}\frac{c'_x}{T_t}\left(\frac{\mathbf{c}'^2}{T_t} - \frac{5}{2}\right)\right] \\
&F_1^r = TF_M(T)\left[1 + \frac{8}{15}\omega_0 \frac{q_x^t}{\rho T}\frac{c'_x}{T}\left(\frac{\mathbf{c}'^2}{T} - \frac{5}{2}\right) + 4\omega_1(1-\delta)\frac{q_i^r c'_i}{\rho T^2}\right] \\
&F_1^t = T_r F_M(T_t)\left[1 + \frac{8}{15}\frac{q_x^t}{\rho T_t}\frac{c'_x}{T_t}\left(\frac{\mathbf{c}'^2}{T_t} - \frac{5}{2}\right) + 4(1-\delta)\frac{q_i^r c'_i}{\rho T_t T_r}\right] \\
&F_M(T) = \frac{\rho}{(\pi T)^{3/2}}\exp\left(-\frac{\mathbf{c}'^2}{T}\right) \\
&\frac{5}{2}T = \frac{3}{2}T_t + T_r
\end{aligned}
\tag{4.10}
$$

where the total collision time τ is expressed as $\mu_t/\rho T_t$ with the viscosity determined from the translational temperature. In a system of colliding particles, energy is transferred between the various internal modes and the collision number associated to a mode represents the inverse of the fraction of particle collisions involving that mode, see appendix F. The Rykov model is based on the assumption that the rotational collision number Z_r is a given constant or a function of the flow temperatures. Several works provide an expression of Z_r as a function of the temperature in the flow field. Probably the first attempt to appear in the literature is the theoretical work of Parker [154] where, employing an empirical non impulsive model and assuming coplanar collisions and zero initial rotational energy, the following approximate expression is obtained

$$
Z_r^{Par.} = \frac{(Z_r)_\infty}{1 + (\pi^{3/2}/2)(T^*/T)^{1/2} + (\pi^2/4 + \pi)(T^*/T)} \tag{4.11}
$$

$T* = 91.5K$ is the characteristic temperature of the intermolecular potential and $(Z_r)_\infty = 23.5$ is the limiting value suggested in [12]. While Parker's expression, (4.11), is derived involving a large number

of simplifying assumptions the overall dependence on the temperature is in agreement with the more rigorous treatment of [155]. However, this expression does not involve any dependence on the different translational and rotational temperatures. Thus, in the recent literature, models derived from data fitting, either from numerical or experimental results, have been employed. In [28, 153, 4] the following expression for the collision number is presented to be used with the Rykov model

$$\begin{aligned} Z_r^{Ryk.} &= \frac{3}{4}\pi\frac{\psi(\tilde{T})}{\tilde{T}^{1/6}}\frac{9\tilde{T}}{\tilde{T}+8}\frac{T_r}{T_t}\left[0.461+0.5581\left(\frac{T_r}{T_t}\right)+0.0358\left(\frac{T_r}{T_t}\right)^2\right] \\ \psi(\tilde{T}) &= 0.767+0.233\tilde{T}^{-1/6}\exp\left(-1.17\left[\tilde{T}-1\right]\right) \\ \tilde{T} &= T_t/T^*. \end{aligned} \tag{4.12}$$

An alternative expression for $Z_r(T_t, T_r)$ derived from molecular dynamics simulations can be found in [156] as

$$Z_r^{Val.} = \left[a_1\left(\frac{T_t}{1K}\right)^{1/4}+a_2\left(\frac{T_t}{1K}\right)^{-1/4}-a_3\left(\frac{T_t}{1K}-1000\right)\right]\left[1-b\left(1-\frac{T_r}{T_t}\right)\right] \tag{4.13}$$

where $a_1 = 1.33868$, $a_2 = -6.19992$, $a_3 = -0.00107942$ and $0 < b \leq 1$. It is important to notice that, considering the moments of the Rykov model collision term shown in appendix E, the relaxation process in the model is described as

$$\frac{\rho(T-T_r)}{Z_r\tau} \tag{4.14}$$

while in [154, 156] Jeans equation is considered, leading to

$$\frac{\rho(T_t-T_r)}{Z_r\tau}. \tag{4.15}$$

This means that the collision number in the Rykov model results

$$Z_r = 0.6\times Z_r^{Par./Val.}. \tag{4.16}$$

All the mentioned expressions for the rotational collision number are available in MΦC. Regarding the viscosity law, the expression proposed by Rykov and his co-workers [28, 153, 4]

$$\mu(T_t) = \mu(T^*)\frac{\tilde{T}^{2/3}}{\psi(\tilde{T})} \tag{4.17}$$

or a simpler power law

$$\mu(T_t) = \mu(T_\infty)\left(\frac{T_t}{T_\infty}\right)^\omega \tag{4.18}$$

can be selected in the framework. Usually an exponential factor of 0.72 [151] is chosen for the power law. To make the system (4.10) complete, the value of the constants δ, ω_0 and ω_1, need to be determined. In [157] $\omega_0 = 0.2354$ and $\omega_1 = 0.3049$ or $\omega_0 = 0.5$ and $\omega_1 = 0.286$ are given for diatomic gases. Both pairs of values have been successfully employed in [153, 4, 157, 158] with $\delta^{-1} = 1.55$. In the present work the values $\omega_0 = 0.5$ and $\omega_1 = 0.286$ are employed. The dimensionless macroscopic quantities can be obtained from the following moments

$$\left(\rho,\ \rho u_x,\ \frac{3}{2}\rho T_t + \rho u_x^2 + \rho T_r,\ \rho T_r,\ q_x^t + q_x^r,\ q_x^r\right)^T = \int_{-\infty}^{+\infty} \left[\boldsymbol{\Psi}_0 F_0 + \boldsymbol{\Psi}_1 F_1\right] d\mathbf{c}. \tag{4.19}$$

where $\boldsymbol{\Psi}_0 = (1,\ \mathbf{c},\ \frac{1}{2}\mathbf{c}^2,\ 0,\ \frac{1}{2}\mathbf{c}'c'^2,\ 0)^T$ of $\boldsymbol{\Psi}_1 = (0,\ 0,\ 1,\ 1,\ 1,\ 1)^T$.

4.5 The Hybrid Approach in MΦC

The first important step in the setup of an hybrid simulation is the definition of the continuum and rarefied flow regions. In the literature, the domain decomposition is generally done during the simulation on the basis of a breakdown parameter, for example as done by other researchers in [2, 1]. At the moment, this feature is still under development in MΦC and the domain decomposition, of which an example is shown in figure 6.9d of chapter 6, has to be defined by the user in an input file. However, the framework can perform a reconfiguration of the different regions throughout the calculation when the domain definition file is modified by the user. The information transfer between the two solvers can be handled in the current framework using the state-based method depicted in figure 4.1. The state-based coupling assigns boundary cells on the edge of one domain based on the flow solution of the other leaving the evaluation of the numerical fluxes to the respective solver through the relative boundary procedures. For the case of DVM/Continuum hybrid approach, this is achieved by computing moments of the kinetic solution to obtain a macroscopic state on one side of the interface and at the same time reconstructing a velocity distribution function from a macroscopic state, employing the CE solution of the kinetic model, on the other side of the interface. To obtain more accurate solutions, an overlap region, in which both approach are used, is required as a buffer zone to relax possible inaccurate kinetic boundary conditions provided by the continuum solver. In MΦC the number of cells composing this overlap region is a user defined variable.

In the current work, the DVM for kinetic approximation of the Boltzmann equations has been employed coupled mainly with the GKS method proposed in chapter 5 and for some calculation with a more traditional finite-volume approach using the AUSM$^+$ scheme. An overlap of 10 cells has been chosen for the hybrid simulations presented in chapter 6.

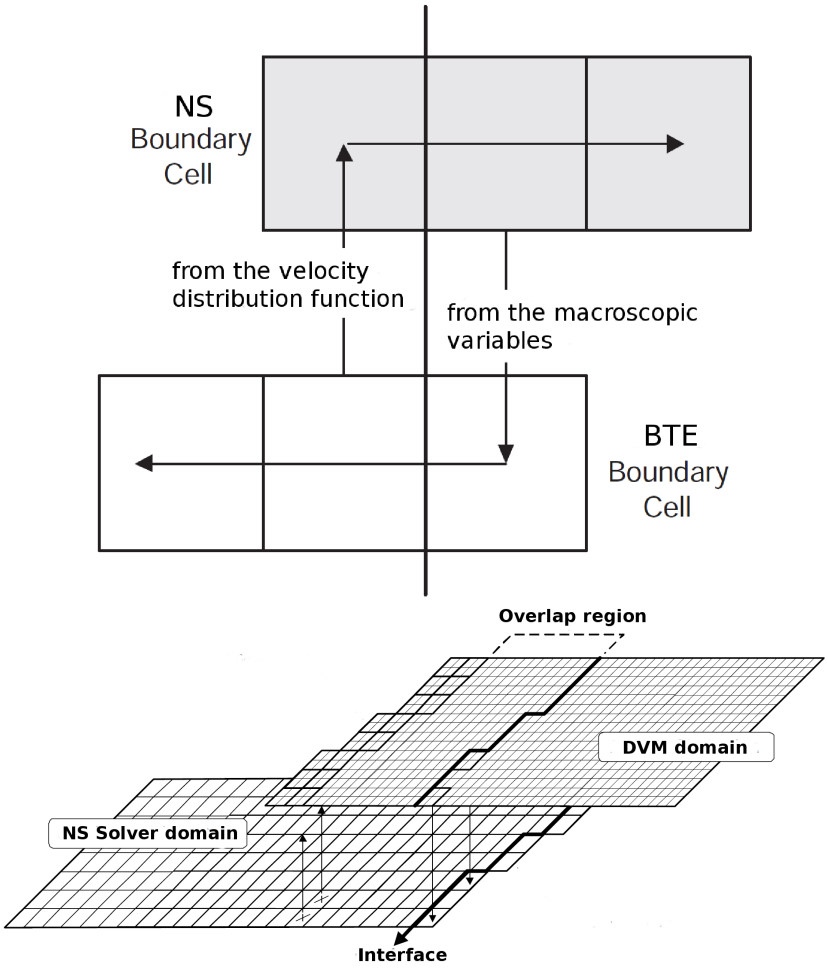

Figure 4.1: State-based coupling techniques, adapted from [2, 1].

4.6 Discrete Velocity Method for Kinetic Boltzmann Equations in MΦC

For non-continuum flow modelling, the Shakhov and ES models are included for monoatomic gas flows, while, for the present work, the Rykov model and a polyatomic ES model [29] have been implemented in MΦC to predict flow fields in rotational non-equilibrium.

The standard approach [159] to discretise kinetic model equations is to employ the discrete ordinate method [160]. Its core idea is to define a discrete velocity (phase) domain $\mathbf{c}|_m$, where m represents the index in the velocity space, in order to replace the velocity distribution function $F(\mathbf{x}, t, \mathbf{c})$ with a vector where each component $F|_m(\mathbf{x}, t)$ is an approximation of $F(\mathbf{x}, t, \mathbf{c}|_m)$. Then, the discrete kinetic model results

$$\frac{\partial F|_m}{\partial t} + \mathbf{c}\frac{\partial F|_m}{\partial \mathbf{x}} = \frac{F_{eq} - F|_m}{\tau} \tag{4.20}$$

and the fluid macroscopic quantities are given by the same moments except that the integrals in the phase space are replaced by discrete sums as follow

$$\mathbf{\Phi} = \sum_m \mathbf{\Psi} F|_m \Delta \mathbf{c}|_m. \tag{4.21}$$

In MΦC the velocity space is discretised using either a uniformly spaced method and the trapezoidal rule for the evaluation of the moments of the distribution functions or a Gauss-quadrature method with modified Hermite polynomials [161]. The Gauss-quadrature method is more efficient for low-speed microfluidic gas flows, while for high-speed flows the trapezoidal rule is the preferred approach. Moreover, it has to be mentioned that in the literature different approaches for an adaptive velocity space discretisation are available [162, 22], but due to their complexity this feature is not currently implemented in the framework. Thus, for the present high-speed flows related work, the uniform velocity space with the trapezoidal rule has been the preferred approach and was used exclusively.

An important aspect is to consistently evaluate a discrete approximation of the "target" equilibrium function F_{eq} of the collision term in the kinetic model. The classical approach [159]

$$F_{eq}|_m = F_{eq}(\mathbf{x}, t, \mathbf{c}|_m) \tag{4.22}$$

does not exactly satisfy the conservation properties, i.e. compatibility condition, of the model equation [20, 163]; as example equations (5.18) and (5.40) for the Shakhov and Rykov models respectively. For this reason, methods have been proposed in the literature to ensure that the conservation principles [163] as well as the entropy production property [20] are satisfied. In the current framework the approach of [163] for both Shakhov and Rykov models is used. In this case the discrete collision integrals are modified as follow

$$\frac{\partial F|_m}{\partial t} + \mathbf{c}\frac{\partial F|_m}{\partial \mathbf{x}} = \frac{F_{eq}(\mathbf{\Phi}'(\mathbf{x},t),\mathbf{c}|_m) - F|_m}{\tau} \tag{4.23}$$

where the modified vector of macroscopic variables $\mathbf{\Phi}'$ is obtained as solution of the discrete approximation of the moments of the distribution function relative to mass, momentum, energy and heat transfer

$$\sum_m \mathbf{\Psi}\frac{F_{eq}(\mathbf{\Phi}'(\mathbf{x},t),\mathbf{c}|_m) - F|_m}{\tau}\Delta\mathbf{c}|_m = J_{\mathbf{\Psi}} \tag{4.24}$$

where $J_{\mathbf{\Psi}}$ represents the exact moments of the kinetic model collision term. System (4.24) can be solved by means of a Newton iteration methods. In the present work a LU decomposition [164], i.e. Gaussian elimination, is employed to compute the update of the modified continuum state in each Newton iteration step.

Each of equations (4.23) can now be discretised in physical space and time using a finite-difference or a finite-volume approach and an explicit [159, 20] or implicit [20, 24] time marching scheme as well as more novel methods [21, 23]. The previously described discrete velocity method is employed in MΦC within a finite-volume scheme [103], shown here in one-dimensional formulation for simplicity, for multi-block structured grids

$$\frac{\partial F_{i,j,k}|_m}{\partial t} + \frac{F^{flux}_{i+1/2,j,k}|_m - F^{flux}_{i-1/2,j,k}|_m}{\Delta x_{i,j,k}} = \frac{F_{eq}(\mathbf{\Phi}'(\mathbf{x}_{i,j,k},t),\mathbf{c}|_m) - F_{i,j,k}|_m}{\tau} \tag{4.25}$$

and a second order TVD time marching approach [165, 166]

$$\begin{aligned}
F^{(1)}_{i,j,k}|_m &= F^n_{i,j,k}|_m + \Delta t L(F^n_{i,j,k}|_m) \\
F^{n+1}_{i,j,k}|_m &= \frac{1}{2}(F^n_{i,j,k}|_m + F^{(1)}_{i,j,k}|_m) + \Delta t L(F^(1)_{i,j,k}|_m)) \\
L(F^n_{i,j,k}|_m) &= -\frac{F^{flux}_{i+1/2,j,k}|_m - F^{flux}_{i-1/2,j,k}|_m}{\Delta x_{i,j,k}} + \frac{F^n_{eq}(\phi'(\mathbf{x}_{i,j,k},t^n),\mathbf{c}|_m) - F^n_{i,j,k}|_m}{\tau}
\end{aligned} \tag{4.26}$$

with discretised physical space $\mathbf{x}_{i,j,k}$ and time t^n. The first- and second-order numerical fluxes are as described in [167]

$$F^{flux}_{i+1/2,j,k}|_m = \frac{1}{2}\left[(\mathbf{c}\cdot\mathbf{n})\left(F_{i+1,j,k}|_m + F_{i,j,k}|_m\right) - |\,(\mathbf{c}\cdot\mathbf{n})\,|\left(\Delta F_{i+1/2,j,k}|_m + \Theta_{i,j,k}\right)\right]$$

$$\Theta_{i,jk} = \begin{cases} 0 & \text{first-order} \\ minmod(\Delta F_{i-1/2,j,k}|_m,\ \Delta F_{i+1/2,j,k}|_m,\ \Delta F_{i+3/2,j,k}|_m) & \text{second-order} \end{cases} \tag{4.27}$$

$$\Delta F_{i+1/2,j,k}|_m = F_{i+1,jk}|_m - F_{i,jk}|_m$$

where $\mathbf{n}$ is the cell face normal. For the approach employed here, a comprehensive discussion about its entropy production property is available in the literature [166].

Finally, due to the large computational time and memory overhead created by the discretisation in velocity space (in contrast to the continuum solver, which typically stores 5 continuum flow quantities, the kinetic solver stores $O(10^4)$ degrees of freedom per cell), an efficient parallel implementation involving 'two' levels of parallelism was conceived in MΦC. In this parallelisation strategy, the phase space as well as the flow domain are distributed over the processes. First, the phase space is partitioned in regular subspaces, each to be assigned to separate processes within separate MPI communicators. The overall number of processes is then divided by the number partitions to obtain the required number of communicators. The mesh-blocks in physical space are then equally distributed over these communicators. An important factor in the performance is the number of process assigned to the velocity space discretisation. Limiting the size of these communicators will minimise the overhead in collective operations required for the evaluations of the moments of the distribution functions. However, this implies an increasing number of communicators over which the mesh-blocks are divided, potentially creating a load imbalance in physical space.

4.6.1 Diffuse Wall Boundary Conditions

The gas evolution at a solid boundary is modelled assuming that particles hit the wall with a distribution function according to the flow conditions whereas they are reflected with:

- a Maxwellian distribution according to the wall state for fully accommodating boundary (viscous wall),
- the same distribution function for specular reflection boundary (inviscid wall),
- a combination of diffuse and specular boundaries depending on the accommodation coefficient σ.

Therefore, the final gas distribution function at the wall can be written as

$$F = \sigma F_{M\,u>0} + F_{u<0} + (1-\sigma)F_{u>0} \tag{4.28}$$

where $u < 0$ and $u > 0$ represent the velocities of particles hitting the wall and reflected by the wall respectively while F_M and F are the Maxwellian and the non-equilibrium distribution functions at the wall. The fluid state at the wall can be extrapolated from the domain. In the present work, fully accommodating walls have been employed, i.e. $\sigma = 1$.

Chapter 5

Analytical Definition of Gas-Kinetic Schemes for Slightly Rarefied Flows

To improve the capability of the continuum solver in MΦC to predict flow fields in thermal non-equilibrium, two GKS schemes based on the limit for a well-resolved flow of the UGKS written for the Shakhov and Rykov models, see appendices I and J, have been analytically derived and implemented in the framework. In contrast to the Taylor series expansions employed by Xu and co-workers [63, 75, 77, 7, 85, 46, 47], here the derivatives of the equilibrium function are defined fully analytically by means of properties of the employed kinetic model. Moreover, employing directly a kinetic model which involves a Prandtl number correction, instead of a rescaling the energy flux to fix the Prandtl number [63], should lead to more accurate results for diatomic gases where thermal non-equilibrium effects are important as discussed in section 1.4. Finally, the update of the non-equilibrium distribution function is neglected, which then it is not needed to be stored, reducing the memory cost of the approach. The proposed GKS schemes are limited to near-continuum regions but are simpler than the UGKS [46, 47]. However, the validity of the approach can be extended considering a modified collision time. Also the latter, in the present work, is defined fully analytically for both schemes. The schemes are presented in the current chapter and are part of the following publications:

- Kinetic Models with Rotational Degrees of Freedom for Hybrid Methods. Colonia S., Steijl R. and Barakos G.N., 6th European Conference on Computational Fluid Dynamics (ECFD VI), ECCOMAS 2014, 20-25 July 2014, Barcelona (Spain).

- Kinetic Models and Gas Kinetic Schemes for Hybrid Simulation of Partially Rarefied Flows. Colonia

S., Steijl R. and Barakos G.N., AIAA Atmospheric Flight Mechanics Conference 2015, 5-9 January 2015, Kissimmee (Florida), DOI: 10.2514/6.2015-0521.

- Kinetic Models and Gas Kinetic Schemes for Hybrid Simulation of Partially Rarefied Flows. Colonia S., Steijl R. and Barakos G.N., AIAA Journal (Articles in Advance), DOI: 10.2514/1.J054137.

- Gas Kinetic Schemes for Hybrid Simulation of Partially Rarefied Flows. Colonia S., Steijl R. and Barakos G.N., 6^{th} European Conference for Aeronautics and Space Sciences, 29 June to 3 July 2015, Krakow (Poland).

- A Gas Kinetic Scheme for Hybrid Simulation of Partially Rarefied Flows. Colonia S., Steijl R. and Barakos G.N., Progress in Flight Physics Volume 8 - EUCASS book series, accepted.

5.1 The BGK-NS Method and the Unified Gas-Kinetic Scheme

Among the gas-kinetic schemes available in the literature [86] a successful approach is represented by the BGK-NS method [63, 75] here briefly described. Integrating in time the BGK equation for a one-dimensional flow in a control volume dx with a continuous particle velocity c_x and discretised space x_i and time t^n, with step sizes of Δx and Δt respectively, one obtains

$$F|_i^{n+1} = F|_i^n + \frac{1}{\Delta x}\int_{t^n}^{t^{n+1}} \left([c_x F]|_{i-1/2} - [c_x F]|_{i+1/2}\right) dt + \frac{\Delta t}{2}\left(\frac{F_M|_i^{n+1} - F|_i^{n+1}}{\tau^{n+1}} + \frac{F_M|_i^n - F|_i^n}{\tau^n}\right) \quad (5.1)$$

where the trapezoidal rule has been employed for the collision term integral, and $[c_x F]|_{i\mp 1/2}$ are the fluxes of the distribution function across the cell interface. Then, taking the moments $\mathbf{\Psi} = (1,\ c_x,\ \mathbf{c}^2)^T$ of equation (5.1), the update of the conservative variables can be found as

$$\mathbf{W}_i^{n+1} = \mathbf{W}_i^n + \frac{1}{\Delta x}\int_{t^n}^{t^{n+1}}\int_{-\infty}^{+\infty} \mathbf{\Psi}\left([c_x F]|_{i-1/2} - [c_x F]|_{i+1/2}\right) d\mathbf{c}dt \quad (5.2)$$

since the compatibility conditions for the BGK model give

$$\int_{-\infty}^{+\infty} \mathbf{\Psi}\frac{F_M - F}{\tau} d\mathbf{c} = (0,\ 0,\ 0)^T. \quad (5.3)$$

It is well known that the BGK model recovers the incorrect Prandtl number in the continuum limit and for this reason a simple correction consisting in scaling the energy numerical flux has been proposed by Xu [63] as

$$\mathbf{f}_{energy}^{new} = \mathbf{f}_{energy} + \left(\frac{1}{Pr} - 1\right) q \quad (5.4)$$

Recently, an alternative to the finite-volume approach employed in the BGK-NS method has been presented in [168] where a hybrid finite-element/finite-volume node-pair discretisation of the NS equations has been reformulated to be employed with Xu's scheme.

The BGK-NS scheme has been applied by Xu and co-workers [77, 7] also to predict flows with internal

degrees of freedom employing the following multi-temperature BGK model

$$\frac{\partial F}{\partial t} + \mathbf{c}\frac{\partial F}{\partial \mathbf{x}} = \frac{F_* - F}{\tau} + \frac{F_M(T) - F_*}{Z_r \tau}$$

$$F_M(T) = \frac{\rho}{(\pi T)^{3/2}} \exp\left(-\frac{\mathbf{c}'^2}{T}\right) \tag{5.5}$$

$$F_* = \frac{\rho}{(\pi T_r)^{3/2}\, \pi T_r} \exp\left(-\frac{\mathbf{c}'^2}{T_t} - \frac{\zeta^2}{T_r}\right).$$

In the above F_* is an intermediate equilibrium state including the rotational degrees of freedom, ζ. The assumption that the fraction of collisions exciting the rotational degrees of freedom is a given constant or a function of the flow temperatures is also made as in the Rykov model. In this case, only mass, momentum and total energy are conserved during a particle collision and the moments $\mathbf{\Psi'} = (1,\ c_x,\ \mathbf{c}^2,\ \zeta^2)^T$ of the collision term are given by

$$\int_{-\infty}^{+\infty} \mathbf{\Psi'} \left(\frac{F_* - F}{\tau} + \frac{F_M(T) - F_*}{Z_r \tau}\right) d\mathbf{c} = (0,\ 0,\ 0,\ S)^T \tag{5.6}$$

then, the update of the macroscopic variables is

$$\mathbf{W}_i^{n+1} = \mathbf{W}_i^n + \frac{1}{\Delta x} \int_{t^n}^{t^{n+1}} \int_{-\infty}^{+\infty} \mathbf{\Psi'} \left([c_x F]|_{i-1/2} - [c_x F]|_{i+1/2}\right) d\mathbf{c} dt + \frac{\Delta t}{2}\left(\mathbf{S}_i^{n+1} + \mathbf{S}_i^n\right) \tag{5.7}$$

with the source terms S modelled through the Landau-Teller-Jeanes-type relaxation model [7].

In [85] the BGK-NS method has been improved, resulting in the Unified Gas Kinetic Scheme, and then successfully employed with the Shakhov kinetic model [46]. The S-UGKS also involves the update of the non-equilibrium distribution function F_i^{n+1} and employs a discrete integration method in the phase space with $c_x|_m$ the m^{th} discrete velocity, then, equation (5.2) becomes

$$\mathbf{W}_i^{n+1} = \mathbf{W}_i^n + \frac{1}{\Delta x} \sum_m \int_{t^n}^{t^{n+1}} \mathbf{\Psi} \left([c_x|_m F]|_{i-1/2} - [c_x|_m F]|_{i+1/2}\right) dt \Delta c_x \tag{5.8}$$

where the aforementioned Prandtl correction is no longer needed, with F reconstructed on the basis of the equilibrium distribution function of the Shakhov model. Recently [47] a UGKS for diatomic gas flow has been developed employing the Rykov model, (4.10). Also in this case, as for the modified BGK model discussed above, a source term (that needs to be determined) arises in the update of the macroscopic

variables as

$$\begin{aligned}\mathbf{W}_i^{n+1} = \quad & \mathbf{W}_i^n + \frac{1}{\Delta x}\sum_m \int_{t^n}^{t^{n+1}} \mathbf{\Psi}_0 \left([c_x|_m F_0]|_{i-1/2} - [c_x|_m F_0]|_{i+1/2} \right) dt \Delta c_x + \\ & + \frac{1}{\Delta x}\sum_m \int_{t^n}^{t^{n+1}} \mathbf{\Psi}_1 \left([c_x|_m F_1]|_{i-1/2} - [c_x|_m F_1]|_{i+1/2} \right) dt \Delta c_x + \frac{\Delta t}{2}\left(\mathbf{S}_i^{n+1} + \mathbf{S}_i^n \right)\end{aligned} \tag{5.9}$$

where $\mathbf{\Psi}_0 = (1,\ c_x,\ \mathbf{c}^2,\ 0)^T$ and $\mathbf{\Psi}_1 = (0,\ 0,\ 1,\ 1)^T$.

The method is not complete till a procedure is defined to reconstruct the time-dependent gas distribution function at the cell interfaces, $F|_{i+1/2}$. For most cases [63, 75, 85, 46, 47], the following general solution of the kinetic model equation (under the assumption of a locally constant collision time) has been employed with the BGK, Shakhov and Rykov models

$$\begin{aligned}F(x_{i+1/2}, t, c_x|_m) = \quad & \frac{1}{\tau}\int_{t^n}^{t} F_{eq}(x_{i+1/2} - c_x|_m (t-t'), t', c_x|_m) \exp\left(-\frac{t-t'}{\tau}\right) dt' + \\ & + \exp\left(-\frac{t}{\tau}\right) F^0(x_{i+1/2} - c_x|_m (t-t^n), t^n, \mathbf{c}|_m))\end{aligned} \tag{5.10}$$

where F_{eq} is the equilibrium distribution function of the employed kinetic model, and F^0 the reconstructed initial state. In the early BGK-NS approach [63] an equilibrium initial state is considered, while in the later version [75] and its successive UGKS a non-equilibrium initial distribution function, based on the CE expansion of the kinetic model, is used to extend the validity of the scheme towards rarefied flow conditions. In the limiting case of a well-resolved flow, equation (5.10) assumes a simplified form; as example for the BGK model, when a non-equilibrium initial distribution is considered, it becomes

$$F = F_M - \tau\left(\frac{\partial F_M(T)}{\partial t} + \mathbf{c}\frac{\partial F_M(T)}{\partial \mathbf{x}}\right) + t\frac{\partial F_M(T)}{\partial t}. \tag{5.11}$$

The latter limit approach has also been applied in [77, 7] with the multi-temperature BGK model (5.5) and more recently in [78] including the vibrational degrees of freedom. Recently a GKS has been proposed in [80] where, instead of equations (5.10) or (5.11), an analytical solution of the BGK equation up to a second order CE expansion (which results in the Burnett equations in the continuum limit) is used.

Considering that the assumption of a well-resolved flow rules out discontinuities in the reconstructed distribution function, equation (5.11) leads to simpler schemes but, strictly speaking, valid only for relatively small perturbances from equilibrium. Moreover, when a departure from the local equilibrium

condition occurs an approximation of first order in τ is not adequate, and it becomes necessary to include effects of higher order terms. In this case, it is possible to regularise the CE expansion in order to increase the validity of the approach. Indeed, as suggested in [79], the collision time in equations (5.11) can be replaced by a generalised one which depends on not only the local macroscopic variables, but also their gradients, and is obtained in order to have the kinetic equation satisfied. If, as example, we substitute equation (5.11) with a modified collision time τ^* in the extended Shakhov model (4.5) we obtain

$$\tau^* = \frac{\tau}{1 + \tau(D^2 F_M(T) M / D F_M(T))} \tag{5.12}$$

where

$$D = \frac{\partial}{\partial t} + \mathbf{c}\frac{\partial}{\partial \mathbf{x}} \quad ; \quad D^2 = \frac{\partial^2}{\partial t^2} + 2\mathbf{c}\frac{\partial^2}{\partial \mathbf{x}\partial t} + \mathbf{c}^2\frac{\partial^2}{\partial \mathbf{x}^2}. \tag{5.13}$$

Then, assuming that the particle collision times are independent of the particle velocity, we can take the moments of the above equation.

Finally, the equilibrium distribution function, if equation (5.10) is employed, (or its derivatives if the limit equation (5.11) is used) are expressed as Taylor expansions in terms of the internal degrees of freedom with the coefficients that can be obtained by means of the macroscopic variables relations, as example equations (4.8) for the Shakhov model, and the compatibility conditions relative to the model employed, for example equations (5.3) for the BGK model.

Summarising, the BGK-NS and UGKS approaches involve the following steps:

1. reconstruction of the initial condition at the cells interface;
2. evaluation of the coefficient of the Taylor expansions of the equilibrium function or its derivatives;
3. calculation of the numerical fluxes of the macroscopic variables $\mathbf{W}_i^{n+1}$;
   (a) for the UGKS, calculation of the numerical fluxes of the non-equilibrium distribution function F_i^{n+1};
4. update of the macroscopic variables $\mathbf{W}_i^{n+1}$ employing the relative equation;
   (a) for the UGKS, update of the non-equilibrium distribution function F_i^{n+1} employing the relative equation.

5.2 Gas-Kinetic Scheme for Near-Continuum Flows based on the Shakhov Model: S-GKS

Integrating in time the non-dimensional Shakhov model system (4.5), in a one-dimensional control volume dx with discretised space and time steps of Δx and Δt respectively, and taking the moments $\mathbf{\Psi} = (1,\ c_x,\ \mathbf{c}^2)^T$ of $F|_i^{n+1}$ the updated non-dimensional macroscopic variables can be obtained as in equation (5.8). Here, a uniformly spaced method is employed to discretise the velocity space and the trapezoidal rule is used to evaluate the moments of the distribution functions. Moreover, we reconstruct the time dependant distribution function at the cell-faces, i.e. $F|_{i\pm1/2}$ (5.10), where the initial condition is given by the CE solution of the Shakhov model given in appendix G

$$F = F_S - \tau \left[\frac{\partial F_M(T)}{\partial t} + \mathbf{c} \frac{\partial F_M(T)}{\partial \mathbf{x}} \right]. \tag{5.14}$$

Then, for a well-resolved, as shown in appendix I, we obtain

$$F = F^S - \tau \left(\frac{\partial F_M(T)}{\partial t} + c_x \frac{\partial F_M(T)}{\partial x} \right) + t \frac{\partial F_M(T)}{\partial t}. \tag{5.15}$$

Instead of representing the derivatives of the Maxwellian distribution function employing the following Taylor series in terms of the internal degrees of freedom

$$\frac{\partial F_M}{\partial \alpha} = (a_1 + a_2 c_x + a_3 c_x^2) F_M \tag{5.16}$$

as done by Xu and co-workers [7], here we proceed analytically to obtain the derivatives of the Maxwellian distribution function in terms of the macroscopic variables and their derivatives as follow

$$\frac{\partial F_M}{\partial \alpha} = F_M \left[\frac{1}{\rho} \frac{\partial \rho}{\partial \alpha} + \frac{1}{T} \left(\frac{\mathbf{c}'^2}{T} - \frac{3}{2} \right) \frac{\partial T}{\partial \alpha} + 2 \frac{c'_x}{T} \frac{\partial u_x}{\partial \alpha} \right]. \tag{5.17}$$

These can then be computed at the interface knowing the values at the cells centres. Employing equation (5.17) in place of equation (5.16) do not require the evaluation of the coefficients $a_{n=1,2,3...}$ and provide the exact analytical derivatives of the Maxwellian distribution function. The time and space derivatives of the macroscopic variables can be linked by means of the compatibility condition, i.e. conservation constraint, for the Shakhov model

$$\int_{-\infty}^{+\infty} \mathbf{\Psi} \frac{F_S - F}{\tau} d\mathbf{c} = 0 \tag{5.18}$$

evaluated for the employed CE solution

$$\int_{-\infty}^{+\infty}\left[\mathbf{\Psi}\left(\frac{\partial F_M(T)}{\partial t}+c_x\frac{\partial F_M(T)}{\partial x}\right)\right]d\mathbf{c}=0. \tag{5.19}$$

Thus, we obtain

$$\int_{-\infty}^{+\infty}\mathbf{\Psi}\frac{\partial F_M(T)}{\partial t}d\mathbf{c}=-\int_{-\infty}^{+\infty}\mathbf{\Psi}c_x\frac{\partial F_M(T)}{\partial x}d\mathbf{c} \tag{5.20}$$

which results in

$$\frac{\partial \mathbf{W}_S}{\partial t}=-\frac{\partial \mathbf{Q}_S}{\partial x} \tag{5.21}$$

with

$$\mathbf{W}_S=\left(\rho,\ \rho u_x,\ \frac{3}{2}\rho T u_x+\rho u_x^2\right)^T\quad;\quad \mathbf{Q}_S=\left(\rho u_x,\ \frac{1}{2}\rho T+\rho u_x^2,\ \frac{5}{2}\rho T u_x+\rho u_x^3\right)^T. \tag{5.22}$$

since

$$\begin{aligned}\int_{-\infty}^{+\infty}\mathbf{\Psi}F_M(T)d\mathbf{c}&=\left(\rho,\ \rho u_x,\ \frac{3}{2}\rho+\rho u_x^2\right)^T\\ \int_{-\infty}^{+\infty}\mathbf{\Psi}c_xF_M(T)d\mathbf{c}&=\left(\rho u_x,\ \frac{1}{2}\rho T+\rho u_x^2,\ \frac{5}{2}\rho T u_x+\rho u_x^3\right)^T.\end{aligned} \tag{5.23}$$

To regularise the CE solution (5.14) employed in the time dependant distribution function (5.15), we introduce a modified collision time τ^* as follow

$$F=F_S-\tau^*\left(\frac{\partial F_M(T)}{\partial t}+\mathbf{c}\frac{\partial F_M(T)}{\partial \mathbf{x}}\right) \tag{5.24}$$

and substituting the above equation in the Shakhov model (4.5) the following relation can be obtained

$$\tau^*=\frac{\tau DF_S}{DF_M(T)+\tau D^2F_M(T)}. \tag{5.25}$$

If we consider the particle collision times independent from the particle velocity, we can take moments of equation (5.25). We decide to take the moment ${c'}_x{c'}^2$, thus

$$\tau^*=\frac{\tau\langle DF_S\rangle}{\langle DF_M(T)\rangle+\tau\langle D^2F_M(T)\rangle} \tag{5.26}$$

Since the latter τ^* represents a numerical evaluation of the CE expansion closure we decide to simplify the approach here neglecting the terms relative to the Prandtl number correction, thus

$$\tau^*=\frac{\tau}{1+\tau\dfrac{\langle D^2F_M(T)\rangle}{\langle DF_M(T)\rangle}} \tag{5.27}$$

where

$$
\begin{aligned}
\langle DF_M(T)\rangle = \quad & \frac{5}{4}\frac{\partial\left(\rho T^2\right)}{\partial x}+\frac{5}{2}\rho T\left(\frac{\partial u_x}{\partial t}+u_x\frac{\partial u_x}{\partial x}\right)\\
\langle D^2F_M(T)\rangle = \quad & \frac{5}{2}\left(\frac{\partial^2\left(\rho T^2\right)}{\partial t\partial x}+\frac{\partial^2\left(\rho T^2u_x\right)}{\partial x^2}\right)+\\
& +T\left(5\frac{\partial\rho}{\partial t}\frac{\partial u_x}{\partial t}+\frac{5}{2}u_x\left(\frac{\partial\rho}{\partial t}\frac{\partial u_x}{\partial x}+\frac{\partial\rho}{\partial x}\frac{\partial u_x}{\partial t}\right)+\left(\frac{11}{2}T+5u_x^2\right)\frac{\partial\rho}{\partial x}\frac{\partial u_x}{\partial x}\right)+\\
& +\rho T\left(5\frac{\partial T}{\partial t}\frac{\partial u_x}{\partial t}+\frac{5}{2}u_x\left(\frac{\partial T}{\partial t}\frac{\partial u_x}{\partial x}+\frac{\partial T}{\partial x}\frac{\partial u_x}{\partial t}\right)+\left(11T+5u_x^2\right)\frac{\partial T}{\partial x}\frac{\partial u_x}{\partial x}\right)+\\
& +\rho T\left(\frac{5}{2}\left(\frac{\partial u_x}{\partial t}\right)^2+\frac{5}{2}u_x\frac{\partial^2u_x}{\partial t\partial x}+8\frac{\partial u_x}{\partial t}\frac{\partial u_x}{\partial x}+\left(\frac{11}{4}T+\frac{5}{2}u_x^2\right)\frac{\partial^2u_x}{\partial^2x}+16u_x\left(\frac{\partial u_x}{\partial x}\right)^2\right).
\end{aligned}
\tag{5.28}
$$

Equations (5.28) have been obtained considering equations (5.13) in one-dimension, the chain-rule for the following derivatives

$$
\begin{aligned}
\frac{\partial}{\partial\alpha}\left({c'}_x{c'}^2c_x^nF_M(T)\right) = \quad & c_x^nF_M(T)\frac{\partial}{\partial\alpha}\left({c'}_x{c'}^2\right)+{c'}_x{c'}^2\frac{\partial}{\partial\alpha}\left(c_x^nF_M(T)\right)\\
\frac{\partial^2}{\partial\alpha\partial\beta}\left({c'}_x{c'}^2c_x^nF_M(T)\right) = \quad & c_x^nF_M(T)\frac{\partial^2}{\partial\alpha\partial\beta}\left({c'}_x{c'}^2\right)+{c'}_x{c'}^2\frac{\partial^2}{\partial\alpha\partial\beta}\left(c_x^nF_M(T)\right)+\\
& +c_x^nF_M(T)\left(\frac{\partial F_M(T)}{\partial\alpha}\frac{\partial}{\partial\beta}\left({c'}_x{c'}^2\right)+\frac{\partial F_M(T)}{\partial\beta}\frac{\partial}{\partial\alpha}\left({c'}_x{c'}^2\right)\right)
\end{aligned}
\tag{5.29}
$$

and the integrals

$$
\int_{-\infty}^{+\infty}{c'}_x{c'}^2F_M(T)d\mathbf{c}=0 \quad ; \quad \int_{-\infty}^{+\infty}{c'}_x^2{c'}^2F_M(T)d\mathbf{c}=\frac{5}{4}\rho T^2 \quad ; \quad \int_{-\infty}^{+\infty}{c'}_x^2{c'}^2{c'}^2F_M(T)d\mathbf{c}=\frac{35}{8}\rho T^3. \tag{5.30}
$$

The required second derivatives ∂^2/∂^2t and $\partial^2/\partial t\partial x$ can be expressed deriving the compatibility condition (5.21) as follow

$$
\begin{aligned}
\frac{\partial^2\mathbf{W_S}}{\partial^2t} &= -2\int_{-\infty}^{+\infty}\mathbf{\Psi}c_x\frac{\partial^2F_M(T)}{\partial t\partial x}d\mathbf{c}-\int_{-\infty}^{+\infty}\mathbf{\Psi}c_x^2\frac{\partial^2F_M(T)}{\partial^2x}d\mathbf{c}\\
\frac{\partial^2\mathbf{W_S}}{\partial t\partial x} &= -\frac{\partial^2\mathbf{Q_S}}{\partial x^2}
\end{aligned}
\tag{5.31}
$$

with W_S and Q_S defined in equations (5.22). Finally, similar to [77, 7], since $\langle DF_M(T)\rangle$ and $\langle D^2F_M(T)\rangle$ will be sensitive to numerical errors (especially close to equilibrium regions where they tend to vanish) a limiter is needed. In the current work, the following non-linear limiter is used

$$
\tau^*=\frac{\tau}{1+max\left(-0.5,min\left(0.0,\tau\frac{\langle D^2F_M(T)\rangle}{\langle DF_M(T)\rangle}\right)\right)}. \tag{5.32}
$$

Moreover, since equation (5.32) does not guarantee a continuous modification of the collision time, specially in the transient towards the steady state solution, and this may reduce the stability of the method; a Laplacian smoothing, see appendix K, is applied to the term

$$\tau_{correction} = \frac{1}{1 + max\left(-0.5, min\left(0.0, \tau \frac{\langle D^2 F_M(T)\rangle}{\langle DF_M(T)\rangle}\right)\right)}. \tag{5.33}$$

Finally the following blending

$$\tau^* = \begin{cases} \tau\left[1 + \left(\tau_{correction} - 1\right)\left(\exp\left(-a\left\{Kn - 0.05\right\}\right)\right)\right] & \text{for } Kn \geq 0.05 \\ 1 & \text{for } Kn < 0.05 \end{cases} \tag{5.34}$$

function of a locally defined Knudsen number

$$Kn = max(Kn_\rho, Kn_V, Kn_T) \tag{5.35}$$

with Kn_Q defined in equation (1.2), is applied to avoid spurious numerical values when $\langle DF_M(T)\rangle \sim 0$ and $\langle D^2 F_M(T)\rangle \sim 0$, i.e. towards continuum conditions where $Kn < 0.05$. The value $a = 12.84849226$ is employed here to have the full correction applied when Kn is of the unit order.

5.3 Gas-Kinetic Scheme for Near-Continuum Flows based on the Rykov Model: R-GKS

Integrating in time the non-dimensional, reduced, Rykov model system (4.10) and taking the moments $\mathbf{\Psi}_0 = (1,\ c_x,\ \mathbf{c}^2,\ 0)^T$ of $F_0|_i^{n+1}$ and $\mathbf{\Psi}_1 = (0,\ 0,\ 1,\ 1)^T$ of $F_1|_i^{n+1}$, equation (5.9) with, as discussed in appendix E, the following source term

$$\frac{\Delta t}{2}\left(\mathbf{S}_i^{n+1} + \mathbf{S}_i^n\right) = \frac{\Delta t}{2}\left(0,\ 0,\ 0,\ \frac{\rho(T|_i^{n+1} - T_r|_i^{n+1})}{Z_r \tau_i^{n+1}} + \frac{\rho(T|_i^n - T_r|_i^n)}{Z_r \tau_i^n}\right)^T \tag{5.36}$$

can be obtained for the update of the non-dimensional macroscopic variables. As for the monoatomic formulation, the velocity space is discretised using a uniformly spaced method and the moments of the distribution functions are evaluated by means of the trapezoidal rule. Reconstructing the time dependant distribution functions at the cell-faces, i.e. $F_0|_{i\pm1/2}$ and $F_1|_{i\pm1/2}$, consistently on the basis of the CE solution of the Rykov model, see appendix H for the derivation,

$$\begin{aligned} F_0 &= F_0^{eq} - \tau\left[\frac{\partial F_M(T_t)}{\partial t} + \mathbf{c}\frac{\partial F_M(T_t)}{\partial \mathbf{x}}\right] \\ F_1 &= F_1^{eq} - \tau\left[\frac{\partial\left(T_r F_M(T_t)\right)}{\partial t} + \mathbf{c}\frac{\partial\left(T_r F_M(T_t)\right)}{\partial \mathbf{x}}\right]. \end{aligned} \tag{5.37}$$

for a well-resolved flow, as shown in appendix J, it is possible to obtain

$$\begin{aligned} F_0 &= F_0^{eq} - \tau\left(\frac{\partial F_M(T_t)}{\partial t} + c_x\frac{\partial F_M(T_t)}{\partial x}\right) + t\frac{\partial F_M(T_t)}{\partial t} \\ F_1 &= F_1^{eq} - \tau\left(\frac{\partial\left(T_r F_M(T_t)\right)}{\partial t} + c_x\frac{\partial\left(T_r F_M(T_t)\right)}{\partial x}\right) + t\frac{\partial\left(T_r F_M(T_t)\right)}{\partial t} \end{aligned} \tag{5.38}$$

where all derivatives are obtained analytically with the derivative of the Maxwellian defined in equation (5.17) and

$$F_0^{eq} = F_0^t + \frac{F_0^r - F_0^t}{Z_r} \quad ; \quad F_1^{eq} = F_1^t + \frac{F_1^r - F_1^t}{Z_r}. \tag{5.39}$$

The time derivatives of the macroscopic variables can be obtained in terms of the space derivatives by means of the compatibility condition for the Rykov model

$$\int_{-\infty}^{+\infty}\left[\mathbf{\Psi}_0\frac{F_0^{eq} - F_0}{\tau} + \mathbf{\Psi}_1\frac{F_1^{eq} - F_1}{\tau}\right] d\mathbf{c} = \mathbf{S} \tag{5.40}$$

written for the CE solutions employed

$$\int_{-\infty}^{+\infty}\left[\boldsymbol{\Psi}_0\left(\frac{\partial F_M(T_t)}{\partial t}+c_x\frac{\partial F_M(T_t)}{\partial x}\right)+\boldsymbol{\Psi}_1\left(\frac{\partial T_r F_M(T_t)}{\partial t}+c_x\frac{\partial T_r F_M(T_t)}{\partial x}\right)\right]d\mathbf{c}=\mathbf{S}. \tag{5.41}$$

Thus

$$\int_{-\infty}^{+\infty}\left[\boldsymbol{\Psi}_0\frac{\partial F_M(T_t)}{\partial t}+\boldsymbol{\Psi}_1\frac{\partial T_r F_M(T_t)}{\partial t}\right]d\mathbf{c}=\mathbf{S}-\int_{-\infty}^{+\infty}\left(\boldsymbol{\Psi}_0 c_x\frac{\partial F_M(T_t)}{\partial x}+\boldsymbol{\Psi}_1 c_x\frac{\partial T_r F_M(T_t)}{\partial x}\right)d\mathbf{c} \tag{5.42}$$

which leads to

$$\frac{\partial \mathbf{W_R}}{\partial t}=\mathbf{S}-\frac{\partial \mathbf{Q_R}}{\partial x} \tag{5.43}$$

where

$$\mathbf{W_R}=\left(\rho,\ \rho u_x,\ \frac{5}{2}\rho T+\rho u_x^2,\ \rho T_r\right)^T\quad;\quad \mathbf{Q_R}=\begin{bmatrix}\rho u_x\\ \frac{1}{2}\rho T_t+\rho u_x^2\\ \frac{5}{2}\rho T_t u_x+\rho u_x^3+\rho T_r u_x\\ \rho T_r u_x\end{bmatrix}. \tag{5.44}$$

being

$$\begin{aligned}
&\int_{-\infty}^{+\infty}\boldsymbol{\Psi}_0 F_M(T_t)d\mathbf{c}=\left(\rho,\ \rho u_x,\ \frac{3}{2}\rho T_t+\rho u_x^2,\ 0\right)^T\\
&\int_{-\infty}^{+\infty}\boldsymbol{\Psi}_1 T_r F_M(T_t)d\mathbf{c}=(0,\ 0,\ \rho T_r,\ \rho T_r)^T\\
&\int_{-\infty}^{+\infty}\boldsymbol{\Psi}_0 c_x F_M(T_t)d\mathbf{c}=\left(\rho u_x,\ \frac{1}{2}\rho T_t+\rho u_x^2,\ \frac{5}{2}\rho T_t u_x+\rho u_x^3,\ 0\right)^T\\
&\int_{-\infty}^{+\infty}\boldsymbol{\Psi}_1 c_x T_r F_M(T_t)d\mathbf{c}=(0,\ 0,\ \rho T_r u_x,\ \rho T_r u_x)^T
\end{aligned} \tag{5.45}$$

As for the monoatomic case, we introduce the CE solutions (5.37) of the Rykov model (4.10) with a modified collision time τ^*

$$\begin{aligned}
F_0&=F_0^{eq}-\tau^*\left(\frac{\partial F_M(T_t)}{\partial t}+\mathbf{c}\frac{\partial F_M(T_t)}{\partial \mathbf{x}}\right)\\
F_1&=F_1^{eq}-\tau^*\left(\frac{\partial\left(T_r F_M(T_t)\right)}{\partial t}+c_x\frac{\partial\left(T_r F_M(T_t)\right)}{\partial x}\right)
\end{aligned} \tag{5.46}$$

back in the model equation, it is possible to obtain

$$\tau^* D F_M(T_t)+\tau^*\tau D^2 F_M(T_t)=\tau D F_0^{eq}\quad;\quad \tau^* D\left(T_r F_M(T_t)\right)+\tau^*\tau D^2\left(T_r F_M(T_t)\right)=\tau D F_1^{eq}. \tag{5.47}$$

Since the difference in the relaxation rate between translational and rotational processes is inherited in the collision number, Z_r, we define a single modified collision time by taking the moment relative to the total heat flux. Thus, multiplying the first of equations (5.47) by $c'_x c'^2$ and the second one by c'_x, and adding the two resulting equations we obtain

$$\tau^* = \frac{\tau\left(\langle DF_0^{eq}\rangle + \langle DF_1^{eq}\rangle\right)}{\left(\langle DF_M(T_t)\rangle + \langle D\left\{T_r F_M(T_t)\right\}\rangle\right) + \tau\left(\langle D^2 F_M(T_t)\rangle + \langle D^2\left\{T_r F_M(T_t)\right\}\rangle\right)}. \tag{5.48}$$

As for the S-GKS, we simplify the numerical evaluation of this closure of the CE expansion by neglecting the terms relative to the Prandtl number correction introduced in the Rykov model, then

$$\tau^* = \frac{\tau}{1 + \tau\dfrac{\left(\langle D^2 F_M(T_t)\rangle + \langle D^2\left\{T_r F_M(T_t)\right\}\rangle\right)}{\left(\langle DF_M(T_t)\rangle + \langle D\left\{T_r F_M(T_t)\right\}\rangle\right)}} \tag{5.49}$$

where

$$\begin{aligned}
\langle DF_M(T_t)\rangle = \quad & \frac{5}{4}\frac{\partial\left(\rho T_t^2\right)}{\partial x} + \frac{5}{2}\rho T_t\left(\frac{\partial u_x}{\partial t} + u_x\frac{\partial u_x}{\partial x}\right) \\
\langle D^2 F_M(T_t)\rangle = \quad & \frac{5}{2}\left(\frac{\partial^2\left(\rho T_t^2\right)}{\partial t\partial x} + \frac{\partial^2\left(\rho T_t^2 u_x\right)}{\partial x^2}\right) + \\
& + T_t\left(5\frac{\partial\rho}{\partial t}\frac{\partial u_x}{\partial t} + \frac{5}{2}u_x\left(\frac{\partial\rho}{\partial t}\frac{\partial u_x}{\partial x} + \frac{\partial\rho}{\partial x}\frac{\partial u_x}{\partial t}\right) + \left(\frac{11}{2}T_t + 5u_x^2\right)\frac{\partial\rho}{\partial x}\frac{\partial u_x}{\partial x}\right) + \\
& + \rho\left(5\frac{\partial T_t}{\partial t}\frac{\partial u_x}{\partial t} + \frac{5}{2}u_x\left(\frac{\partial T_t}{\partial t}\frac{\partial u_x}{\partial x} + \frac{\partial T_t}{\partial x}\frac{\partial u_x}{\partial t}\right) + \left(11T_t + 5u_x^2\right)\frac{\partial T_t}{\partial x}\frac{\partial u_x}{\partial x}\right) + \\
& + \rho T_t\left(\frac{5}{2}\left(\frac{\partial u_x}{\partial t}\right)^2 + \frac{5}{2}u_x\frac{\partial^2 u_x}{\partial t\partial x} + 8\frac{\partial u_x}{\partial t}\frac{\partial u_x}{\partial x} + \left(\frac{11}{4}T_t + \frac{5}{2}u_x^2\right)\frac{\partial^2 u_x}{\partial^2 x} + 16u_x\left(\frac{\partial u_x}{\partial x}\right)^2\right)
\end{aligned} \tag{5.50}$$

and

$$
\begin{aligned}
\langle D\left\{T_r F_M(T_t)\right\}\rangle = \quad & \frac{1}{2}\frac{\partial\left(\rho T_r T_t\right)}{\partial x} + \rho T_r\left(\frac{\partial u_x}{\partial t} + u_x\frac{\partial u_x}{\partial x}\right) \\
\langle D^2\left\{T_r F_M(T_t)\right\}\rangle = \quad & \frac{\partial^2\left(\rho T_r T_t\right)}{\partial t\partial x} + \frac{\partial^2\left(\rho T_r T_t u_x\right)}{\partial x^2} + \\
& + T_r\left(2\frac{\partial\rho}{\partial t}\frac{\partial u_x}{\partial t} + 2u_x\frac{\partial\rho}{\partial t}\frac{\partial u_x}{\partial x} + 2u_x\frac{\partial\rho}{\partial x}\frac{\partial u_x}{\partial t} + \left(T_t + 2u_x^2\right)\frac{\partial\rho}{\partial x}\frac{\partial u_x}{\partial x}\right) + \\
& + \rho T_r\frac{\partial T_t}{\partial x}\frac{\partial T_r}{\partial x} + \\
& + \rho\left(2\frac{\partial T_r}{\partial t}\frac{\partial u_x}{\partial t} + 2u_x\frac{\partial T_r}{\partial t}\frac{\partial u_x}{\partial x} + 2u_x\frac{\partial T_r}{\partial x}\frac{\partial u_x}{\partial t} + \left(T_t + 2u_x^2\right)\frac{\partial\rho}{\partial x}\frac{\partial u_x}{\partial x}\right) + \\
& + \rho T_r\left(\frac{\partial^2 u_x}{\partial^2 t} + 2u_x\frac{\partial^2 u_x}{\partial t\partial x} + 4\frac{\partial u_x}{\partial t}\frac{\partial u_x}{\partial x} + \left(\tfrac{T_t}{2} + u_x^2\right)\frac{\partial^2 u_x}{\partial^2 x} + 4u_x\left(\frac{\partial u_x}{\partial x}\right)^2\right).
\end{aligned}
\tag{5.51}
$$

can be obtained employing equations (5.13) considering the derivatives defined in equations (5.29), plus the following derivatives

$$
\begin{aligned}
\frac{\partial}{\partial\alpha}\left(c'_x c_x^n T_r F_M(T_t)\right) = \quad & c_x^n T_r F_M(T_t)\frac{\partial c'_x}{\partial\alpha} + c'_x\frac{\partial}{\partial\alpha}\left(c_x^n T_r F_M(T_t)\right) \\
\frac{\partial^2}{\partial\alpha\partial\beta}\left(c'_x c_x^n T_r F_M(T_t)\right) = \quad & c_x^n T_r F_M(T_t)\frac{\partial^2 c'_x}{\partial\alpha\partial\beta} + c'_x\frac{\partial^2}{\partial\alpha\partial\beta}\left(c_x^n T_r F_M(T_t)\right) + \\
& + c_x^n T_r F_M(T_t)\left(\frac{\partial T_r F_M(T_t)}{\partial\alpha}\frac{\partial c'_x}{\partial\beta} + \frac{\partial T_r F_M(T_t)}{\partial\beta}\frac{\partial c'_x}{\partial\alpha}\right)
\end{aligned}
\tag{5.52}
$$

and integrals

$$
\begin{gathered}
\int_{-\infty}^{+\infty} c'_x c'^2 F_M(T_t) d\mathbf{c} = 0 \quad ; \quad \int_{-\infty}^{+\infty} c'^2_x c'^2 F_M(T_t) d\mathbf{c} = \frac{5}{4}\rho T_t^2 \quad ; \quad \int_{-\infty}^{+\infty} c'^2_x c'^2 c'^2 F_M(T) d\mathbf{c} = \frac{35}{8}\rho T_t^3 \\
\int_{-\infty}^{+\infty} c'_x T_r F_M(T_t) d\mathbf{c} = 0 \quad ; \quad \int_{-\infty}^{+\infty} c'^2_x T_r F_M(T_t) d\mathbf{c} = \frac{1}{2}\rho T_r T_t.
\end{gathered}
\tag{5.53}
$$

The second derivatives $\partial^2/\partial t\partial x$ can be expressed in term of only spatial derivatives employing the compatibility condition (5.42) as follow

$$
\frac{\partial^2 \mathbf{W_R}}{\partial t\partial x} = \frac{\partial \mathbf{S}}{\partial x} - \frac{\partial^2 Q_R}{\partial x^2}
\tag{5.54}
$$

where W_R and Q_R are defined in equations (5.44), while the required second time derivative of the mean velocity can be obtained considering the first of equations (5.31) for the translational part

$$
\frac{\partial^2 \mathbf{W_t}}{\partial^2 t} = -2\int_{-\infty}^{+\infty} \mathbf{\Psi}_1 c_x \frac{\partial^2 F_M(T_t)}{\partial t\partial x} d\mathbf{c} - \int_{-\infty}^{+\infty} \mathbf{\Psi}_1 c_x^2 \frac{\partial^2 F_M(T_t)}{\partial^2 x} d\mathbf{c}.
\tag{5.55}
$$

Finally, the same limiting and blending approach employed for the monoatomic case in equations (5.32) and (5.34) as well as a Laplacian smoothing on the term

$$\tau_{correction} = \frac{1}{1 + \tau \frac{(\langle D^2 F_M(T_t) \rangle + \langle D^2 \{T_r F_M(T_t)\} \rangle)}{(\langle D F_M(T_t) \rangle + \langle D \{T_r F_M(T_t)\} \rangle)}} \tag{5.56}$$

is used for the R-GKS. To involve also an index of the translational-rotational relaxation process, the following definition of the local Knudsen number given in [1]

$$Kn = max(Kn_\rho, Kn_V, Kn_{T_t}, Kn_{T_r}, \frac{|T_t - T_r|}{2T_r}) \tag{5.57}$$

is employed for the diatomic case.

Chapter 6

Partially-Rarefied High-Speed Flows Results and Discussion - MΦC

To verify the implementation of the new polyatomic kinetic models and evaluate the proposed gas-kinetic schemes alone and in the context of hybrid simulations, different practical applications for a wide range of Mach numbers and flow conditions have been considered.

Test Case	λ_∞	T_∞	T_{wall}	Particle vel. space	Δu
$M = 2.05$ Shock				$c_x = (-16u_\infty; 16u_\infty)$ $c_y = (-16u_\infty; 16u_\infty)$	$0.5u_\infty$
$M = 3.8$ Shock				$c_x = (-24u_\infty; 24u_\infty)$ $c_y = (-24u_\infty; 24u_\infty)$	$0.5u_\infty$
$M = 9$ Shock				$c_x = (-24u_\infty; 24u_\infty)$ $c_y = (-24u_\infty; 24u_\infty)$	$0.5u_\infty$
$M = 2.8$ Shock				$c_x = (-16u_\infty; 16u_\infty)$ $c_y = (-16u_\infty; 16u_\infty)$	$0.125u_\infty \div 0.5u_\infty$
$M = 10$ Shock				$c_x = (-24u_\infty; 24u_\infty)$ $c_y = (-24u_\infty; 24u_\infty)$	$0.5u_\infty$
$M = 5$ Cylinder	$Diameter/400$			$c_x = (-24u_\infty; 24u_\infty)$ $c_y = (-16u_\infty; 16u_\infty)$	$0.5u_\infty$
$M = 4.89$ Plate	$1.2mm$	$116K$	$290K$	$c_x = (-6u_\infty; 10u_\infty)$ $c_y = (-8u_\infty; 8u_\infty)$	$0.5u_\infty$
$M = 4$ Wedge	$0.1mm$	$185.6K$	$293.3K$	$c_x = (-12u_\infty; 12u_\infty)$ $c_y = (-8u_\infty; 8u_\infty)$	$0.5u_\infty$
$M = 12$ Cylinder	$Diameter/100$	$217.5K$	$1000K$	$c_x = (-24u_\infty; 24u_\infty)$ $c_y = (-16u_\infty; 16u_\infty)$	$0.5u_\infty$

Table 6.1: Test cases details.

Details of the simulations are reported in table 6.1 and wall boundary conditions are considered fully accommodating. The results presented in the current chapter are part of the following publications:

- Kinetic Models with Rotational Degrees of Freedom for Hybrid Methods. Colonia S., Steijl R. and Barakos G.N., 6th European Conference on Computational Fluid Dynamics (ECFD VI), ECCOMAS 2014, 20-25 July 2014, Barcelona (Spain).

- Kinetic Models and Gas Kinetic Schemes for Hybrid Simulation of Partially Rarefied Flows. Colonia S., Steijl R. and Barakos G.N., AIAA Atmospheric Flight Mechanics Conference 2015, 5-9 January 2015, Kissimmee (Florida), DOI: 10.2514/6.2015-0521.

- Kinetic Models and Gas Kinetic Schemes for Hybrid Simulation of Partially Rarefied Flows. Colonia S., Steijl R. and Barakos G.N., AIAA Journal (Articles in Advance), DOI: 10.2514/1.J054137.

- Gas Kinetic Schemes for Hybrid Simulation of Partially Rarefied Flows. Colonia S., Steijl R. and Barakos G.N., 6^{th} European Conference for Aeronautics and Space Sciences, 29 June to 3 July 2015, Krakow (Poland).

- A Gas Kinetic Scheme for Hybrid Simulation of Partially Rarefied Flows. Colonia S., Steijl R. and Barakos G.N., Progress in Flight Physics Volume 8 - EUCASS book series, accepted.

6.1 Discrete Velocity Method - Assessment of the Rykov Model Implementation

For a monoatomic gas the Rykov and the polyatomic ES models reduce, respectively, to the Shakhov model and the monoatomic ES model [27] and as mentioned in the previous section in [150] a comparison of monoatomic models is presented showing that the Shakhov model in the majority of cases predicts more accurate numerical solutions.

Firstly, the implementation of the Rykov model in the framework DVM has been evaluated. Thus, MΦC has been employed to predict a shock structure at Mach 7 in the same conditions and settings of the one presented in the literature by Rykov et al. in [4]. As shown in figure 6.1 the solution obtained is in excellent agreement with the results available in the literature and this confirms the correctness of the implemented Rykov model.

Afterwards, the Rykov model has been compared with the polyatomic ES model of Andries and his co-workers [29] with respect to the DSMC results reported in [5] for a normal shock at Mach number 2.8. From figures 6.2 it is clear that the Rykov model achieves a slightly better agreement with the DSMC results than the polyatomic ES model.

As a final step, the implemented polyatomic kinetic models have been used to predict the 2D flow field around a flat plate for which experimental data of temperature profiles in the boundary layer are available [6]. For all simulations a fully accommodating wall boundary has been employed. The temperatures relative difference contours in proximity of the leading edge are shown in figure 6.3d. The Rykov model leads to good agreement with both experimental and DSMC results, but it slightly over-predicts the translational temperature in the thermal layer, as it can be seen from figure 6.3a. Moreover, employing different expressions for the rotational collision number does not affect particularly the solution of this test case. Looking at figure 6.3b, it is clear that the polyatomic ES model slightly under-predicts the rotational temperature near the wall, leading also to a higher temperature gradients at the wall compared to the Rykov model. As the Rykov model, the polyatomic ES model predicts a higher translational temperature in the thermal layer. Figure 6.3c confirms the same conclusions also for the flow at $20mm$ from the plate leading edge. However, in this case it is important to notice that the ES model, at the

moment, does not consider a variation of the ratio of elastic and inelastic collisions with translational and rotational temperature and this may represent an advantage in terms of accuracy for the Rykov model.

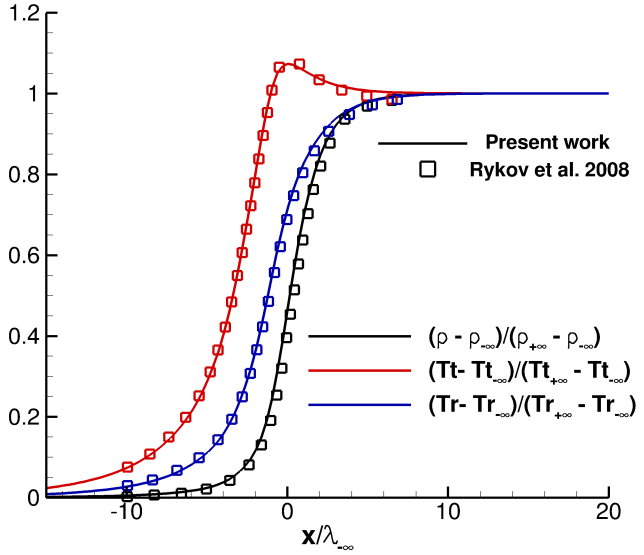

Figure 6.1: Non-dimensional ρ, T_r and T_t normalised profiles for M = 7 normal shock in Nitrogen, Z_r eq. (4.12) and μ eq. (4.17). DVM physical space cell's size equal to $0.25\lambda_{-\infty}$. Comparison between DVM results form present work and [4].

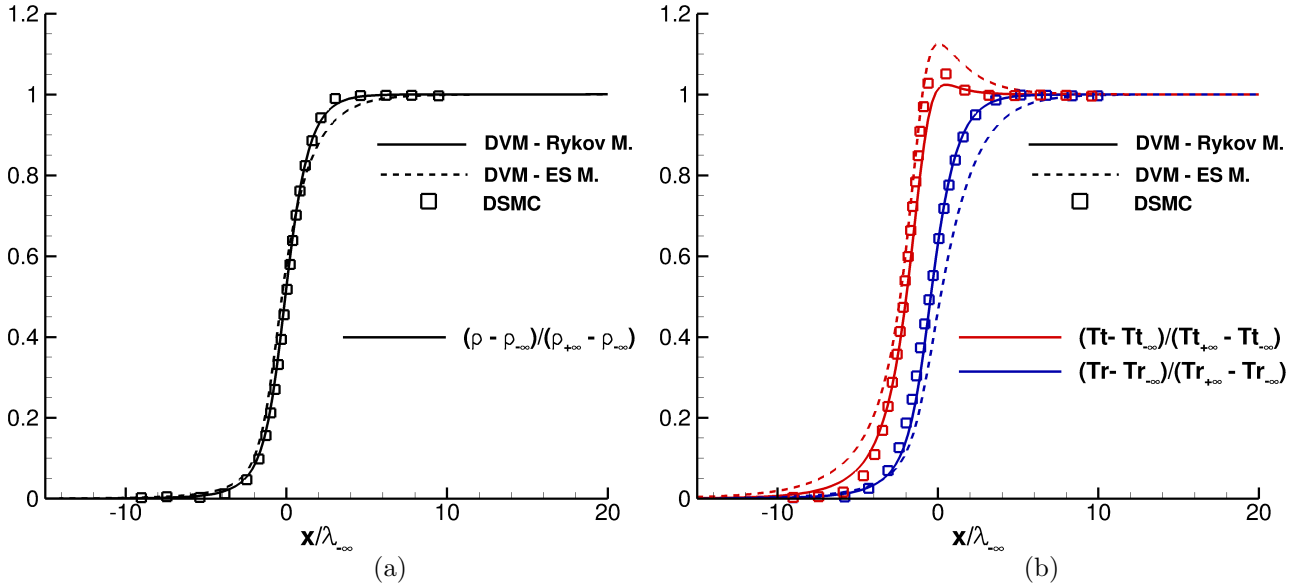

Figure 6.2: Non-dimensional ρ, T_r and T_t normalised profiles for M = 2.8 normal shock in Nitrogen, constant $Z_r = 4.2$ (i.e. $Z_r = 2.52$ for the Rykov model) and μ eq. (4.18). DVM physical space cell's size equal to $0.25\lambda_{-\infty}$. DSMC results from [5].

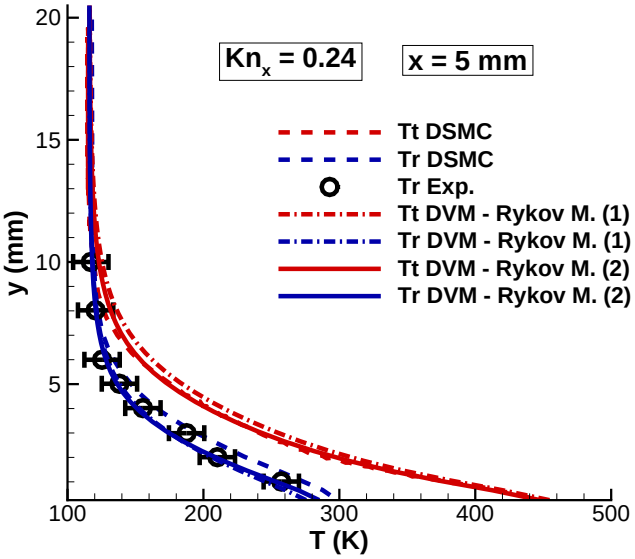

(a) T_t and T_r profiles at $x = 5mm$ from the flat leading edge. (1) Z_r eq. (4.12) and μ eq. (4.17); (2) Z_r eq. (4.13) and μ eq. (4.18).

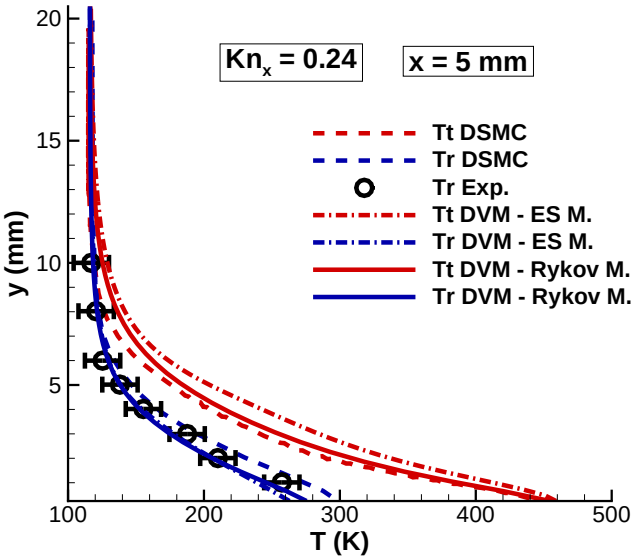

(b) T_t and T_r profiles at $x = 5mm$ from the flat plate leading edge.

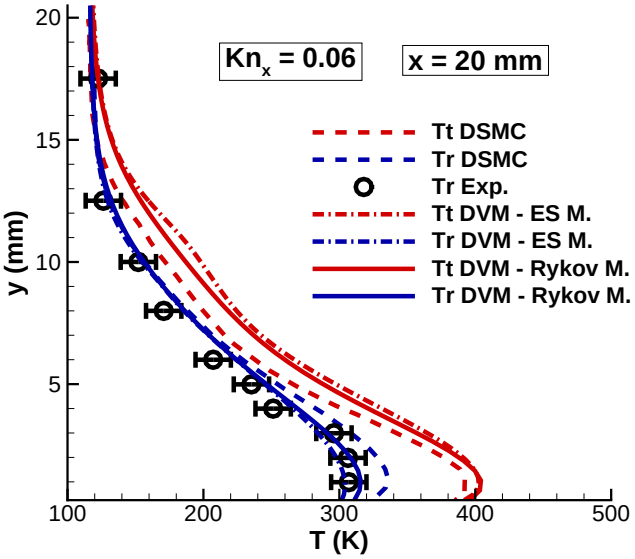

(c) T_t and T_r profiles at $x = 20mm$ from the flat leading edge.

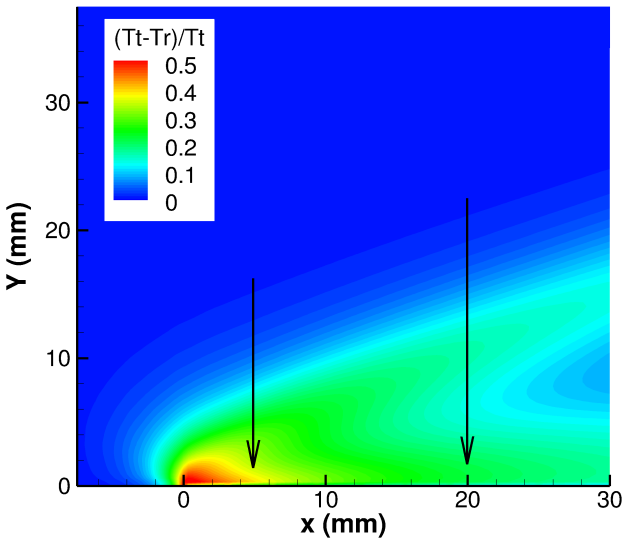

(d) $(T_t - T_r)/T_t$ contours over the flat plate.

Figure 6.3: DVM results for Nitrogen flow over a 2D flat plate: M = 4.89, Re = 422, Kn = 0.024 and $x_{ref} = 5cm$. DSMC and experimental results from[6].

6.2 Assessment of the Analytical Gas-Kinetic Schemes

Computational and memory cost is a major drawback for DVM in hybrid simulations and the use of the GKS to reduce the extension of the domain where it is strictly required represents a preferable alternative. To support this assertion different test cases for a wide range of Mach numbers have been considered, see table 6.1.

Firstly, a simple grid refinement study, for a Mach 2.8 normal shock in Nitrogen, has been conducted for both physical and phase spaces. As observed from figures 6.4a-b, reducing the velocity step size further than $0.5u_\infty$ seems not to affect the accuracy of the solution while a physical step size of at least $0.25\lambda_\infty$ is required to obtain a grid independent solution. Thus the latter settings have been preferred in all studies shown in this section, however for the test cases that involve fully accommodating wall boundaries a physical step size of at least $0.125\lambda_\infty$ is employed at the wall.

Figure 6.5a presents a comparison between the AUSM$^+$ presented in chapter 2 and the GKS for a monoatomic gas flow around an infinite cylinder at Mach 5. As also reported in the literature [76], it was confirmed that the GKS is less affected by shock anomalies than more commonly employed numerical schemes like the AUSM$^+$. Furthermore, the AUSM$^+$ solution displays spurious pressure oscillations at the edge of the boundary layer, as previously reported in [169], while the GKS solution is not affected by this issue.

As shown in figures 6.6a-c for Argon and figures 6.7a-d and 6.8a-d for Nitrogen; the GKS is able to resolve shock structures with and without rotational non-equilibrium in contrast to more traditional single-/multi-temperature NS approaches [15, 14], where shock capturing approaches are used to solve models in which it is assumed a single temperature to describe the distribution of energy in the translational and rotational modes. However, due to the continuum formulation, it predicts steeper shocks when compared to the DSMC solutions presented in [5]. A better shock structure prediction can be obtained when equations (5.26) or (5.49) are employed to modify the collision time as it is possible to notice from figures 6.6a-c, 6.7c-d and 6.8c-d. Even so, significant differences between GKS and DSMC results can still be observed for the higher Mach number cases in figures 6.6c and 6.8c-d. This is probably due to

the well-resolved flow assumption which does not allow to represent the typical bi-modal behaviour of the distribution function across shock waves at very high Mach numbers (Mach > 4).

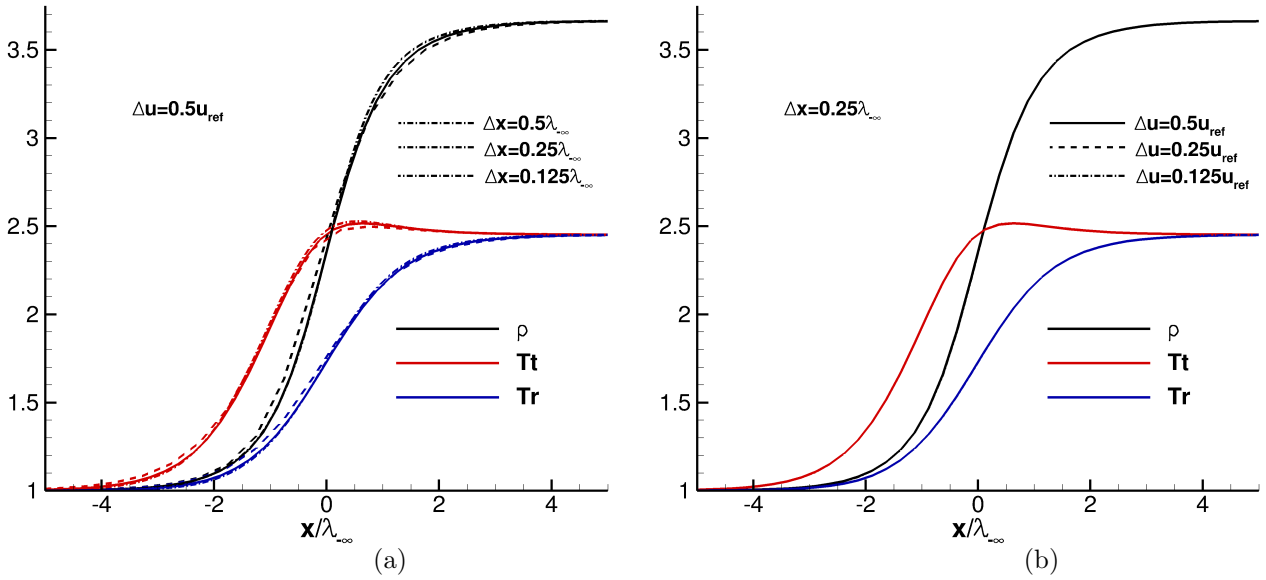

Figure 6.4: Non-dimensional ρ, T_r and T_t profiles for M $= 2.8$ normal shock in Nitrogen, constant Z_r and μ eq. (4.18). GKS physical space cell's size equal to $0.125 \div 0.5\lambda_{-\infty}$.

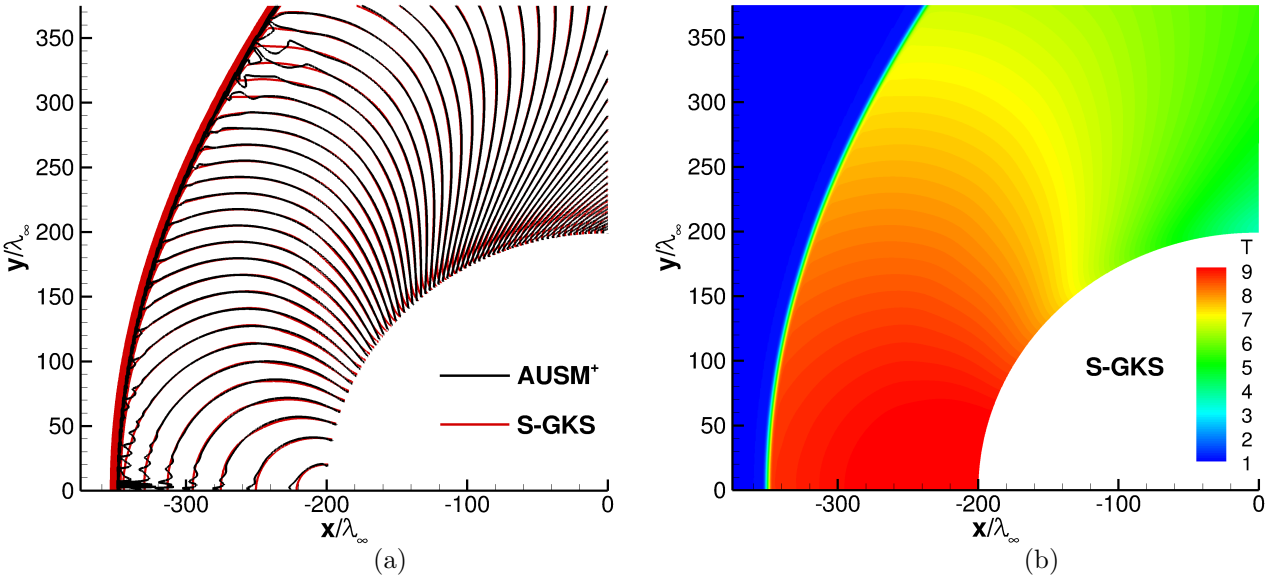

Figure 6.5: Non-dimensional T contours for M $= 5$ monoatomic gas flow over an infinite cylinder with $Kn = 0.0025$, based on the diameter, and adiabatic inviscid wall boundary condition. Comparison between GKS and AUSM$^+$ results from present work.

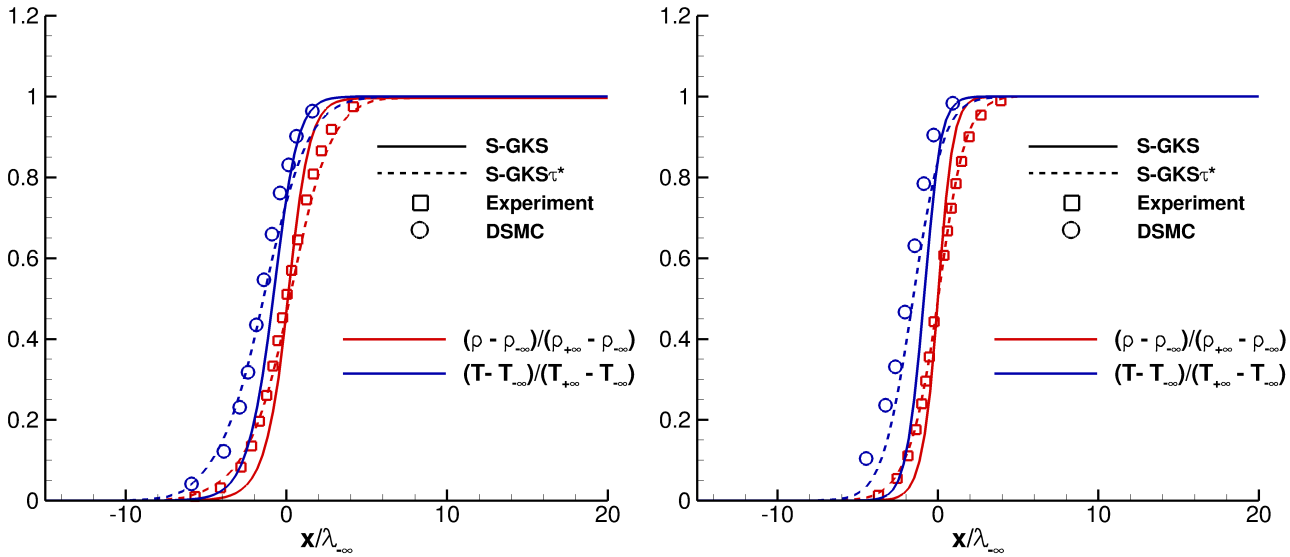

(a) M = 2.05.

(b) M = 3.8.

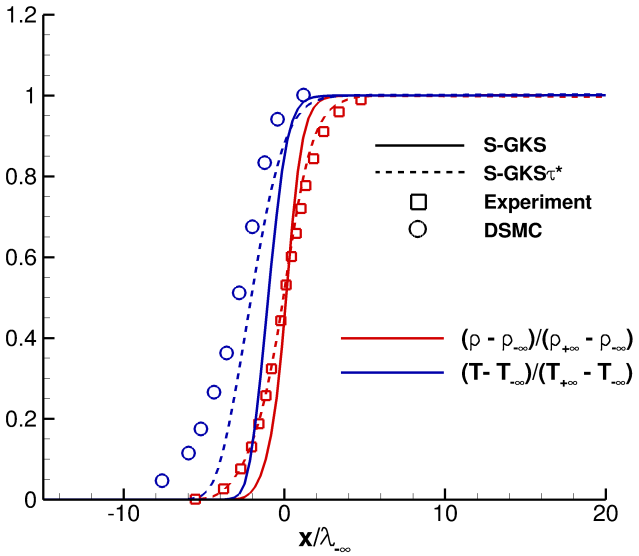

(c) M = 9.

Figure 6.6: Non-dimensional ρ and T normalised profiles for normal shocks in Argon at different Mach numbers, μ eq. (4.18). GKS physical space cell's size equal to $0.25\lambda_{-\infty}$. DSMC and experimental results from [5].

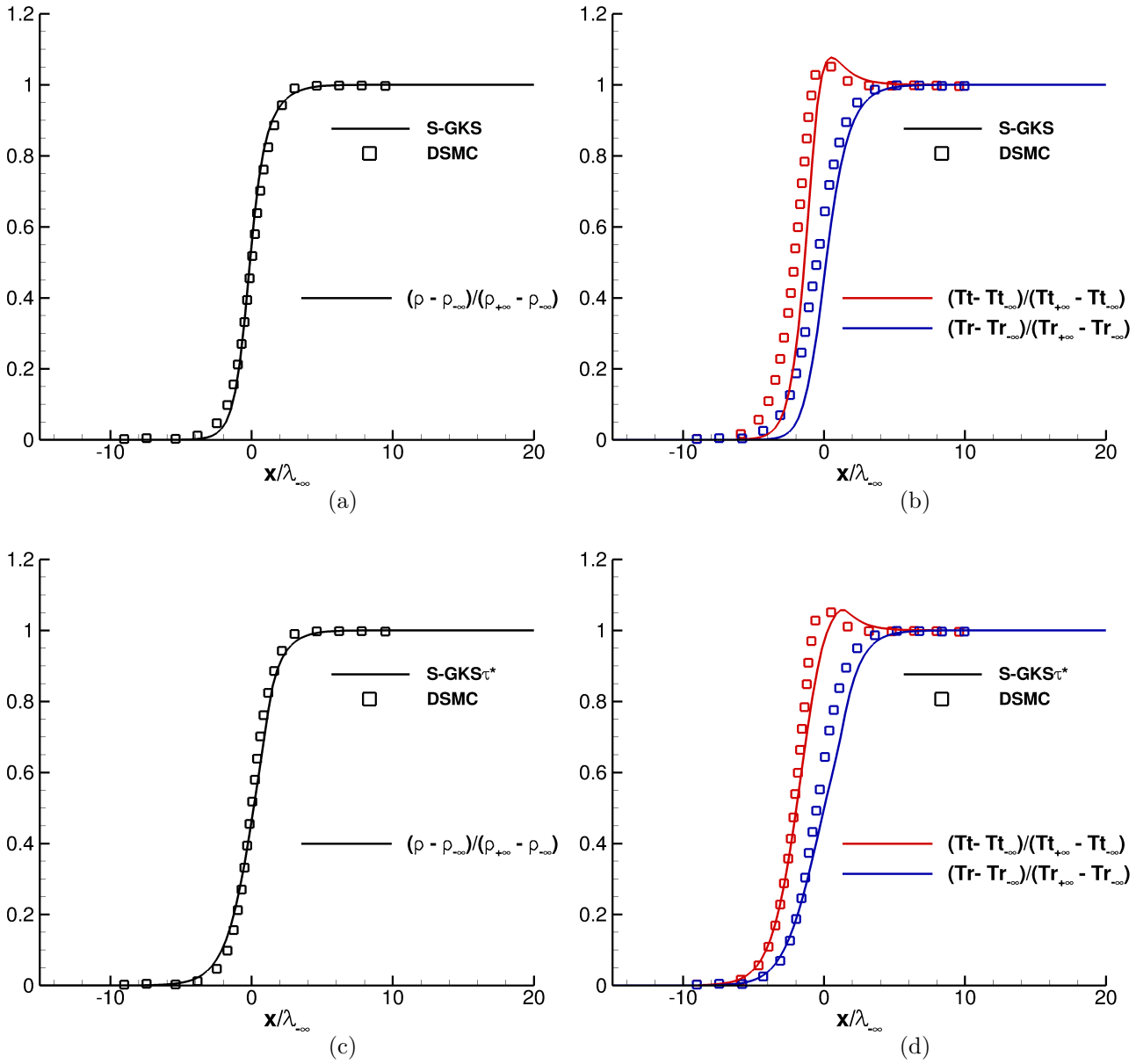

Figure 6.7: Non-dimensional ρ, T_r and T_t normalised profiles for M = 2.8 normal shocks in Nitrogen, constant $Z_r = 4.2$ (i.e. $Z_r = 2.52$ for the Rykov model) and μ eq. (4.18). GKS physical space cell's size equal to $0.25\lambda_{-\infty}$. DSMC results from [5].

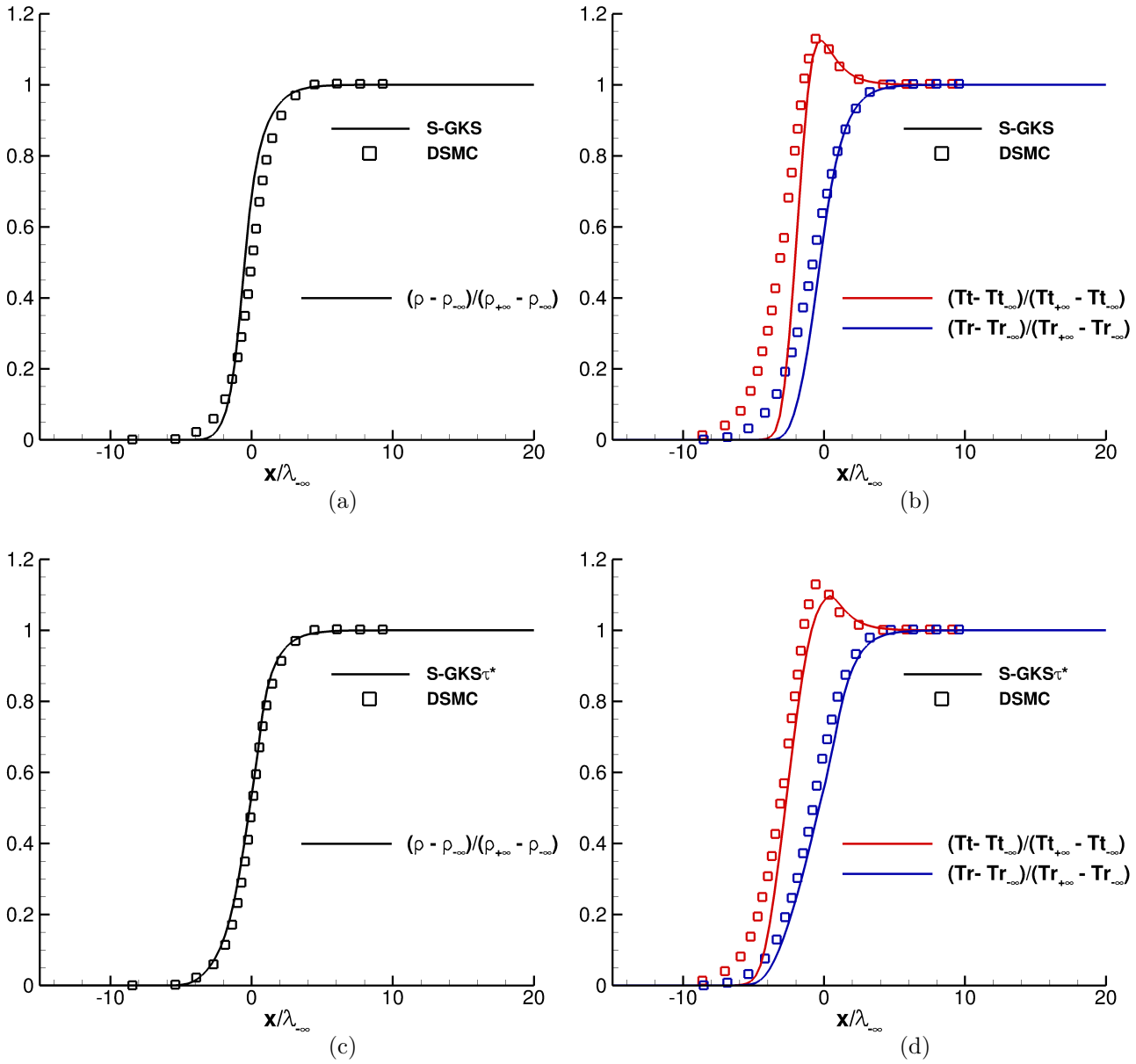

Figure 6.8: Non-dimensional ρ, T_r and T_t normalised profiles for M = 10 normal shocks in Nitrogen, constant $Z_r = 5$ (i.e. $Z_r = 3$ for the Rykov model) and μ eq. (4.18). GKS physical space cell's size equal to $0.25\lambda_{-\infty}$. DSMC results from [5].

To further evaluate the proposed GKS, different two-dimensional cases, shown in table 6.1, have been investigated. In all cases the gas considered was Nitrogen and wall boundaries were fully accommodating, i.e. equation (4.28) with $\sigma = 1$ is employed as mentioned in section 4.6.1. For the flat plate and the 25° wedge predictions have been obtained employing the GKS, with and without modified collision time; while for the infinite cylinder also a hybrid approach, where the DVM is employed to solve the bow shock while the GKS is used in the rest of the domain, has been considered. The computational grids are presented in figures 6.9a-c and the hybrid setup for the cylinder case is shown in figure 6.9d. Some additional details about number of cells and computational times can be found in table 6.2 of the next section.

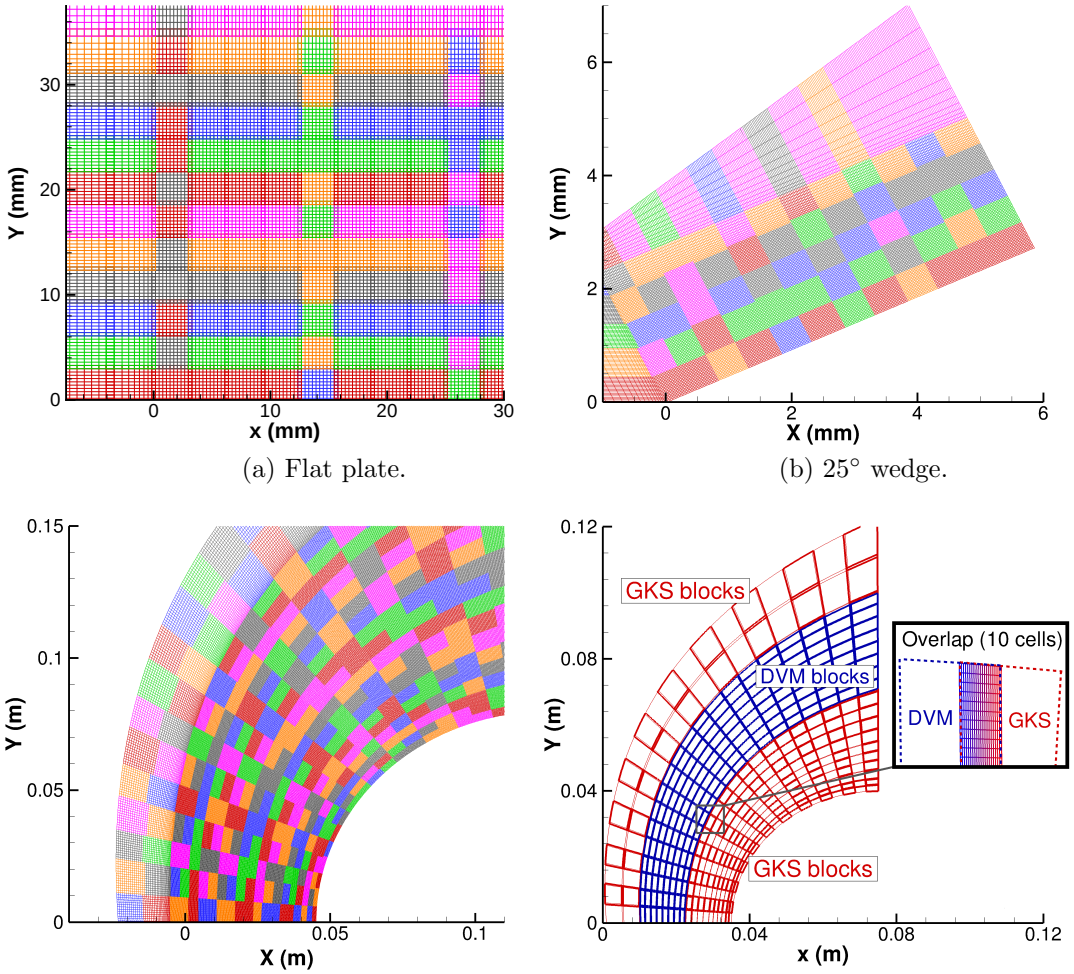

(a) Flat plate.

(b) 25° wedge.

(c) Cylinder, diameter $8cm$.

(d) Cylinder, DVM and GKS domains.

Figure 6.9: Computational grids for two-dimensional flat plate, wedge and cylinder test cases. In (a), (b) and (c) different colors represent different blocks; in (d) the part of the domain solved employing the GKS is defined in red while the DVM region in blue.

Figures 6.10c and 6.11c present the relative difference between translational and rotational temperatures for the flat plate predicted by the GKS approach with and without modified collision time. As expected, the main differences between the two temperatures can be observed in the first part of the plate where strong viscous interaction and rarefaction effects occur. When compared with figure 6.3d obtained with the DVM approach, it is clear that, due to its continuum formulation, both the GKS and the GKSτ^* methods can not correctly predict the rarefaction effects extending upstream of the plate. Nevertheless, looking at figure 6.10a, the GKS results prove to be in good agreement with the DVM and both the experimental data and the DSMC calculations from [6] at $5mm$ from the plate leading edge. The biggest differences between GKS and DVM predictions, defined here as

$$\triangle = \frac{|\Phi_{DVM} - \Phi_{GKS}|}{|\Phi_{DVM}|} \times 100\%, \tag{6.1}$$

occur when the local Knudsen number, equation (5.57), is much higher than the commonly employed threshold, i.e. 0.05 [49], as shown in figure 6.10b. As it is possible to notice from figures 6.11a, when the modified collision time is employed a slightly thicker thermal layer, in better agreement with the one predicted by the DVM, is predicted and smaller differences between the GKSτ^* and the DVM are observed where the Kn number is around the continuum breakdown limit, as shown in figure 6.11b. However, both GKS and GKSτ^* predict the quantities at the wall with a difference less then 5% relative to DVM calculations. In figure 6.13, $\tau_{correction}$, equation (5.56), contours are presented showing that the collision time correction is mainly active in the first part of the plate where strong non-equilibrium effects are predominant in accordance with the flow features previously described. When compared with the results from Xu et al. [7], as shown in figure 6.12, the proposed GKS is in better agreement with experimental data and DSMC results for the translational temperature at the wall. This is probably due to the fact that in the present work the GKS is based on the Rykov model which directly involves a correction that in the continuum limit leads to a variable Prandtl number, depending on the collision number Z_r, as demonstrated in appendix H. Instead, in [7] the scheme is based on a multi-temperature BGK model and a rescaling of the energy fluxes involving a fixed Prandtl number is employed as shown in equation (5.4). Therefore, considering a variable Prandtl number in region where important thermal

non-equilibrium effects occur, such as the wall for the current test case, should lead to more accurate predictions. Moreover, in [7] equation (4.11) for the collision number Z_r is employed. The latter neglect any dependence on the difference between translational and rotational temperatures.

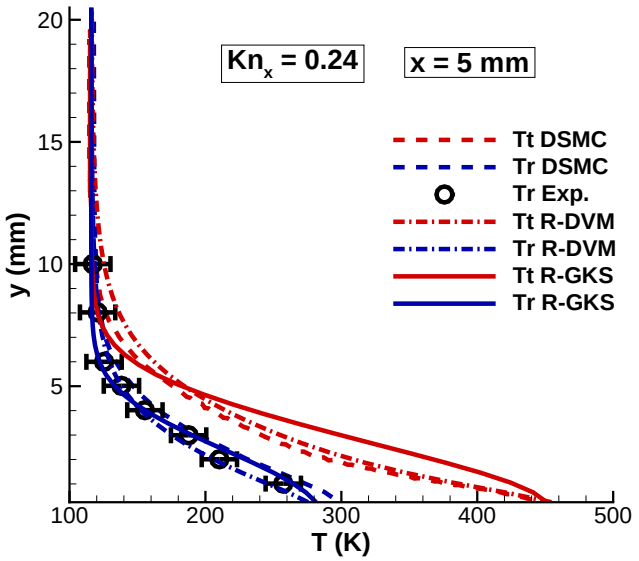

(a) T_t and T_r profiles at $x = 5mm$ from the flat plate leading edge. DSMC and experimental results from [6].

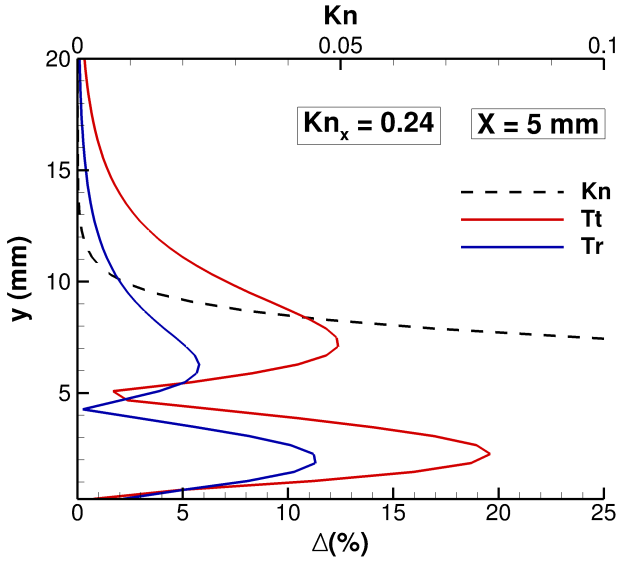

(b) R-GKS and DVM results difference and local Kn, equation (5.57), at $x = 5mm$ from the flat plate leading edge.

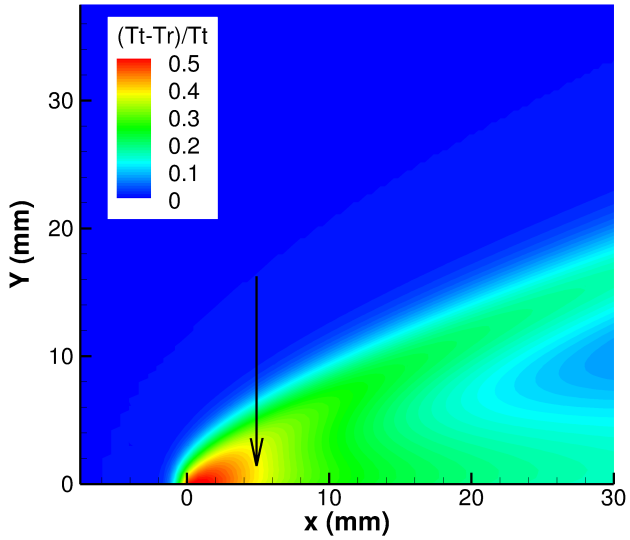

(c) $(T_t - T_r)/T_t$ contours.

Figure 6.10: R-GKS results for Nitrogen flow over a 2D flat plate: M = 4.89, Re = 422, Kn = 0.024 and $x_{ref} = 5cm$. Z_r eq. (4.12) and μ eq. (4.17).

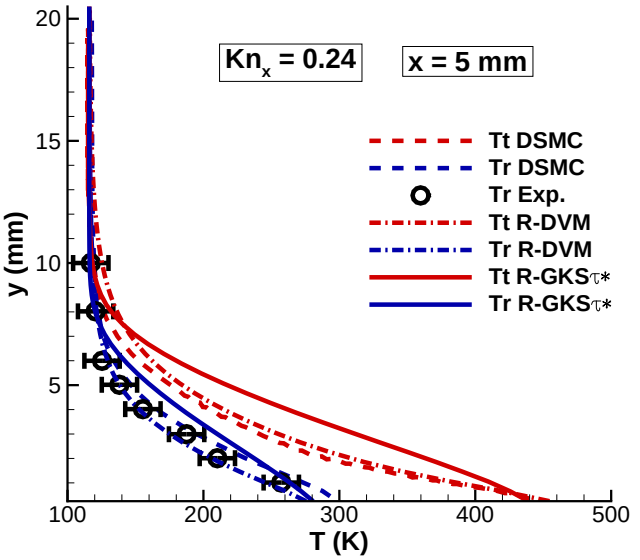

(a) T_t and T_r profiles at $x = 5mm$ from the flat plate leading edge. DSMC and experimental results from [6].

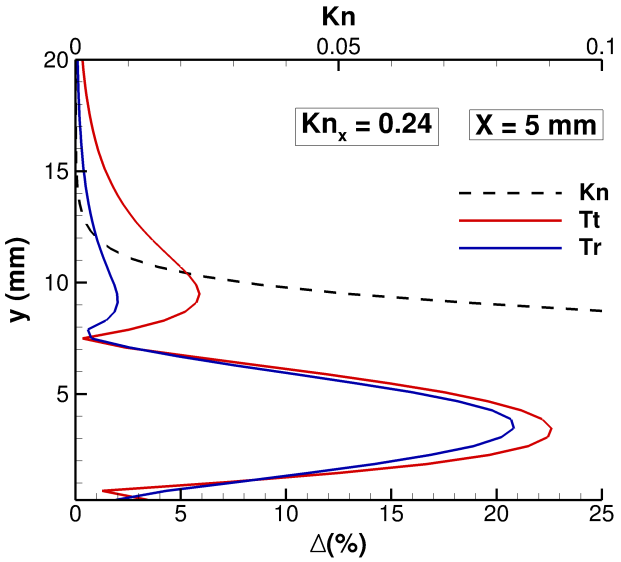

(b) R-GKSτ^* and DVM results difference and local Kn, equation (5.57), at $x = 5mm$ from the flat plate leading edge.

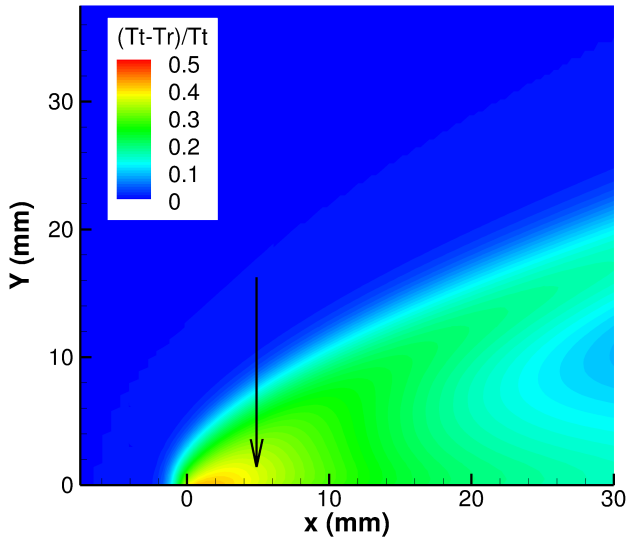

(c) $(T_t - T_r)/T_t$ contours.

Figure 6.11: R-GKSτ^* results for Nitrogen flow over a 2D flat plate: M = 4.89, Re = 422, Kn = 0.024 and $x_{ref} = 5cm$. Z_r eq. (4.12) and μ eq. (4.17).

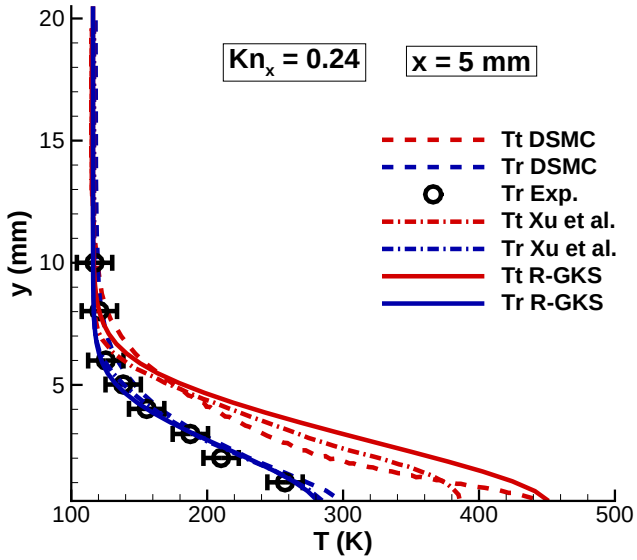

Figure 6.12: R-GKS and Xu et al. [7] results comparison for Nitrogen gas flow over a 2D flat plate: M = 4.89, Re = 422, Kn = 0.024 and $x_{ref} = 5cm$. Z_r eq. (4.12) and μ eq. (4.17). DSMC and experimental results from [6].

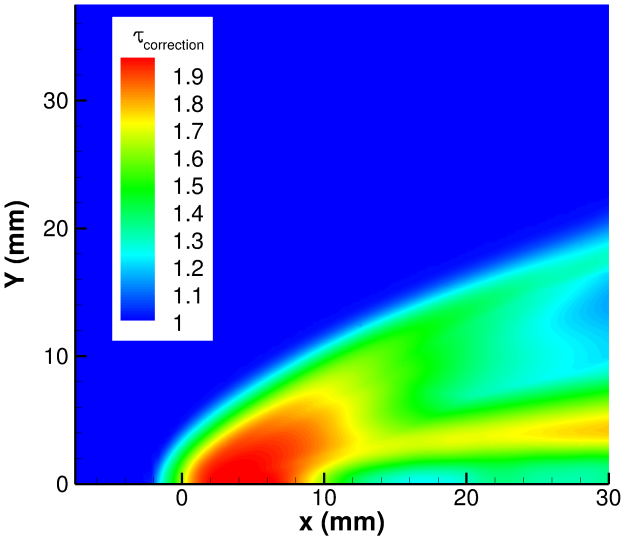

Figure 6.13: $\tau_{correction}$, equation (5.56), contours for Nitrogen flow over a 2D flat plate: M = 4.89, Re = 422, Kn = 0.024 and $x_{ref} = 5cm$. Z_r eq. (4.12) and μ eq. (4.17).

For the 25° wedge strong non-equilibrium effects can be observed not only at the leading edge but also across the oblique shock, see figures 6.14c and 6.15c obtained respectively employing the GKS, the GKSτ^* and the DVM approaches. As for the flat plate, again, the GKS is not able to correctly predict the rarefaction effects upstream of the wedge in contrast to the DVM approach, figure 6.17, even when the modified collision time is used. In figures 6.14a-b a comparison between GKS results and the calculations of [45] at $5mm$ from the leading edge is presented. As observed before for the normal shock cases, the GKS is able to resolve the shock structure, moreover the results are in good agreement with both hybrid and DSMC solutions presented in [45]. In [45] hybrid solutions have been obtained employing the DSMC method in regions of the domain with a local Knudsen number higher than 0.02 leaving the simulation of the rest of the domain to a traditional single-temperature NS approach. As shown in figure 6.14c, the biggest differences between GKS and DVM results take place across the shock where the local Knudsen number is greater than 0.1. Looking at Figure 6.15a-b, it is clear that considering the modified collision time leads to a solution in better agreement with the DVM approach. However, the difference between the two solution also becomes minimal across the shock as shown in figure 6.15c. This was expected since the DVM predicts a solution of the Rykov model of which the GKS can represent only a first order approximation and regularising the CE expansion should lead towards the more accurate solution of the model. What was not expected is that the GKS results are in better agreement with the hybrid and DSMC calculations from the literature respect the DVM and the GKSτ^* solutions. The differences between the DVM and the DSMC predictions can be explained considering that the former solves a simplified deterministic model of the BTE where the collision time τ does not depend on the particle velocities. Thus, the behaviour of the GKS is only fortuitous in this case. Anyhow, also for the wedge, as for the flat plate, both GKS and GKSτ^* predict the quantities at the wall with a difference less then 5% relative to DVM calculations. Finally, as expected considering the flow field characteristics mentioned above, the correction is mainly active at the leading edge and across the oblique shock, as can be seen figure 6.16.

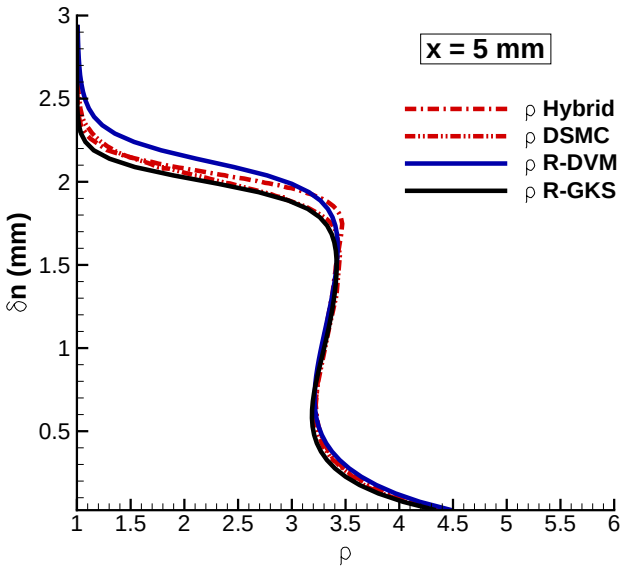

(a) ρ profiles at $x = 5mm$ from the wedge leading edge. Hybrid results from [45].

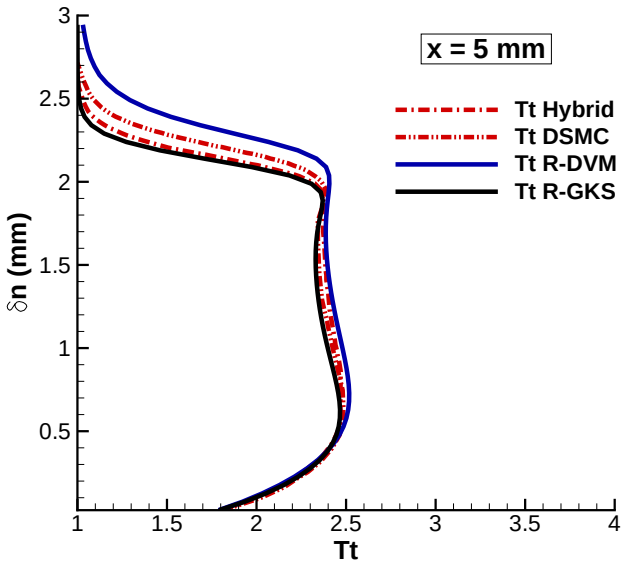

(b) T_t profiles at $x = 5mm$ from the wedge leading edge. Hybrid results from [45].

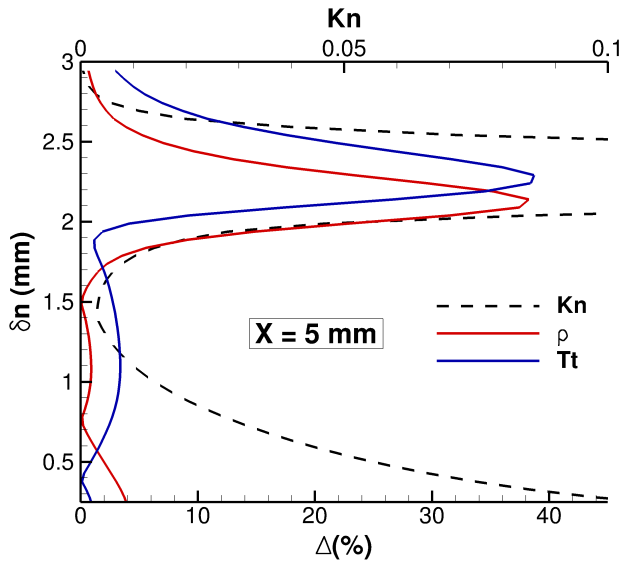

(c) R-GKS and DVM results difference and local Kn, eq. (5.57), at $x = 5mm$ from the wedge leading edge.

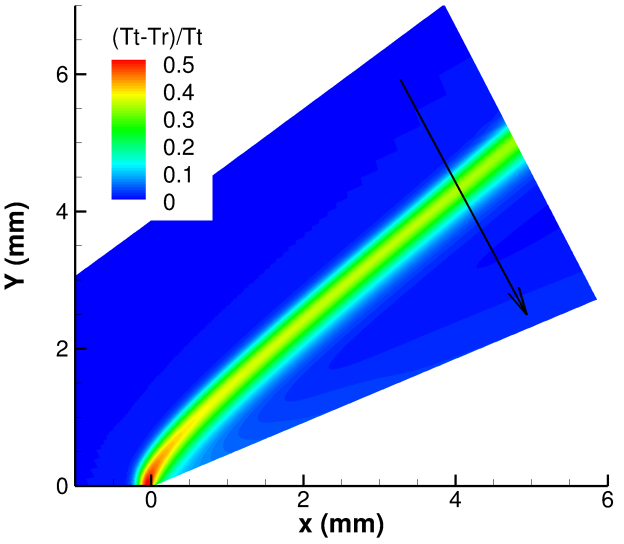

(d) $(T_t - T_r)/T_t$ contours.

Figure 6.14: R-GKS results for Nitrogen flow over a 25° 2D wedge: M = 4. Z_r eq. (4.12) and μ eq. (4.17).

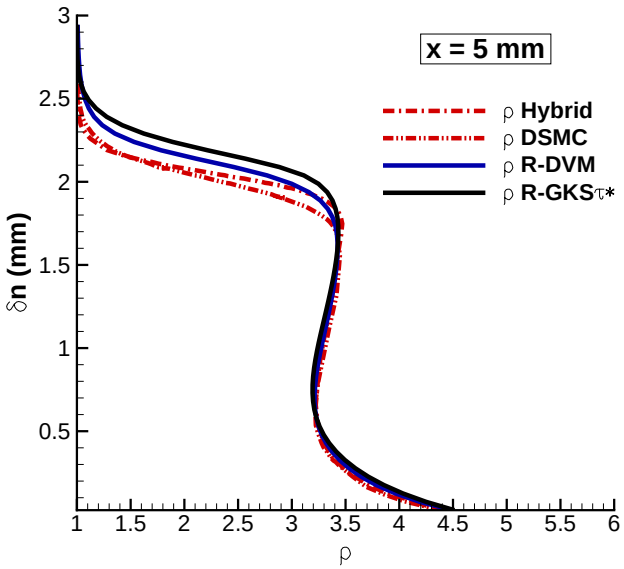

(a) ρ profiles at $x = 5mm$ from the wedge leading edge. Hybrid results from [45].

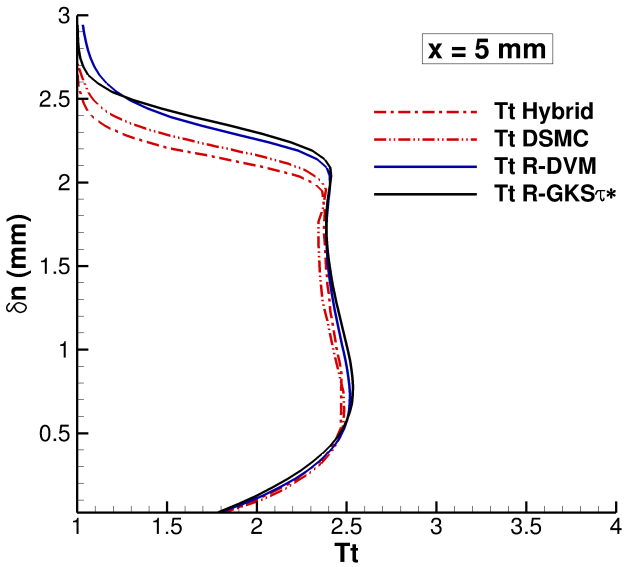

(b) T_t profiles at $x = 5mm$ from the wedge leading edge. Hybrid results from [45].

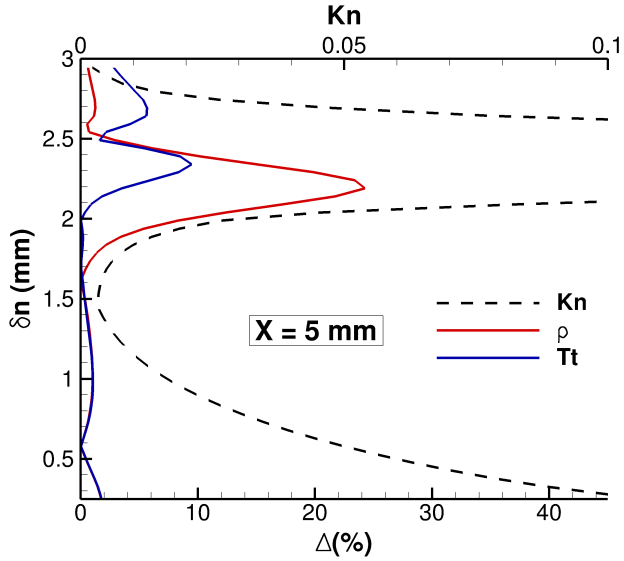

(c) R-GKS and DVM results difference and local Kn, eq. (5.57), at $x = 5mm$ from the wedge leading edge.

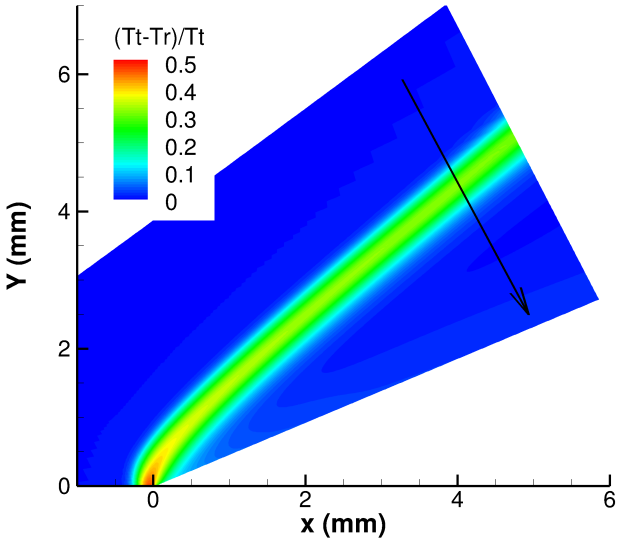

(d) $(T_t - T_r)/T_t$ contours.

Figure 6.15: R-GKSτ^* results for Nitrogen flow over a 25° 2D wedge: M = 4. Z_r eq. (4.12) and μ eq. (4.17).

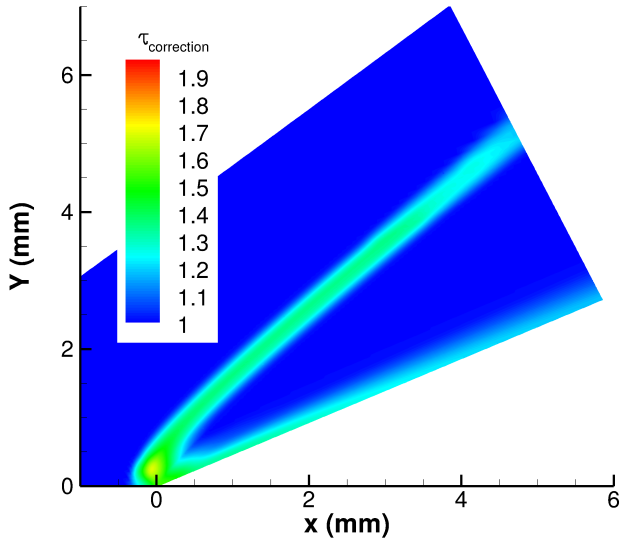

Figure 6.16: $\tau_{correction}$, equation (5.56), contours for Nitrogen flow over a 25° 2D wedge: M = 4. Z_r eq. (4.12) and μ eq. (4.17).

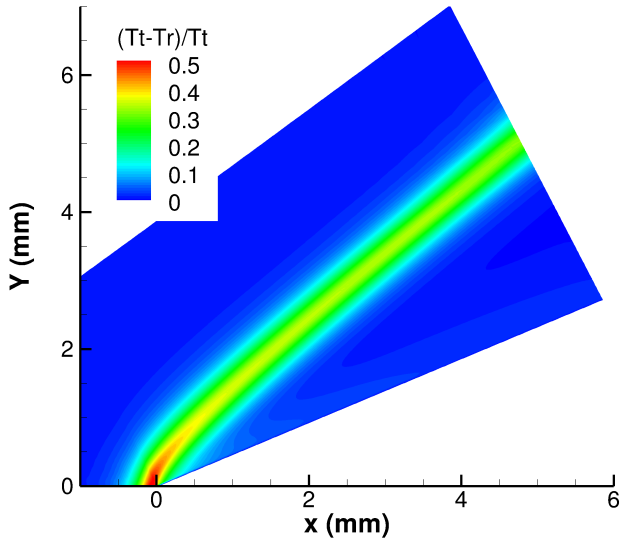

Figure 6.17: R-DVM prediction of $(T_t - T_r)/T_t$ contours for Nitrogen flow over a 25° 2D wedge: M = 4. Z_r eq. (4.12) and μ eq. (4.17).

Regarding the cylinder test case, looking at the relative differences between translational and rotational temperatures shown in figures 6.18 and 6.19c, it is possible to notice that high level of thermal non-equilibrium occur across the bow shock. Moreover, a region where the rotational temperature is bigger than the translational one can be observed towards the shoulder of the cylinder due to the expansion waves generated by the cylinder curvature. Figures 6.18a-b and 6.19a-b show density and temperatures profiles for the section at 45° respect the cylinder symmetry plane. Both GKS and GKSτ^* correctly predict the shock position as well as quantities and gradients at the wall in comparison to the results of the Modular Particle-Continuum (MPC) method of [54]. However, a thinner shock is obtained even when the modified collision number is employed. This was previously observed for the normal shock cases at high Mach numbers and the same explanation can be applied here. In figure 6.21 the collision time correction contours are presented, confirming once again that the correction is active where non-equilibrium effects occur accordingly with the flow field features. In this case across the bow shock and at the wall in the expansion region towards the cylinder shoulder. A better shock structure prediction can be obtained using the hybrid approach as can be observed in figures 6.20a-b. Here for the hybrid approach the DVM is employed in a region around the bow shock while the rest of the domain is simulated using the GKS, see figure 6.9d. The information exchange between the two solver has been handled employing the state-based coupling described in section 4.5 with an overlap region extension of about 10 cells. Differences can be still observed between the hybrid results from the present work and the ones in [54]. As for the wedge case the reason of this discrepancies can be found in the different methods employed. Indeed in [54] a DSMC method is used where rarefaction effect are dominant while in the present work a DVM, which solves only a simplified model of the BTE, is employed. When employed in a hybrid simulation, as noticeable in figures 6.20c, the transition between the GKS and the DVM solvers at the interface is naturally smooth, no blending of the two solutions has been applied in the overlap region, due to the common root of the approaches. This and the extended validity of the the GKS also suggest a reduction of the hybrid simulations' sensitivity to the positioning of the interfaces. However, the latter point requires further investigations.

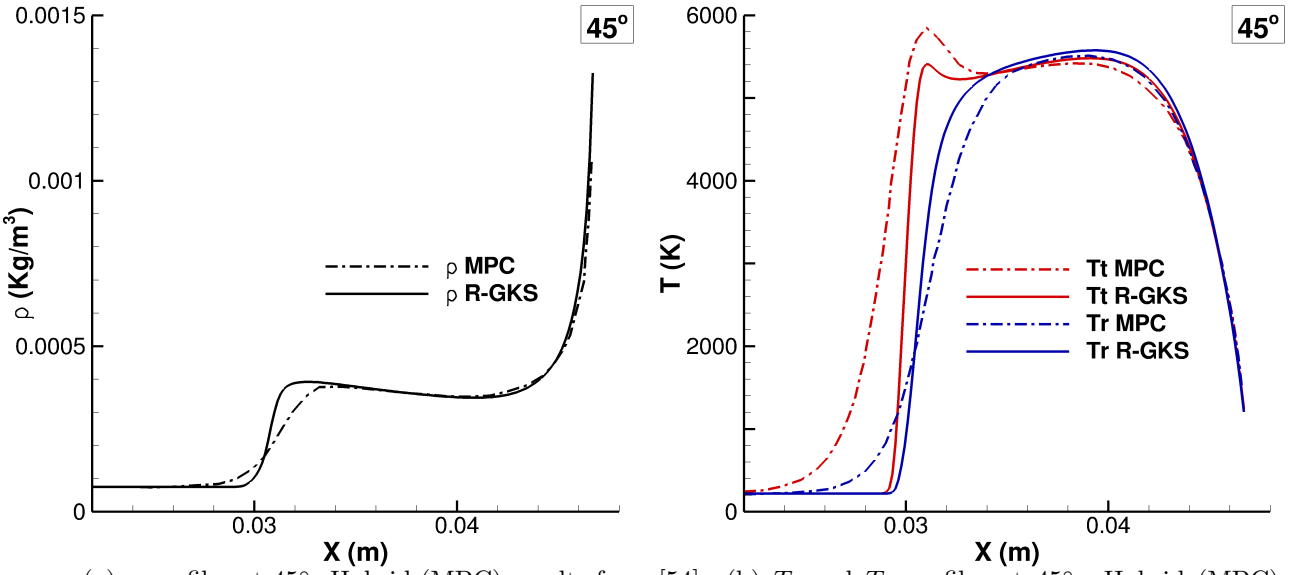

(a) ρ profiles at 45°. Hybrid (MPC) results from [54]. (b) T_t and T_r profiles at 45°. Hybrid (MPC) results from [54].

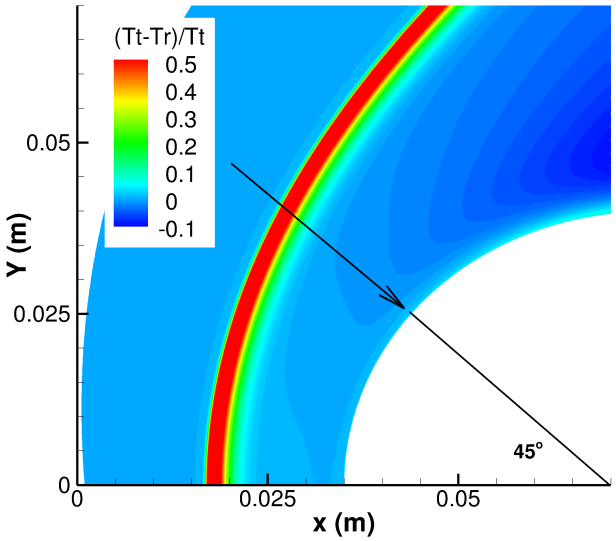

(c) $(T_t - T_r)/T_t$ contours.

Figure 6.18: R-GKS results for Nitrogen flow over a 2D cylinder: M = 12, Kn = 0.01 and $x_{ref} = 8cm$. Z_r eq. (4.12) and μ eq. (4.17).

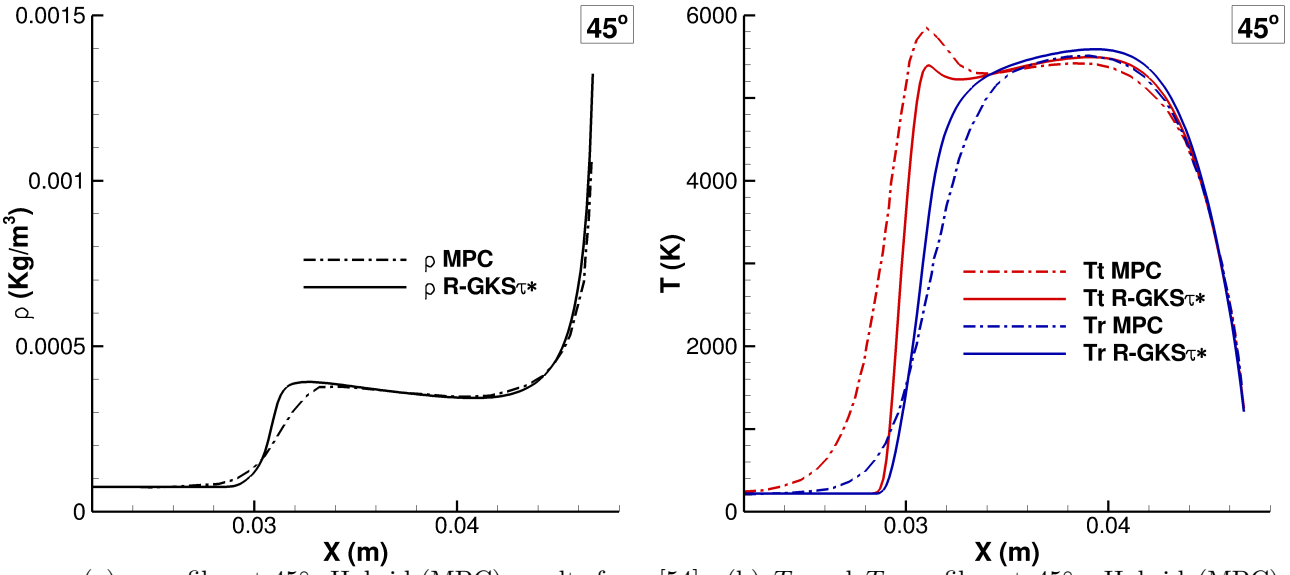

(a) ρ profiles at 45°. Hybrid (MPC) results from [54]. (b) T_t and T_r profiles at 45°. Hybrid (MPC) results from [54].

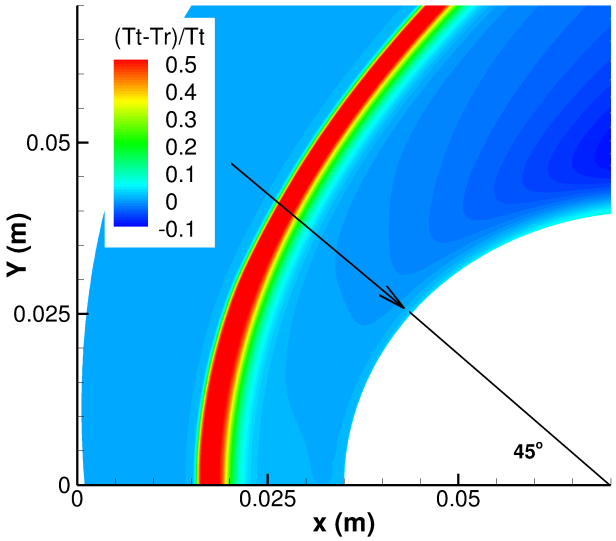

(c) $(T_t - T_r)/T_t$ contours.

Figure 6.19: R-GKSτ^* results for diatomic gas flow over a 2D cylinder: M = 12, Kn = 0.01 and $x_{ref} = 8cm$. Z_r eq. (4.12) and μ eq. (4.17).

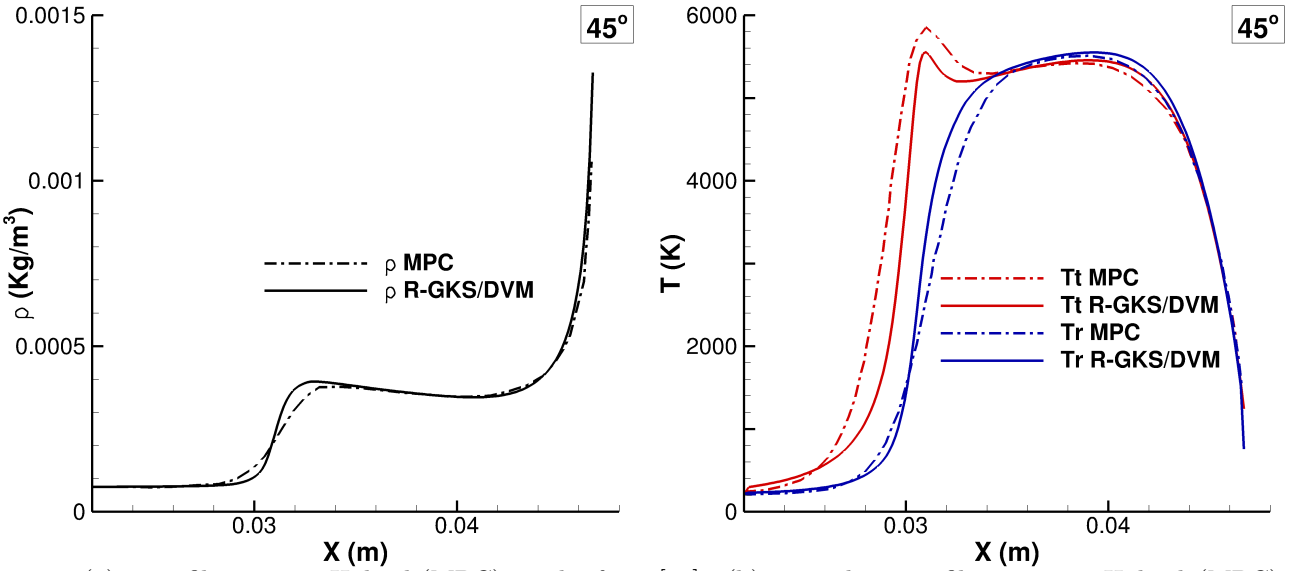

(a) ρ profiles at 45°. Hybrid (MPC) results from [54]. (b) T_t and T_r profiles at 45°. Hybrid (MPC) results from [54].

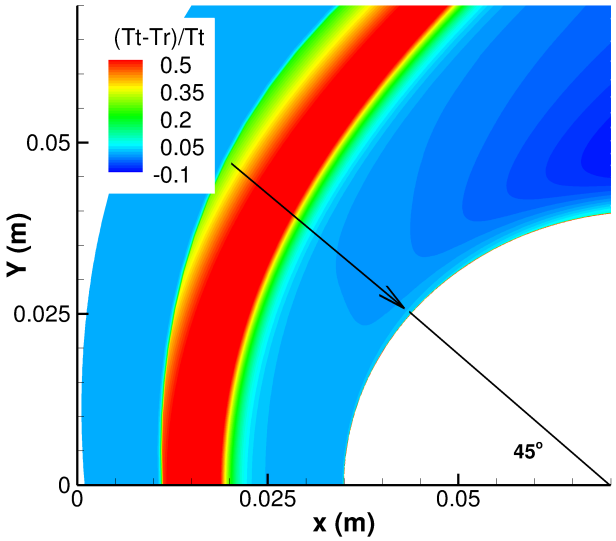

(c) Mach contours.

Figure 6.20: R-GKS/DVM hybrid results for Nitrogen flow over a 2D cylinder: M = 12, Kn = 0.01 and $x_{ref} = 8cm$. Z_r eq. (4.12) and μ eq. (4.17).

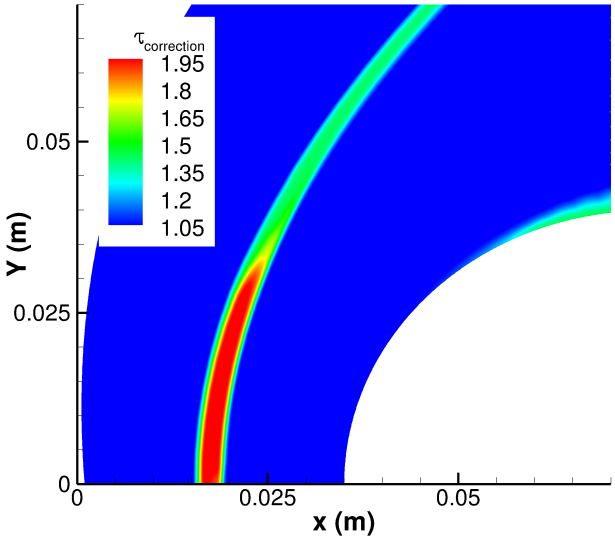

Figure 6.21: $\tau_{correction}$, equation (5.56), contours for Nitrogen flow over a 2D cylinder: M = 12, Kn = 0.01 and $x_{ref} = 8cm$. Z_r eq. (4.12) and μ eq. (4.17).

6.3 Computational and memory cost

The GKS is implemented with an optimisation feature so that the particle velocity space dimensions depend on the local state, while at the moment due its complexity this feature is not available in the DVM for the kinetic Boltzmann equations in $M\Phi C$. To perform a fair comparison about the computational time for the two approaches constant velocity spaces were used. Furthermore, it needs to be reminded that the halo exchange in the GKS involves only the flow state while the DVM needs to exchange the full velocity space and this represents an advantage of the GKS relative to the DVM and the full UGKS when a parallel calculation is performed. All simulations are steady state and a local time stepping is

Test Case	Phys. Cells	Vel. Cells	Solver	CFL	Cores	Iterations	Time (min)
$M = 2.8$ Shock	352	64×64	DVM	0.9	8	1838	15
$M = 2.8$ Shock	352	64×64	GKS	0.9	8	8066	6.5
$M = 2.8$ Shock	352	64×64	GKSτ^*	0.7	8	8336	7
$M = 4.89$ Plate	12996	32×32	DVM	0.7	16	9178	877.5
$M = 4.89$ Plate	12996	32×32	GKS	0.9	16	16526	81
$M = 4.89$ Plate	12996	32×32	GKSτ^*	0.9	16	16865	86
$M = 4.0$ Wedge	28016	48×32	DVM	0.7	64	29494	1925
$M = 4.0$ Wedge	28016	48×32	GKS	0.9	64	24552	107
$M = 4.0$ Wedge	28016	48×32	GKSτ^*	0.9	64	25397	115
$M = 12.0$ Cylinder	110544	96×64	GKS	0.9	256	178598	17177
$M = 12.0$ Cylinder	110544	96×64	GKSτ^*	0.9	256	173373	17159
$M = 12.0$ Cylinder	DVM: 50544 GKS: 61000	96×64	DVM/GKS	0.7	256	160656	75669

Table 6.2: Test cases details and computational time.

employed. The runs have been performed on Intel® Xeon® processors at the University of Liverpool cluster "Chadwick" and solution have been considered converged when the L^2-norm of the update between two consecutive solution, defined in appendix L, is of order 10^{-8} for all the macroscopic variables. The reason for the latter choice was the necessity to define a common convergence index for DVM and GKS to compare their performance, since being completely different approaches the relative residuals, normally used as convergence index, have different meanings. In table 6.2 the computational time for the

studied cases are reported and the GKS is found to be from 50% to 90% faster than the DVM depending on the case considered. This is due to the smaller time needed by the GKS per iteration, around 10 times smaller than the DVM. Moreover only a minimal increase in computational time is observed when the modified collision time is employed. In fact, in this case only the further requirement of evaluating the second derivatives is needed since the collision time modification is defined fully analytically as shown in sections 5.2 and 5.3 for monoatomic and diatomic gases respectively. Figures 6.22, 6.23 and 6.24 show the trends of L^2-norm of the update between two consecutive solution steps with the number of iterations for some of the two-dimensional cases considered in the current chapter. Finally, in terms of the memory cost of the GKS, the latter is drastically reduced compared with the DVM and the full UGKS. Indeed, in the DVM and the UGKS the values of the distribution function need to be stored for each physical cell in the full velocity space while the GKS being employed in the context of a continuum solver requires only the storage of the primitive variables.

Thus, employing the GKS in place of the DVM where the fluid is near thermal equilibrium, the performance of the hybrid solver can be improved in both memory and CPU time requirements, this without significantly compromising the accuracy as shown in section 6.2.

Considering an implicit approach can allow much larger CFL numbers to be used and relieve the restriction in time step due to the presence of the source term in the kinetic Boltzmann equations. However, this represents a complex step when the DVM is involved. Indeed, implicit time integrations require to store the solution at different time levels and in the case of the DVM this would include also the velocity distribution function. Thus, this would further increase the memory cost of the method. Instead, regarding the GKS an implicit implementation should be considered since, as more conventional NS approaches, it would require to store only the flow solution at different time levels. However, an important limitation when employing GKS methods is the higher computational cost than more traditional NS approaches. This is due to the numerical integrals required to obtain the the update of the conservative variables, see equation (5.2). For this reason, before considering an implicit implementation, the evaluation the Jacobian whould be affected by the high number of operations necessary to compute the integrals, a first improvement should be the fully analytical definition of the scheme.

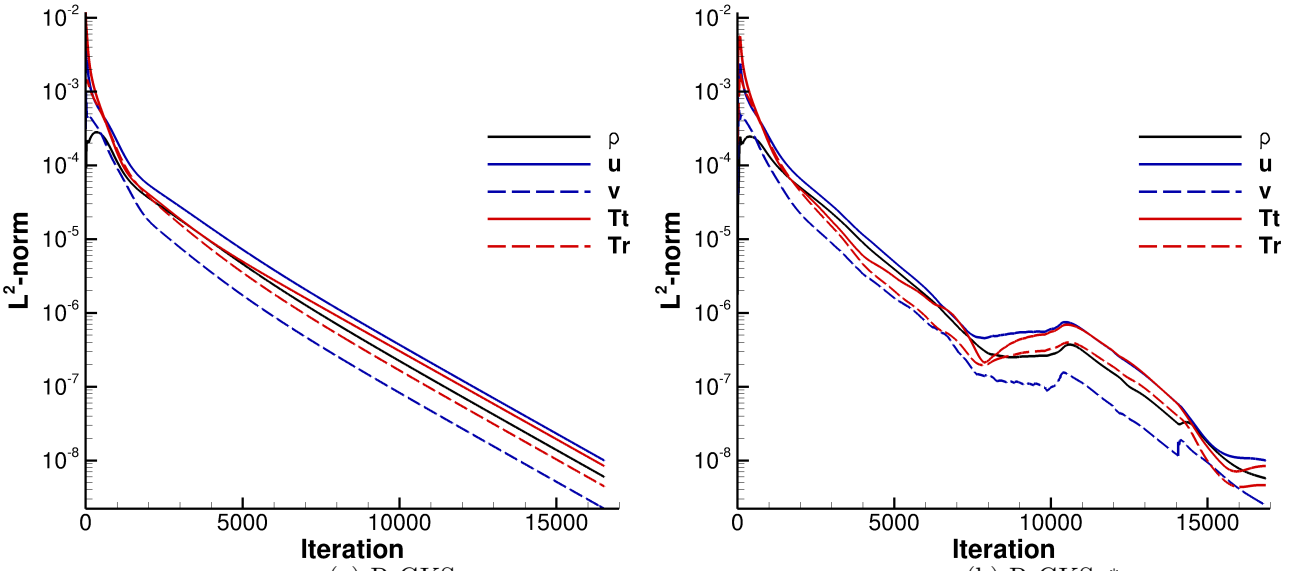

(a) R-GKS. (b) R-GKSτ^*.

Figure 6.22: L^2-norm of the update between two consecutive solution for the flat plate test case.

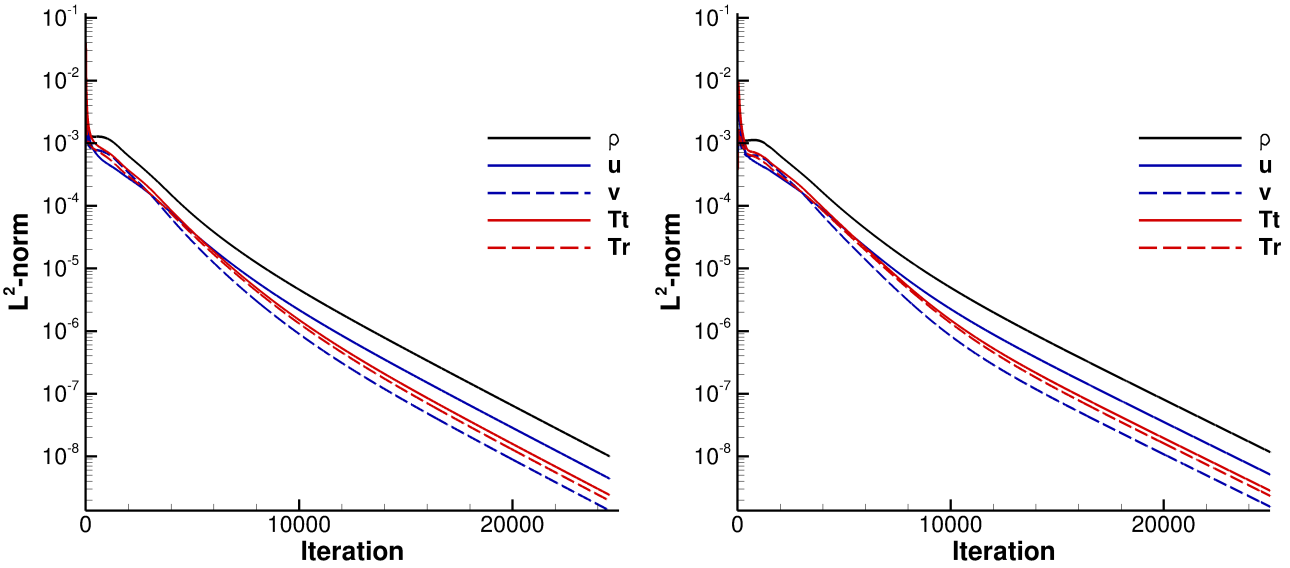

(a) R-GKS. (b) R-GKSτ^*.

Figure 6.23: L^2-norm of the update between two consecutive solution for the 25° wedge test case.

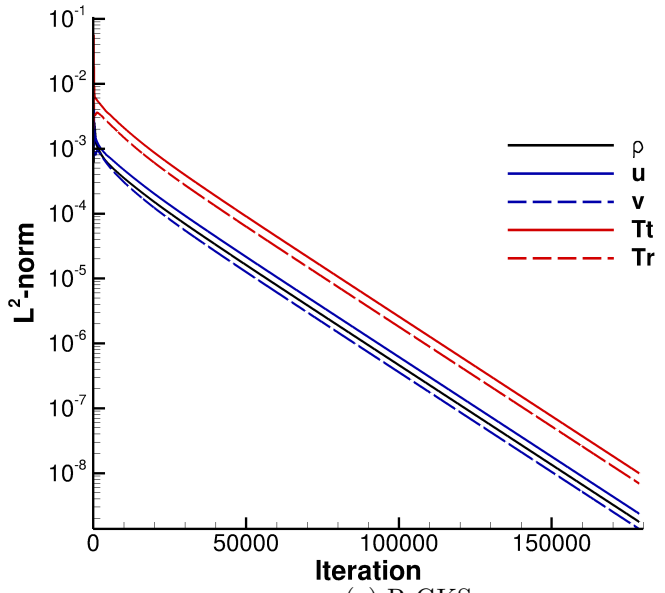

(a) R-GKS.

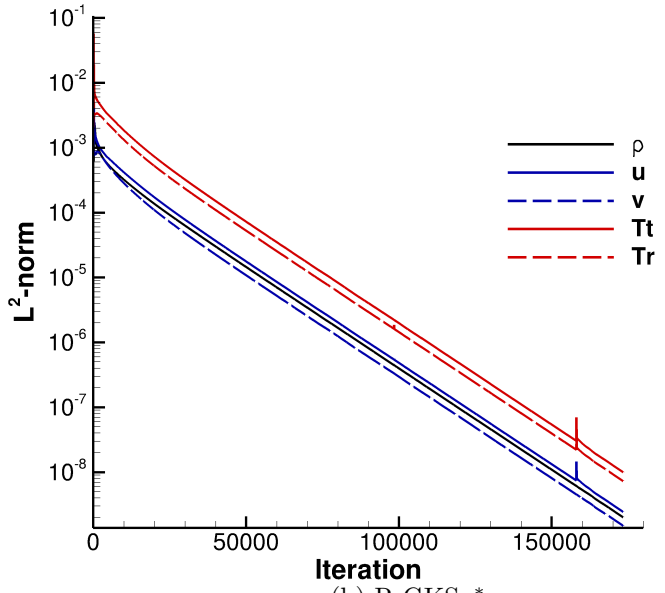

(b) R-GKSτ^*.

Figure 6.24: L^2-norm of the update between two consecutive solution for the cylinder test case.

6.4 Conclusions

It has been observed that the Shakhov and Rykov models achieve a generally better behaviour for flows with strong shocks than the ES models confirming what was previously reported in [150]. For this reason and the simpler mathematical formulation of the Shakhov and Rykov models, relative to the ES models, the former models have been chosen for the derivation of the analytical GKS in chapter 5.

The prediction of flow fields where rarefied and continuum regions coexist requires the solution of two models, the NS equations and the BTE. Since the methods to solve the BTE equation are expensive, the reduction of the region where this is strictly required could improve the performance of hybrid simulations. For these reasons a GKS for near-continuum regime has been proposed.

The scheme has been tested for various cases and Mach numbers proving to produce reliable predictions for near-continuum flows. Regarding the computational time, when compared with a kinetic DVM solver, the near-continuum GKS solver was found to be between from 50% to 90% faster than the former. Furthermore, due to the lower number of variables that need to be stored the GKS is less expensive in terms of memory than the DVM and the full UGKS. The memory usage of the proposed GKS is similar to traditional NS solvers which store only the continuum variables at the cell centres at different time levels. This proves that GKS can be a viable way to improve the performance of hybrid simulations maintaining an acceptable level of reliability when used in place of more complex methods for weekly rarefied flows. Finally, when employed in a hybrid simulation the transition between the GKS and the DVM solvers at the interface is naturally smooth, suggesting a reduction of the hybrid simulations' sensitivity to the positioning of the interfaces.

Chapter 7

Complex Three-Dimensional Cases for the GKS: Waveriders

7.1 Introduction

The recent successes of the Boeing X-51 (figure 7.2a) and the ESA IXV (figure 7.2b) as well as ongoing projects, such as the ESA HEXAFLY and LAPCAT projects (figure 7.2c) show a renewed interest in high-speed vehicles, designed following waverider's principles, for commercial and defense applications. Moreover, this is driving research on design solution, performance and optimisation in United States [170, 171, 172, 173], Europe [174, 175, 176, 177, 178] and China [179, 180] as well as in other countries [181, 182, 183, 184, 185].

The easy access to methods to design own waveriders shapes [186, 187, 188] makes them an appealing candidate to evaluate the capability of numerical methods for high-speed flows to predict complex 3D flow fields. A waverider is a shape designed from a known hypersonic, typically conical, flow field such that the shock is attached along the outer leading edge, see figure 7.1. The design procedure of a waverider is an inverse process which requires as inputs the definition of the shock generating surface, the vehicle's trailing edge and the design free stream Mach number. Then, the lower surface is generated tracing backwards stream-lines from the prescribed trailing edge, while the upper surface is generally aligned with the free-stream. Thanks to the leading edge attached shock wave, forming a high pressure zone on the lower surface, a waverider is able to generate lift and the corresponding wave drag.

The easiest way to construct the lower surface of a waverider is to employ a wedge flow [189] for which the flow conditions are exactly determined by the oblique shock relations. More general shapes can be

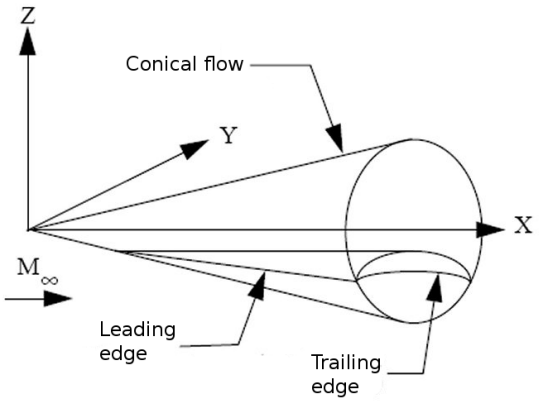

Figure 7.1: Example of a waverider shape from a conical flow.

obtained by employing circular cone flow [186]. In this case, introducing conical coordinates and assuming inviscid flows, the flow variables between the shock and the cone surface can be exactly calculated by solving the Taylor-Maccoll equation [190] or the hypersonic small disturbances theory. To increase the design flexibility for more general shocks geometries the osculating cone design method was developed in [187, 188] based on the class of methods to compute the flow field behind a given oblique shock wave presented in [187].

The classical waverider design procedures consider inviscid flow fields. Therefore, a realistic design requires that viscous effects must be accounted. Viscous effects, taken into account in the design process for the first time in [191], in this context are wall-shear stress and weak or strong hypersonic viscous interaction as well as, at high altitudes, rarefaction effects. Generally, viscous effects reduce the aerodynamic performance roughly from 25% to 50% [192]. Moreover, due to manufacturing limits and aero-heating issues, in reality waveriders have blunted leading edges and this also significantly reduces the lift-to-drag ratio [193]. However, the various studies on the performance of waveriders with blunt leading edges available in the literature show that optimum design points in terms of aerodynamic performance and aero-heating issues can be found [194].

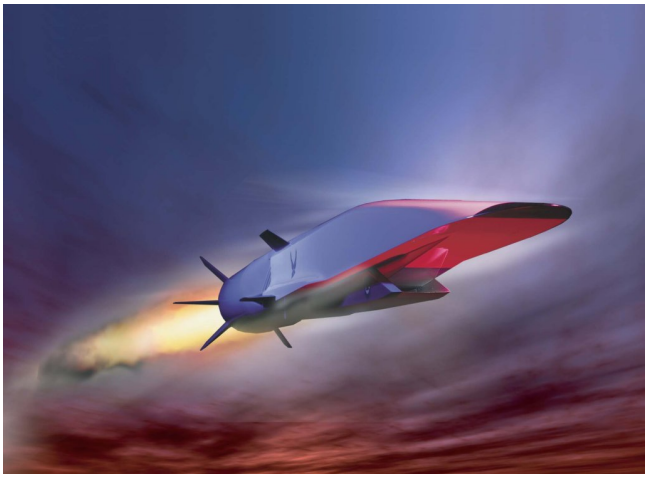

(a) Boeing X-51 Waverider [195].

(b) ESA Intermediate eXperimental re-entry Vehicle (IXV) [196].

(c) ESA completely integrated vehicle concept for Mach 8 flight, designed in the context of the HEXAFLY [197] and LAPCAT [198] projects.

Figure 7.2: Example of current vehicles designed employing waverider concepts.

7.2 Results

As mentioned in section 1.4, for the development of a CFD method it is important to guarantee the capability to cope with practical and realistic applications. For this reason also a fully three-dimensional formulation of the proposed GKS has been implemented in MΦC. In this section we present some results where the 3D GKS method have been employed alone, i.e. not coupled with DVM, to simulate the flow field around the waverider vehicle shown in figures 7.3a-b at Mach 8 for different Knudsen numbers with $T_\infty = 116K$ and $T_{wall} = 2.5T_\infty$. The choice of this design was driven by the availability in the literature of methods to build own waverider shapes and the renewed interest in this type of vehicle for high-velocity commercial and defense applications, as discussed in section 7.1. The shape has been derived following the work of Rasmussen and co-workers [186], but employs the higher order formulation of the hypersonic small disturbances theory presented in [199] to obtain a more accurate prediction of the shock angle in the design process. A generating cone angle of 10° and a straight-line compression-surface trailing edge, placed around 50% of the shock radius at the base of the generating cone as shown in figure 7.3c, have been chosen as design parameters. Finally, a blending of the leading edge has been considered with a constant radius of 0.05% the length of the waverider. The gas considered was Nitrogen. For this test case, the GKS method has been employed without modified collision time. Moreover, the power law defined in equation (4.18) with $\omega = 0.72$ has been used for the viscosity and the expression of [156], equation (4.13) with $b = 1$, was considered for the rotational collision number Z_r.

As expected, looking at figure 7.4a it is clear that for the highest Knudsen number case, $Kn_L = \lambda_\infty / Length = 0.001$ ($Kn_{d_{LE}} = \lambda_\infty / diameter_{LE} = 1$), the flow fields shows high thermal non-equilibrium around the waverider nose where also important viscous interaction effects occur. Significant rarefaction effects can be observed also across the shock wave and in the boundary layer over the upper body surface, see figure 7.4b. As can be noticed from figures 7.5a-b, when the Knudsen number is reduced to $Kn_L = 0.0004$ ($Kn_{d_{LE}} = 0.4$) the non-equilibrium region around the vehicle nose becomes smaller as well as less intense rarefaction effects occur in the boundary layer. By further reducing the Knudsen number to $Kn_L = 0.0002$ ($Kn_{d_{LE}} = 0.2$) less rarefaction effects can be observed except for the region

downstream the bow shock around the nose, see figure 7.6a. Indeed, the Knudsen number based on the nose diameter is still clearly in the rarefied domain. Furthermore, figure 7.6b shows how the shock becomes ever thinner relative to the waverider dimensions with decreasing Kn.

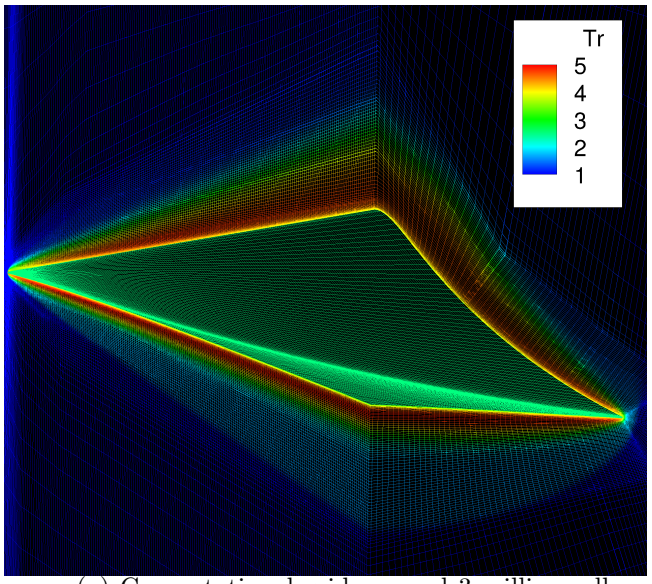

(a) Computational grid, around 3 million cells, and T_r contours.

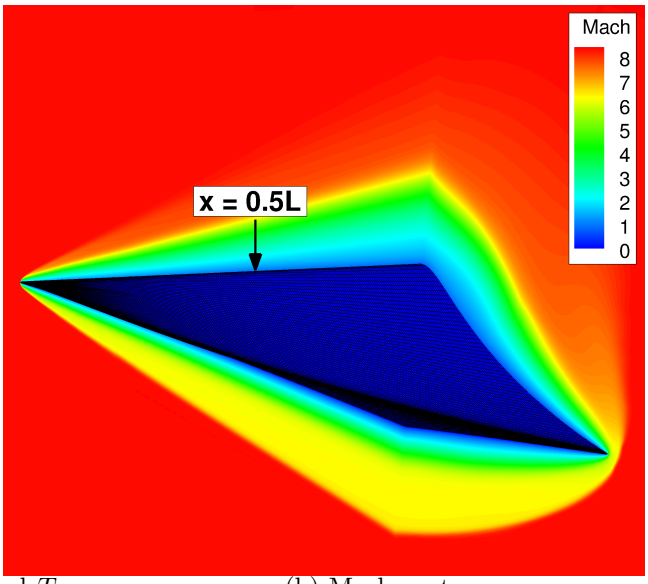

(b) Mach contours.

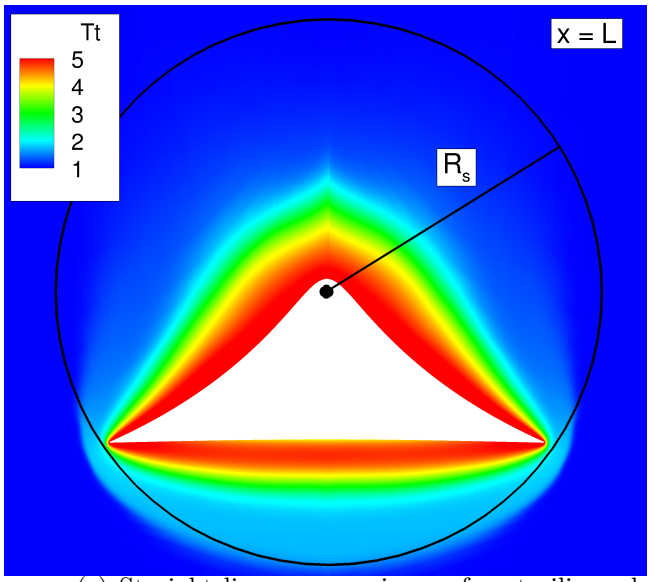

(c) Straight line compression-surface trailing edge and T_t contours.

Figure 7.3: Waverider design, $d_{LE} = Length/10^3$.

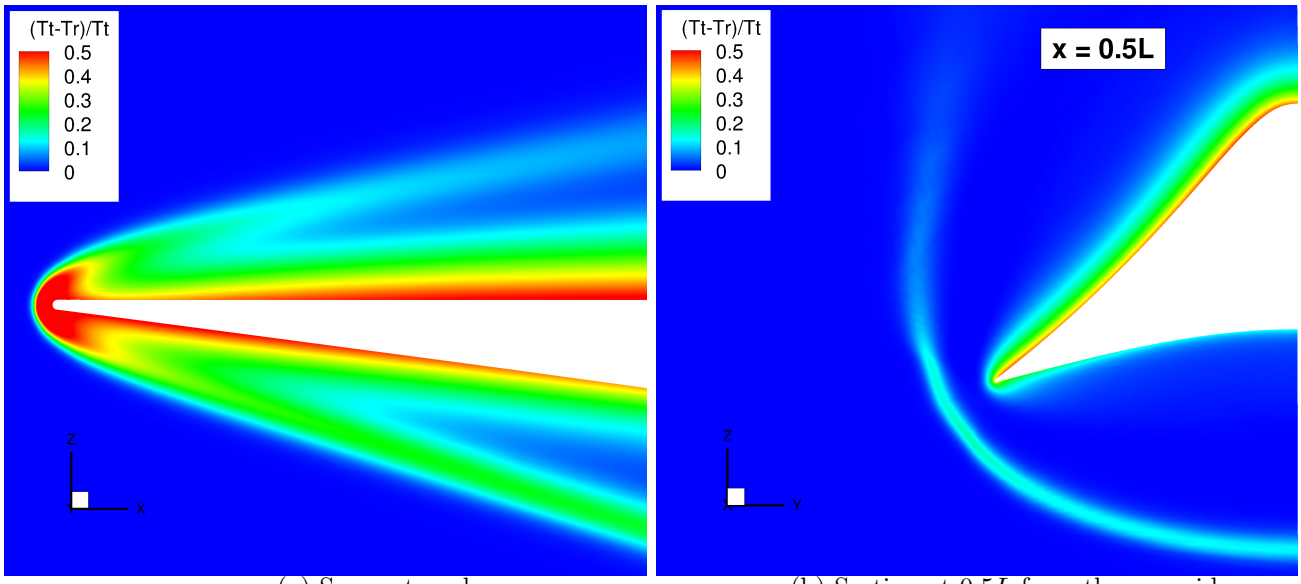

(a) Symmetry plane. (b) Section at $0.5L$ from the waverider nose.

Figure 7.4: $(T_t - T_r)/T_t$ contours for Nitrogen flow over a waverider at $Kn_L = 0.001$ ($Kn_{d_{LE}} = 1$), R-GKS solution.

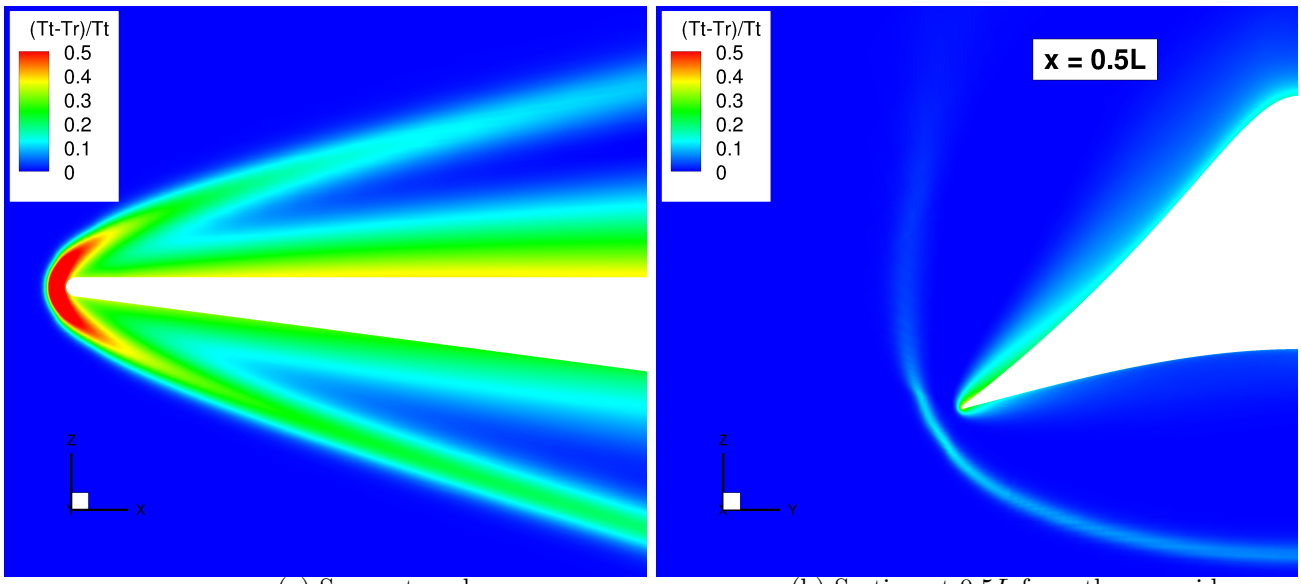

(a) Symmetry plane. (b) Section at $0.5L$ from the waverider nose.

Figure 7.5: $(T_t - T_r)/T_t$ contours for Nitrogen flow over a waverider at $Kn_L = 0.0004$ ($Kn_{d_{LE}} = 0.4$), R-GKS solution.

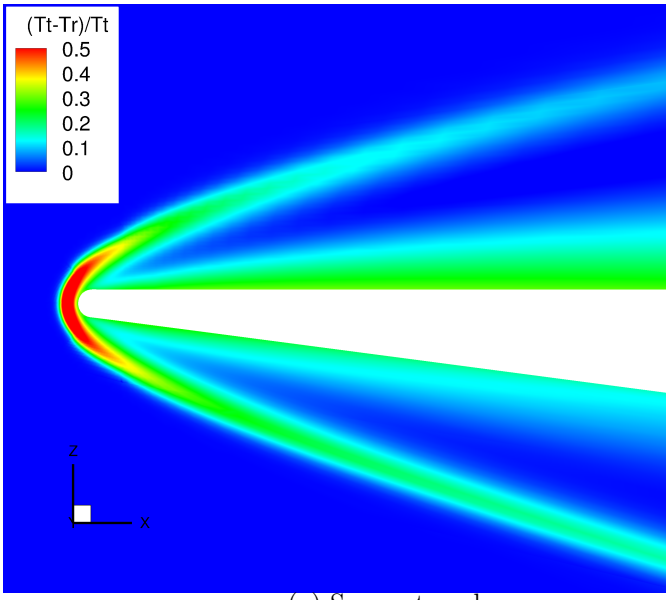

(a) Symmetry plane.

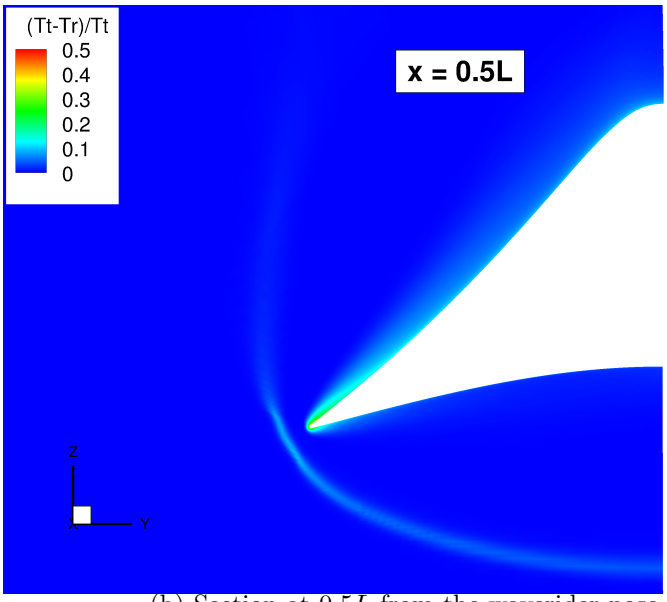

(b) Section at $0.5L$ from the waverider nose.

Figure 7.6: $(T_t - T_r)/T_t$ contours for Nitrogen flow over a waverider at $Kn_L = 0.0002$ ($Kn_{d_{LE}} = 0.2$), R-GKS solution.

7.3 Conclusions

In this chapter we have seen that the GKS can cope with flow fields around complex three-dimensional geometries such as waverider shapes and correctly predict the main flow features. Moreover, from the discussion presented in section 6.2 can be assumed that the predicted shock position, quantities and gradients at the wall as well as boundary layer thickness are reliable. This, as shown in section 6.3, at a considerably smaller cost in computational time and memory when compared to DVM calculations. Indeed, previous simulations of the flow field around a waverider presented in [100, 102] and obtained using a DVM/AUSM$^+$ hybrid approach required the use of tier-0 supercomputers, such as the SuperMUC supercomputer [9], due to the memory cost of the DVM; while the GKS allowed to obtain the results presented in the current chapter employing the local cluster Chadwick [8]. Therefore the GKS methods can represent a valid alternative to perform preliminary studies on complex high-speed vehicles, with important rarefaction effects, employing a limited amount of computational resources than the one required by more advanced methods such as the DVM and hybrid approaches.

Chapter 8

Conclusions and Future Works

8.1 Summary of Findings

As discussed in section 1.3, the aim of this work was to develop the numerical tools available at the CFD Laboratory of the University of Liverpool towards the simulation of high-speed flow, particularly partially-rarefied flows with fully excited translational and rotational modes. The CFD codes improved in the context of the present work are the Helicopter Multi-Block (HMB2) solver and the Multi-Physics Code (MΦC) described in sections 2 and 4, respectively. The former is a continuum solver previously employed in a wide range of fluid dynamics applications and the latter is a computational framework which allows different mathematical models to be employed in different regions of the flow domain.

Firstly, to improve the capability of the two codes to predict continuum high-speed flow, the implicit implementation of the AUSM$^+$ and AUSM$^+$*up* schemes with an analytically defined Jacobian has been considered. A novel formulation of the AUSM$^+$ and AUSM$^+$*up* schemes has been proposed in chapter 2 where a blending has been introduced by means of parametric sigmoidal functions at the points of discontinuity of the numerical fluxes. This to remove the different branches present in the original formulation, which would increase the computational cost and reduce the stability for cases with complex flow transient or grid geometry. In chapter 3 the predictions obtained employing the proposed AUSM$^+$ and AUSM$^+$up formulations have been compared with results available in the literature showing that the reliability of the schemes has been preserved in the proposed formulation.

A DVM solver is the preferable approach employed in MΦC to predict flows in rarefied conditions. In rarefied gas flows at high velocities it is necessary to take into account the excitation of the internal

degrees of freedom, thus, as a step towards realistic simulations, the framework has been firstly improved with the addition of the Rykov model and an Ellipsoidal-Statistical (ES) model [29] for diatomic gases with rotational non-equilibrium. In chapter 6 it has been observed that the Shakhov and Rykov models achieve a generally better behaviour for flows with strong shocks than the ES models confirming what was previously reported by [150]. For this reason and the simpler mathematical formulation, relative to the ES models, of the Shakhov and Rykov models, the latter have been chosen for the derivation of the analytical GKS in chapter 5.

A major drawback using a DVM in the hybrid approach available in MΦC is its computational and memory cost. Based on the literature survey of related works, GKS methods have been identified as efficient approaches, relative to DVM, capable of modelling complex diatomic gas flows with moderate rarefaction effects but with significant rotational non-equilibrium and thus, when employed in the context of hybrid simulation, they can reduce the extent of the domain where more complex numerical methods, such as the DVM, are needed.

For this reason, two GKS methods, analytically-defined on the basis of the CE expansion of non-dimensional Shakhov and Rykov models, have been proposed in chapter 5 to simulate weakly rarefied flows. In chapters 6 and 7 the scheme has been tested for various cases and Mach numbers proving to produce reliable predictions for near-continuum flows for a wide range of test cases including complex 3D flows. When compared with a kinetic DVM solver in chapter 6, the near-continuum GKS solver was found to be between from 50% to 90% faster than the former and due to the lower number of variables that need to be stored, the GKS is less expensive in terms of memory than the DVM and the full UGKS. Moreover, when employed in a hybrid simulation the transition between the GKS and the DVM solvers at the interface is naturally smooth suggesting a reduction of the hybrid simulations' sensitivity to the positioning of the interfaces. Thus, in chapter 6 it has been shown that GKS can be a viable way to improve the performance of hybrid simulations maintaining an acceptable level of reliability if used in place of more complex methods for weekly rarefied flows. Although more advanced approaches can represent the flow physics to a deeper level, this come to a cost in computational resources not always readily accessible. In this context the GKS methods can be employed to perform preliminary studies

on complex high-speed vehicles with important rarefaction effects, as shown in chapter 7, employing less computational resources than the one required by more advanced methods such as the DVM or hybrid approaches.

8.2 Future Works

An important limitation observed while employing GKS methods is the higher computational cost, relative to more traditional NS approaches, due to the numerical evaluation of the required moments in velocity space [86]. For this reason, a first improvement should be the fully analytical definition of the moments to obtain a formulation of the scheme where no numerical evaluation of integrals is needed. This would lead to a more efficient algorithm respect the presented formulation where a trapezoidal rule is employed to evaluate the required integrals making the efficiency of the scheme dependant on the Mach number which affect the velocity space dimensions. The latter improvement is currently under development in the present framework.

Furthermore, based on previous theoretical works [81], recent studies in [82, 83] employing the BGK-NS scheme showed how GKS methods can also improve simulations of turbulent flows thanks to their multiscale approach. In this cases [82, 83] the BGK-NS method is used, however in high-speed flows thermal non-equilibrium often occurs. Thus, as a further development, the modification of the proposed schemes to include the relation between the relaxation time and the turbulent quantities presented in [82, 83] would also open the possibility to include turbulence phenomena when simulating flows with strong thermal non-equilibrium effects using GKS methods.

In the current work only translational and rotational non-equilibrium have been considered, limiting the applications of the presented methods to flow field with temperatures lower than 800K. Thus, a third suggested improvement is the extension of the proposed GKS to include also vibrational degrees of freedom. In real world applications, the latter are gradually excited, in contrast to the translational and rotational ones that are in general fully excited. Although kinetic models with the correct transport properties in the continuum limit that consider also the vibrational degrees of freedom are not available following the work in [78], for the BGK-NS method in one-dimensional problems, a three temperature equilibrium Maxwellian could be considered in the Rykov model. As in [78] a Landau-Teller-Jeans type relaxation model could be used for the vibrational energy equation source term and a simple harmonic oscillator model could be considered to evaluate the effective number of degrees of freedom depending on

the temperature. In the literature examples are given where vibrational non-equilibrium is considered in an hybrid method [1]. Finally, another important aspect in high-speed and re-entry flows are chemical reactions. Then, after the introduction of vibrational non-equilibrium, chemical reactions models should also be considered in the framework. As a first step the latter can be considered employing a classical approach as done for more traditional NS solvers [15, 14, 200]. In this approach, it is assumed that the translational and rotational modes are in equilibrium and are treated as a single temperature, while the other energy modes are treated as different non-equilibrium temperatures, as already mentioned in section 1.1. Alternatively, more advanced methods such as state-to-state models are available in the literature, as example in [201, 202, 203, 204]. The latter represent the non-equilibrium kinetic processes in terms of master equations which take into account the cross sections for the chemical reactions and the vibrational transition probabilities.

Appendix A

Dimensionless Temperature in HMB2

In HMB2 the the Navier-Stokes, or Euler, equation are solved in terms of the dimensionless pressure, $\tilde{p}$, and the density, $\tilde{\rho}$. For this reason the temperature field has to be evaluated from the pressure and density fields, known the properties of the heat capacity ratio, γ, and free stream Mach number, M_∞. Considering the ideal gas law:

$$p = \rho R T \tag{A.1}$$

the speed of sound definition

$$a = \sqrt{\gamma R T} \tag{A.2}$$

and the dimensionless quantities

$$\tilde{\phi} = \frac{\phi}{\phi_\infty} \tag{A.3}$$

the following relation to evaluate the dimensionless temperature from the pressure and density fields

$$\tilde{T} = \frac{T}{T_\infty} = \frac{p}{\rho R}\frac{1}{T_\infty} = \frac{p}{\rho R}\frac{\gamma R}{a_\infty^2} = \frac{\gamma p}{\rho a_\infty^2} = \frac{\gamma p_\infty \tilde{p}}{\rho_\infty \tilde{\rho} a_\infty^2} = \frac{\gamma \rho_\infty V_\infty^2 \tilde{p}}{\rho_\infty \tilde{\rho} a_\infty^2} = \frac{\gamma \tilde{p}}{\tilde{\rho}} M_\infty^2 \tag{A.4}$$

Appendix B

L2-Norm of the Residual

The following L2-norm of the residual is used in HMB2 as index of the convergence of the solution

$$log\left(\frac{L_2(Res.\ t>0)}{L_2(Res.\ t=0)}\right) \tag{B.1}$$

indeed, the latter represents the order of magnitude of the residual at time t scaled by the initial residual. Clearly if the sign is negative (or positive) means that the residual is decreasing (or increasing) with respect to the initial one.

Appendix C

Modified AUSM$^+$ and AUSM$^+$up Schemes and Relative Jacobians

C.1 Modified AUSM$^+$ and AUSM$^+$up Schemes

C.1.1 AUSM$^+$

Interface fluxes formula:

$$\begin{gathered}
\mathbf{f}_{i-1/2} = \dot{m}_{1/2}\mathbf{\Psi} + \mathbf{p}_{1/2} \\
\mathbf{\Psi} = sig(\dot{m}_{1/2}, 0)\mathbf{\Psi}_L + [1 - sig(\dot{m}_{1/2}, 0)]\mathbf{\Psi}_R \\
\mathbf{\Psi_{L/R}} = \left\{1,\ u_{L/R},\ v_{L/R},\ w_{L/R},\ H_{L/R}\right\}^T \\
\dot{m}_{1/2} = a_{1/2}M_{1/2}\rho \\
\rho = sig(M_{1/2}, 0)\rho_L + [1 - sig(M_{1/2}, 0)]\rho_R \\
\mathbf{p}_{1/2} = \left\{0,\ p_{1/2}n_x,\ p_{1/2}n_y,\ p_{1/2}n_z,\ 0\right\}^T
\end{gathered} \tag{C.1}$$

sigmoidal function:

$$\begin{gathered}
sig(x, y) = \tfrac{1}{2}\left(-(1+K)\tfrac{x-y}{-|x-y|-K} + 1\right) \\
K = 10^{-16}
\end{gathered} \tag{C.2}$$

left and right state Mach numbers:

$$M_L = \tfrac{u_{n,L}}{a_{1/2}} \quad M_R = \tfrac{u_{n,R}}{a_{1/2}} \tag{C.3}$$

interface speed of sound formula:

$$a_{1/2} = (1 - sig(\widehat{a}_L, \widehat{a}_R))\frac{a_L^{*2}}{\widehat{a}(a_L^*, u_{n,L})} + sig(\widehat{a}_L, \widehat{a}_R)\frac{a_R^{*2}}{\widehat{a}(a_R^*, -u_{n,R})}$$

$$\widehat{a}(x,y) = sig(x,y)x + (1 - sig(x,y))y \tag{C.4}$$

$$a_{L/R}^{*2} = \frac{2(\gamma-1)}{\gamma+1}H_{L/R}$$

interface Mach number:

$$M_{1/2} = M_{(4)}^{+}(M_L) + M_{(4)}^{-}(M_R)$$

$$M_{(4)}^{\pm}(M) = \begin{cases} M_{(1)}^{\pm}(M) & \text{if } |M| \geq 1 \\ M_{(2)}^{\pm}(M)(1 \mp 16\beta M_{(2)}^{\mp}(M)) & \text{otherwise} \end{cases} \tag{C.5}$$

$$M_{(1)}^{\pm}(M) = \tfrac{1}{2}(M \pm |M|); \quad M_{(2)}^{\pm}(M) = \pm\tfrac{1}{4}(M \pm 1)^2$$

$$\beta = 1/8$$

interface pressure formula:

$$p_{1/2} = P_{(5)}^{+}(M_L)p_L + P_{(5)}^{-}(M_R)p_R$$

$$P_{(5)}^{\pm}(M) = \begin{cases} \frac{1}{M}M_{(1)}^{\pm}(M) & \text{if } |M| \geq 1 \\ M_{(2)}^{\pm}(M)(\pm 2 - M \mp 16\alpha M M_{(2)}^{\mp}(M)) & \text{otherwise} \end{cases} \tag{C.6}$$

$$\alpha = 3/16$$

C.1.2 AUSM$^+$up

Interface Mach number with pressure diffusion term:

$$M_{1/2} = M_{(4)}^{+}(M_L) + M_{(4)}^{-}(M_R) + M_p$$

$$M_p = -2\frac{K_p}{f_a}sig(1 - \sigma\bar{M}^2, 0)(1 - \sigma\bar{M}^2)\frac{p_R - p_L}{a_{1/2}(\rho_L + \rho_R)} \tag{C.7}$$

scaling factor:

$$f_a = M_0(2 - M_0)$$

$$M_0^2 = min(1, sig(\bar{M}^2, M_\infty^2)\bar{M}^2 + (1 - sig(\bar{M}^2, M_\infty^2))M_\infty^2)) \tag{C.8}$$

$$\bar{M}^2 = \tfrac{1}{2}(M_L^2 + M_R^2)$$

interface pressure formula with velocity diffusion term:

$$p_{1/2} = P^{+}_{(5)}(M_L)p_L + P^{-}_{(5)}(M_R))p_R + p_u$$

$$\alpha = \tfrac{3}{16}(-4 + 5f_a^2) \in \left[-\tfrac{3}{4};\ \tfrac{3}{16}\right] \tag{C.9}$$

$$p_u = -K_u f_a P^{+}_{(5)}(M_L)P^{-}_{(5)}(M_R)(\rho_L + \rho_R)a_{1/2}(u_{n,R} - u_{n,L})$$

C.2 Jacobian Matrix

C.2.1 Modified AUSM$^+$

Full analytical Jacobian formulation:

$$\left(\frac{\partial \mathbf{f}}{\partial \mathbf{P_{L/R}}}\right) = \begin{pmatrix} \frac{\partial f_\rho}{\partial \rho_{L/R}} & \frac{\partial f_\rho}{\partial u_{L/R}} & \frac{\partial f_\rho}{\partial v_{L/R}} & \frac{\partial f_\rho}{\partial w_{L/R}} & \frac{\partial f_\rho}{\partial p_{L/R}} \\ \frac{\partial f_u}{\partial \rho_{L/R}} & \frac{\partial f_u}{\partial u_{L/R}} & \frac{\partial f_u}{\partial v_{L/R}} & \frac{\partial f_u}{\partial w_{L/R}} & \frac{\partial f_u}{\partial p_{L/R}} \\ \frac{\partial f_v}{\partial \rho_{L/R}} & \frac{\partial f_v}{\partial u_{L/R}} & \frac{\partial f_v}{\partial v_{L/R}} & \frac{\partial f_v}{\partial w_{L/R}} & \frac{\partial f_v}{\partial p_{L/R}} \\ \frac{\partial f_w}{\partial \rho_{L/R}} & \frac{\partial f_w}{\partial u_{L/R}} & \frac{\partial f_w}{\partial v_{L/R}} & \frac{\partial f_w}{\partial w_{L/R}} & \frac{\partial f_w}{\partial p_{L/R}} \\ \frac{\partial f_H}{\partial \rho_{L/R}} & \frac{\partial f_H}{\partial u_{L/R}} & \frac{\partial f_H}{\partial v_{L/R}} & \frac{\partial f_H}{\partial w_{L/R}} & \frac{\partial f_H}{\partial p_{L/R}} \end{pmatrix}$$

$$\frac{\partial \mathbf{f}_P}{\partial P_{L/R}} = \frac{\partial \dot{m}_{1/2}}{\partial \mathbf{P}_{L/R}}\mathbf{\Psi} + \dot{m}_{1/2}\frac{\partial \mathbf{\Psi}}{\partial \mathbf{P}_{L/R}} + \frac{\partial \mathbf{p}_{1/2}}{\partial \mathbf{P}_{L/R}} \tag{C.10}$$

$$\frac{\partial \mathbf{\Psi}}{\partial P_{L/R}} = sig(\dot{m}_{1/2}, 0)\frac{\partial \mathbf{\Psi}_L}{\partial \mathbf{P}_{L/R}} + [1 - sig(\dot{m}_{1/2}, 0)]\frac{\partial \mathbf{\Psi}_R}{\partial \mathbf{P}_{L/R}}$$

$$\frac{\partial \mathbf{\Psi}_L}{\partial \mathbf{P}_L} = \frac{\partial \mathbf{\Psi}_R}{\partial \mathbf{P}_R} = \begin{pmatrix} 0 & 0 & 0 & 0 & 0 \\ 0 & 1 & 0 & 0 & 0 \\ 0 & 0 & 1 & 0 & 0 \\ 0 & 0 & 0 & 1 & 0 \\ -\frac{\gamma}{\gamma-1}\frac{p}{\rho^2} & u & v & w & \frac{\gamma}{\gamma-1}\frac{1}{\rho} \end{pmatrix};\quad \frac{\partial \mathbf{\Psi}_L}{\partial \mathbf{P}_R} = \frac{\partial \mathbf{\Psi}_R}{\partial \mathbf{P}_L} = 0$$

derivative of the interface mass flux:

$$\frac{\partial \dot{m}_{1/2}}{\partial \mathbf{P}_{L/R}} = \frac{\partial a_{1/2}}{\partial \mathbf{P}_{L/R}}M_{1/2}\rho + a_{1/2}\frac{\partial M_{1/2}}{\partial \mathbf{P}_{L/R}}\rho + a_{1/2}M_{1/2}\frac{\partial \rho}{\partial \mathbf{P}_{L/R}}$$

$$\frac{\partial \rho}{\partial \mathbf{P}_{L/R}} = sig(M_{1/2}, 0)\frac{\partial \rho_L}{\partial \mathbf{P}_{L/R}} + [1 - sig(M_{1/2}, 0)]\frac{\partial \rho_R}{\partial \mathbf{P}_{L/R}} \tag{C.11}$$

$$\frac{\partial \rho_L}{\partial \mathbf{P}_L} = \frac{\partial \rho_R}{\partial \mathbf{P}_R} = \{1,\ 0,\ 0,\ 0,\ 0\};\quad \frac{\partial \rho_L}{\partial \mathbf{P}_R} = \frac{\partial \rho_R}{\partial \mathbf{P}_L} = 0$$

derivative of the pressure term:

$$\frac{\partial \mathbf{p}_{1/2}}{\partial \mathbf{P}_{L/R}} = \left\{0,\ \frac{\partial p_{1/2}}{\partial \mathbf{P}_{L/R}}n_x,\ \frac{\partial p_{1/2}}{\partial \mathbf{P}_{L/R}}n_y,\ \frac{\partial p_{1/2}}{\partial \mathbf{P}_{L/R}}n_z,\ 0\right\}^T \tag{C.12}$$

derivative of the interface speed of sound:

$$\frac{\partial a_{_{1/2}}}{\partial \mathbf{P}_{_{L/R}}} = \quad (1 - sig(\widehat{a}_{_L}, \widehat{a}_{_R})) \left(\frac{2a^*_{_L}}{\widehat{a}(a^*_{_L}, u_{_{n,L}})} \frac{\partial a^*_{_L}}{\partial \mathbf{P}_{_{L/R}}} - \frac{a^{*2}_{_L}}{\widehat{a}^2(a^*_{_L}, u_{_{n,L}})} \frac{\partial \widehat{a}(a^*_{_L}, u_{_{n,L}})}{\partial \mathbf{P}_{_{L/R}}} \right)$$

$$+ sig(\widehat{a}_{_L}, \widehat{a}_{_R}) \left(\frac{2a^*_{_R}}{\widehat{a}(a^*_{_R}, -u_{_{n,R}})} \frac{\partial a^*_{_R}}{\partial \mathbf{P}_{_{L/R}}} - \frac{a^{*2}_{_R}}{\widehat{a}^2(a^*_{_R}, -u_{_{n,R}})} \frac{\partial \widehat{a}(a^*_{_R}, -u_{_{n,R}})}{\partial \mathbf{P}_{_{L/R}}} \right)$$

$$\frac{\partial a^*_{_{L/R}}}{\partial \mathbf{P}_{_{L/R}}} = \frac{\gamma - 1}{a^*_{_{L/R}}(\gamma+1)} \left\{ -\frac{\gamma}{\gamma-1} \frac{p_{_{L/R}}}{\rho^2_{_{L/R}}},\ u_{_{L/R}},\ v_{_{L/R}},\ w_{_{L/R}},\ \frac{\gamma}{\gamma-1} \frac{1}{\rho_{_{L/R}}} \right\}; \quad \frac{\partial a^*_{_L}}{\partial \mathbf{P}_{_R}} = \frac{\partial a^*_{_R}}{\partial \mathbf{P}_{_L}} = 0 \tag{C.13}$$

$$\frac{\partial u_{_{n,L}}}{\partial \mathbf{P}_{_L}} = \frac{\partial u_{_{n,R}}}{\partial \mathbf{P}_{_R}} = \{0,\ n_x,\ n_y,\ n_z,\ 0\}; \quad \frac{\partial u_{_{n,L}}}{\partial \mathbf{P}_{_R}} = \frac{\partial u_{_{n,R}}}{\partial \mathbf{P}_{_L}} = 0$$

$$\frac{\partial \widehat{a}(x,y)}{\partial \mathbf{P}_{_{L/R}}} = sig(x,y) \frac{\partial x}{\partial \mathbf{P}_{_{L/R}}} + (1 - sig(x,y)) \frac{\partial y}{\partial \mathbf{P}_{_{L/R}}}$$

derivatives of the interface Mach number:

$$\frac{\partial M_{_{1/2}}}{\partial \mathbf{P}_{_{L/R}}} = \frac{\partial M^+_{_{(4)}}(M_{_L})}{\partial \mathbf{P}_{_{L/R}}} + \frac{\partial M^-_{_{(4)}}(M_{_R})}{\partial \mathbf{P}_{_{L/R}}}$$

$$\frac{\partial M^{\pm}_{_{(4)}}(M)}{\partial \mathbf{P}_{_{L/R}}} = \begin{cases} \frac{1}{2} \left(\frac{\partial M}{\partial \mathbf{P}_{_{L/R}}} \pm \frac{\partial M}{\partial \mathbf{P}_{_{L/R}}} \right) & \text{if } M \geq 1 \\ \frac{1}{2}(\pm 8\beta M^3 \mp (8\beta - 1)M + 1) \frac{\partial M}{\partial \mathbf{P}_{_{L/R}}} & \text{if } -1 \geq M \leq 1 \\ \frac{1}{2} \left(\frac{\partial M}{\partial \mathbf{P}_{_{L/R}}} \mp \frac{\partial M}{\partial \mathbf{P}_{_{L/R}}} \right) & \text{if } M \leq -1 \end{cases} \tag{C.14}$$

derivative of the left and right state Mach numbers:

$$\frac{\partial M_{_L}}{\partial \mathbf{P}_{_L}} = \frac{1}{a_{_{1/2}}} \frac{\partial u_{_{n,L}}}{\partial \mathbf{P}_{_L}} - \frac{u_{_{n,L}}}{a^2_{_{1/2}}} \frac{\partial a_{_{1/2}}}{\partial \mathbf{P}_{_L}}$$

$$\frac{\partial M_{_L}}{\partial \mathbf{P}_{_R}} = -\frac{u_{_{n,L}}}{a^2_{_{1/2}}} \frac{\partial a_{_{1/2}}}{\partial \mathbf{P}_{_R}}$$

$$\frac{\partial M_{_R}}{\partial \mathbf{P}_{_R}} = \frac{1}{a_{_{1/2}}} \frac{\partial u_{_{n,R}}}{\partial \mathbf{P}_{_R}} - \frac{u_{_{n,R}}}{a^2_{_{1/2}}} \frac{\partial a_{_{1/2}}}{\partial \mathbf{P}_{_R}} \tag{C.15}$$

$$\frac{\partial M_{_R}}{\partial \mathbf{P}_{_L}} = -\frac{u_{_{n,R}}}{a^2_{_{1/2}}} \frac{\partial a_{_{1/2}}}{\partial \mathbf{P}_{_L}}$$

derivative of the interface pressure formula:

$$\frac{\partial p_{_{1/2}}}{\partial \mathbf{P}_{_{L/R}}} = \frac{\partial P^+_{_{(5)}}(M_{_L})}{\partial \mathbf{P}_{_{L/R}}} p_{_L} + \frac{\partial P^-_{_{(5)}}(M_{_R})}{\partial \mathbf{P}_{_{L/R}}} p_{_R} + P^+_{_{(5)}}(M_{_L}) \frac{\partial p_{_L}}{\partial \mathbf{P}_{_{L/R}}} + P^-_{_{(5)}}(M_{_R}) \frac{\partial p_{_R}}{\partial \mathbf{P}_{_{L/R}}}$$

$$\frac{\partial p_{_L}}{\partial \mathbf{P}_{_L}} = \frac{\partial p_{_R}}{\partial \mathbf{P}_{_R}} = \{0,\ 0,\ 0,\ 0,\ 1\} \quad \frac{\partial p_{_L}}{\partial \mathbf{P}_{_R}} = \frac{\partial p_{_R}}{\partial \mathbf{P}_{_L}} = 0 \tag{C.16}$$

$$\frac{\partial P^{\pm}_{_{(5)}}(M)}{\partial \mathbf{P}_{_{L/R}}} = \begin{cases} 0 & \text{if } |M| \geq 1 \\ \frac{1}{2} \left(\pm 10\alpha M^4 \mp (\frac{3}{2} + 12\alpha) M^2 \pm (\frac{3}{2} + 2\alpha) \right) \frac{\partial M}{\partial \mathbf{P}_{_{L/R}}} & \text{otherwise} \end{cases}$$

C.2.2 Modified AUSM$^+$up

Derivative of the interface Mach number with the pressure diffusion term:

$$\begin{aligned}\frac{\partial M_{1/2}}{\partial \mathbf{P}_{L/R}} &= \frac{\partial M^+_{(4)}(M_L)}{\partial \mathbf{P}_{L/R}} + \frac{\partial M^-_{(4)}(M_R)}{\partial \mathbf{P}_{L/R}} + \frac{\partial M_p}{\partial \mathbf{P}_{L/R}} \\ \frac{\partial M_p}{\partial \mathbf{P}_{L/R}} &= \frac{\partial}{\partial \mathbf{P}_{L/R}}\left(-\frac{K_p}{f_a} sig(1-\sigma \bar{M}^2, 0)\frac{p_R - p_L}{a_{1/2}(\rho_L+\rho_R)}\right)\end{aligned} \tag{C.17}$$

derivative of the scaling factor f_a for $M_\infty < 1$:

$$\begin{aligned}\frac{\partial f_a}{\partial \mathbf{P}_{L/R}} &= f(\bar{M}, M_\infty)\left(M_L \frac{\partial M_L}{\partial \mathbf{P}_{L/R}} + M_R \frac{\partial M_R}{\partial \mathbf{P}_{L/R}}\right) \\ f(\bar{M}, M_\infty) &\begin{cases} 0 & \text{if } \bar{M}^2 > 1 \\ sig(\bar{M}^2, M_\infty^2)\frac{1-\bar{M}}{\bar{M}} & \text{otherwise} \end{cases}\end{aligned} \tag{C.18}$$

derivative of the interface pressure formula with the velocity diffusion term:

$$\begin{aligned}\frac{\partial p_{1/2}}{\partial \mathbf{P}_{L/R}} &= \frac{\partial P^+_{(5)}(M_L)}{\partial \mathbf{P}_{L/R}} p_L + \frac{\partial P^-_{(5)}(M_R)}{\partial \mathbf{P}_{L/R}} p_R + P^+_{(5)}(M_L)\frac{\partial p_L}{\partial \mathbf{P}_{L/R}} + P^-_{(5)}(M_R)\frac{\partial p_R}{\partial \mathbf{P}_{L/R}} + \frac{\partial p_u}{\partial \mathbf{P}_{L/R}} \\ \frac{\partial p_u}{\partial \mathbf{P}_{L/R}} &= \frac{\partial}{\partial \mathbf{P}_{L/R}}\left(-K_u f_a P^+_{(5)}(M_L) P^-_{(5)}(M_R)(\rho_L+\rho_R) a_{1/2}(u_{n,R} - u_{n,L})\right) \\ \frac{\partial P^\pm_{(5)}(M)}{\partial \mathbf{P}_{L/R}} &= \left(\frac{\partial P^\pm_{(5)}(M)}{\partial \mathbf{P}_{L/R}}\right)_{\text{AUSM}^+} + \begin{cases} 0 & \text{if } |M_{L/R}| \geq 1 \\ \pm M(M^2-1)^2 \frac{\partial \alpha}{\partial \mathbf{P}_{L/R}} & \text{otherwise} \end{cases} \\ \frac{\partial \alpha}{\partial \mathbf{P}_{L/R}} &= \tfrac{15}{8} f_a \frac{\partial f_a}{\partial \mathbf{P}_{L/R}}\end{aligned} \tag{C.19}$$

Appendix D

Non-dimensional ES Model with Rotational Degrees of Freedom

In [29], a polyatomic ES model is presented, where a parameter K_{int} is introduced to define the number of internal degrees of freedom. For a diatomic molecule without vibrational excitation, two rotational degrees of freedom are present, i.e. $K_{int} = 2$. Considering the non-dimensional variables defined in equations (4.3) the latter model can be written as

$$\frac{\partial F_0}{\partial t} + \mathbf{c}\frac{\partial F_0}{\partial \mathbf{x}} = \frac{F_0^{ES} - F_0}{\tau\big(1-\nu+\theta\nu\big)} \quad ; \quad \frac{\partial F_1}{\partial t} + \mathbf{c}\frac{\partial F_1}{\partial \mathbf{x}} = \frac{F_1^{ES} - F_1}{\tau\big(1-\nu+\theta\nu\big)} \tag{D.1}$$

where the equilibrium function is an anisotropic Gaussian

$$F_0^{ES} = \frac{\rho}{\sqrt{det(\pi\mathbf{\Lambda})}} \exp\left(-\mathbf{c}' \cdot \mathbf{\Lambda}^{-1} \cdot \mathbf{c}'\right) \quad ; \quad F_1^{ES} = T_{rel} F_0. \tag{D.2}$$

The matrix $\mathbf{\Lambda}$ is defined as

$$\mathbf{\Lambda} = (1-\theta)\left((1-\nu)\, T_{tr}\mathbf{I} + \nu\mathbf{\Theta}\right) + \theta T_{eq}\mathbf{I} \quad ; \quad \rho\mathbf{\Theta} = \int_{-\infty}^{\infty} \mathbf{c}' \otimes \mathbf{c}' F_0 d\vec{u} \tag{D.3}$$

with $\rho\mathbf{\Theta}$ the opposite of the stress tensor and $0 < \theta < 1$ and $-1/2 \leq \nu < 1$ two relaxation parameters. The pressure is assumed to depend on the equilibrium temperature T, and furthermore a relaxation temperature is introduced to represent the thermodynamic non-equilibrium between the translational and internal degrees of freedom,

$$p = \rho T \quad ; \quad T_{rel} = \theta T + (1-\theta) T_{rot}. \tag{D.4}$$

The equivalent continuum state is given by

$$\begin{aligned} &\rho = \int_{-\infty}^{\infty} F_0 d\mathbf{c} \quad ; \quad \rho u_i = \int_{-\infty}^{\infty} c_i F_0 d\mathbf{c} \quad ; \quad \frac{3}{2}\rho T_t + \rho(u_x^2 + u_y^2 + u_z^2) = \int_{-\infty}^{+\infty} c^2 F_0 d\mathbf{c} \\ &\frac{5}{2}T = \frac{3}{2}T_t + T_r \quad ; \quad \rho T_r = \int_{-\infty}^{\infty} F_1 d\mathbf{c}. \end{aligned} \tag{D.5}$$

Appendix E

Moments of the Rykov Model Collision Term

With $\hat{\mathbf{\Psi}}_0 = (1,\ c_x,\ \mathbf{c}^2,\ 0)^T$ and $\hat{\mathbf{\Psi}}_1 = (0,\ 0,\ 1,\ 1)^T$ the moments of the Rykov model collision term result

$$\int_{-\infty}^{+\infty} \left[\hat{\mathbf{\Psi}}_0 \left(\frac{F_0^t - F_0}{\tau} + \frac{F_0^r - F_0^t}{Z_r \tau} \right) + \hat{\mathbf{\Psi}}_1 \left(\frac{F_1^t - F_1}{\tau} + \frac{F_1^r - F_1^t}{Z_r \tau} \right) \right] d\mathbf{c} = \begin{pmatrix} 0 \\ 0 \\ 0 \\ \dfrac{\rho(T - T_r)}{Z_r \tau} \end{pmatrix}. \tag{E.1}$$

Indeed

$$\begin{aligned} \int_{-\infty}^{+\infty} \hat{\mathbf{\Psi}}_0 \frac{F_0^t - F_0}{\tau} &= (0,\ 0,\ 0,\ 0)^T \\ \int_{-\infty}^{+\infty} \hat{\mathbf{\Psi}}_0 \frac{F_0^r - F_0^t}{Z_r \tau} &= \left(0,\ 0,\ \frac{3}{2} \frac{\rho(T - T_t)}{Z_r \tau},\ 0 \right)^T \end{aligned} \tag{E.2}$$

and

$$\begin{aligned} \int_{-\infty}^{+\infty} \hat{\mathbf{\Psi}}_1 \frac{F_1^t - F_1}{\tau} &= (0,\ 0,\ 0,\ 0)^T \\ \int_{-\infty}^{+\infty} \hat{\mathbf{\Psi}}_1 \frac{F_1^r - F_1^t}{Z_r \tau} &= \left(0,\ 0,\ \frac{\rho(T - T_r)}{Z_r \tau},\ \frac{\rho(T - T_r)}{Z_r \tau} \right)^T \end{aligned} \tag{E.3}$$

from which, remembering the relation between T, T_t and T_r defined in equations (4.19), it is straightforward to find equations (E.1)

Appendix F

Collision Numbers

For a gas in thermal non-equilibrium, energy is transferred between the various internal modes and the internal energy distributions are driven towards their respective equilibrium state by means of particle collisions; however, not all the modes are involved in every collision. The collision number Z associated to a mode is defined as the inverse of the particle collisions fraction involving it and generally [152]

$$Z_{translation} < Z_{rotation} < Z_{vibration} \tag{F.1}$$

therefore, the number of collisions required for the vibrational mode to reach the equilibrium is greater than the one required for the rotational energy which in turn is higher than the one associated with the translational mode. This implies that the time required for the different modes to relax towards the equilibrium state is different. Indeed, if we define the collision times $\tau_{t,r,v}$ as usual in the literature

$$\tau_{t,r,v} = Z_{t,r,v}\tau \tag{F.2}$$

where τ is the mean time between collisions, from relation (F.1) it follows that

$$\tau_{translation} < \tau_{rotation} < \tau_{vibration}. \tag{F.3}$$

Appendix G

The Chapman-Enskog Solution of the Shakhov Model

Considering the non-dimensional variable (4.3) with the difference of employing the free stream mean-free-path λ_∞ as reference length, the Shakhov model (4.5) can be written as follows

$$\xi \left[\frac{\partial F}{\partial t} + \mathbf{c} \frac{\partial F}{\partial \mathbf{x}} \right] = \frac{F^S - F}{\tau} \tag{G.1}$$

where

$$\xi = \frac{\sqrt{2RT_\infty}\mu}{\lambda_\infty p_\infty}. \tag{G.2}$$

Note that the non-dimensional variables (4.3) are chosen to give $\xi = 1$ so that the unit length in the computational grid is approximately the free stream mean path. The parameter ξ is a measure of the degree of departure from the local thermodynamic equilibrium and when it is sufficiently small the flow is collision dominated [11]. The CE method employs a series expansion of the distribution function F. For mall values of ξ, i.e. near the continuum regime, the CE expansion can be truncated after the first order terms as follow

$$F = F^{(0)} \left(1 + \xi \phi\right) \tag{G.3}$$

where $F^{(0)}$ is the solution of the zeroth order approximation, i.e. $\circ(\xi^0)$, of the model equation. Introducing the CE expansion (G.3) in the Shakhov model (4.5) we obtain

$$\begin{aligned} \xi \left[\frac{\partial F^{(0)}}{\partial t} + \mathbf{c} \frac{\partial F^{(0)}}{\partial \mathbf{x}} \right] + \xi^2 \left[\frac{\partial \left(F^{(0)} \phi_S \right)}{\partial t} + \mathbf{c} \frac{\partial \left(F^{(0)} \phi_S \right)}{\partial \mathbf{x}} \right] = & \quad \frac{F_M(T) - F^{(0)}}{\tau} + \\ & + \frac{\xi}{\tau} F_M(T) \phi_S - \frac{\xi}{\tau} F_M(T) \phi \end{aligned} \tag{G.4}$$

where it has been considered

$$F_S = F_M(T)\left(1+\xi\phi_S\right) = F_M(T)\left[1+\xi\frac{8}{15}\frac{q_i}{p}\frac{c'_i}{T}\left(\frac{\mathbf{c}'^2}{T}-\frac{5}{2}\right)\right] \tag{G.5}$$

since from the CE solution of the BGK model [11] we know

$$\hat{q}_i \propto R^2\hat{\rho}\hat{T}^2\hat{\tau}\frac{\partial\hat{T}}{\partial\hat{x}_i} \tag{G.6}$$

which, with the non-dimensional variables (4.3) and employing λ_∞ as reference length, leads to

$$\hat{q}_i \propto \rho_\infty\left(2RT_\infty\right)^{3/2}\xi q_i. \tag{G.7}$$

Neglecting all terms of order $\circ(\xi)$ and $\circ(\xi^2)$ in equation (G.4) we have the zeroth order approximation $F^{(0)} = F_M(T)$. Considering this and retaining only terms up the first order, equation (G.4) becomes

$$\xi\left[\frac{\partial F^{(0)}}{\partial t}+\mathbf{c}\frac{\partial F^{(0)}}{\partial\mathbf{x}}\right] = -\frac{\xi}{\tau}F_M(T)\left[\phi-\phi_S\right] \tag{G.8}$$

from which

$$F_M(T)\xi\phi = F_M(T)\xi\phi_S - \xi\tau\left[\frac{\partial F_M(T)}{\partial t}+\mathbf{c}\frac{\partial F_M(T)}{\partial\mathbf{x}}\right] \tag{G.9}$$

thus, the first order CE solution of the Shakhov model (4.5) results

$$F = F_M(T)\left(1+\xi\phi\right) = F_S - \xi\tau\left[\frac{\partial F_M(T)}{\partial t}+\mathbf{c}\frac{\partial F_M(T)}{\partial\mathbf{x}}\right]. \tag{G.10}$$

Employing the CE solution (G.10) it is possible to demonstrate that the Shakhov model (4.5) recovers the correct monoatomic Prandtl number, i.e. $Pr = 2/3$, in the continuum limit. In fact, from the CE solution of the BGK model [11] we know that

$$\begin{aligned}\xi\left[\frac{\partial F_M(T)}{\partial t}+\mathbf{c}\frac{\partial F_M(T)}{\partial\mathbf{x}}\right] &= -\frac{\xi}{\tau}F_M(T)\phi_{BGK} = \\ &= \frac{\xi}{\tau}F_M(T)\tau\left[c'_i\left(\frac{c'^2}{T}-\frac{5}{2}\right)\frac{\partial T}{\partial x_i}+\frac{1}{T}\left(c'_ic'_j-\frac{2}{3}c'^2\delta_{ij}\right)\frac{\partial u_i}{\partial x_j}\right]\end{aligned} \tag{G.11}$$

thus, using the CE solution (G.10) to obtain the continuum stress tensor

$$\begin{aligned}\tau_{ij} &= -2\left[\int c'_ic'_jF_M(T)d\mathbf{c} - \left(\int c'_ic'_jF_M(T)\xi\phi_{BGK}d\mathbf{c}-\tfrac{p}{2}\delta_{ij}\right) - \int c'_ic'_jF_M(T)\xi\phi^S d\mathbf{c}\right] = \\ &= 0+\xi\rho T\tau\left[\frac{\partial u_i}{\partial x_j}+\frac{\partial u_j}{\partial x_i}-\frac{2}{3}\frac{\partial u_l}{\partial x_l}\delta_{ij}\right]+0;\end{aligned} \tag{G.12}$$

and the heat flux vector

$$\begin{aligned} q_i &= \int \frac{c'_i c'^2}{2} F_M(T) d\mathbf{c} + \int \frac{c'_i c'^2}{2} F_M(T) \xi \phi_{BGK} d\mathbf{c} + \int \frac{c'_i c'^2}{2} F_M(T) \xi \phi^S d\mathbf{c} = \\ &= 0 - \xi \frac{5}{8} \rho T \tau \frac{\partial T}{\partial x_i} + \frac{1}{3} q_i = -\xi \frac{15}{16} \rho T \tau \frac{\partial T}{\partial x_i}; \end{aligned} \tag{G.13}$$

and returning to the dimensional form we find $Pr = c_p \mu / k = 2/3$, known that $c_p = 5/2R$ for monoatomic gases.

Appendix H

The Chapman-Enskog Solution of the Rykov Model

Considering the non-dimensional variable (4.3) with the the free stream mean-free-path λ_∞ employed as reference length, the Rykov model (4.10) can be written as follow

$$\xi\left[\frac{\partial F_0}{\partial t}+\mathbf{c}\frac{\partial F_0}{\partial \mathbf{x}}\right]=\frac{F_0^{eq}-F}{\tau}\quad;\quad\xi\left[\frac{\partial F_1}{\partial t}+\mathbf{c}\frac{\partial F_1}{\partial \mathbf{x}}\right]=\frac{F_1^{eq}-F}{\tau} \tag{H.1}$$

with the ξ as defined in equation (G.2). We consider the CE expansions of the two distribution functions F_0 and F_1 truncated after the first order terms for small values of ξ typical of near continuum conditions

$$F_0=F_0^{(0)}\left(1+\xi\phi_0\right)\quad;\quad F_1=F_1^{(0)}\left(1+\xi\phi_1\right) \tag{H.2}$$

where $F_0^{(0)}$ and $F_1^{(0)}$ are the solutions of the zeroth order approximations of the model equations. Substituting expansions (H.2) in the respective Rykov model equations (4.10) we obtain

$$\begin{aligned}\xi\left[\frac{\partial F_0^{(0)}}{\partial t}+\mathbf{c}\frac{\partial F_0^{(0)}}{\partial \mathbf{x}}\right]+\xi^2\left[\frac{\partial\left(F_0^{(0)}\phi_0^R\right)}{\partial t}+\mathbf{c}\frac{\partial\left(F_0^{(0)}\phi_0^R\right)}{\partial \mathbf{x}}\right]= &\ \frac{1}{\tau}\left[F_M(T_t)-F_0^{(0)}\right]+\\ &+\frac{F_M(T)-F_M(T_t)}{Z_r\tau}+\\ &+\frac{\xi}{\tau}F_M(T_t)\phi_0^R(T_t)-\frac{\xi}{\tau}F_0^{(0)}\phi_0+\\ &+\tfrac{\xi}{\tau}\left[\frac{F_M(T)\omega_0\phi_0^R(T)-F_M(T_t)\phi_0^R(T_t)}{Z_r}\right]\end{aligned} \tag{H.3}$$

$$\xi\left[\frac{\partial F_1^{(0)}}{\partial t}+\mathbf{c}\frac{\partial F_1^{(0)}}{\partial \mathbf{x}}\right]+\xi^2\left[\frac{\partial\left(F_1^{(0)}\phi_1^R\right)}{\partial t}+\mathbf{c}\frac{\partial\left(F_1^{(0)}\phi_1^R\right)}{\partial \mathbf{x}}\right]= \frac{1}{\tau}\left[T_rF_M(T_t)-F_1^{(0)}\right]+$$
$$+\frac{TF_M(T)-T_rF_M(T_t)}{Z_r\tau}+$$
$$+\frac{\xi}{\tau}TrF_M(T_t)\left(\phi_0^R(T_t)+\phi_1^R(T_t,T_r)\right)-\frac{\xi}{\tau}F_1^{(0)}\phi_1+$$
$$+\frac{\xi}{\tau}\left[\frac{TF_M(T)\left(\omega_0\phi_0^R(T)+\omega_1\phi_1^R(T,T)\right)-T_rF_M(T_t)\left(\phi_0^R(T_t)+\phi_1^R(T_t,T_r)\right)}{Z_r}\right] \tag{H.4}$$

where it has been considered

$$F_0^{eq}= F_M(T_t)+\frac{F_M(T)-F_M(T_t)}{Z_r}+\xi\left[F_M(T_t)\phi_0^R(T_t)+\frac{F_M(T)\omega_0\phi_0^R(T)-F_M(T_t)\phi_0^R(T_t)}{Z_r}\right]$$

$$F_1^{eq}= T_rF_M(T_t)+\frac{TF_M(T)-T_rF_M(T_t)}{Z_r}+\xi\left[T_rF_M(T_t)\left(\phi_0^R(T_t)+\phi_1^R(T_t,T_r)\right)\right]+ \tag{H.5}$$
$$+\xi\frac{TF_M(T)\left(\omega_0\phi_0^R(T)+\omega_1\phi_1^R(T,T)\right)-T_rF_M(T_t)\left(\phi_0^R(T_t)+\phi_1^R(T_t,T_r)\right)}{Z_r}$$

with

$$\xi\phi_0^R(T_1)=\xi\frac{8}{15}\frac{q_i^t c'_i}{\rho T_1^2}\left(\frac{\mathbf{c}'^2}{T_1}-\frac{5}{2}\right)\quad;\quad \xi\phi_1^R(T_1,T_2)=\xi 4(1-\delta)\frac{q_i^r c'_i}{\rho T_1 T_2} \tag{H.6}$$

thanks to relation (G.7). Gathering, for each of equations (H.3) and (H.4), all terms of order $\circ(\xi^0)$ we can obtain the zeroth order approximations for the CE expansions (H.2) as

$$F_0^{(0)}=F_M(T_t)\quad;\quad F_1^{(0)}=T_rF_M(T_t) \tag{H.7}$$

knowing that it is possible to demonstrate [205]

$$\frac{F_M(T)-F_M(T_t)}{Z_r}\sim\circ(\xi)\quad;\quad\frac{TF_M(T)-T_rF_M(T_t)}{Z_r}\sim\circ(\xi). \tag{H.8}$$

Considering expressions (H.7) and neglecting second order terms, equations (H.3) and (H.4) become

$$\xi\left[\frac{\partial F_M(T_t)}{\partial t}+\mathbf{c}\frac{\partial F_M(T_t)}{\partial \mathbf{x}}\right]= \frac{F_M(T)-F_M(T_t)}{Z_r\tau}+$$
$$+\frac{\xi}{\tau}F_M(T_t)\phi_0^R(T_t)-\frac{\xi}{\tau}F_0^{(0)}\phi_0+ \tag{H.9}$$
$$+\frac{\xi}{\tau}\left[\frac{F_M(T)\omega_0\phi_0^R(T)-F_M(T_t)\phi_0^R(T_t)}{Z_r}\right]$$

$$\xi\left[\frac{\partial\left(T_rF_M(T_t)\right)}{\partial t}+\mathbf{c}\frac{\partial\left(T_rF_M(T_t)\right)}{\partial\mathbf{x}}\right]= \frac{TF_M(T)-T_rF_M(T_t)}{Z_r\tau}$$

$$+\frac{\xi}{\tau}TrF_M(T_t)\left(\phi_0^R(T_t)+\phi_1^R(T_t,T_r)\right)-\frac{\xi}{\tau}F_1^{(0)}\phi_1+ \tag{H.10}$$

$$+\tfrac{\xi}{\tau}\left[\frac{TF_M(T)\left(\omega_0\phi_0^R(T)+\omega_1\phi_1^R(T,T)\right)-T_rF_M(T_t)\left(\phi_0^R(T_t)+\phi_1^R(T_t,T_r)\right)}{Z_r}\right]$$

from which

$$\begin{aligned}
F_M(T_t)\xi\phi_0 = \quad & \frac{F_M(T)-F_M(T_t)}{Z_r}+\xi F_M(T_t)\phi_0^R(T_t)+\xi\left[\frac{F_M(T)\omega_0\phi_0^R(T)-F_M(T_t)\phi_0^R(T_t)}{Z_r}\right]+\\
& -\xi\tau\left[\frac{\partial F_M(T_t)}{\partial t}+\mathbf{c}\frac{\partial F_M(T_t)}{\partial\mathbf{x}}\right]\\
T_rF_M(T_t)\xi\phi_1 = \quad & \frac{TF_M(T)-T_rF_M(T_t)}{Z_r}+\xi TrF_M(T_t)\left(\phi_0^R(T_t)+\phi_1^R(T_t,T_r)\right)+\\
& +\xi\left[\frac{TF_M(T)\left(\omega_0\phi_0^R(T)+\omega_1\phi_1^R(T,T)\right)-T_rF_M(T_t)\left(\phi_0^R(T_t)+\phi_1^R(T_t,T_r)\right)}{Z_r}\right]+\\
& -\xi\tau\left[\frac{\partial\left(T_rF_M(T_t)\right)}{\partial t}+\mathbf{c}\frac{\partial\left(T_rF_M(T_t)\right)}{\partial\mathbf{x}}\right].
\end{aligned} \tag{H.11}$$

Thus, the CE solutions of the Rykov model equations (4.10) are

$$\begin{aligned}
F_0 &= F_0^{(0)}\left(1+\xi\phi_0\right)=F_0^{eq}-\xi\tau\left[\frac{\partial F_M(T_t)}{\partial t}+\mathbf{c}\frac{\partial F_M(T_t)}{\partial\mathbf{x}}\right]\\
F_1 &= F_1^{(0)}\left(1+\xi\phi_1\right)=F_1^{eq}-\xi\tau\left[\frac{\partial\left(T_rF_M(T_t)\right)}{\partial t}+\mathbf{c}\frac{\partial\left(T_rF_M(T_t)\right)}{\partial\mathbf{x}}\right].
\end{aligned} \tag{H.12}$$

Using the CE solutions (H.12) in the limit $T=T_t=T_r$ [1] and considering equation (G.11), it is possible to obtain the continuum stress tensor

$$\begin{aligned}
\tau_{ij} &= -2\left[\int c'_ic'_jF_M(T)d\mathbf{c}-\left(\int c'_ic'_jF_M(T)\xi\phi_{BGK}d\mathbf{c}-\tfrac{p}{2}\delta_{ij}\right)-\tfrac{\omega_0+Z-1}{Z}\int c'_ic'_jF_M(T)\xi\phi_0^Rd\mathbf{c}\right]=\\
&= 0+\xi\rho T\tau\left[\frac{\partial u_i}{\partial x_j}+\frac{\partial u_j}{\partial x_i}-\tfrac{2}{3}\frac{\partial u_l}{\partial x_l}\delta_{ij}\right]+0;
\end{aligned} \tag{H.13}$$

translational heat flux vector

$$\begin{aligned}
q_i^t &= \int\tfrac{c'_ic'^2}{2}F_M(T)d\mathbf{c}+\int\tfrac{c'_ic'^2}{2}F_M(T)\xi\phi_{BGK}d\mathbf{c}+\tfrac{\omega_0+Z-1}{Z}\int\tfrac{c'_ic'^2}{F}_M(T)\xi\phi_0^Rd\mathbf{c}=\\
&= 0-\xi\tfrac{5}{8}\rho T\tau\frac{\partial T}{\partial x_i}+\tfrac{\omega_0+Z-1}{3Z}q_i^t=-\xi\tfrac{15}{16}\rho T\tau\left(1+\tfrac{1-\omega_0}{2Z}\right)^{-1}\frac{\partial T}{\partial x_i};
\end{aligned} \tag{H.14}$$

[1] Note that, as shown in [7], the model equations obtained in the continuum limit with $T_t\neq T_r$ present relaxation terms between translational and rotational energy corresponding to the bulk viscosity terms in the standard NS equations.

rotational heat flux vector

$$\begin{aligned} q_i^r = & \int \tfrac{c'}{2} F_M(T) d\mathbf{c} + \int \tfrac{c'}{2} F_M(T) \xi \phi_{BGK} d\mathbf{c} + \int \tfrac{c'}{2} F_M(T) \xi \left[c'_i \frac{\partial T}{\partial x_i} + \tfrac{2}{3} T \frac{\partial u_i}{\partial x_i} \right] d\mathbf{c} + \\ & + \tfrac{\omega_0 + Z - 1}{Z} \int c'^2 F_M(T) \xi \phi_0^R d\mathbf{c} + \tfrac{\omega_1 + Z - 1}{Z} \int c'^2 F_M(T) \xi \phi_1^R d\mathbf{c} = \\ = & \; 0 + 0 - \xi \tfrac{1}{4} \rho T \tau \frac{\partial T}{\partial x_i} + 0 + \tfrac{\omega_1 + Z - 1}{Z} (1 - \delta) q_i^r = -\xi \tfrac{1}{4} \rho T \tau \left(\delta + \tfrac{(1-\delta)(1-\omega_1)}{Z} \right)^{-1} \frac{\partial T}{\partial x_i} \end{aligned} \tag{H.15}$$

and total heat flux

$$q_i = -\xi \frac{1}{4} \rho T \tau \left[\frac{15}{4} \left(1 + \frac{1 - \omega_0}{2Z} \right)^{-1} + \left(\delta + \frac{(1-\delta)(1-\omega_1)}{Z} \right)^{-1} \right] \frac{\partial T}{\partial x_i} \tag{H.16}$$

Finally, after returning to the dimensional form it is possible to evaluate the Prandtl number $Pr = c_p \mu / k$ that the Rykov model recover in the continuum limit

$$Pr = \frac{7}{5} \left[\frac{3}{2} \left(1 + \frac{1 - \omega_0}{2Z} \right)^{-1} + \frac{2}{5} \left(\delta + \frac{(1-\delta)(1-\omega_1)}{Z} \right)^{-1} \right]^{-1} \tag{H.17}$$

considering that $c_p = 7/2R$ for diatomic gases when the rotational degrees of freedom are in non-equilibrium. Figure H.1 shows the variation of the Prandtl number with the collision number Z_r for the

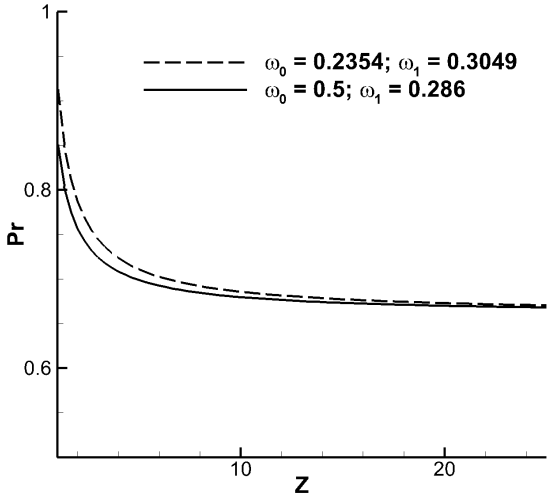

Figure H.1: Rykov Model Prandtl number in the continuum regime limit.

values of ω_0 and ω_1 cited in section 4.4. As expected for $Z \to \infty$ the model reduces to the Shakhov model and $Pr = 2/3$ is obtained while the diatomic Prandtl number of 5/7 is obtained, as expected, for $Z = 3 - 5$ that are usual values of the collision number at standard conditions.

Appendix I

The S-GKS as a Limit of the S-UGKS for a Well-resolved Flow

In [46] equation (5.10) is employed to derive the time dependant distribution function solution of the Shakhov model. In this case

$$\begin{aligned} F_{eq} &= F_S = F_M(T) + F^+ \\ F^+ &= F_M(T)\frac{8}{15}\frac{q_i}{p}\frac{c'_i}{T}\left(\frac{\mathbf{c}'^2}{T} - \frac{5}{2}\right). \end{aligned} \tag{I.1}$$

The Maxwellian term in F_S can be expanded around the cell interface in series of Taylor as follow

$$F_M(T) = F_M^0(T)\left[1 + (1 - H(x))a^l x + H(x)a^r x + At\right] \tag{I.2}$$

where the terms of the expansion are defined as

$$\left(\frac{\partial F_M(T)}{\partial x}\right)^{l/r} = a^{l/r}F_M^0(T) \quad ; \quad \frac{\partial F_M(T)}{\partial t} = AF_M^0(T), \tag{I.3}$$

with $F_M^0(T)$ the Maxwellian distribution at the interface, and $H(x)$ is the Heaviside function

$$H(x) = \begin{cases} 0 & x < 0 \\ 1 & x \geq 0 \end{cases}. \tag{I.4}$$

Likewise, the initial distribution function can be reconstructed based on the CE solution (G.10) of the Shakhov model as

$$\begin{aligned} F^0 = &\left(F_S^l + F_M^l(T)\left[a^l x - \tau\left(a^l u + At\right)\right]\right)(1 - H(x)) + \\ &+ \left(F_S^r + F_M^r(T)\left[a^r x - \tau\left(a^r u + At\right)\right]\right)H(x). \end{aligned} \tag{I.5}$$

Now, introducing expressions (I.1), (I.2) and (I.5) in equation (5.10) and integrating we obtain

$$\begin{aligned} F(0,t,c_x|_m) = \quad & \left(1-\exp\left(-t/\tau\right)\right) F_S^0 + \\ & +\tau\left(-1+\exp\left(-t/\tau\right)\right)\left[(1-H(c_x|_m))a^l + H(c_x|_m)a^r\right] c_x|_m F_M^0(T) + \\ & +t\exp\left(-t/\tau\right)\left[(1-H(c_x|_m))a^l + H(c_x|_m)a^r\right] c_x|_m F_M^0(T) + \\ & +\tau\left(t/\tau - 1 + \exp\left(-t/\tau\right)\right) A F_M^0(T) + \\ & +\exp\left(-t/\tau\right)\left(F_S^l + F_M^l(T)\left[-a^l t c_x|_m - \tau a^l c_x|_m + At\right]\right)\left(1-H(c_x|_m)\right) \\ & +\exp\left(-t/\tau\right)\left(F_S^r + F_M^r(T)\left[-a^r t c_x|_m - \tau a^r c_x|_m + At\right]\right) H(c_x|_m). \end{aligned} \tag{I.6}$$

where $x_{i+1/2} = 0$ is considered for a simpler formulation. If we assume the hypothesis of a well-resolved flow

$$a^l = a^r \quad ; \quad F_S^l = F_S^r = F_S^0 \quad ; \quad F_M^l(T) = F_M^r(T) = F_M^0(T) \tag{I.7}$$

and consider definitions (I.3), equation (I.6) reduces to the simplified form in equation (5.15).

Appendix J

The R-GKS as a Limit of a UGKS based on the Rykov Model for a Well-resolved Flow

We will employ equation (5.10) to derive the time dependant distribution functions solutions of the Rykov model. In this case

$$
\begin{aligned}
F_1^{eq} &= F_M(T_t) + F_0^+ \\
F_2^{eq} &= T_R F_M(T_t) + F_1^+ \\
F_2^+ &= \frac{F_M(T) - F_M(T_t)}{Z_r} + \xi \left[F_M(T_t)\phi_0^R(T_t) + \frac{F_M(T)\omega_0\phi_0^R(T_t) - F_M(T_t)\phi_0^R(T_t)}{Z_r} \right] \\
F_1^+ = &\ \frac{TF_M(T) - T_r F_M(T_t)}{Z_r} + \xi \left[T_r F_M(T_t) \left(\phi_0^R(T_t) + \phi_1^R(T_t, T_r) \right) \right] + \\
&+\xi \frac{TF_M(T) \left(\omega_0\phi_0^R(T_t) + \omega_1\phi_1^R(T,T) \right) - T_r F_M(T_t) \left(\phi_0^R(T_t) + \phi_1^R(T_t, T_r) \right)}{Z_r}.
\end{aligned}
\tag{J.1}
$$

To be consistent with the CE solutions (H.12) only the Maxwellian terms, i.e. $\circ(\xi^0)$, in F_0^{eq} and F_1^{eq} are expanded around the cell interface in Taylor series

$$
\begin{aligned}
F_M(T_t) &= F_M^0(T_t) \left[1 + (1 - H(x))a^l x + H(x)a^r x + At \right] \\
T_r F_M(T_t) &= T_r F_M(T_t)|^0 \left[1 + (1 - H(x))b^l x + H(x)b^r x + Bt \right]
\end{aligned}
\tag{J.2}
$$

with $H(x)$ the Heaviside function defined in equation (I.4), $F_M^0(T_t)$ and $T_r F_M(T_t)|^0$ the Maxwellian distributions at the interface and the terms of the expansions defined as follow

$$\begin{aligned}
\left(\frac{\partial F_M(T_t)}{\partial x}\right)^{l/r} &= a^{l/r} F_M^0(T_t) \qquad ; \quad \frac{\partial F_M(T_t)}{\partial t} = A F_M^0(T_t) \\
\left(\frac{\partial \left(T_r F_M(T_t)\right)}{\partial x}\right)^{l/r} &= b^{l/r} T_r F_M(T_t)|^0 \quad ; \quad \frac{d\left(T_r F_M(T_t)\right)}{dt} = B T_r F_M(T_t)|^0.
\end{aligned} \tag{J.3}$$

Consistently, the initial distribution functions are reconstructed based on the CE solutions (H.12) of the Rykov as

$$\begin{aligned}
F_0^0 = \; & \left(F_0^{eq}|^l + F_M^l(T_t)\left[a^l x - \tau\left(a^l u + At\right)\right]\right)(1 - H(x)) + \\
& + \left(F_0^{eq}|^r + F_M^r(T_t)\left[a^r x - \tau\left(a^r u + At\right)\right]\right) H(x) \\
F_1^0 = \; & \left(F_1^{eq}|^l + T_r F_M(T_t)|^l\left[b^l x - \tau\left(b^l u + Bt\right)\right]\right)(1 - H(x)) + \\
& + \left(F_1^{eq}|^r + T_r F_M(T_t)|^r\left[a^r x - \tau\left(b^r u + Bt\right)\right]\right) H(x)
\end{aligned} \tag{J.4}$$

If we introduce expressions (J.1), (J.2) and (J.4) in equation (5.10), written for F_0 and F_1 at $x_{i+1/2} = 0$ to simplify the formulation, and integrating we obtain

$$\begin{aligned}
F_0(0,t,c_x|_m) = \; & \left(1 - \exp\left(-t/\tau\right)\right) F_0^{eq}|^0 + \\
& + \tau\left(-1 + \exp\left(-t/\tau\right)\right)\left[(1 - H(c_x|_m))a^l + H(c_x|_m)a^r\right] c_x|_m F_M^0(T_t) + \\
& + t\exp\left(-t/\tau\right)\left[(1 - H(c_x|_m))a^l + H(c_x|_m)a^r\right] c_x|_m F_M^0(T_t) + \\
& + \tau\left(t/\tau - 1 + \exp\left(-t/\tau\right)\right) A F_M^0(T_t) + \\
& + \exp\left(-t/\tau\right)\left(F_0^{eq}|^l + F_M^l(T_t)\left[-a^l t c_x|_m - \tau\left(a^l c_x|_m + At\right)\right]\right)(1 - H(c_x|_m)) \\
& + \exp\left(-t/\tau\right)\left(F_0^{eq}|^r + F_M^r(T_t)\left[-a^r t c_x|_m - \tau\left(a^r c_x|_m + At\right)\right]\right) H(c_x|_m)
\end{aligned} \tag{J.5}$$

$$\begin{aligned}
F_1(0,t,c_x|_m) = \; & \left(1 - \exp\left(-t/\tau\right)\right) F_1^{eq}|^0 + \\
& + \tau\left(-1 + \exp\left(-t/\tau\right)\right)\left[(1 - H(c_x|_m))b^l + H(c_x|_m)b^r\right] c_x|_m T_r F_M(T_t)|^0 + \\
& + t\exp\left(-t/\tau\right)\left[(1 - H(c_x|_m))b^l + H(c_x|_m)b^r\right] c_x|_m T_r F_M(T_t)|^0 + \\
& + \tau\left(t/\tau - 1 + \exp\left(-t/\tau\right)\right) B T_r F_M(T_t)|^0 + \\
& + \exp\left(-t/\tau\right)\left(F_1^{eq}|^l + T_r F_M(T_t)|^l\left[-b^l t c_x|_m - \tau\left(b^l c_x|_m + Bt\right)\right]\right)(1 - H(c_x|_m)) \\
& + \exp\left(-t/\tau\right)\left(F_1^{eq}|^r + T_r F_M(T_t)|^r\left[-b^r t c_x|_m - \tau\left(b^r c_x|_m + Bt\right)\right]\right) H(c_x|_m).
\end{aligned} \tag{J.6}$$

Assuming the hypothesis of a well-resolved flow

$$\begin{gathered} a^l = a^r \quad ; \quad b^l = b^r \quad ; \quad F_0^{eq}|^l = F_0^{eq}|^r = F_1^{eq}|^0 \quad ; \quad F_1^{eq}|^l = F_1^{eq}|^r = F_1^{eq}|^0 \\ F_M^l(T_t) = F_M^r(T_t) = F_M^0(T_t) \quad ; \quad T_r F_M(T)|^l = T_r F_M(T)|^r = T_r F_M(T)|^0 \end{gathered} \tag{J.7}$$

and considering definitions (J.3), equations (J.5) and (J.6) reduce to the simplified form in equations (H.12).

Appendix K

Laplacian Smoothing

The Laplacian smoothing is a method that can be used to smooth a mathematical function in a point based on neighbour values. As example in one-dimension it assumes the following form

$$\Phi_i^{m+1} = \Phi_i^n + aL\left(\Phi_i^n\right) \tag{K.1}$$

where $L\left(\Phi_i^n\right)$ is the one-dimensional Laplacian of the function

$$L\left(\Phi_i^n\right) = \frac{1}{2}\left(\Phi_{i-1}^n + \Phi_{i+1}^n\right) \tag{K.2}$$

and m is the required number of iteration to obtain a sufficiently smooth function. A value of $a = 0.5$ and $m = 50$ is employed in MΦC for this work.

Appendix L

L2-Norm Between to Consecutive Solutions

The following L2-norm between two consecutive solutions can be used in MΦC as index of the convergence of steady state solutions

$$\sqrt{\frac{\sum_i^{n_{cells}}(\Phi_i^{t^{n+1}} - \Phi_i^{t^n})^2}{n_{cells}}}. \tag{L.1}$$

where n_{cells} is the number of cells in which the computational physical domain is discretised.

Bibliography

[1] T.R. Deschenes. *Extension of a Modular Particle-Continuum Method for Non-equilibrium, Hypersonic Flows*. PhD dissertation, The University of Michigan, 2011.

[2] T.E. Schwartzentruber. *A Modular Particle-Continuum Numerical Algorithm for Hypersonic Non-equilibrium Flows*. PhD dissertation, The University of Michigan, 2007.

[3] K.J. Murphy, K.L. Bibb, G.J. Brauckmann, M.N. Rhode, B. Owens, D.T. Chan, E.L. Walker, J.H. Bell, and T.M. Wilson. Orion Crew Module Aerodynamic Testing. In *29th AIAA Applied Aerodynamics Conference*, 27-30 June, Honolulu, Hawaii 2011.

[4] V.A. Rykov, V.A. Titarev, and E.M. Shakhov. Shock Wave Structure in a Diatomic Gas Based on a Kinetic Model. *Fluid Dynamics*, 43(2):316–326, 2008.

[5] H. Alsmeyer. Density Profiles in Argon and Nitrogen Shock Waves Measured by the Absorption of an Electron Beam. *Journal of Fluid Mechanics*, 74(3):497–513, 1976.

[6] N. Tsuboi and Y. Matsumoto. Experimental and Numerical Study of Hypersonic Rarefied Gas Flow over Flat Plates. *AIAA Journal*, 43(6):1243–1255, 2005.

[7] K. Xu, X. He, and C. Cai. Multiple Temperature Kinetic Model and Gas-Kinetic Method for Hypersonic Non-equilibrium Flow Computations. *Journal of Computational Physics*, 227:6779–6794, 2008.

[8] Chadwick cluster at University of Liverpool High Performance Computing Services. http://www.liv.ac.uk/csd/advanced-research-computing/facilities/high-performance-computing (accessed August, 2015).

[9] SuperMUC supercomputer at Leibniz-Rechenzentrum. www.lrz.de/services/compute/supermuc (accessed August, 2015).

[10] N8 HPC facilities provided by the EPSRC and N8 consortium. n8hpc.org.uk (accessed August, 2015).

[11] W.G. Vincenti and C.H. Kruger. *Introduction to Physical Gas Dynamics*. John Wiley and Sons, Inc., 1965.

[12] G.A. Bird. *Molecular Gas Dynamics and the Direct Simulation of Gas Flows*. Oxford Science Publications, 1994.

[13] L. Saint-Raymond. *Hydrodynamic Limits of the Boltzmann Equation*. Springer-Verlag Berlin Heidelberg, 2009.

[14] P.A. Gnoffo, N.G. Roop, and L.S. Judy. Conservation Equations and Physical Models for Hypersonic Air Flows in Thermal and Chemical Nonequilibrium. *NASA/TP-2867*, 1989.

[15] G.A. Candler. On the Computation of Shock Shapes in Nonequilibrium Hypersonic Flows. In *27th Aerospace Sciences Meeting*, 9-12 January, Reno, Nevada 1989.

[16] C. Park. Review of Chemical-Kinetic Problems of Future NASA Missions, I: Earth Entries. *Journal of Thermophysics and Heat Transfer*, 7(3):385–398, 1993.

[17] G.A. Bird. *The DSMC Method*. CreateSpace, 2013.

[18] I.D. Boyd. Rotational and Vibrational Nonequilibrium Effects in Rarefied Hypersonic Flow. *Journal of Thermophysics and Heat Transfer*, 4(4):478–484, 1990.

[19] M.H. Gorji and P. Jenny. Fokker-Planck-DSMC Algorithm for Simulations of Rarefied Gas Flows. *Computers & Fluids*, 287:110129, 2015.

[20] L. Mieussens. Discrete-Velocity Model and Implicit Scheme for the BGK Equation of Rarefied Gas Dynamics. *Mathematical Models and Methods in Applied Sciences*, 10(8):1121–1149, 2000.

[21] S. Pieraccini and G. Puppo. Microscopically ImplicitMacroscopically Explicit Schemes for the BGK Equation. *Journal of Computational Physics*, 231:299327, 2012.

[22] R.R. Arslanbekov, V. Kolobov, and A.A. Frolova. Kinetic Solvers with Adaptive Mesh in Phase Space. *AIP Conference Proceedings*, 1501:294–301, 2012.

[23] G. Dimarco and R. Loubere. Towards an Ultra Efficient Kinetic Scheme Part II: The High Order Case. *Journal of Computational Physics*, 255:699719, 2013.

[24] V. Titarev, M. Dumbserc, and S. Utyuzhnikov. Construction and Comparison of Parallel Implicit Kinetic Solvers in Three Spatial Dimensions. *Journal of Computational Physics*, 256:17–33, 2014.

[25] P.L. Bhatnagar, E.P. Gross, and M. Krook. A Model for Collision Processes in Gases. I. Small Amplitude Processes in Charged and Neutral One-Component Systems. *Physical Review*, 94(3):511–525, 1954.

[26] E.M. Shakhov. Generalization of the Krook Kinetic Relaxation Equation. *Mekhanika Zhidkosti i Gaza*, 3(5):142–145, 1968.

[27] L.H. JR. Holway. Kinetic Theory of Shock Structure Using an Ellipsoidal Distribution Function. *Rarefied Gas Dynamics, Proceedings of the Fourth International Symposium held at the Institute for Aerospace Studies, Toronto, 1964*, 1:193–215, 1965.

[28] V.A. Rykov. A Model Kinetic Equation for a Gas with Rotational Degrees of Freedom. *Fluid Dynamics*, 10(6):959–966, 1975.

[29] P. Andries, P. LeTallec, J.-P. Perlat, and B. Perthame. The Gaussian-BGK Model of Boltzmann Equation with Small Prandtl Number. *European Journal of Mechanics - B/Fluids*, 19(6):813–830, 2000.

[30] L. Wu, C. White, T.J. Scanlon, J.M. Reese, and Y. Zhang. A Kinetic Model of the Boltzmann Equation for Non-Vibrating Polyatomic Gases. *Journal of Fluid Mechanics*, 763:24–50, 2015.

[31] Y. Zheng, J.M. Reese, and H. Struchtrup. Comparing Macroscopic Continuum Models for Rarefied Gas Dynamics: A New Test Methods. *Journal of Computational Physics*, 218:748–769, 2006.

[32] C. Cercignani. *Microflows and Nanoflows: Fundamentals and Simulation*. Springer-Verlaq, 2005.

[33] C.J. Greenshields and J.M. Reese. Rarefied Hypersonic Flow Simulations Using the Navier-Stokes Equations with Non-equilibrium Boundary Conditions. *Progress in Aerospace Sciences*, 52(1):80–87, 2012.

[34] D. Chapman. *The Mathematical Theory of Non-uniform Gases*. Cambridge University Press, 1970.

[35] D. Burnett. The Distribution of Velocities in a Slightly Non-Uniform Gas. *Proceedings of the London Mathematical Society*, 39(1):385430, 1935.

[36] K. Fiscko and D. D. Chapman. Comparison of Burnett, Super-Burnett and Monte Carlo Solutions for Hypersonic Shock Structure. *Rarefied gas dynamics: Theoretical and Computational Techniques*, 118:374–395, 1989.

[37] H. Struchtrup. Failures of the Burnett and Super-Burnett Equations in Steady State Processes. *Continuum Mechanics and Thermodynamics*, 17(1):43–50, 2005.

[38] H. Grad. On the Kinetic Theory of Rarefied Gases. *Communications on Pure and Applied Mathematics*, 2(4):331–407, 1949.

[39] H. Struchtrup and M. Torrilhon. Regularisation of Grads 13-Moment Equations: Derivation and Linear Analysis. *Physics of Fluids*, 15:2668, 2003.

[40] M.Yu. Timokhin, Ye.A. Bondar, A.A. Kokhanchik, M.S. Ivanov, I.E. Ivanov, and I.A. Kryukov. Study of the Shock Wave Structure by Regularized Grads Set of equations. *Physics of Fluids*, 27(037101), 2015.

[41] J.G. McDonald and C.P.T. Groth. Towards Realizable Hyperbolic Moment Closures for Viscous Heat-Conducting Gas Flows Based on a Maximum-Entropy Distribution. *Continuum Mechanics and Thermodynamics*, 25:573–603, 2013.

[42] J.-F. Bourgat, P. Le Tallec, and M.D. Tidriri. Coupling Boltzmann and Navier-Stokes Equations by Friction. *Journal of Computational Physics*, 127:227–245, 1996.

[43] P. Le Tallec and F. Mallinger. Coupling Boltzmann and Navier-Stokes Equation by Half Fluxes. *Journal of Computational Physics*, 136:51–67, 1997.

[44] C.E. Glass and T.J. Horvarth. Comparison of a 3-D CFD-DSMC Solution Methodology With a Wind Tunnel Experiment. *NASA/TM-2002-211777*, 2002.

[45] W.-L. Wang, Q. Sun, and I.D. Boyd. Towards Development of a Hybrid DSMC-CFD Method for Simulating Hypersonic Interacting Flows. In *8th AIAA/ASME Joint Thermophysics and Heat Transfer Conference*, 24-26 June, St. Louis, Missouri 2002.

[46] K. Xu and J.-C. Huang. An Improved Unified Gas-Kinetic Scheme and the Study of Shock Structures. *IMA Journal of Applied Mathematics*, 76:698–711, 2011.

[47] S. Liu, Y. Pubing, K. Xu, and C. Zhong. Unified Gas-Kinetic Scheme for Diatomic Molecular Simulations in all Flow Regimes. *Journal of Computational Physics*, 259:96–113, 2014.

[48] G.A. Bird. Breakdown of Translational and Rotational Equilibrium in Gaseous Expansions. *AIAA Journal*, 8(11):1998–2003, 1970.

[49] I.D. Boyd, G. Chen, and G.A. Candler. Predicting Failure of the Continuum Fluid Equations in Transitional Hypersonic Flows. *Physics of Fluids*, 7(1):210–219, 1995.

[50] W.-L. Wang and I.D. Boyd. Predicting Continuum Breakdown in Hypersonic Viscous Flow. *Physics of Fluids*, 15(1):91–100, 2003.

[51] T.E. Schwartzentruber and I.D. Boyd. A Hybrid Particle-Continuum Method Applied to Shock Waves. *Journal of Computational Physics*, 215:402–416, 2006.

[52] T.E. Schwartzentruber, L.C. Scalabrin, and I.D. Boyd. A Modular Particle-Continuum Numerical Method for Hypersonic Non-equilibrium Gas Flows. *Journal of Computational Physics*, 225:1159–1174, 2007.

[53] T.R. Deschenes and I.D. Boyd. Extension of a Modular Particle-Continuum Method to Vibrationally Exited, Hypersonic Flows. *AIAA Journal*, 49(9), 2011.

[54] T.R. Deschenes, T.D. Holman, and I.D. Boyd. Effects of Rotational Energy Relaxation in a Modular Particle-Continuum Method. *Journal of Thermophysics and Heat Transfer*, 25(2):218–227, 2011.

[55] V.I. Kolobov, R.R. Arslanbenkov, V.V. Aristov, A.A. Frolova, and S.S. Zabelok. Unified Solver for Rarefied and Continuum Flows with Adaptive Mesh and Algorithm Refinement. *Journal of Computational Physics*, 223:589–608, 2007.

[56] C.R. Abbate, G. Kleijn and B.J. Thijsse. Hybrid Continuum/Molecular Simulations of Transient Gas Flows with Rarefaction. *AIAA Journal*, 47:1741–1749, 2009.

[57] P. Degond and G. Dimarco. Fluid Simulations with Localised Boltzmann Upscaling by Direct Simulation Monte-Carlo. *Journal of Computational Physics*, 231:2414–2437, 2012.

[58] P. Degond, G. Dimarco, and L. Mieussens. A Multiscale Kinetic-Fluid Solver with Dynamic Localization of Kinetic Effects. *Journal of Computational Physics*, 229:4907–4933, 2010.

[59] A. Alaia and G. Puppo. A Hybrid Method for Hydrodynamic-Kinetic Flow - Part II - Coupling of Hydrodynamic and Kinetic Models. *Journal of Computational Physics*, 231:5217–5242, 2012.

[60] N.G. Hadjiconstantinou, A.L. Garcia, M.Z. Bazant, and G. He. Statistical Error in Particle Simulation of Hydrodynamic Phenomena. *Journal of Computational Physics*, 187:274–297, 2003.

[61] Q. Sun and I.D. Boyd. Evaluation of Macroscopic Properties in the Direct Simulation Monte Carlo Method. *Journal of Thermophysics and Heat Transfer*, 19(3):329–335, 2005.

[62] A. Alaia and G. Puppo. A Hybrid Method for Hydrodynamic-Kinetic Flow - Part I - A Particle-Grid Method for Reducing Stochastic Noise in Kinetic Regimes. *Journal of Computational Physics*, 230:5660–5683, 2011.

[63] K. Xu. A Gas-Kinetic BGK Scheme for the Navier-Stokes Equations and its Connection with Artificial Dissipation and Godunov Method. *Journal of Computational Physics*, 171:289–335, 2001.

[64] J.M. Burt and I.D. Boyd. A Hybrid particle Approach for Continuum and Rarefied Flow Simulation. *Journal of Computational Physics*, 228:460–475, 2009.

[65] S. Tiwari, A. Klar, and S. Hardt. A Particle-Particle Hybrid Method for Kinetic and Continuum Equations. *Journal of Computational Physics*, 228:7109–7124, 2009.

[66] Eun Ji Jun. *All-Particle Multiscale Computation of Hypersonic Rarefied Flows*. PhD dissertation, The University of Michigan, 2012.

[67] R. Roveda, D.B. Goldstein, and P.L. Varghese. Hybrid Euler/Direct Simulation Monte Carlo Calculation of Unsteady Slit Flow. *Journal of Spacecraft and Rockets*, 37(6):753–760, 2000.

[68] V.I. Kolobov, S.A. Bayyuk, R.R. Arslanbenkov, V.V. Aristov, A.A. Frolova, and S.S. Zabelok. Unified Flow Solver for Transient Rarefied-Continuum Flows. *AIP Conference Proceedings*, 1501:414–421, 2012.

[69] A. Harten, P.D. Lax, and B. van Leer. On Upstream Differencing and Godunov-Type Schemes for Hyperbolic Conservation Laws. *SIAM Rev.*, 25(1):35–61, 1983.

[70] D.I. Pullin. Direct Simulation Methods for Compressible Inviscid Ideal Gas Flow. *Journal of Computational Physics*, 34(2):231–244, 1980.

[71] J.C. Mandal and S.M. Deshpande. Kinetic Flux Vector Splitting for Euler Equations. *Computers & Fluids*, 23(2):447–478, 1994.

[72] S.V.R. Rao and S.M. Deshpande. Kinetic Theory Based Wave-Particle Splitting Scheme for Euler Equations. *Aeronautical Society of India Journal*, 44(4):329–333, 1992.

[73] K. Acheson and R. Agarwal. A Kinetic Theory-Based Wave/Particle Flux-Splitting Scheme for the Euler Equations. In *26th AIAA Computational Fluid Dynamics Conference*, 19-22 June, San Diego, California 1995.

[74] J.M. Moschetta and D. Pullin. A Robust Low Diffusive Kinetic Scheme for the Navier-Stokes/Euler Equations. *Journal of Computational Physics*, 133:193–204, 1997.

[75] K. Xu. A Multidimensional Gas-Kinetic BGK Scheme for Hypersonic Viscous Flow. *Journal of Computational Physics*, 203:405–421, 2005.

[76] K. Xu. Gas-Kinetic Schemes for Unsteady Compressible Flow Simulations. *von Karman Institute for Fluid Dynamics, 29th Computational Fluid Dynamics Lecture Series*, pages 289–335, 1998.

[77] K. Xu and E. Josyula. Continuum Formulation for Non-equilibrium Shock Structure Calculation. *Communications in Computational Physics*, 1(3):425–450, 2006.

[78] C. Cai, D.L. Danny, and K. Xu. One-Dimensional Multiple-Temperature Gas-Kinetic Bhatnagar-Gross-Krook Scheme for Shock Wave Computation. *AIAA Journal*, 46(2):1054–1062, 2008.

[79] K. Xu. Regularisation of the Chapman-Enskog Expansion and its Description of Shock Structures. *Physics of Fluids*, 14(4):L17, 2002.

[80] Li-J. Xuan and K. Xu. A New Gas-Kinetic scheme Based on Analytical Solutions of the BGK Equation. *Journal of Computational Physics*, 234:524–539, 2013.

[81] H. Chen, S.A. Orszag, I. Staroselsky, and S. Succi. A Comparison and Unification of Ellipsoidal Statistical and Shakhov BGK Models. *Journal of Fluid Mechanics]*, 519:301–314, 2004.

[82] M. Righi. A Gas-Kinetic Scheme for the Simulation of Turbulent Flows. *AIP Conference Proceedings*, 1501:481–488, 2012.

[83] M. Righi. A Gas-Kinetic Scheme for Turbulent Flow. In *7th AIAA Theoretical Fluid Mechanics Conference*, 16-20 June 2014, Atlanta, Georgia 2014.

[84] V.V. Aristov and O.I. Rovenskaya. Kinetic Description of the Turbulence in the Supersonic Compressible Flow Over a Backward/Forward-facing Step. *Computers & Fluids*, 111:150–158, 2015.

[85] K. Xu and J.-C. Huang. A Unified Gas-Kinetic Scheme for Continuum and Rarefied Flows. *Journal of Computational Physics*, 229:7747–7764, 2010.

[86] L. Tang. Progress in gas-kinetic upwind schemes for the solution of Euler/Navier−Stokes equations − I: Overview. *Computers & Fluids*, 56:39–48, 2012.

[87] S.-J. Lawson, R. Steijl, M. Woodgate, and G.N. Barakos. High Performance Computing for Challenging Problems in Computational Fluid Dynamics. *Progress in Aerospace Science*, 52:19–29, 2012.

[88] G.N. Barakos, R. Steijl, A. Brocklehurst, and K. Badcock. Development of CFD Capability for Full Helicopter Engineering Analysis. In *31st European Rotorcraft Forum*, pages 19–29, 2005.

[89] M. Carrión, M. Woodgate, R. Steijl, and G.N. Barakos. CFD and Aeroelastic Analysis of the MEXICO Wind Turbine. In *The Science of Making Torque from Wind*, 9-11 October, Oldenburg, Germany 2012.

[90] R. Steijl and G.N. Barakos. Coupled Navier-Stokes-Molecular Dynamics simulations Using a Multiphysics Flow Simulation Framework. *International Journal for Numerical Methods in Fluids*, 62:1081–1106, 2010.

[91] R. Steijl and G.N. Barakos. Coupled Navier-Stokes/Molecular Dynamics Simulations in Non-periodic Domains on Particle Forcing. *International Journal for Numerical Methods in Fluids*, 69:1326–1349, 2012.

[92] R. Steijl and G.N. Barakos. Computational Fluid dynamics of Partially Rarefied Flows with Coupled Kinetic Boltzmann/Navier-Stokes Methods. In *ECCOMAS 2012*, 10-14 September, Vienna, Austria 2012.

[93] M.-S. Liou and C.J. Steffen Jr. A New Flux Splitting Scheme. *Journal of Computational Physics*, 107:23–39, 1993.

[94] M.-S. Liou. A Sequel to AUSM, Part II: AUSM+-up for All Speed. *Journal of Computational Physics*, 214:137–170, 2006.

[95] M.-S. Liou. Ten Years in the Making - AUSM-family. *NASA/TM*, 2001.

[96] M.-S. Liou. The Evolution of AUSM Schemes. *Defense Science Journal*, 60(6):606–613, 2010.

[97] S. Colonia, R. Steijl, and G.N. Barakos. Assessment of Implicit Implementation of the AUSM$^+$ Method and the SST Model for Viscous High Speed Flow. In *5th European Conference for Aeronautics and Space Science*, 1-5 July, Munich, Germany 2013.

[98] S. Colonia, R. Steijl, and G.N. Barakos. Implicit Implementation of the AUSM$^+$ and AUSM$^+$up Schemes. *International Journal for Numerical Methods in Fluids*, 75(10):687–712, 2014.

[99] S. Colonia, R. Steijl, and G.N. Barakos. Kinetic Models with Rotational Degrees of Freedom for Hybrid Methods. In *ECCOMAS - 6th European Conference on Computational Fluid Dynamics*, 20-25 July, Barcelona, Spain 2014.

[100] S. Colonia, R. Steijl, and G.N. Barakos. Kinetic Models and Gas Kinetic Schemes for Hybrid Simulation of Partially Rarefied Flows. In *AIAA Atmospheric Flight Mechanics Conference, AIAA Science and Technology Forum*, 5-9 January, Kissimmee, Florida 2015.

[101] S. Colonia, R. Steijl, and G.N. Barakos. Kinetic Models and Gas Kinetic Schemes for Hybrid Simulation of Partially Rarefied Flows. *AIAA Journal*, under review.

[102] S. Colonia, R. Steijl, and G.N. Barakos. A Gas Kinetic Scheme for Hybrid Simulation of Partially Rarefied Flows. In *6th European Conference for Aeronautics and Space Science*, 29 June - 3 July, Krakov, Poland 2015.

[103] C. Hirsch. *Numerical Computation of internal and External Flows - Volume 1-2*. Wiley-Interscience, 1989.

[104] P.L. Roe. Approximate Riemann Solvers, Parameter Vectors and Difference Schemes. *Journal of Computational Physics*, 43:357–372, 1981.

[105] E.F. Toro. *Riemann solvers and numerical methods for fluid dynamics*. Berlin: Springer, 2006.

[106] E.F. Toro, M. Spruce, and W. Speares. Restoration of the contact surface in the HLL-Riemann solver. *Shock Waves*, 4:25–34, 1994.

[107] B. van Leer. Towards the Ultimate Conservative Difference Scheme, V. A Second Order Sequel to Godunov's Method. *Journal of Computational Physics*, 32:101–136, 1979.

[108] P.D. Orkwis and D. Scot McRae. Newton's Method Solver for High-Speed Viscous Separated Flow Fields. *AIAA Journal*, 30(1):78–85, 1992.

[109] P.D. Orkwis and D. Scot McRae. Newton's Method Solver for the Axisymmetric Navier-Stokes Equations. *AIAA Journal*, 30(6):1507–1514, 1992.

[110] S.P. Spekreijse. Multigrid Solution of the Steady Euler Equations. *Ph.D. Dissertation - Centrum voor Wiskunde en Informatica (Amsterdam)*, 1987.

[111] G.D. Van Albada, B. Van Leer, and W.W. Roberts. A Comparative study of Computational methods in Cosmic Gas Dynamics. *Astronomy and Astrophysics*, 108, 1982.

[112] M.-S. Liou. A Sequel to AUSM: AUSM+. *Journal of Computational Physics*, 129:364–382, 1996.

[113] V. Venkatakrishnan. Newton Solution of Inviscid and Viscous Problems. *AIAA Journal*, 27:885–891, 1989.

[114] L.B. Wigton. Application of MACSYMA and Sparse Matrix Technology to Multi-element Airfoil Calculations. In *8th AIAA Computational Fluid Dynamics Conference*, 9-12 June, Honolulu, Hawaii 1987.

[115] V. Venkatakrishnan and BarthT.J. Application of Direct Solvers to Unstructured Meshes for the Euler and Navier-Stokes Equations Using Upwind Schemes. *AIAA 27th Aerospace Sciences Meeting*, 1989.

[116] W.R. Briley and H. McDonald. Solution of the Multidimensional Compressible Navier-Stokes Equations by a Generalized Implicit Method. *Journal of Computational Physics*, 24(4):372–397, 1977.

[117] S.R. Chakravarthy. Relaxation Methods for Unfactored Implicit Upwind Schemes. In *22nd AIAA Aerospace Sciences Meeting*, 9-12 January, Reno, Nevada 1984.

[118] S. Yoon and A. Jameson. Lower-upper Symmetric-Gauss-Seidel Method for the Euler and Navier-Stokes Equations. *AIAA Journal*, 26(9):1025–1026, 1988.

[119] O. Axelsson. Conjugate Gradient Type Methods for Unsymmetric and inconsistent System of Linear Equation. *Linear Algebra and its Applications*, 29:1–16, 1980.

[120] Y. Liu and C. Storey. Efficient Generalized Conjugate Gradient Algorithms, Part 1: Theory. *Journal of Optimization Theory and Applications*, 69, 1991.

[121] Y.F. Hu and C. Storey. Efficient Generalized Conjugate Gradient Algorithms, Part 2: Implementation. *Journal of Optimization Theory and Applications*, 69, 1991.

[122] Y. Saad and M.H. Schultz. GMRES: A Generalized Minimum Residual Algorithm for Solving Non-symmetric Linear Systems. *SIAM Journal on Scientific and Statistical Computing*, 7:856–869, 1986.

[123] J.A. Meijerink and H.A. van der Vorst. Guidelines for the Usage of Incomplete Decompositions in Solving Sets of Linear Equations as They Occur in Practical Problems. *Journal of Computational Physics*, 44(1):134–155, 1981.

[124] P.D. Orkwis. Comparison of Newton's and Quasi-Newton's Method Solvers for the Navier-Stokes Equations. *AIAA Journal*, 31(5):832–836, 1993.

[125] V. Venkatakrishnan. Preconditioned Conjugate Gradient Methods for the Compressible Navier-Stokes Equations. *AIAA Journal*, 29(7):1092–1100, 1991.

[126] D. Darracq, S. Campagneux, and A. Corjon. Computation of Unsteady Turbulent Airfoils Flows with an Aeroelastic AUSM+ Implicit Solver. In *16th AIAA Applied Aerodynamics Conference*, 15-18 June, Albuquerque, New Mexico 1998.

[127] D. Vigneron and J.-A. Vaassen, J.-M. Essers. An Implicit Finite Volume Method for the Solution of 3D Low Mach Number Viscous Flows Using Local Preconditioning Technique. *Journal of Computational and Applied Mathematics*, 215:610–617, 2008.

[128] D. Guo-Hao and W. Wen-Long. Parallel Computation in Hypersonic Aerodynamic Heating Problem. *World Academy of Science, Engineering and Technology*, 55:190–196, 2011.

[129] S. Amaladas and H. Kamath. Implicit and Multigrid Procedures for Steady-State Computations with Upwind Algorithms. *Computers & Fluids*, 28:187–212, 1999.

[130] S. Langer and D. Li. Application of Point Implicit Runge-Kutta Method to Inviscid and Laminar Flow Problems using $AUSM$ and $AUSM^+$ Upwinding. *International Journal of Computational Fluid Dynamics*, 25:255–269, 2011.

[131] W. Sutherland. The viscosity of gases and molecular force. *Philosophical Magazine*, 5(36):507–531, 1893.

[132] Ph. Spalart and S.R. Allmaras. A One-Equation Turbulence Model for Aerodynamic Flows. *La Recherche Aérospatiale*, 1:5–21, 1994.

[133] D.C. Wilcox. Multiscale Model for Turbulent Flows. *AIAA Journal*, 26(11):1311–1320, 1988.

[134] F.R. Menter. Two-Equation Eddy-Viscosity Turbulence Models for Engineering Applications. *AIAA Journal*, 32(8):1598–1605, 1994.

[135] P.H. Cook, M.A. McDonald, and M.C.P. Firmin. Aerofoil RAE 2822 - Pressure Distributions, and Boundary Layer and Wake Measurements. *Experimental Data Base for Computer Program Assessment*, AGARD AR 138, 1979.

[136] V. Schmitt and F. Charpin. Pressure Distributions on the ONERA-M6-Wing at Transonic Mach Numbers. *Experimental Data Base for Computer Program Assessment*, AGARD AR 138, 1979.

[137] F.S. Billing. Shock-Wave Shapes Around Spherical- and Cylindrical-Nosed Bodies. *Journal of Spacecraft and Rockets*, 4:822–834, 1967.

[138] K. Kitamura, E. Shima, and P.L. Roe. Evaluation of Euler Fluxes for Hypersonic Heating Computations. *AIAA Journal*, 48(4):763–776, 2010.

[139] K. Kitamura, E. Shima, and P.L. Roe. Carbuncle Phenomena and Other Shock Anomalies in Three Dimensions. *AIAA Journal*, 50(12):2655–2669, 2012.

[140] R.W. MacCormack. The Carbuncle CFD Problem. In *49th AIAA Aerospace Sciences Meeting including the New Horizons Forum and Aerospace Exposition*, 4-7 January, Orlando, Florida 2011.

[141] K.-C. Muck, J. Andreopoulos, and J.-P. Dussauge. Unsteady Nature of Shock-Wave/Turbulent Boundary-Layer Interaction. *AIAA Journal*, 26(2):179–187, 1988.

[142] B.R. Holis. Experimental investigation of Project Orion Crew Exploration Vehicle Aeroheating: LaRC 20-Inch Mach 6 Air Tunnel Test 6931. *NASA/TM-2009-215718*, 2009.

[143] P.A. Gnoffo. An Upwind-Based Point-Implicit Algorithm for Viscous, Compressible Perfect-Gas Flows. *NASA/TP-2953*, 1990.

[144] M. Carrión, M. Woodgate, R. Steijl, and G.N. Barakos. Implementation of all-Mach Roe-type Schemes in Fully Implicit CFD Solvers - Demonstration for Wind Turbine Flows. *International Journal for Numerical Methods in Fluids*, 73(8):693–728, 2013.

[145] ESDU 90008. Introduction to Transonic Aerodynamics of Aerofoils and Wings. *Product issue: 2007-04*, 2007.

[146] D.M. Somers. Design and Experimental Results for the S809 Airfoil. *Subcontract Report SR-440–6918*, NREL, Colorado, USA, 1997.

[147] H. Snel, J.G. Schepers, and B. Montgomerie. The MEXICO Project (Model Experiments in Controlled Conditions): The Database and First Results of Data Processing and Interpretation. 2007.

[148] R.R. Ramsay, M.J. Hoffmann, and G.M. Gregorek. Effects of Grit Roughness and Pitch Oscillations on the S809 Airfoil. *National Renewable Energy Laboratory*, 1995.

[149] C. Cercignani. *Theory and Application of the Boltzmann Equation*. Scottish Academic Press, 1975.

[150] S. Chen, K. Xu, and Q. Cai. Expanded Analogy Between Boltzmann Kinetic Theory of Fluids and Turbulence. *arXiv:1304.0865v2 [physics.flu-dyn]*, 2013.

[151] F.E. Jones. NBS TN-1186 - Interpolation Formulas for Viscosity of Six Gases: Air, Nitrogen, Carbon Dioxide,Helium, Argon, and Oxygen. *U.S. Department of Commerce/National Bureau of Standards*, 1984.

[152] I.D. Boyd. Rotational-Translational Energy Transfer in Rarefied Non-equilibrium Flows. *Physics of Fluids A*, 2(3), 1990.

[153] V.A. Rykov, V.A. Titarev, and E.M. Shakhov. Numerical Study of the Transverse Supersonic Flow of a Diatomic Rarefied Gas past a Plate. *Computational Mathematics and Mathematical Physics*, 47(1):136–150, 2007.

[154] J.G. Parker. Rotational and Vibrational Relaxation in Diatomic Gases. *Physics of Fluids*, 2(4):449–462, 1959.

[155] J.A. Lordi and R.E. Mates. Rotational Relaxation in Non-polar Diatomic Gases. *Physics of Fluids*, 9(4):291–308, 1970.

[156] P. Valentini, C. Zhang, and T.E. Schwartzentruber. Molecular Dynamics Simulation of Rotational Relaxation in Nitrogen: Implications for Rotational Collision Number Models. *Physics of Fluids*, (24):106101:1–23, 2012.

[157] I.N. Larina and V.A. Rykov. Kinetic Model of the Boltzmann Equation for a Diatomic Gas with Rotational Degrees of Freedom. *Computational Mathematics and Mathematical Physics*, 50(12):2118–2130, 2010.

[158] I.N. Larina and V.A. Rykov. Computation of a Rarefied Diatomic Gas Flows through a Plane Microchannel. *Computational Mathematics and Mathematical Physics*, 52(4):637–648, 2010.

[159] J.Y. Yang and J.C. Huang. Rarefied Flow Computations Using Nonlinear Model Boltzmann Equation. *Journal of Computational Physics*, 120:323–339, 1995.

[160] S. Chandrasekhar. *The Mathematical Theory of Non-uniform Gases.* Dover Publications, New York, 1960.

[161] M. Abramowitz and I.A. Stegun. *Handbook of Mathematical Functions: with Formulas, Graphs, and Mathematical Tables*. Dover Publications, New York, 1964.

[162] C. Baranger, J. Claudel, N. Hérouard, and L. Mieussens. Locally Refined Discrete Velocity Grids for Deterministic Rarefied Flow Simulations. *AIP Conference Proceedings*, 1501:389–396, 2012.

[163] V. Titarev. Conservative Numerical Methods for Model Kinetic Equations. *Computers & Fluid*, 36:1446–1459, 2007.

[164] A.M. Turing. Rounding-Off Errors in Matrix Processes. *The Quaterly Journal of Mechanics & Applied Mathematics*, 1(1):287–308, 1948.

[165] A. Harten. High Resolution Schemes for Hyperbolic Conservation Laws. *Journal of Computational Physics*, 49:357–393, 1983.

[166] S. Chigullapallu, A. Venkattraman, M.S. Ivanov, and A.A. Alexeenko. Entropy Consideration in Numerical simulations of Non-Equilibrium Rarefied Flows. *Journal of Computational Physics*, 229:2139–2158, 2010.

[167] L. Mieussens and Struchtrup. Numerical Comparison of Bhatnagar-Gross-Krook Models with Proper Prandtl Number. *Physics of Fluids*, 16(8):2797–2813, 2004.

[168] M. Fossati and K. Xu. Kinetic Node-Pair Formulation for Two-Dimensional Flows from Continuum to Transitional Regime. *AIAA Journal*, 51(4):784–796, 2013.

[169] E.F. Toro. *Godunov Methods: Theory and Applications*. Berlin: Springer, 2012.

[170] R.P. Starkey and M.J. Lewis. Shock-Based Waverider Design with Pressure Gradient Corrections and Computational Simulations. *Journal of Aircraft*, 42(5):1350–1352, 2005.

[171] R.P. Starkey. Design of Waverider Based Re-Entry Vehicles. In *13th AIAA/CIRA International Space Planes and Hypersonics Systems and Technologies*, 17-20 May, Capua, Italy 2005.

[172] T.W. Drayna, I. Nompelis, and G.V. Candler. Numerical Simulation of the AEDC Waverider at Mach 8. In *25th AIAA Aerodynamic Measurement Technology and Ground Testing Conference*, 5-8 June, San Francisco, California 2006.

[173] D.J-K. Jackson. CFD Analysis of a Generic Waverider. In *36th AIAA Fluid Dynamics Conference*, 5-8 June, San Francisco, California 2006.

[174] B. Mangin, A. Chpoun, R. Benay, and B. Chanetz. Comparison Between Methods of Generation of Waveriders Derived from Conical Flows. *Comptes Rendus Mecanique*, 334:117–122, 2006.

[175] G. Pezzella, M. Marini, B. Reimann, and J. Steelant. Aerodynamic Design Analysis of the Hexafly-INT Hypersonic Glider. In *20th AIAA International Space Planes and Hypersonic Systems and Technologies Conference*, 6-9 July, Glasgow, Scotland 2015.

[176] J. Steelant, T. Langener, F. Di Matteo, J. Riehmer, M. Kuhn, C. Ditter, F. Scheuerpflug, W. Jung, K. Hannemann, M. Marini, G. Pezzella, M. Cicala, and L. Serre. Conceptual Design of the High-Speed Propelled Experimental Flight Test Vehicle HEXAFLY. In *20th AIAA International Space Planes and Hypersonic Systems and Technologies Conference*, 6-9 July, Glasgow, Scotland 2015.

[177] G. Favaloro, A. Rispoli, L. Vecchione, G. Pezzella, V. Carandente, R. Scigliano, M. Cicala, G. Morani, and J. Steelant. Design Analysis of the High-Speed Experimental Flight Test Vehicle HEXAFLY-International. In *20th AIAA International Space Planes and Hypersonic Systems and Technologies Conference*, 6-9 July, Glasgow, Scotland 2015.

[178] P. Roncioni, P. Natale, M. Marini, T. Langener, and J. Steelant. Numerical Simulations and Performance Assessment of a Scramjet Powered Cruise Vehicle at Mach 8. *Aerospace Science and Technology*, 42:218–228, 2015.

[179] Q. Chen, X, Z.-X. Hou, J.-X. Liu, and X.-Z. Gao. Bluntness Impact on Performance of Waverider. *Computers & Fluids*, 48:30–43, 2011.

[180] J.-X. Liu, Z.-X. Hou, G.-H. Ding, Q. Chen, X, and Q. Chen, X. Numerical and Experimental Study on Waverider with Blunt Leading Edge. *Computers & Fluids*, 84:203–217, 2013.

[181] W.F.N. Santos and M.J. Lewis. Aerothermodynamic Performance Analysis of Hypersonic Flow on Power Law Leading Edges. *Journal of Spacecraft and Rockets*, 42(4):588–597, 2005.

[182] T.B. Silvester, T.J. McIntyre, and R.G. Morgan. Superorbital Expansion Tube Tests of a Caret Waverider. *Shock Waves*, 17:51–63, 2007.

[183] I.I. Mazhul. Off-Design Regimes of Flow Past Waveriders Based on Isentropic Compression Flows. *Fluid Dynamics*, 45(2):271–280, 2010.

[184] T. Cavalcanti Rolim, P.G. de Paula Toro, A. Sala Minucci, M.A. de Carlos de Oliveira, and R. da Cunha Follador. Experimental Results of a Mach 10 Conical-Flow Derived Waverider to 14-X Hypersonic Aerospace Vehicle. *Journal of Aerospace Technology and Management*, 3(2):127–136, 2010.

[185] A. Ueno, S. Imamura, and H. Taguchi. Experimental and Numerical Study on Aerodynamic Design of Hypersonic Vehicle. In *17th AIAA International Space Planes and Hypersonic Systems and Technologies Conference*, 11-14 April, San Francisco, California 2011.

[186] M.L. Rasmussen and X. He. Analysis of Cone-Derived Waveriders by Hypersonic Small-Disturbance Theory. In *Proceedings of the First International Hypersonic Waverider Symposium*, 17-19 October, University of Maryland, College Park, Maryland 1990.

[187] H. Sobieczky, F.C. Dougherty, and K.D. Jones. Hypersonic Waverider Design from Given Shock Waves. In *Proceedings of the First International Hypersonic Waverider Symposium*, 17-19 October, University of Maryland, College Park, Maryland 1990.

[188] K.D. Jones, H. Sobieczky, A.R. Seebass, and F.C. Dougherty. Waverider Design for Generalized Shock Geometries. *Journal of Spacecraft and Rockets*, 32(6):957–963, 1995.

[189] T.R.F. Nonweiler. Delta Wings of Shape Amenable to Exact Shock Wave Theory. *Journal of the Royal Aeronautical Society*, 67:39, 1962.

[190] G.I. Taylor and J.W. Maccoll. The Air Pressure on a Cone Moving at High Speeds. *Proceedings of the Royal Society of London A*, 139:279–311, 1933.

[191] K.G. Bowcutt, J.D. Anderson, and D Capriotti. Viscous Optimized Hypersonic Waveriders. In *25th AIAA Aerospace Sciences Meeting*, 12-15 January, Reno, Nevada 1987.

[192] E.H. Hirschel and C. Weiland. *Selected Aerothermodynamic Design Problems of Hypersonic Flight Vehicles*. Springer-Verlag Berlin Heidelberg, 2009.

[193] M.J. Gillum and M.J. Lewis. Experimental Results on a Mach 14 Waverider with Blunt Leading Edges. *Journal of Aircraft*, 34(3):296–303, 1997.

[194] R.P. Starkey and M.J. Lewis. Simple Analytical Model for Parametric Studies of Hypersonic Waveriders. *Journal of Spacecraft and Rockets*, 36(4):516–523, 1999.

[195] Boeing X-51 Waverider. www.af.mil/AboutUs/FactSheets/Display/tabid/224/Article/104467/x-51a-waverider.aspx (accessed August, 2015).

[196] Intermediate eXperimental re-entry Vehicle (IXV). www.esa.int/Our_Activities/Launchers/IXV (accessed August, 2015).

[197] HEXAFLY project. www.esa.int/Our_Activities/Space_Engineering_Technology/High-Speed_Experimental_Fly_Vehicles (accessed August, 2015).

[198] LAPCAT project. www.esa.int/Our_Activities/Space_Engineering_Technology/LAPCAT_II (accessed August, 2015).

[199] Y.F. Chou, S.C. Lin, and C.K. Feng. Nonlinear Asymptotic Theory of Hypersonic flow past a Circular Cone. *Acta Mechanica*, 130:1–15, 1998.

[200] G.A. Candler. Rate-Dependent Energetic Processes in Hypersonic Flows. *Progress in Aerospace Sciences*, 72:37–48, 2015.

[201] M. Capitelli, I. Armenise, and C. Gorse. State-to-State Approach in the Kinetics of Air Components Under Re-Entry Conditions. *Journal of Thermophysics and Heat Transfer*, 11(4):570–578, 1997.

[202] E.V. Kustova and D. Giordano. Cross-Coupling Effects in Chemically Non-Equilibrium Viscous Compressible Flows. *Chemical Physics*, 379:83–91, 2011.

[203] E.V. Kustova and G.M. Kremer. Chemical Reaction Rates and Non-Equilibrium Pressure of Reacting Gas Mixtures in the State-to-State Approach. *Chemical Physics*, 445:82–94, 2014.

[204] J.G. Kim and I.D. Boyd. State-Resolved Master Equation Analysis of Thermochemical Nonequilibrium of Nitrogen. *Chemical Physics*, 415:237–246, 2013.

[205] V.A. Rykov. Macroscopic Description of the Motions of a Gas with Rotational Degrees of Freedom. *Fluid Dynamics*, 13(1):144–147, 1978.